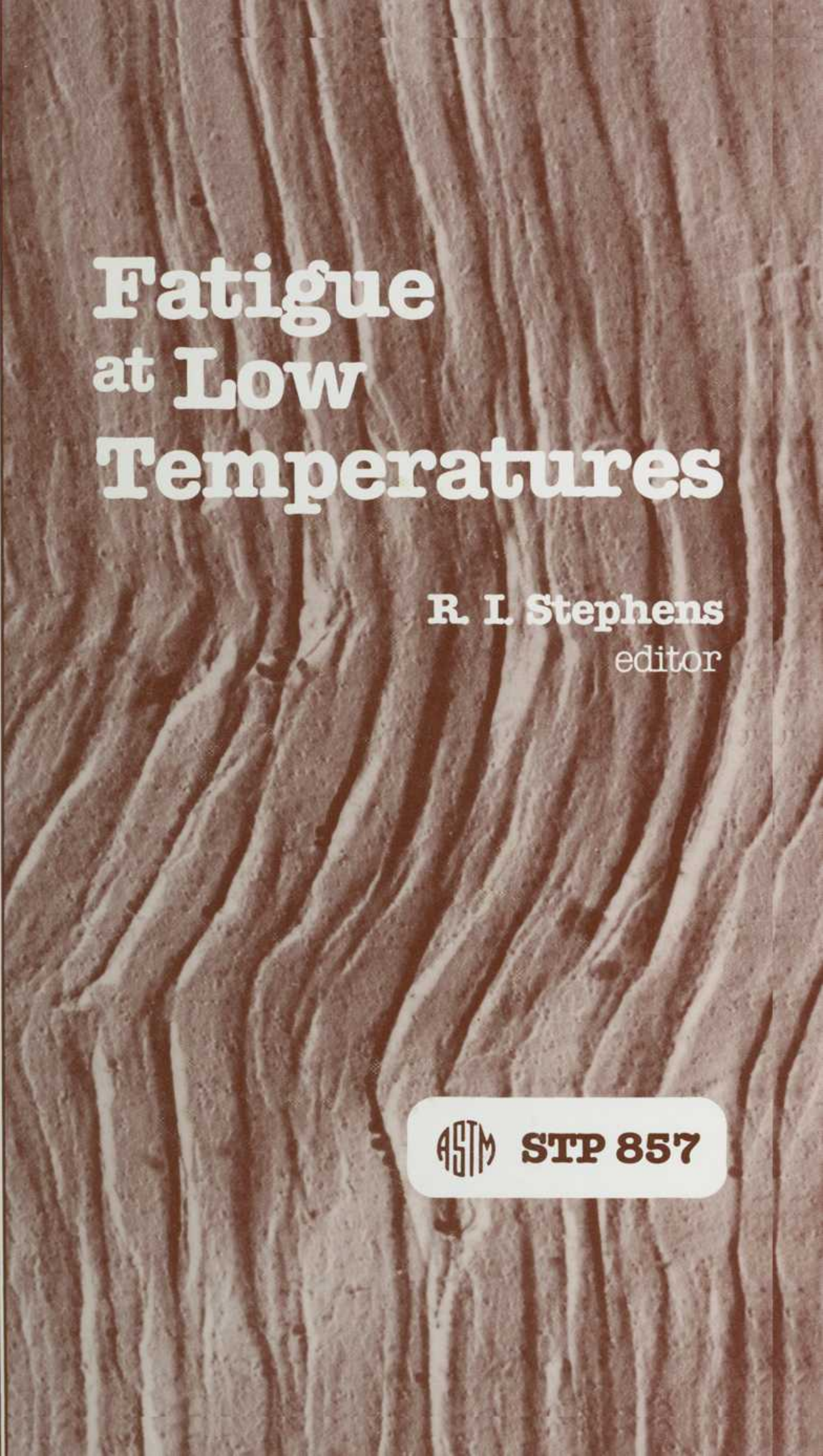

Fatigue at Low Temperatures

R. I. Stephens
editor

ASTM STP 857

FATIGUE AT LOW TEMPERATURES

A symposium sponsored by
ASTM Committees E-9 on Fatigue
and E-24 on Fracture Testing
Louisville, KY, 10 May 1983

ASTM SPECIAL TECHNICAL PUBLICATION 857
R. I. Stephens, The University of Iowa, editor

ASTM Publication Code Number (PCN)
04-857000-30

ASTM 1916 Race Street, Philadelphia, PA 19103

Library of Congress Cataloging in Publication Data

Fatigue at low temperatures.

(ASTM special technical publication; 857)
Papers from the Symposium on Fatigue at Low Temperatures.
Includes bibliographies and index.
"ASTM publication code number PCN 04-857000-30."
1. Metals—Fatigue—Congresses. 2. Metals at low temperatures—Congresses. I. Stephens, R. I. (Ralph Ivan) II. American Society for Testing and Materials. Committee E-9 on Fatigue. III. ASTM Committee E-24 on Fracture Testing. IV. Symposium on Fatigue at Low Temperatures (1983; Louisville, Ky.) V. Series.
TA460.F37 1985 620.1'63 84-70334
ISBN 0-8031-0411-1

Library of Congress Catalog Card Number: 84-70334

NOTE

The Society is not responsible, as a body,
for the statements and opinions
advanced in this publication.

Printed in Ann Arbor, MI
March 1985

Foreword

The Symposium on Fatigue at Low Temperatures was presented in Louisville, Kentucky, on 10 May 1983 at the ASTM May committee week. ASTM Committees E-9 on Fatigue and E-24 on Fracture Testing sponsored the event. R. I. Stephens, The University of Iowa, served as symposium chairman and has also edited this publication. The symposium organizing committee and session chairmen were W. W. Gerberich, The University of Minnesota, D. E. Pettit, Lockheed-California Company, R. L. Tobler, National Bureau of Standards, and R. I. Stephens.

Related ASTM Publications

Fatigue Mechanisms: Advances in Quantitative Measurement of Physical Damage, STP 811 (1983), 04-811000-30

Design of Fatigue and Fracture Resistant Structures, STP 761 (1982), 04-761000-30

Fatigue Mechanisms, STP 675 (1979), 04-675000-30

Properties of Materials for Liquefied Natural Gas Tankage, STP 579 (1975), 04-579000-30

Fatigue and Fracture Toughness—Cryogenic Behavior, STP 556 (1974), 04-556000-30

Fracture Toughness Testing at Cryogenic Temperatures, STP 496 (1971), 04-496000-30

A Note of Appreciation to Reviewers

The quality of the papers that appear in this publication reflects not only the obvious efforts of the authors but also the unheralded, though essential, work of the reviewers. On behalf of ASTM we acknowledge with appreciation their dedication to high professional standards and their sacrifice of time and effort.

ASTM Committee on Publications

Contents

SUMMARY

Introduction

Many fatigue designs, in quite diversified fields of engineering, must operate at temperatures below room temperature. These operating temperatures may be as low as 219 K (−54°C) for ground vehicles, civil structures, pipelines, and aircraft, 110 K (−163°C) for natural gas storage and transport, 77 K (−196°C) for liquid nitrogen storage and transport, 20 K (−253°C) for aerospace structures, and 4 K (−269°C) for superconducting electrical machinery. This volume brings together the latest basic and applied research on fatigue at these low temperatures.

There has long been a need for a publication such as this. An appreciable period of time has passed since the major reviews on the subject (Teed in 1950 and Forrest in 1963).[1] Also, a review of fatigue textbooks indicates that they give little attention (from zero to about four pages) to fatigue at low temperatures. Many of these textbooks have suggested that fatigue design at room temperature is very often satisfactory for low temperatures. Substantial fatigue data do exist that promote this concept; however, most of these data have been obtained under constant-amplitude conditions, which can lead to erroneous design decisions. Even with constant-amplitude tests, however, sufficient data exist that invalidate the general concept that fatigue resistance at low temperatures is equal to or better than fatigue resistance at room temperature. In addition, variable-amplitude low-temperature fatigue behavior data are quite scarce. Thus a general lack of complete confidence in and understanding of fatigue behavior at low temperatures currently exists. It is hoped that this ASTM publication will lead to improving our knowledge concerning fatigue at low temperatures.

This volume consists of 16 papers on low-temperature fatigue. Seven papers involve cryogenic temperatures with liquid nitrogen (77 K), liquid hydrogen (20 K), or liquid helium (4 K), and nine papers deal with noncryogenic temperatures. The book is divided into two sections: (1) Mechanisms and Material Properties, and (2) Spectrum Loading, Structures, and Applications. Within each section, the cryogenic temperature papers have been separated from the noncryogenic papers.

[1] Teed, P. L., *The Properties of Metallic Materials at Low Temperatures,* Chapman and Hall, London, 1950; Forrest, P. G., *Fatigue of Metals,* Pergamon Press, Elmsford, N.Y., 1963.

The international flavor of this volume should be noted. Papers have been contributed by authors from the United States, Japan, the Soviet Union, Israel, China, and the United Kingdom. The authors' affiliations include universities (Metallurgy, Material Science, and Mechanical Engineering Departments), industry (including aerospace, steel, and nuclear fields), and five different governmental research laboratories.

The principal aspect of fatigue at low temperatures studied in this volume is fatigue crack growth of metals using compact type, center cracked panels, or bend specimens under constant-amplitude loading. The fatigue crack growth rates investigated range from 5×10^{-11} to 10^{-4} m/cycle, with a fairly even distribution between threshold and near-threshold interests, to that above 10^{-8} m/cycle. Four papers discuss fatigue crack growth behavior under spectrum loading; one of these papers also studies fatigue crack initiation under spectrum loading using a notched specimen. Low-cycle strain-controlled fatigue using smooth uniaxial specimens with ϵ–N (strain versus cycles to failure) and cyclic softening/hardening behavior is covered in two papers, and fiberglass epoxy laminate S–N (stress versus cycles to failure) fatigue behavior is investigated in another. The metal alloy systems discussed include carbon or low alloy wrought and cast steels, austenitic stainless steels, high-manganese austenitic stainless steels, and base alloys of aluminum, magnesium, titanium, and nickel. Analysis of fatigue behavior has relied heavily on electron fractography, especially in the areas of ductile- and cleavage-type fatigue crack growth. Crack closure, crack-tip plasticity, yield strength, ductile/brittle transitions, and dislocation dynamics are the principal means of discussing the test results.

It is believed that this volume, with its wide-ranging coverage of materials processing, loading types, temperatures, fractographics, mechanisms, and its 325 cited references (some repeated in different papers), provides an important contribution to the subject of fatigue at low temperatures. This publication will be beneficial to material scientists, metallurgists, and engineers involved in research and design under fatigue conditions at both cryogenic and noncryogenic low temperatures.

R. I. Stephens
Mechanical Engineering Department,
The University of Iowa,
Iowa City, IA; symposium
chairman and editor

Mechanisms and Material Properties

Cryogenic Temperatures

Ralph L. Tobler and Yi-Wen Cheng

Midrange Fatigue Crack Growth Data Correlations for Structural Alloys at Room and Cryogenic Temperatures

REFERENCE: Tobler, R. L. and Cheng, Y. W., "**Midrange Fatigue Crack Growth Data Correlations for Structural Alloys at Room and Cryogenic Temperatures,**" *Fatigue at Low Temperatures, ASTM STP 857,* R. I. Stephens, Ed., American Society for Testing and Materials, Philadelphia, 1985, pp. 3–30.

ABSTRACT: Fatigue crack growth rate data for pure metals, structural alloys, and welds at temperatures from 295 to 4 K are selectively reviewed. The data for more than 200 material and temperature combinations are discussed in terms of the parameters C and n for the midrange of the da/dN-versus-ΔK curve. Fatigue resistance varies greatly among the different alloy classes and crystal structure types, especially at extreme cryogenic temperatures, where alternative failure mechanisms emerge. Good general correlations were achieved on the basis of Young's modulus, fracture toughness, and empirical equations relating C and n for each alloy class.

KEY WORDS: austenitic stainless steels, cryogenic properties of metals, fatigue, fatigue crack growth, fracture toughness, structural alloys, Young's modulus

To the surprise of many at the time, Paris and his colleagues [*1,2*] correlated fatigue crack growth rates (da/dN) with the linear-elastic stress intensity factor range (ΔK). For the midrange of the da/dN-versus-ΔK curve they proposed the power-law equation

$$da/dN = C(\Delta K)^n \tag{1}$$

where the parameters C and n were interpreted as material constants. Subsequent studies have shown that material behavior in this range is governed by continuum mechanics and is strongly dependent on Young's modulus (E). Often there is a remarkable insensitivity to metallurgical and microstructural variables [*3,4*]. In theory, the conventional mechanical properties, such as

The work described in this paper is supported by the Office of Fusion Energy, Department of Energy, and is not subject to copyright.

The authors are with the Fracture and Deformation Division of the National Bureau of Standards in Boulder, CO 80303.

yield strength (σ_y) and fracture toughness (K_{Ic}), play significant roles, but in practice their influence has been difficult to predict.

For alloy families at room temperature, it has been shown that the coefficients and exponents of Eq 1 are related by the expression

$$C = A(1/\Delta K_0)^n \tag{2}$$

or, equivalently,

$$\log C = \log A + n \log (1/\Delta K_0) \tag{3}$$

Kitagawa and Misumi [*5,6*] first demonstrated these relationships for ferritic steels. Correlations for austenitic steels, titanium alloys, and aluminum alloys (all at room temperature) indicate that for each alloy system A and ΔK_0 depend on the fatigue stress ratio (R), but are independent of metallurgical and microstructural variations and environment to a considerable extent [*7–15*]. Here, the parameters A (mm/cycle) and ΔK_0 (MPa·m$^{1/2}$) correspond to the coordinates of a pivot point where the da/dN-versus-ΔK curves for a given alloy system intersect [*15*].

The present paper surveys the available data for cryogenic structural alloys, seeking simple correlations between fatigue crack growth rates and conventional mechanical properties. Following a previous study [*16*], Eqs 2 and 3 are used to describe data at cryogenic temperatures where the C and n parameters for materials show great variations. Pivot points for various alloy families are calculated and compared, and the concepts of structure-sensitive and structure-insensitive da/dN behavior are discussed.

Materials and Procedures

The C and n parameters for a variety of materials [*17–44*][1] were collected and reviewed. The alloys of interest are grouped as follows:

1. Ferritic nickel steels (high-modulus body-centered-cubic [bcc] alloys).
2. Austenitic stainless steels (high-modulus face-centered-cubic [fcc] alloys, stable or metastable with respect to martensitic phase transformations at cryogenic temperatures).
3. Nickel-base superalloys (high-modulus fcc alloys).
4. Titanium-base alloys (intermediate-modulus hexagonal close-packed [hcp] or hcp + bcc alloys).
5. Aluminum-base alloys (low-modulus fcc alloys).

[1] See also Tobler, R. L. and Reed, R. P., "Interstitial Carbon and Nitrogen Effects on the Cryogenic Fatigue Crack Growth of AISI Type 304 Stainless Steels," submitted to *Journal of Testing and Evaluation.*

Data describing pure metals and austenitic steel or nickel-base alloy welds produced by various processes and filler metals are also briefly considered.

The majority of the data were measured at the National Bureau of Standards by using compliance methods and compact or bend specimens with constant-amplitude loading, typically at a stress ratio of $R = 0.1$ and at frequencies of 20 ± 10 Hz. Additional relevant data from other sources are included for comparison and confirmation, but an exhaustive search was not attempted. Three temperatures and media are of primary interest: 296 ± 2 K (room-temperature air), 76 or 77 K (liquid nitrogen), and 4 or 4.2 K (liquid helium). At these temperatures, substantial tensile, fracture, and elastic property data are available for correlations. The K_{Ic} values referred to in the text are direct measurements or estimates from J-integral tests. The E moduli are taken from original publications, handbooks, or review papers [*45–47*]. For further details it is necessary to refer to the original publications [*17–44*].

Results

General data trends for alloy systems of major engineering significance are presented in Fig. 1. Each alloy system shows greater property variations at cryogenic temperatures than at room temperature. Three alloy systems are considered: (1) ferritic steels containing up to 18% nickel (Ni) (bcc structures), (2) austenitic stainless steels (fcc, both stable and metastable alloys), and (3) austenitic nickel-base alloys (stable fcc structure). The pivot points

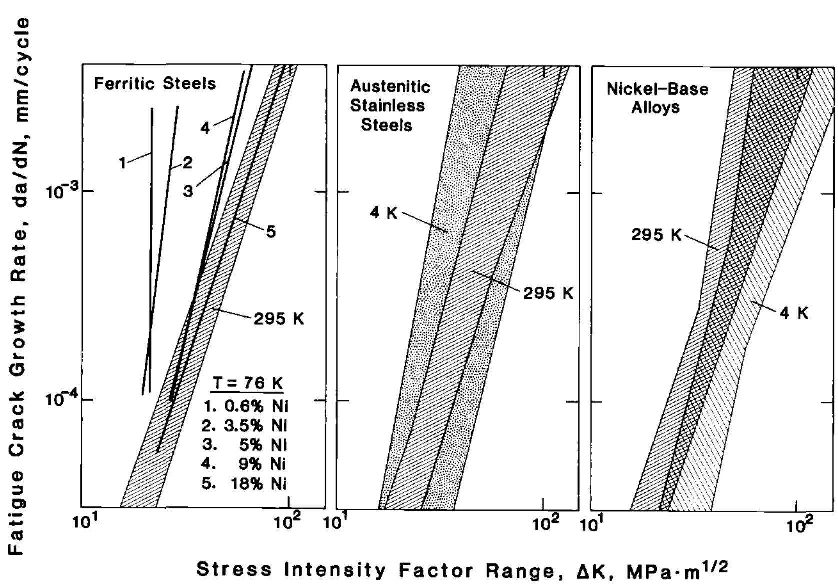

FIG. 1—*Fatigue crack growth rate data trends for alloys at room and cryogenic temperatures.*

for these data are discussed later in the text. The general behavior is summarized below.

At 295 K, the materials are ductile and tough, and fatigue crack growth is produced by reversed plastic flow in the crack tip zones. The fatigue exponent (n) typically ranges from 2 to 4. Striation formations, resolvable by scanning electron microscopy at higher ΔK, are the principal failure mechanisms.

At 76 or 4 K, behavior is more diverse. Systematic compositional effects emerge, such as the effect of nickel content in the ferritic steels at low temperature. In many cases, the ductile striation mechanisms at 295 K are replaced by brittle mechanisms at 76 or 4 K, and the fatigue exponents are inflated to values greater than 4. Transgranular or intergranular fatigue facets are observed, even in some austenitic stainless steels. Extensive martensitic phase transformations occur in some metastable austenitic stainless steels and may affect behavior at cryogenic temperatures.

Correlation of n *with Yield Strength or Fracture Toughness*

Figure 2 illustrates relationships between the fatigue exponents and the conventional material properties for alloys having nearly equivalent values of E. As shown, n tends to increase at high σ_y or at low K_{Ic}. (In general, σ_y is inversely related to K_{Ic}.) The sizable scatter here occurs because data for different steels and nickel-base alloys have been combined with data for welds. The n-versus-K_{Ic} plots for individual alloy families (Figs. 3 and 4) show more uniform trends. In these figures, two regions of behavior are clearly identifiable:

1. *Region I (the low-toughness region)*—The fatigue behavior depends on K_{Ic}, n increasing as K_{Ic} decreases.
2. *Region II (the high-toughness region)*—The fatigue behavior is independent of K_{Ic}, and n remains constant in the range 2 to 4.

This two-stage behavior appears to be a basic feature for all metals. The point of transition from toughness-dependent to toughness-independent behavior is material-dependent and not yet predictable. Apparently the transition point hinges on the type of failure mechanisms operating, and these can be gaged approximately by the magnitude of K_{Ic}. In Region I, brittle fatigue and fracture mechanisms are observed, whereas in Region II, ductile mechanisms are observed. The significance of the failure mechanisms in affecting this two-stage behavior is taken up later in the discussion.

A correlation between n and K_{Ic} (Region I) has significant implications. Like σ_y, K_{Ic} is dependent on metallurgical and microstructural variables and temperature. Since regions of K_{Ic}-dependent and K_{Ic}-independent behavior exist, a broader conclusion follows, namely that the fatigue crack growth data of materials in general must exhibit two regimes of behavior. One is

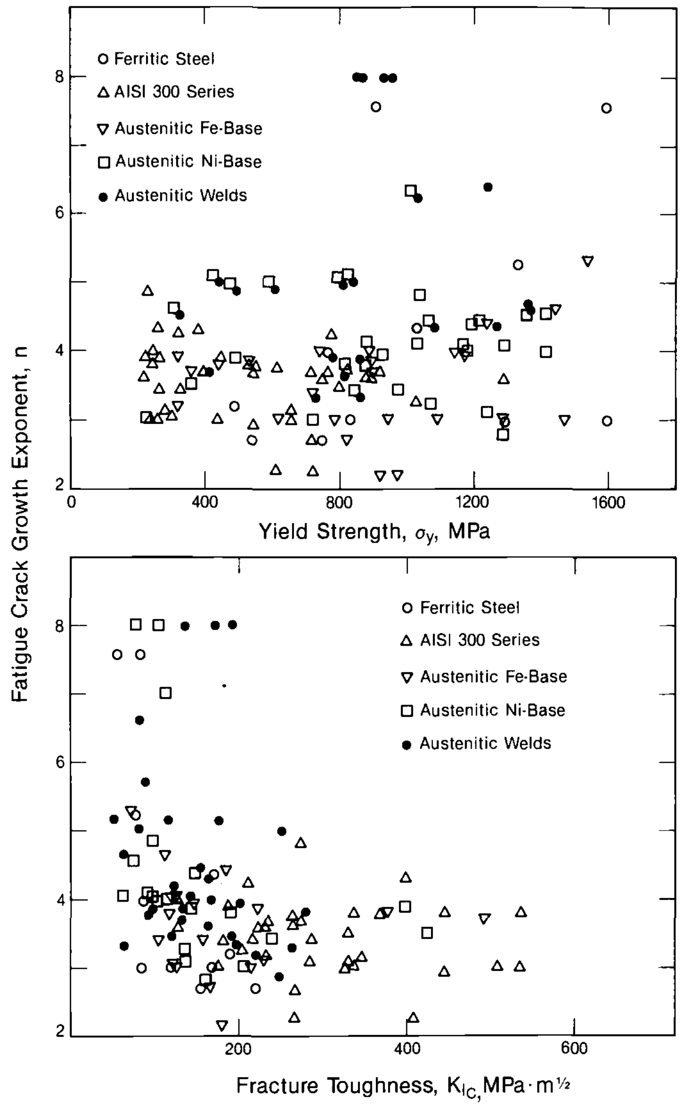

FIG. 2—*Correlation of fatigue exponent* n *with the conventional yield strength and fracture toughness.*

sensitive to metallurgical variables and temperature, while the other is not. The following sections demonstrate some ramifications of this idea for low-temperature fatigue.

Correlation of n *and Temperature*

In Region I, where *n* is inversely related to K_{Ic}, a dependence of *n* on test temperature is expected, since temperature influences K_{Ic}. This is shown in

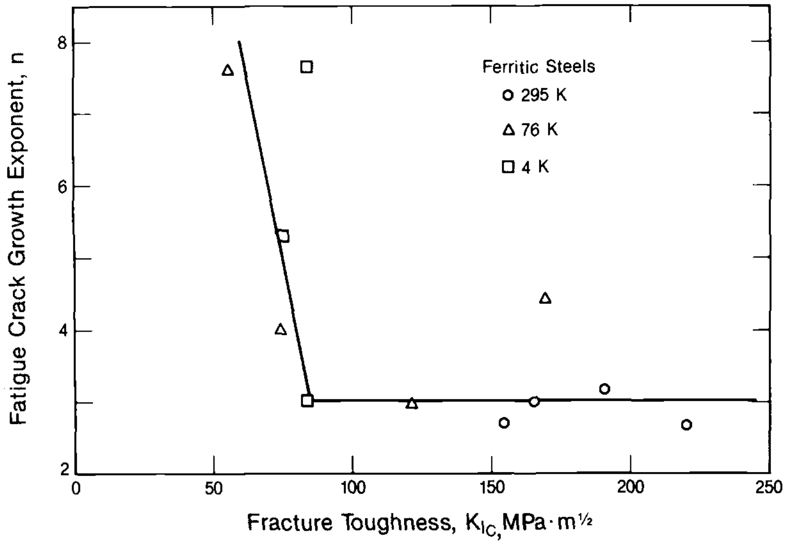

FIG. 3—*Correlation of* n *and* K_{Ic} *for various ferritic nickel steels.*

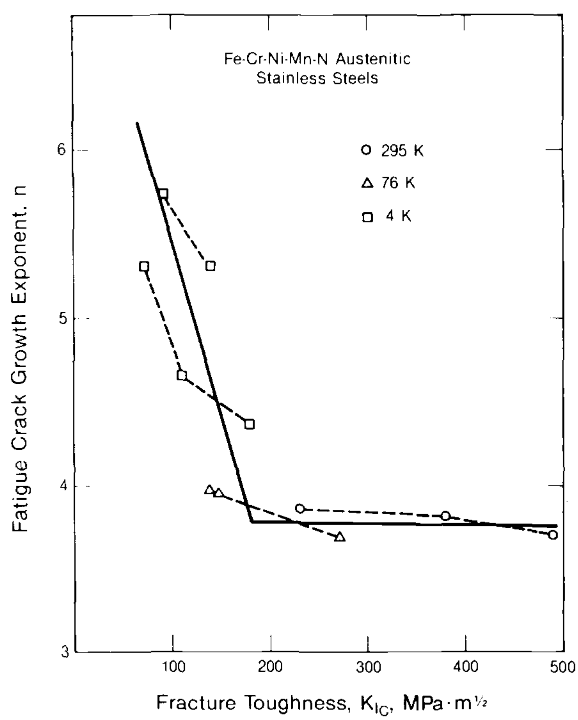

FIG. 4—*Correlation of* n *and* K_{Ic} *for various nitrogen-strengthened Fe-Cr-Ni-Mn austenitic stainless steels.*

Figs. 5 and 6, where *n* and K_{Ic} are plotted versus temperature for 9% Ni ferritic steel and a high-strength Fe-18Cr-3Ni-13Mn-0.37N austenitic steel. In both cases, *n* becomes inversely related to K_{Ic} and increases to values greater than 4 at extreme cryogenic temperatures when K_{Ic} is reduced sufficiently to reach Region I.

As noted previously, there is no similar effect for the conventional AISI 300 series austenitic stainless steels [*16*]. The explanation relates to the correlation between *n* and K_{Ic}, as described above. High-strength alloys such as ferritic steels, are subject to ductile-brittle transitions (DBT). AISI 300 series stainless steels, owing to their fcc structure and relatively low or medium strength, do not exhibit DBT transitions, even at extreme cryogenic temperatures. Thus, as the temperature is decreased to the cryogenic range, ferritic steels shift from Region II to Region I behavior, whereas AISI 300 series steels always maintain Region II behavior.

Correlation of n *and Composition*

Nickel additions to ferritic steels lower the DBT temperature while increasing K_{Ic} at subtransition temperatures. Therefore composition is a crucial influence on ferritic steels at low temperatures. In Fig. 7, *n* for ferritic steels is plotted as a function of nickel content at two temperatures, one ambient and one cryogenic. At 76 K, *n* decreases as nickel increases from 0 to 5%, but at higher nickel contents *n* is insensitive to composition. Again, this

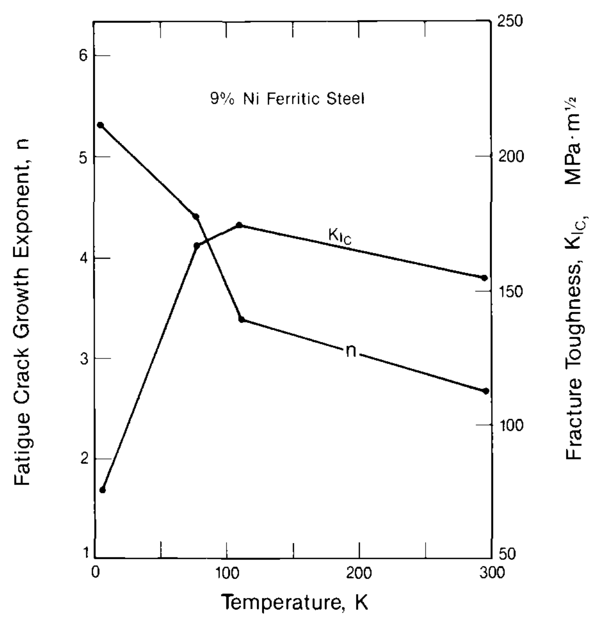

FIG. 5—*Effect of temperature on* n *and* K_{Ic} *for 9% Ni ferritic steel.*

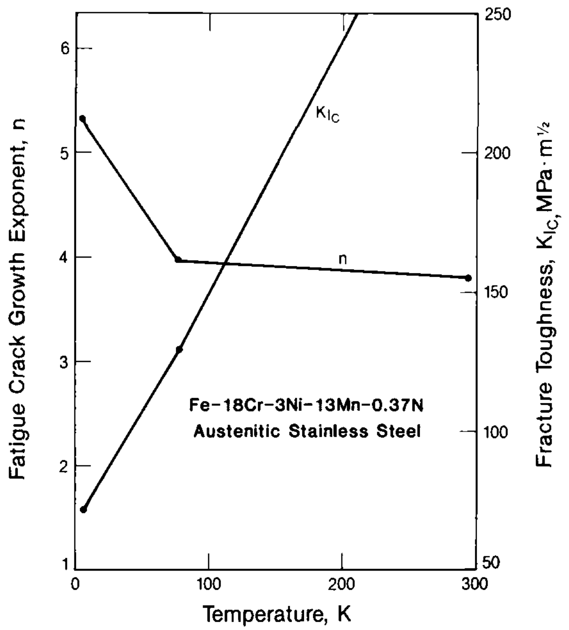

FIG. 6—*Effect of temperature on* n *and* K_{Ic} *for nitrogen-strengthened Fe-Cr-Ni-Mn austenitic stainless steel.*

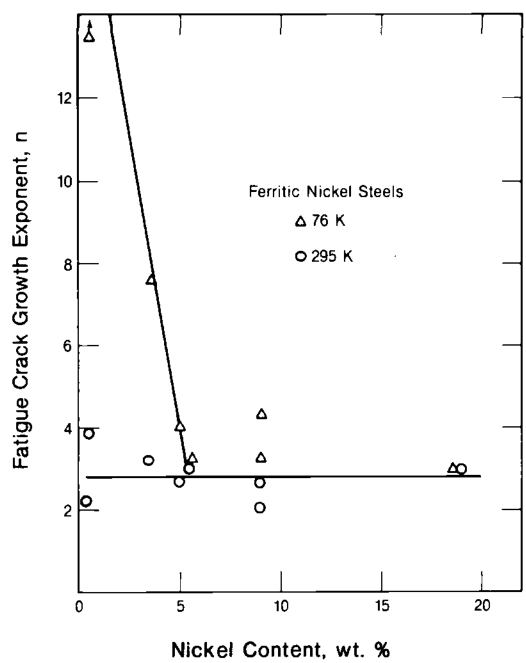

FIG. 7—*Effect of nickel content on fatigue exponent of ferritic steels at 295 and 76 K.*

relates to the interaction of n with K_{Ic}; this time the outcome depends on whether the composition is conducive to Region I or Region II behavior. The Fe-Ni binary alloys behave similarly [*48*].

Correlation of log C *and* n

The purpose of this section is to apply Eqs 2 and 3 to cryogenic data. Accordingly, the log C-versus-n plots for various structural alloys are shown in Figs. 8 and 9. Each data set demonstrates the C and n dependence expected from Eq 3, which makes it possible to seek correlations with one parameter (n) only.

Data for pure iron [*17*], titanium [*39*], and aluminum [*40,41*] are also plotted using solid symbols (● = 295 K, ▲ = 77 K) on the appropriate graphs in Figs. 8 and 9. In comparison, pure metals often do not fit the data trends for their respective alloys. For unalloyed iron and aluminum, the temperature

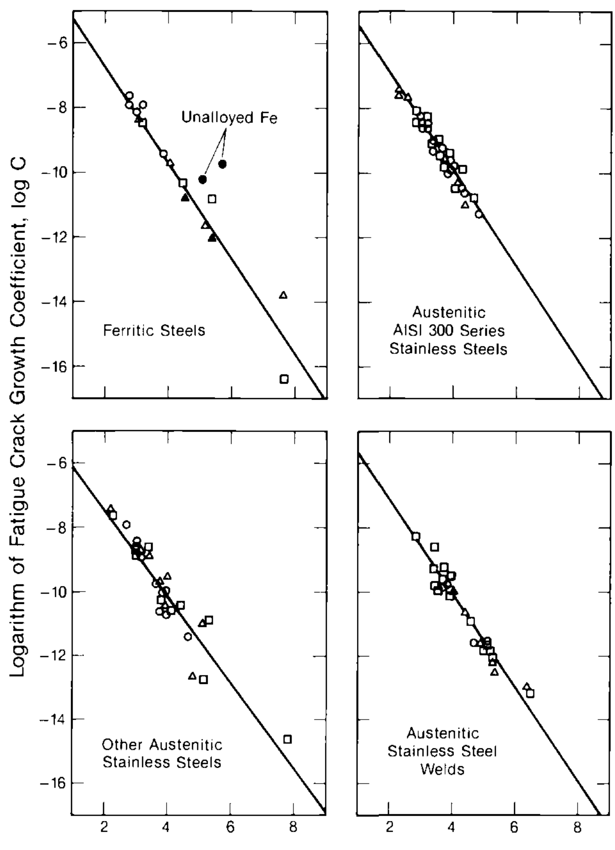

FIG. 8—*Log C-versus-*n *relationship for various steels* (○ = *295 K,* △ = *76 K,* □ = *4 K*).

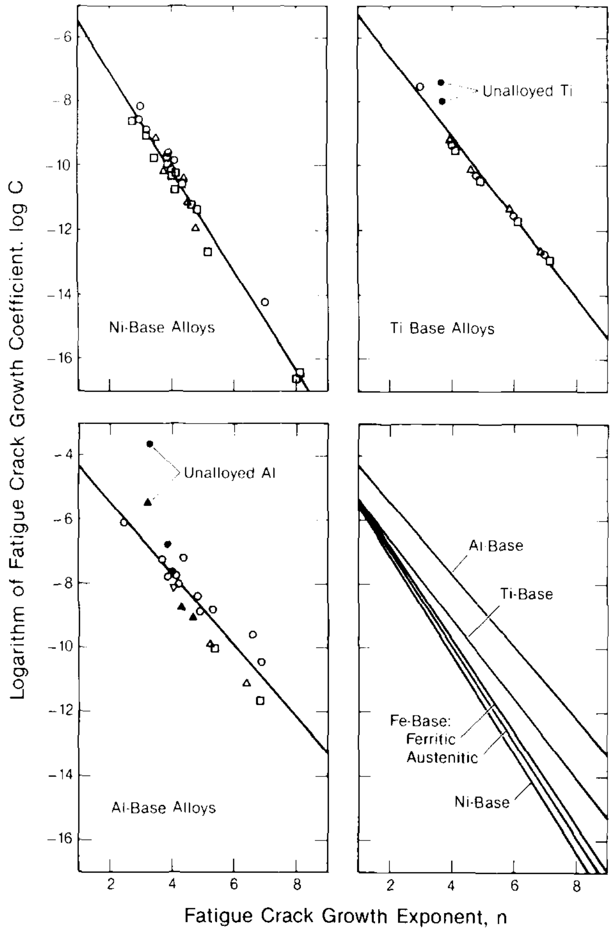

FIG. 9—*Log* C*-versus-*n *relationship for three alloy systems having different elastic moduli and comparison of several systems* (○ = *295 K,* △ = *76 K,* □ = *4 K*).

reduction from 295 to 76 K produces contrary effects: in the case of iron, log *C* decreases while *n* decreases, whereas for aluminum, log *C* decreases while *n* is constant. In contrast, Eq 3 indicates that log *C* should decrease as *n* increases.

Least-squares regression analyses for the log *C*-versus-*n* plots, excluding the nonconforming data for pure metals, are summarized in Table 1. Fairly good fits are obtained, some of which may be improved by distinguishing temperature effects or differences in failure mechanisms. As listed in Table 1, the correlation coefficients range from 0.92 to 0.99 (1.0 implies a perfect correlation). Characteristics of the alloys' distinctive fatigue behavior are noted in the following paragraphs.

Ferritic Steels—The spread of *n* increases at 4 K, reaching values up to 8.

TABLE 1—*Pivot point calculations for structural alloy families.*

Materials Tested	Temperature, K	No. of Data Points	Log A and Standard Deviation	Log $(1/\Delta K_0)$ and Standard Deviation	Correlation Coefficient	A, 10^{-4} mm/cycle	ΔK_0, $MPa \cdot m^{1/2}$
Ferritic nickel steels	295 to 4	16	−3.769, 0.517	−1.468, 0.114	−0.97	1.71	29.4
AISI 300 series stainless steels	295 to 4	50	−3.888, 0.368	−1.497, 0.099	−0.97	1.29	31.4
Various austenitic stainless steels	295 to 4	31	−4.739, 0.338	−1.332, 0.084	−0.95	0.18	21.5
Austenitic stainless steel welds	295 to 4	29	−4.134, 0.553	−1.476, 0.124	−0.92	0.73	29.9
Nickel-base alloys	295 to 4	28	−3.924, 0.234	−1.560, 0.052	−0.98	1.19	36.3
Nickel-base alloys	295 only	8	−4.055, 0.294	−1.448, 0.693	−0.99	0.9	28.0
Nickel-base alloys	76, 4 only	20	−3.974, 0.242	−1.576, 0.519	−0.99	1.1	37.7
Nickel-base alloy welds	295 to 4	14	−2.605, 0.173	−1.750, 0.026	−0.99	24.8	56.2
Titanium-base alloys	295 to 4	13	−4.034, 0.448	−1.255, 0.087	−0.99	0.93	18.0
Aluminum-base alloys	295 to 4	19	−3.242, 0.617	−1.119, 0.135	−0.90	5.73	13.2
Aluminum-base alloys	295 only	13	−3.945, 0.470	−0.889, 0.995	−0.93	1.1	7.7
Aluminum-base alloys	76, 4 only	6	−3.456, 0.313	−1.217, 0.571	−0.99	3.5	16.5

A single log C-versus-n regression apparently fits the majority of data from 295 to 4 K. The scatter increases, however, when cryogenic data are admitted to the correlation, and it is appropriate to exclude data for extraordinarily brittle steels from the correlation [*15*].

AISI 300 Austenitic Series Stainless Steels—The log C-versus-n plot appears to be temperature-independent from 295 to 4 K, and n does not increase significantly at 4 K, in contrast to the behavior of ferritic steels.

Other Austenitic Stainless Steels—In this group are the Fe-Cr-Mn, Fe-Ni-Cr, and Fe-Cr-Ni-Mn-N steels that were not included in the AISI 300 series. Owing to exceptional strength in some grades, a behavior similar to ferritic steels is observed at 4 K: high n values (up to 8) are obtained and the scatter in log C-versus-n plots increases.

Nickel Alloys—The available data are for superalloys having E moduli only slightly higher than steels. For these alloys the correlations slightly improve if temperature effects are separated; the log C-versus-n plots then give a slightly lower pivot point at 76 and 4 K than at 295 K.

Titanium Alloys—The data are limited to measurements for some Ti-5Al-2.5Sn and Ti-6Al-4V alloys, for which the log C-versus-n plot shows a high correlation with no temperature dependence.

Aluminum Alloys—Again, cryogenic data are limited, but the correlation coefficients for log C versus n improve significantly if temperature effects are distinguished. The pivot point and log C-versus-n trend at 76 and 4 K is clearly lower than at 295 K. This is similar to the effect observed in the nickel alloys, but stronger. The 295 K data derive largely from tests of a 3003-0 alloy in various environments, but there is no discernible environmental effect on log C versus n.

Pivot Points

The pivot points corresponding to each of the aforementioned alloy families are listed in Table 2. Approximate agreement among different alloy systems is found after normalization. Two normalizing parameters were considered: $\Delta K_0/E$ and $\Delta K_0/(E\sqrt{b})$ [*14*], where b is the equivalent of the Burgers vector and is taken from Cullity's list [*49*] of the distances of closest atomic approach for unalloyed metals. The correlations based on $\Delta K_0/E$ and on $\Delta K_0/(E\sqrt{b})$ are equally effective.

Discussion

Log C*-versus-*n *Correlations*

In principle, Eq 2 predicts that all da/dN curves must intersect at a single point (A, ΔK_0) and fan out as a function of n [*15*]. In fact, there are numerous materials with da/dN-versus-ΔK trends that fail to intersect at the calculated "pivot points." In practice, therefore, Eq 2 has been used to approxi-

TABLE 2—*Pivot point normalizations for structural alloy families.*

Materials Tested	Temperature, K	Average Modulus, GPa	A, 10^{-4} mm/cycle	ΔK_0, MPa·m$^{1/2}$	$\Delta K_0/E$, 10^{-4} m$^{1/2}$	$\Delta K_0/E(b)^{1/2}$
Ferritic nickel steels	295 to 4	202	1.71	29.4	1.46	9.3
AISI 300 series stainless steels	295 to 4	199	1.29	31.4	1.58	10.0
Various austenitic stainless steels	295 to 4	198	0.18	21.5	1.08	6.9
Austenitic stainless steel welds	295 to 4	198	0.73	29.9	1.51	9.6
Nickel-base alloys	295 to 4	209	1.19	36.3	1.74	11.0
Nickel-base alloys	295 only	203	0.9	28.0	0.138	8.7
Nickel-base alloys	76, 4 only	214	1.1	37.7	0.176	11.1
Nickel-base alloy welds	295 to 4	209	24.8	56.2	2.69	17.0
Titanium-base alloys	295 to 4	116	0.93	18.0	1.55	9.1
Aluminum-base alloys	295 to 4	76	5.73	13.2	17.4	10.3
Aluminum-base alloys	295 only	72	1.1	7.7	0.107	6.3
Aluminum-base alloys	76, 4 only	79	3.5	16.5	0.209	9.7

mate the entire data base, which includes nonconforming material behaviors. Under these circumstances, the calculated pivot points for various material classes are a measure of the center of gravity for the data in a statistical sense.

One limitation of representing fatigue crack growth results in terms of log C-versus-n plots and pivot points is that the ΔK ranges for the associated da/dN are not conveyed. Therefore, interpretations concerning individual alloy behavior must be guarded in view of the unspecified information and the approximate nature of such representations.

Although the log C-versus-n correlations are approximate, their usefulness for certain purposes cannot be denied. In this paper, the format suggested by Eq 3 provided a basis for concise data presentation, summary, and comparison. The trends of Figs. 8 and 9 serve to distinguish the exceptional behavior of pure metals. Similarly, some errors in the published C and n data for structural alloys were identified, since they disagreed with general trends. Finally, the pivot point normalizations conclusively demonstrate the strong effect of Young's modulus on da/dN.

Significance of Young's Modulus

Fatigue is the result of plastic deformation processes, but under the assumption of small-scale yielding, any plastic deformation is limited and localized at the crack tip. It is therefore possible to correlate da/dN with elastic parameters. For midrange behavior, da/dN is directly proportional to ΔK (an elastic stress-intensity factor) and $1/E$ (reciprocal of the elastic modulus). As a fundamental physical property relating to atomic binding forces, Young's modulus figures prominently in dislocation theory as well as continuum mechanics. A dependence of da/dN on $1/E$ is explicit in some analytical models of fatigue crack growth [*3*]. The significance of the modulus in fatigue crack growth is likewise evident from experimental correlations. The normalizing parameter ($\Delta K/E$) was first proposed by Anderson [*2*] and later used to correlate striation spacings [*50*], pivot points [*14*], and macroscopic fatigue crack growth rates [*4*].

From a materials viewpoint, E is fixed mainly by the primary alloy elements and is weakly dependent on secondary alloy elements, microstructure, and such related variables as cold work, heat treatment, or phase transformations [*45*]. Therefore, alloys of a given base metal system are always closely grouped with respect to elastic properties. It follows that if da/dN is strongly influenced by E and weakly dependent on the conventional mechanical properties, as postulated for Region II, then a structure-insensitive behavior is expected, since E itself is structure-insensitive.

Typically, the Young's moduli for metals at low temperature show "regular" behavior [*45*]: a nearly linear increase below 295 K, a plateau near 76 K, and little or no change between 76 K and absolute zero. For the alloys of this survey, the overall increase of E between 295 and 4 K never exceeds 11%. Such small changes are consistent with temperature-insensitive behavior in Region II.

Maraging steels seem to provide an excellent example of the structure- and temperature-insensitive Region II type behavior just described. Data for 18% Ni maraging steel at 295 K show no change in da/dN for the aged and unaged conditions [*51*], while for the unaged condition there is no difference in da/dN at 295 and 76 K [*23*]. In contrast, strong effects on σ_y and K_{Ic} are induced by aging or test-temperature reduction. The observations are plausible, assuming Region II behavior, because the aging step and test-temperature reduction to 76 K will increase E by only 9 and 5%, respectively.

Additional evidence for the role of Young's modulus derives from Fig. 1. If the 295 K data presented there are superimposed, the bands for the three material classes nearly overlap, despite significant differences in composition (iron- versus nickel-base) and crystal structure (bcc versus fcc, stable or metastable). This explanation is offered: these alloys have nearly equivalent moduli, and at 295 K all undergo fatigue by relatively ductile mechanisms involving reversed plastic flow in Region II where rather wide variations of σ_y and K_{Ic} are of minor consequence to fatigue crack growth.

Temperature Dependence

Some alloys show improved fatigue resistance at cryogenic temperatures, whereas others are degraded.

An improved performance cannot be attributed to favorable temperature effects on E, since any increase between 300 and 4 K is too small to account for measurable improvements in fatigue crack growth rates. Instead, we assume that significant temperature effects on the fatigue resistance at cryogenic temperatures are induced when the plastic work for fatigue crack propagation is altered. This may occur in conjunction with failure mode transitions, the effects combining competitively or synergistically to account for the diversity of behaviors observed at 76 or 4 K compared with those at 295 K.

Fine and Davidson [*52*] report the measurements of plastic work. Although few data are available at present, it is clear that temperature reductions can improve the fatigue crack growth resistance of some metals at cryogenic temperatures by increasing the plastic work for fatigue failure. For example, pure aluminum exhibits a hundredfold decrease of rates as temperature drops from 295 to 77 K, and the associated increase of energy required for unit fatigue crack extension at 77 K has been measured [*41*]. For an identical temperature reduction, the rates for the solid-solution alloy 5083-0 decrease three or four times [*42*]. Thus a similar but less powerful effect may operate in alloys. This may explain the improved fatigue crack growth resistance of the aluminum-base, nickel-base, and stable iron-base alloy families at cryogenic temperatures [*26*], but confirmation is needed.

Failure Micromechanisms

Temperature-induced transitions in microfailure mechanisms can introduce beneficial or detrimental effects, since the plastic work required for fatigue crack extension may thereby be increased or decreased. Transitions from ductile to brittle mechanisms cause a shift from Region II to Region I behavior as described in the text. In Fe-18Cr-3Ni-13Mn-0.37N steel, for example, the incidence of brittle mechanisms at 4 K drastically increased n (Fig. 5), eclipsing any favorable trend that may have been expected from a temperature effect on plastic work without a transition in failure mode.

The explanation offered for high n values in low-toughness alloys is that brittle-failure mechanisms associated with monotonic loading begin to operate concurrently with the cyclic mechanisms of crack growth [*53–55*]. This was proposed in a study of ferritic steels at room temperature where the brittle mechanism was intergranular fracture [*54*]. Another brittle mechanism common in ferritic steels at low temperature is transgranular cleavage. Both mechanisms generate brittle facets and both are sensitive to the maximum applied K level because they are subject to a critical tensile-stress failure criterion.

Inflated fatigue exponents with degraded fracture toughness occurs more commonly at cryogenic temperatures, owing to the increased probability of brittle failure mechanisms. In fact, this phenomenon is virtually universal at extreme cryogenic temperatures, having now been observed in some austenitic steels, as well as ferritic steels, and nickel-base, magnesium-base, and titanium-base alloys [*56–58*]. Among austenitic stainless steels, the high-strength Fe-Cr-Ni-Mn-N steels are susceptible at 4 K, whereas the relatively low-strength Fe-Cr-Ni (AISI 300 series) steels are not. Such behavior in austenitic stainless steels may seem surprising, since these materials are generally reputed to be ductile and tough at all temperatures. The newly developed Fe-Cr-Ni-Mn-N steels, however, contain up to 0.4% nitrogen, high enough to elevate σ_y and reduce K_{Ic} sufficiently at 4 K to attain Region I behavior.

The brittle mechanisms operating in cryogenic austenitic alloys may include transgranular crystallographic faceting, slip-band decohesion, twin-boundary parting, and intergranular fracture. Some representative fractographs are shown in Figs. 10 and 11. The brittle mechanisms operating at 4 K are quite distinct from the striation mechanisms operating at 295 K (Fig. 10). For example, a pronounced transgranular faceting occurs in annealed Fe-18Cr-3Ni-13Mn-0.37N austenitic stainless steel at 4 K (Fig. 11*a*). Inter-

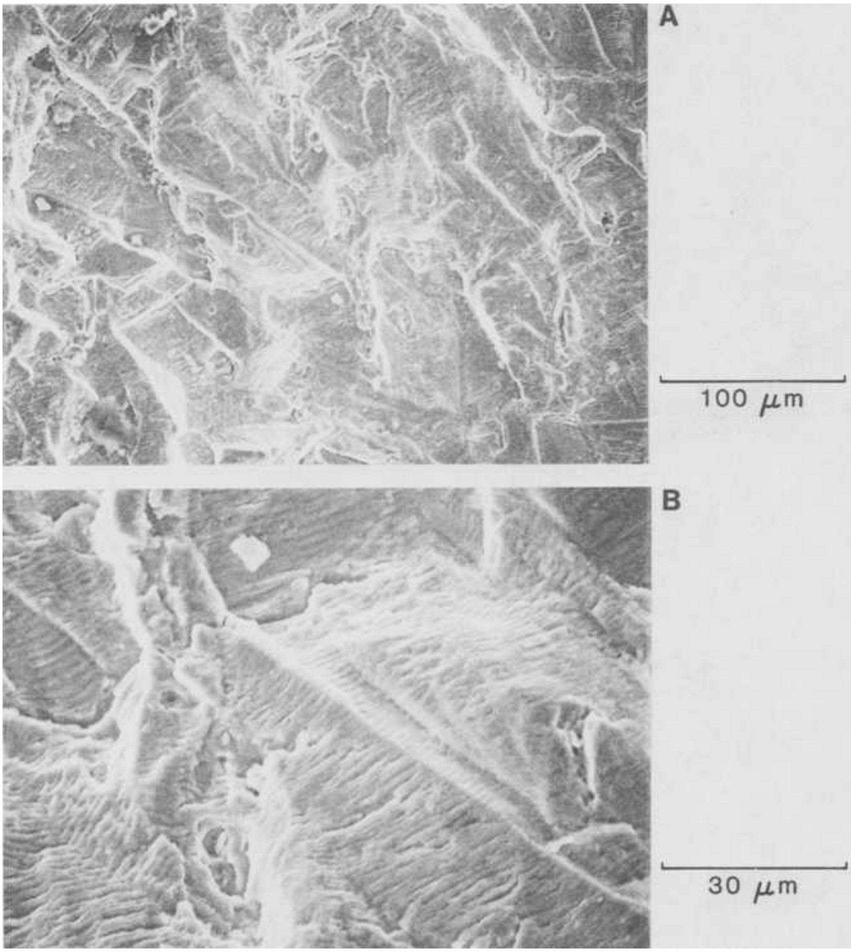

FIG. 10—*Fatigue failure mechanism in Fe-18Cr-3Ni-13Mn-0.37N austenitic stainless steel at 295 K.*

granular failure in this steel at 4 K is also induced after sensitization treatments, owing to the embrittling effects of chromium carbonitride precipitation along the grain boundaries (Figs. 11*b* and 11*c*).

Favorable transitions in fatigue failure mechanisms are also possible, although less common. An outstanding example of a favorable transition occurs in metastable AISI 304L stainless steel. In this steel, the usual transgranular crystallographic mechanism at 295 K (Fig. 12) is replaced at 76 K by a unique transgranular mechanism involving very fine, nondistinct features producing a very smooth macroscopic failure surface (Fig. 13). This

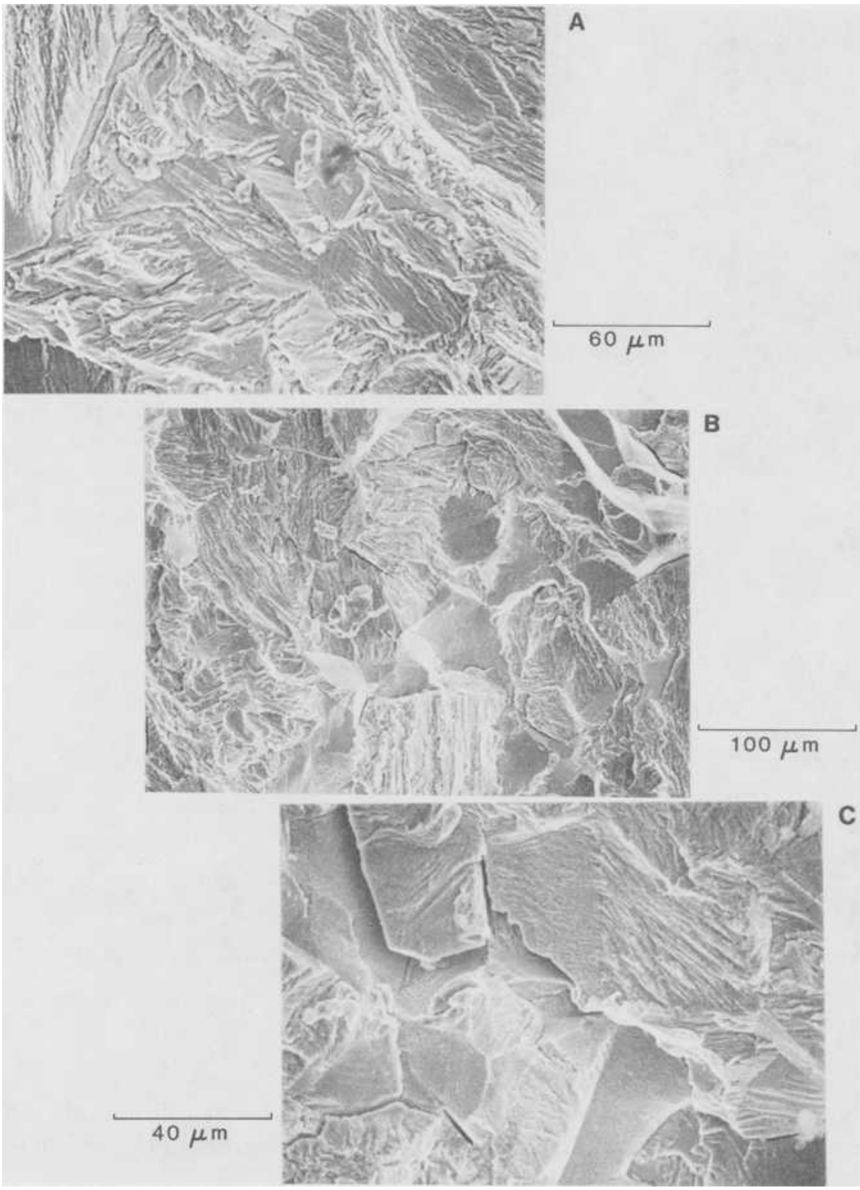

FIG. 11—*Fatigue failure mechanisms in Fe-18Cr-3Ni-13Mn-0.37N austenitic stainless steel at 4 K.*

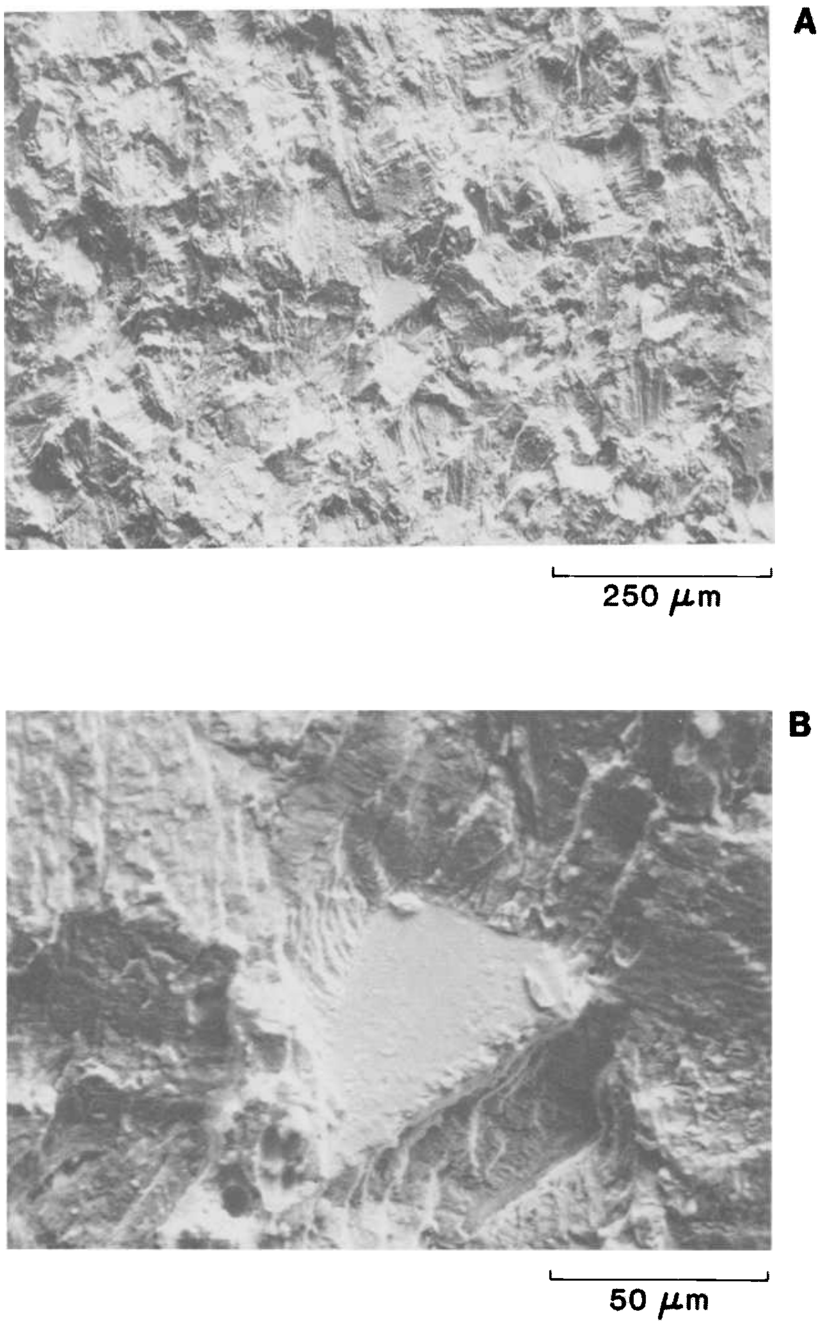

FIG. 12—*Fatigue failure mechanism in AISI 304 L stainless steel at 295 K.*

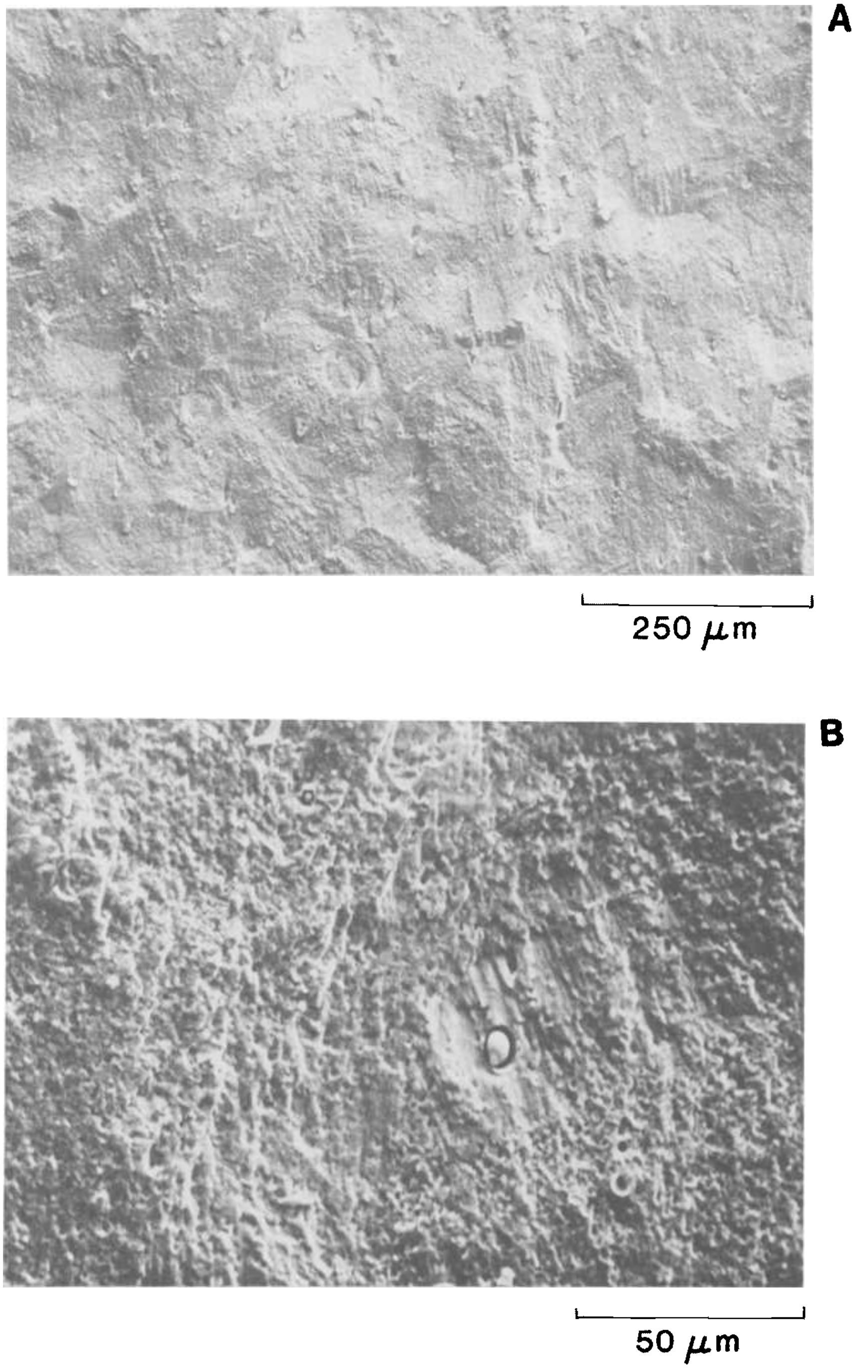

FIG. 13—*Fatigue failure mechanism in AISI 304 L stainless steel at 4 K.*

transition is associated with extensive martensitic phase transformations and a significant reduction of *da/dN*.[1] The austenitic instability appears to be directly responsible for the improved fatigue resistance, for reasons discussed by Schuster and Altstetter [*59*].

Summary and Conclusions

The midrange fatigue crack growth rate data for a variety of structural alloys at room and cryogenic temperatures have been selectively reviewed. The presentation of data follows a format suggested by the Kitagawa-Misumi equation, where log C is plotted versus n. Pivot points are calculated for cryogenic alloys, regions of structure-sensitive and structure-insensitive behavior are identified, and the significance of some factors influencing the temperature dependence of fatigue crack growth are briefly discussed.

On the basis of pivot point calculations, Young's modulus exerts a dominant effect in that $\Delta K_0/E$ approximately normalizes the data for different alloy families. Within each family the behavior is strongly influenced by failure mechanisms. Plastic work and cyclic stress-strain properties are highly relevant to the determination of fatigue property correlations, but such data are generally unavailable for cryogenic alloys. In the absence of these data, correlations were sought by using conventional mechanical properties. Those correlations demonstrate that two regions of behavior exist for structural alloys:

1. In Region I, *da/dN* is temperature- and microstructure-sensitive; E, σ_y, and K_{Ic} influence the results.
2. In Region II, *da/dN* is temperature- and microstructure-insensitive; E influences the results, whereas σ_y and K_{Ic} appear to be irrelevant.

References

[*1*] Paris, P. C. and Erdogan, F., *Journal of Basic Engineering, Transactions of ASME*, Vol. 85D, No. 4, Dec. 1963, pp. 528–534.
[*2*] Paris, P. C. in *Fatigue Thresholds: Fundamentals and Engineering Applications*, J. Backlund, A. F. Blom, and C. J. Beevers, Eds., Engineering Materials Advisory Services, London, U.K., 1982, pp. 3–10.
[*3*] Irving, P. E. and McCartney, L. N., *Metals Science*, Vol. 11, No. 8-9, Aug.-Sept. 1977, pp. 351–361.
[*4*] Lindley, T. C. and McCartney, L. N., "Mechanics and Mechanisms of Fatigue Crack Growth," *Developments in Fracture Mechanics*, G. G. Chell, Ed., Applied Science, London, 1981, pp. 247–322.
[*5*] Kitagawa, H., "Some Recent Japanese Results in the Fracture Mechanics Approaches to Fatigue Crack Problems Related to Welded Structures," *Significance of Defects in Welded Structures*, University of Tokyo Press, Tokyo, 1974, pp. 248–259.
[*6*] Kitagawa, H. and Misumi, M. in *Proceedings*, International Conference on Mechanical Behavior of Materials, Vol. 2, Society of Materials Science, Kyoto, Japan, 1972, p. 218.
[*7*] Koshiga, F. and Kawahara, M., *Journal of the Japanese Society for Naval Architecture*, Vol. 133, June 1973, p. 249.
[*8*] Yokobori, T., Kawada, I., and Hata, H., *Reports of the Research Institute for Strength and Fracture of Materials*, Tohoku University, Vol. 9, 1973, p. 35.

[9] Niccolls, E. H., *Scripta Metallurgica*, Vol. 10, No. 4, April 1976, pp. 295–298.
[10] McCartney, L. N. and Irving, P. E., *Scripta Metallurgica*, Vol. 11, No. 3, March 1977, pp. 181–183.
[11] Bailon, J. P., Masounave, J., and Bathias, L., *Scripta Metallurgica*, Vol. 11, No. 12, Dec. 1977, pp. 1101–1106.
[12] Tanaka, K. and Matsuoka, S., *International Journal of Fracture*, Vol. 13, No. 5, Oct. 1978, pp. 563–583.
[13] Benson, J. P. and Edmonds, D. V., *Scripta Metallurgica*, Vol. 12, No. 7, July 1978, pp. 645–647.
[14] Tanaka, K., Masuda, C., and Nishijima, S., *Scripta Metallurgica*, Vol. 15, No. 3, March 1981, pp. 259–264.
[15] Tanaka, K., *International Journal of Fracture*, Vol. 15, No. 1, Feb. 1979, pp. 57–68.
[16] Cheng, Y. W. and Tobler, R. L. in *Proceedings*, ICF International Symposium on Fracture Mechanics, Tan Deyan and Chen Daning, Eds., Science Press, Beijing, China, 1983, pp. 635–640.
[17] Burck, L. H. and Weertman, J., *Metallurgical Transactions*, Vol. 7A, No. 2, Feb. 1976, pp. 257–264.
[18] Prokopenko, A. V., *Strength of Materials*, Vol. 10, No. 6, June 1978, pp. 673–678.
[19] Pokrovskii, V. V., *Strength of Materials*, Vol. 10, No. 5, May 1978, pp. 534–539.
[20] Stonesifer, F. R., *Engineering Fracture Mechanics*, Vol. 10, No. 2, March 1978, pp. 305–314.
[21] Tobler, R. L., Mikesell, R. P., and Reed, R. P. in *Fracture Mechanics, ASTM STP 677*, C. W. Smith, Ed., American Society for Testing and Materials, Philadelphia, 1979, pp. 85–105.
[22] Tobler, R. L., Mikesell, R. P., Durcholz, R. L., and Reed, R. P. in *Properties of Materials for LNG Tankage, ASTM STP 579*, American Society for Testing and Materials, Philadelphia, 1975, pp. 261–287.
[23] Tobler, R. L., Reed, R. P., and Schramm, R. E., *Journal of Engineering Materials and Technology*, Vol. 100, No. 1, Jan. 1978, pp. 189–194.
[24] Tobler, R. L. and Reed, R. P., *Advances in Cryogenic Engineering*, Vol. 24, 1978, pp. 82–90.
[25] Schwartzberg, F. R. in *Materials Research for Superconducting Machinery-I*, Semiannual Technical Report ADA004586, National Bureau of Standards, 1974; available from NTIS, Springfield, VA.
[26] Tobler, R. L. and Reed, R. P. in *Advances in Cryogenic Engineering*, Vol. 22, Plenum Press, New York, 1977, pp. 35–46.
[27] Read, D. T. and Reed, R. P., *Metal Science of Stainless Steels*, Metallurgical Society of AIME, New York, 1979, pp. 92–121.
[28] Read, D. T. and Reed, R. P., *Cryogenics*, Vol. 21, No. 7, July 1981, pp. 415–417.
[29] Wells, J. M., Kossowsky, R., Logsdon, W. A., and Daniel, M. R. in *Materials Research for Superconducting Machinery-IX*, Semiannual Technical Report ADA036919, National Bureau of Standards, 1976; available from NTIS, Springfield, VA.
[30] Mahoney, M. W. and Paton, N. E., *Nuclear Technology*, Vol. 23, No. 6, June 1974, pp. 53–62.
[31] Wells, J. M., Kossowsky, R., Logsdon, W. A., and Daniel, M. R. in *Materials Research for Superconducting Machinery-VI*, Semiannual Technical Report ADA036919, National Bureau of Standards, 1976; available from NTIS, Springfield, VA.
[32] Tobler, R. L., McHenry, H. I., and Reed, R. P., *Advances in Cryogenic Engineering*, Vol. 24, 1978, pp. 560–572.
[33] Tobler, R. L., "Fatigue Crack Growth In Sensitized Fe-18Cr-3Ni-13Mn-0.37N Austenitic Stainless Steel," in press.
[34] Whipple, T. A., McHenry, H. I., and Read, D. T., *Welding Journal Research Supplement*, Vol. 60, No. 4, April 1981, pp. 72s–78s.
[35] McHenry, H. I. and Whipple, T. A. in *Materials Studies For Magnetic Fusion Energy Applications at Low Temperatures-IV*, NBSIR 80-1627, National Bureau of Standards, Boulder, CO, 1980, pp. 155–165.
[36] Whipple, T. A. and McHenry, H. I. in *Materials Studies For Magnetic Fusion Energy Applications at Low Temperatures-IV*, NBSIR 81-1645, National Bureau of Standards, Boulder, CO, 1981, pp. 273–288.
[37] Tobler, R. L., *Cryogenics*, Vol. 16, No. 11, Nov. 1976, pp. 669–674.

[*38*] McHenry, H. I. and Schramm, R. E., *Advances in Cryogenic Engineering*, Vol. 24, 1978, pp. 161–165.
[*39*] Thompson, A. W., Frandsen, J. D., and Williams, J. C., *Metals Science*, Vol. 9, 1975, pp. 46–48.
[*40*] Ogura, T., Karashima, S., and Tsurukame, K., *Transactions of the Japanese Institute of Metallurgy*, Vol. 16, No. 1, Jan. 1975, pp. 43–48.
[*41*] Liaw, P. K., Fine, M. E., Kiritani, M., and Ono, S., *Scripta Metallurgica*, Vol. 11, No. 12, Dec. 1977, pp. 1151–1155.
[*42*] Tobler, R. L. and Reed, R. P., *Journal of Engineering Materials and Technology*, Vol. 100, 1977, pp. 306–312.
[*43*] McHenry, H. I., Naranjo, S. E., Read, D. T., and Reed, R. P., *Advances in Cryogenic Engineering*, Vol. 24, 1978, pp. 519–527.
[*44*] Roberts, R., Wnek, K., and Tafuri, J. C., *Advances in Cryogenic Engineering*, Vol. 24, 1978, pp. 187–196.
[*45*] Ledbetter, H. M., "Elastic Properties," in *Materials at Low Temperatures*, R. P. Reed and A. F. Clark, Eds., American Society for Metals, Metals Park, OH, 1983, pp. 1–45.
[*46*] Ledbetter, H. M., *Cryogenics*, Vol. 22, No. 12, Dec. 1982, pp. 653–656.
[*47*] Naimon, E. R., Weston, W. F., and Ledbetter, H. M., *Cryogenics*, Vol. 14, No. 5, May 1974, pp. 246–249.
[*48*] Gerberich, W. W. and Moody, N. R. in *Fatigue Mechanisms, ASTM STP 675*, American Society for Testing and Materials, Philadelphia, 1979, pp. 292–341.
[*49*] Cullity, B. D., *Elements of X-Ray Diffraction*, Addison-Wesley, Reading, MA, 1956, pp. 482–484.
[*50*] Bates, R. C. and Clark, W. G., Jr., *Transactions of the American Society for Metals*, Vol. 62, No. 2, June 1969, p. 380.
[*51*] Bathias, C. and Pelloux, R. M., *Metallurgical Transactions*, Vol. 4, No. 5, May 1973, pp. 1265–1273.
[*52*] Fine, M. E. and Davidson, D. L. in *Fatigue Mechanisms: Advances in Quantitative Measurement of Physical Damage, ASTM STP 811*, J. Lankford, D. L. Davidson, W. L. Morris, and R. P. Wei, Eds., American Society for Testing and Materials, Philadelphia, 1983, pp. 350–370.
[*53*] Ritchie, R. O. and Knott, J. F., *Materials Science and Engineering*, Vol. 14, 1974, p. 7.
[*54*] Ritchie, R. O. and Knott, J. F., *Acta Metallurgica*, Vol. 21, No. 5, May 1973, pp. 639–648.
[*55*] Richards, C. E. and Lindley, T. C., *Engineering Fracture Mechanics*, Vol. 4, No. 4, 1972, pp. 951–978.
[*56*] Katz, Y., Bussiba, A., and Matthias, H in *Fatigue at Low Temperatures, ASTM STP 857*, R. I. Stephens, Ed., American Society for Testing and Materials, Philadelphia, 1985, pp. 191–209.
[*57*] Ryder, J. T. and Witzell, W. E. in *Fatigue at Low Temperatures, ASTM STP 857*, R. I. Stephens, Ed., American Society for Testing and Materials, Philadelphia, 1985, pp. 210–237.
[*58*] Verkin, B. I., Grinberg, N. I., and Serdyuk, V. A., in *Fatigue at Low Temperatures, ASTM STP 857*, R. I. Stephens, Ed., American Society for Testing and Materials, Philadelphia, 1985, pp. 84–100.
[*59*] Schuster, G. and Altstetter, C. in *Fatigue Mechanisms: Advances in Quantitative Measurement of Physical Damage, ASTM STP 811*, J. Lankford, D. L. Davidson, W. L. Morris, and R. P. Wei, Eds., American Society for Testing and Materials, Philadelphia, 1983, pp. 445–463.

STP857-EB/Mar. 1985

DISCUSSION

H. O. Fuchs[1] (*written discussion*)—Please explain the significance of ΔK_0.

R. L. Tobler and Y. W. Cheng (*authors' closure*)—An ideal fit to Eq 2 means that the da/dN-versus-ΔK curves for a given body of data will intersect at the pivot point (A, ΔK_0). Then if the data conform to Eq 2 independently of test temperature, the da/dN curves will intersect and fan out as a function of n, as Fig. 14 indicates.

In practice, however, data collections for alloy systems invariably show numerous examples of specific materials with da/dN curves that fail to intersect at the calculated "pivot points". Under these circumstances Eq 2 only approximates the entire data base, which contains nonconforming material behaviors, and the pivot point becomes a measure of the center of gravity of the data scatterband.

Given a linear correlation between log C and n, there are at least two implications of significance. First, it is implied that the power-law constants reduce to one independent variable, C or n; this justifies seeking correlations with other properties using n alone, as in the text. Second, it is implied that alloys with high n values offer superior fatigue crack growth resistance compared to alloys with low n for $\Delta K < \Delta K_0$, whereas the opposite is true for $\Delta K > \Delta K_0$. In other words, low n is desirable at high ΔK, whereas high n is desirable at low ΔK. Optimum alloy selection therefore depends on the ΔK range of engineering applications.

In the text, we were careful to emphasize that judgments concerning the relative merits of individual alloys based on pivot point calculations must be interpreted with caution in view of the approximate nature of such representations.

H. S. Reemsnyder[2] (*written discussion*)—The authors have fitted the simple power equation

$$da/dN = C\ (\Delta K)^n \tag{4}$$

to their crack growth rate versus ΔK data through the determination of the regression parameters C' and n in the linear equation

$$y = C' + nx \tag{5}$$

where C', y, and x are the logarithms of, respectively, the parameters C,

[1] Mechanical Engineering Department, Stanford University, Stanford, CA 94303.
[2] Bethlehem Steel Corp., Homer Research Laboratories, Bethlehem, PA 18016.

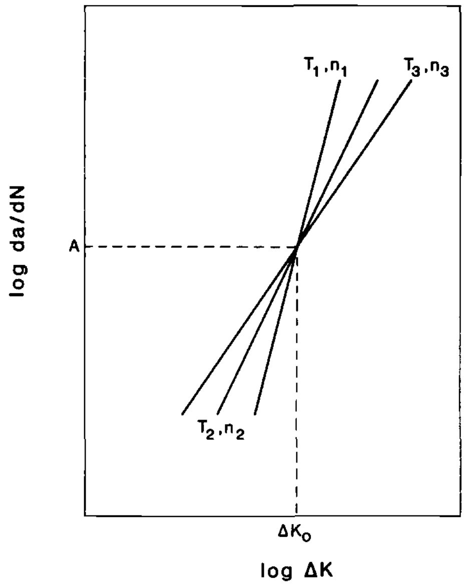

FIG. 14—*Explanation of pivot point.*

da/dN, and ΔK. In such a regression, the parameters are *always* related by

$$C' = y_0 - nx_0 \tag{6}$$

where x_0 and y_0 are the mean values of x and y, that is, the coordinates of the center of gravity of the data to which Eq 2 is fitted. Expressing Eq 6 in a form analogous to Eq 4 results in

$$C = (da/dN)_0 \, (1/\Delta K_0)^n \tag{7}$$

where the subscript 0 denotes the antilogarithm of the mean of the logarithms of *da/dN* and ΔK. In other words, the authors' parameter A is nothing more than the antilogarithm of the mean value of the log (*da/dN*) values for a given material-temperature combination.

If one were to draw many sample sets of x,y from a population of x,y, determine the regression parameters C' and n (Eq 5) for each sample, and plot C' versus n, a scatter diagram would result with variability in both the C' and n (that is, vertical and horizontal) directions. Therefore, when one is plotting C' versus n for various material-temperature combinations, one should recognize that apparent trends reflect, to some undefined extent, sampling variability and not necessarily real relations among fatigue crack growth, material, and test temperature.

In conclusion, there is nothing subtle about the correlation between C and

n, which is instead intrinsic to regression parameters. Perhaps multivariate regression analysis would yield an empirical model relating crack growth, material (composition), and temperature that is superior to the present scheme—for example, fitting a simple power relation to each data set and then seeking relations between the regression parameters and experimental factors.

R. L. Tobler and Y. W. Cheng (*authors' closure*)—We appreciate your helpful suggestions and points of clarification.

Koji Shibata, Yasuo Kishimoto, Natsuki Namura, and Toshio Fujita

Cyclic Softening and Hardening of Austenitic Steels at Low Temperatures

REFERENCE: Shibata, K., Kishimoto, Y., Namura, N., and Fujita, T., "**Cyclic Softening and Hardening of Austenitic Steels at Low Temperatures,**" *Fatigue at Low Temperatures, ASTM STP 857,* R. I. Stephens, Ed., American Society for Testing and Materials, Philadelphia, 1985, pp. 31–46.

ABSTRACT: The fatigue behavior of austenitic stainless steels and nonmagnetic high-manganese steels has been investigated in ambient air, liquid nitrogen, and liquid helium. Particular attention was paid to the influence of nitrogen and carbon additions. Low-cyclic fatigue tests were carried out under tension-compression at a strain rate of 3×10^{-3} s^{-1}. In all the stainless steels, cyclic softening following initial hardening was observed at lower strain amplitudes; the softening was remarkably enhanced by the addition of nitrogen. Solute carbon also had a similar effect, although to a lesser degree than nitrogen. In the high-manganese steels, the amount of softening was significantly affected by manganese content. The effect of the interstitial atoms on the softening was smaller in the 32% manganese series of steels than in the stainless steels. A decrease in the testing temperature increased the softening in both series of steels. Planar structures or less-tangled structures of dislocations were formed, and cellular structures were scarcely observed in all the steels showing the remarkable softening. The tendency of dislocations to form these less-tangled dislocation arrangements, and the softening and hardening behavior of the steels, could not be explained as an effect of stacking fault energy alone, but could be qualitatively interpreted by assuming the existence of some ordering between substitutional and interstitial atoms in the as-solution-treated steels. The significant softening seemed to increase fatigue life under the strain-controlled condition.

KEY WORDS: steels, fatigue (materials), low-cycle fatigue, cyclic load, stresses, strains, damage, hardening (materials), softening, fatigue life, microstructure, cryogenics, helium, nitrogen

Little systematic work has been done on fatigue behavior, especially softening and hardening, of austenitic steels at room and lower temperatures; such behavior thus remains unclear. Zeedijk [*1*] and Nagata et al [*2*], for instance, observed only cyclic hardening followed by the saturation stage in solution-treated austenitic stainless steels, while Polak et al [*3*] showed cyclic

Dr. Shibata is an associate professor and Dr. Fujita a professor in the Department of Metallurgy and Materials Science, Faculty of Engineering, University of Tokyo, Japan. Kishimoto and Namura, formerly graduate students in the same department, are now researchers at Kawasaki Steel Corporation.

softening to occur after initial hardening in similar steels. More study is required of the cyclic deformation behavior of high-manganese steels, which have been recommended as materials for large structures in cryogenic engineering [*4*]. The present study has therefore investigated the cyclic deformation behavior of austenitic stainless steels and high-manganese steels at ambient and lower temperatures, devoting particular attention to the influence of carbon and nitrogen. These interstitial elements, especially nitrogen, have been known to remarkably enhance the strength of the steels under study.

Materials, Apparatus, and Procedure

Table 1 shows the chemical compositions of the steels investigated in this study. The steels were prepared by air and vacuum melting. Cast ingots of about 17 kg were heated at 1473 K, then forged and rolled to 13-mm-diameter bars or 15-mm-thick plates. Fatigue and tension specimens of 5 mm diameter by 10 mm gage length and 3.5 mm diameter by 10 mm gage length were machined from these bars and plates, after which the specimens were solution-treated and water-quenched. The 3.5-mm specimens were used only for tension tests in liquid helium. All specimens were polished electrolytically and tested in ambient air, liquid nitrogen, and liquid helium. The tests in ambient air were carried out with an Instron machine, while the tests in liquid nitrogen and liquid helium were performed with a closed-loop electrohydraulically actuated testing machine equipped with a cryostat. A clip-on gage mounted on the test specimen was used to measure the change in specimen length during cyclic deformation, while the elongation of the specimen during a tension test was measured with linear differential transducers. Cycling was performed under conditions of constant total strain amplitude, ranging from 0.7×10^{-2} to 2.2×10^{-2}, or constant stress amplitude, set at 1.0 to 1.5 times the 0.2% proof stress at a strain rate of 3×10^{-3} s^{-1} with a completely reversed tension-compression triangular wave.

Results and Discussion

Cyclic Deformation Behavior at Ambient Temperature

Cyclic softening was observed after initial cyclic hardening in all the steels investigated, especially at lower strain amplitudes. The amount of softening generally decreased at higher strain amplitudes, although an additional hardening caused by the formation of body-centered-cubic (bcc) martensite during cyclic strain was exhibited in the 304 series steels. Remarkable softening was revealed after initial hardening in steels with a higher nitrogen content.[1]

[1] Cyclic deformation behavior was not affected significantly by specimen preparation—that is, whether specimens were solution-treated and then machined or machined and then solution-treated, furnace-cooled instead of water-quenched following solution treatment, or mechanically polished instead of electrolytically polished.

TABLE 1—*Chemical composition of steels.*

Designation	Composition, wt%									
	C	Si	Mn	P	S	Ni	Cr	Al	N	Mo
304	0.049	0.75	1.01	0.003	0.003	8.84	18.4	0.014	0.009	...
304N	0.051	0.79	1.02	0.003	0.003	8.82	18.5	0.024	0.160	...
316	0.045	0.72	1.32	0.032	0.004	10.9	17.0	0.003	0.033	2.15
316L	0.017	0.56	1.27	0.032	0.004	12.3	17.2	0.004	0.028	2.05
316N	0.017	0.54	1.30	0.004	0.004	13.6	17.2	0.005	0.113	2.42
310S	0.027	0.76	1.48	0.002	0.002	19.8	25.0	0.007	0.010	...
310SN	0.034	0.77	1.47	0.004	0.002	20.2	24.5	0.011	0.174	...
310L[a]	0.011	0.75	1.57	0.004	0.010	20.1	25.1	0.004	0.008	...
310C[a]	0.18	0.74	1.55	0.004	0.010	19.9	24.9	0.003	0.007	...
310N[a]	0.013	0.78	1.54	0.004	0.010	20.2	24.9	0.004	0.17	...
18MnC	0.42	0.68	17.9	0.005	0.004	2.04	5.12	0.018	0.024	...
32MnL[a]	0.020	0.58	31.2	0.002	0.013	0.22	6.94	0.035	0.007	...
32MnC[a]	0.32	0.52	31.8	0.002	0.013	0.17	7.01	0.033	0.012	...
32MnN(m)[a]	0.03	0.57	31.8	0.006	0.013	0.21	6.50	0.028	0.12	...
32MnN(h)[a]	0.03	0.66	31.2	0.004	0.012	0.58	7.51	0.024	0.30	...
32MnNC	0.14	0.60	31.6	0.022	0.006	0.23	7.04	0.012	0.133	...
35MnC	0.41	0.68	35.4	0.002	0.006	0.26	5.10	0.028	0.027	...

[a] Vacuum melt.

Figure 1 shows results for the 316 series steels. Adding nitrogen increased the amount of softening following the initial cyclic hardening. Figure 2 shows the effect of solution treatment temperature, nitrogen, and carbon on the cyclic softening and hardening behavior of 310 series steels. Swann [5] observed that a deformed 70Ni-30Cu alloy exhibited a planar arrangement of dislocations in larger grains and a cell structure in smaller grains. Such a difference in a dislocation structure (i.e., a dislocation interaction) is considered to have an interrelation with differences in cyclic softening and hardening behavior, as shown in the next section. However, the effect of solution treatment temperature on the behavior was small in 310L and 310N steels (Fig. 2), while the grain size of these steels increased from ~40 to ~350 μm as the solution treatment temperature increased from 1323 to 1573 K. In 310C steel, the degree of softening increased with the solution temperature. The grain size of this steel was ~10 μm and ~350 μm in the solution treatment condition at 1323 and 1573 K, respectively.

Observations by transmission electron microscopy indicated that many large carbides were observed in 310C steel heated at 1323 K; these carbides dissolved into the matrix during heating at 1573 K (Fig. 3). In 310N steel, on the other hand, the number of such undissolved precipitates was smaller, even in the specimens heated at 1323 K. No precipitate was observed in 310L steel. Hence it is concluded that the effect of grain size on cyclic softening and hardening behavior is small in the present case and that solute carbon enhanced the softening although not so extensively as nitrogen.

Figure 4 shows results for the 32Mn series of steels. A relatively large amount of softening was observed in 32MnN(h) steel, whereas 32MnC and 32MnN(m) steels did not exhibit so much softening. The effect of nitrogen and carbon on cyclic softening was considered to be smaller in high-manganese steels than in austenitic stainless steels. In high-manganese steels, it was

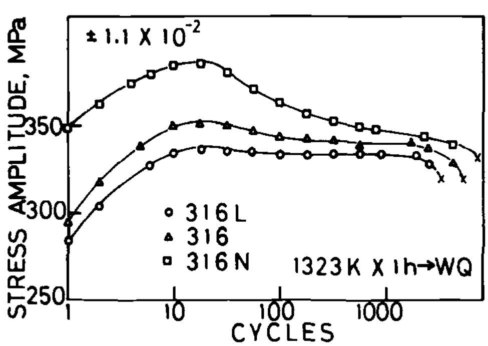

FIG. 1—*Stress amplitude response of 316, 316L, and 316N steels for constant total strain amplitude tests at room temperature. The crosses at the ends of the curves denote fracture and WQ represents water quenching.*

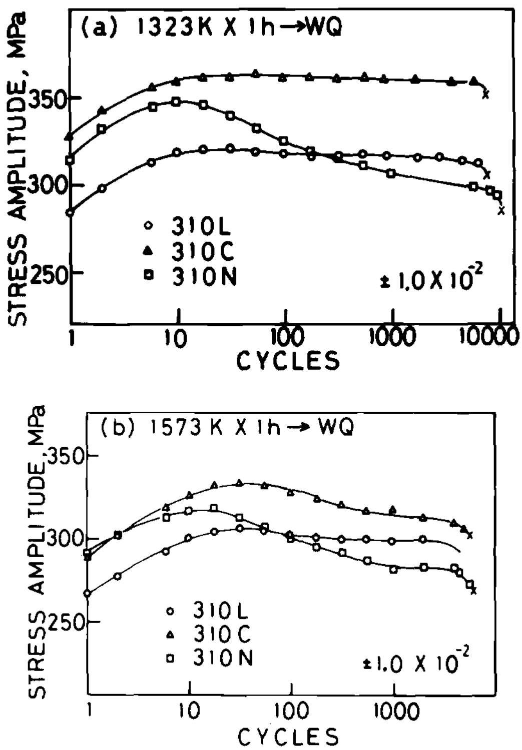

FIG. 2—*Stress amplitude response of 310L, 310C, and 310N steels solution-treated at* (a) *1323 K and* (b) *1573 K for constant total strain amplitude tests at room temperature.*

also observed that the softening trend was significantly affected by the manganese content (Fig. 5).

Temperature Dependence of Cyclic Deformation Behavior

The yield strength of steels containing the interstitial elements, especially nitrogen, increased significantly and the tendency toward softening during cyclic deformation was enhanced as the temperature decreased. Plastic deformation in liquid helium exhibited serrations on the hysteresis curves of all steels through an adiabatic flow mechanism [*6*]. However, the effects of this serrated flow on fatigue behavior could not be clarified in this study. Figure 6 shows the effects of testing temperature on the stress amplitude response of 310L and 310N steels for constant total strain amplitude tests. In the case of 310L steel, the decrease in testing temperature apparently did not affect the cyclic deformation behavior, while the cyclic softening of 310N steel increased dramatically as the temperature decreased. The results for 32Mn series of steels are shown in Fig. 7. Enhanced softening at low temperatures

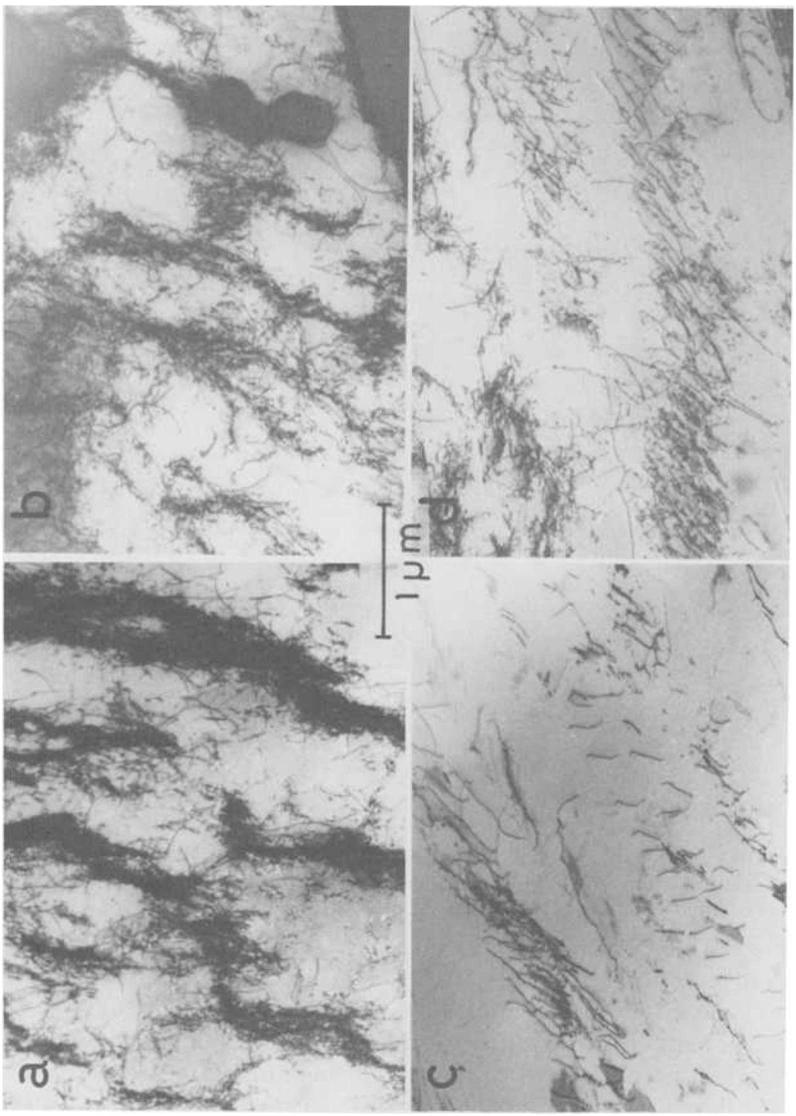

FIG. 3—*Microstructures of* (a) *310L,* (b) *310C, and* (c) *310N steels solution-treated at 1323 K and cycled for 12 900 cycles, and* (d) *310C steel solution-treated at 1573 K and cycled for 8300 cycles. Cyclings were performed at a total strain amplitude of* 0.7×10^{-2} *at room temperature.*

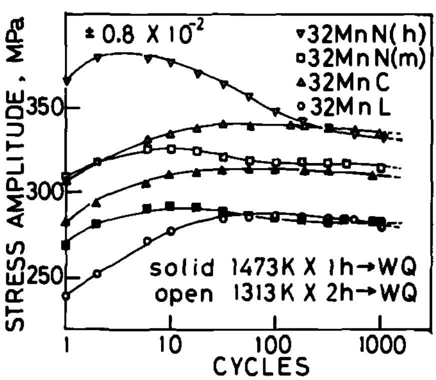

FIG. 4—*Stress amplitude response of 32Mn series of steels for constant total strain amplitude tests at room temperature.*

was exhibited in 32MnNC and 32MnN(h) steels, but this enhancement cannot be observed in 32MnC and 32MnN(m) steels.

Microstructures of Cyclically Deformed Specimen

A trend toward the formation of band structures consisting of tangled dislocations or cellular structures was observed in specimens showing a slight softening or a saturation stage following initial hardening. The dislocations in specimens showing a large amount of softening tended to less tangled band or planar structures (Figs. 3, 8, and 9). Figures 3 and 8 show microstructures developed during the cyclic deformation of 310 and 32Mn series steels, respectively. Figure 9 depicts microstructures observed in 18MnC and 35MnC steels. Cellular structure was scarcely observed in cyclically softened 18MnC steel, while such a structure was frequently observed in cyclically hardened 35MnC steel.

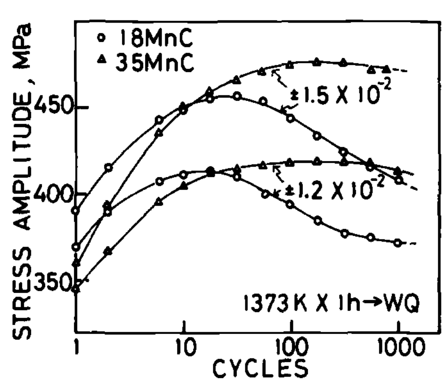

FIG. 5—*Stress amplitude response of 18MnC and 35MnC steels for constant total strain amplitude tests at room temperature.*

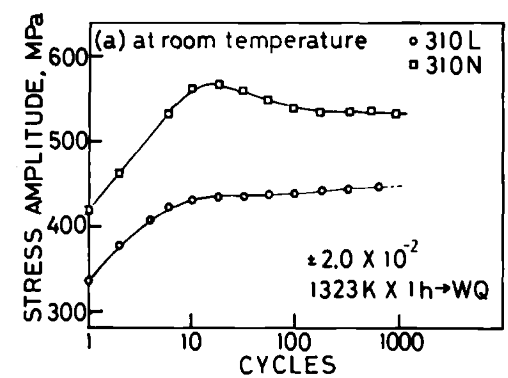

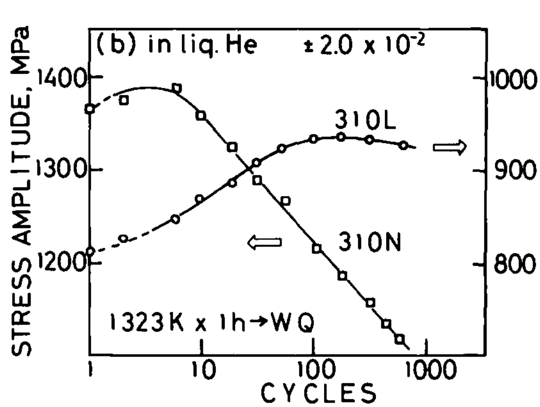

FIG. 6—*Effect of test temperature on the cyclic deformation behavior of 310L and 310N steels.*

The trend toward forming less tangled dislocation structures was enhanced as the temperature decreased. Figure 10 shows the microstructure of 310N steel cyclically deformed at a larger strain amplitude of 2.0×10^{-2}. In the specimen tested at room temperature, cellular structures were developed because of the large strain amplitude, while such structures were not observed in the specimen cyclically strained in liquid helium. Figure 11 shows results for 32MnN(m) steel, which does not clearly exhibit softening even at cryogenic temperatures. A planar structure was scarcely observed, although the degree of dislocation tangling seemed to be smaller in the specimen deformed at the lower temperature.

It is generally accepted that the tendency to form a cellular structure is favored by large strain amplitude and a high stacking fault energy (SFE), both of which are factors promoting cross-slip. Loops and dipoles are created under conditions of cross-slip and low strain amplitude, but dislocation tangling and interaction are inhibited and planar structures formed in low-SFE materials [*7,8*]. In the present work the steels with higher nitrogen contents tended to form less tangled dislocation structures at lower strain amplitudes;

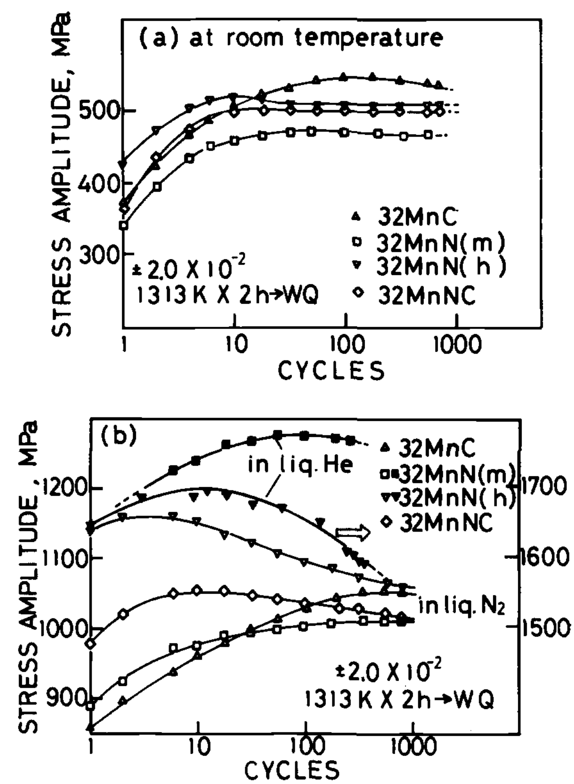

FIG. 7—*Effect of test temperature on the cyclic deformation behavior of 32Mn series steels.*

planar structures occurred more often as the testing temperature decreased, even at larger strain amplitude. Furthermore, 18MnC steel showed a large cyclic softening, while 35MnC steel did not.

These results appear to be consistent with the findings of many researchers [*5,9–11*] that nitrogen decreases the SFE of austenitic stainless steels and that the SFE of alloys decreases with decreasing temperature [*12,13*], while the SFE of Fe-Mn-C alloys shows a low value at 18% manganese [*14*]. Therefore a low SFE seems to enhance the formation of planar structures in the steels investigated. As mentioned before, however, the formation of planar structures was also promoted by solute carbon, which has been considered not to decrease the SFE of austenitic stainless steels [*11,15*]. Moreover, according to the literature [*9,15–18*], it is difficult to consider that the SFE of 310N steel is lower than that of 316 steel, whereas the tendency to form planar structures in the former steel is greater than in the latter. That is, the difference in dislocation structure produced during cyclic deformation cannot be explained by differences in SFE alone. Experimental data on high-manganese steels are limited and the relationship between SFE and dislocation structures cannot be further discussed.

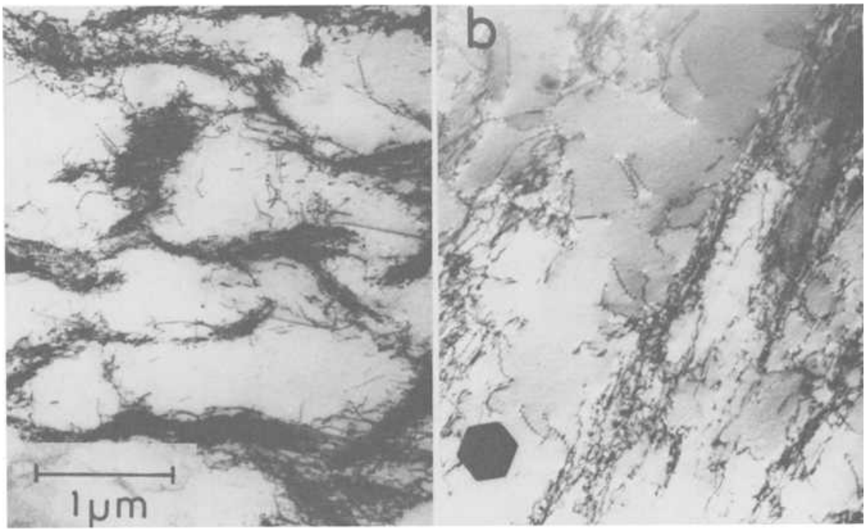

FIG. 8—*Microstructures of* (a) *32MnC and* (b) *32MnN(h) steels cycled at a strain amplitude of* 1.0×10^{-2} *for 3000 cycles at room temperature.*

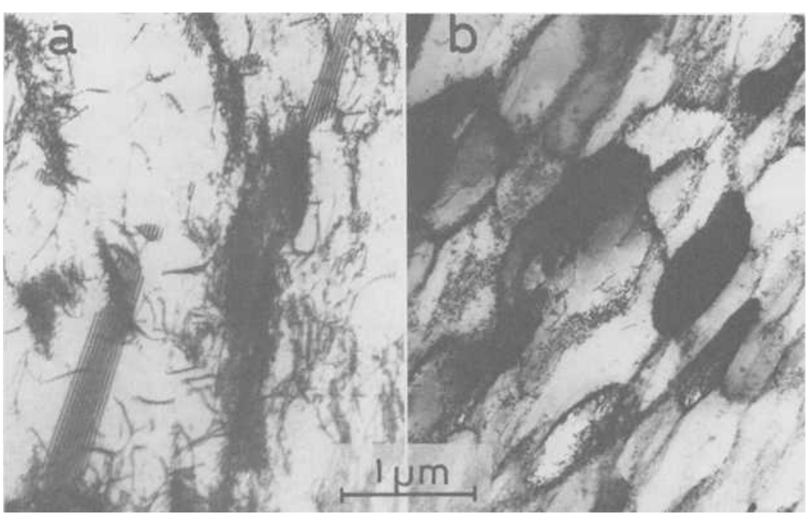

FIG. 9—*Microstructures of* (a) *18MnC and* (b) *35MnC steels cycled at a strain amplitude of* 2.2×10^{-2} *for 1500 cycles at room temperature.*

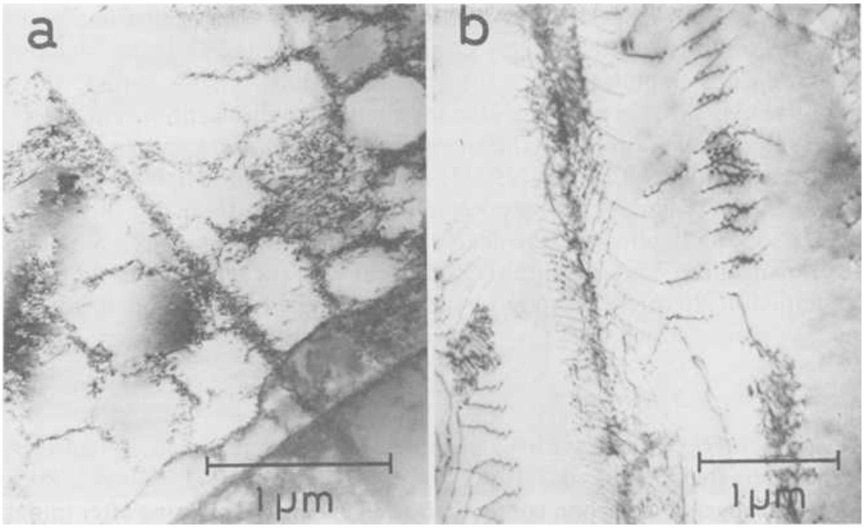

FIG. 10—*Microstructures of 310N steels cycled at a strain amplitude of* 2.0×10^{-2} *for 600 cycles* (a) *at room temperature and* (b) *in liquid helium.*

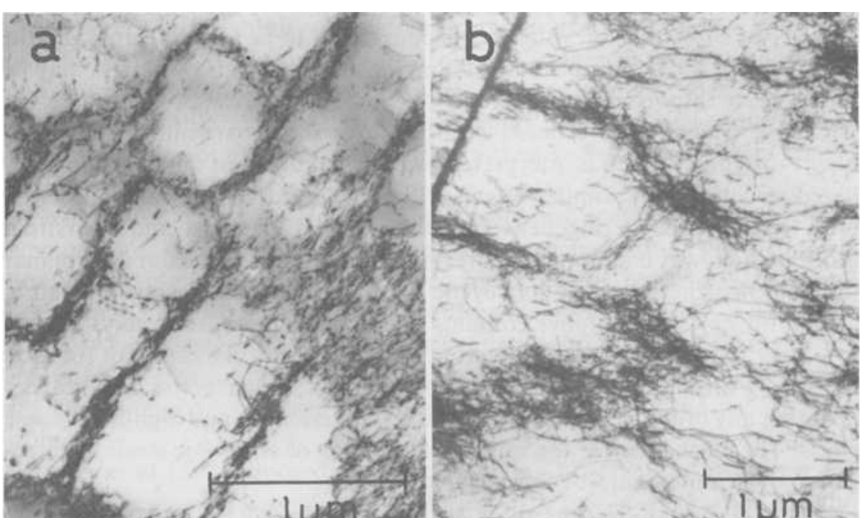

FIG. 11—*Microstructures of 32MnN(m) steel cycled at a strain amplitude of* 2.0×10^{-2} *for 270 cycles* (a) *at room temperature and* (b) *in liquid helium.*

Swann [5] and Douglass et al [18] have suggested that the distribution of dislocations introduced by unidirectional deformation of austenitic stainless steels depends on both SFE and the presence of short-range ordering, which inhibits cross-slip and produces planar structures of dislocations. The energy of interaction of substitutional elements with carbon and nitrogen has been calculated in austenitic steels [19–21], and it has been shown that chromium and manganese have a strong potential to order with these interstitial elements, especially nitrogen, the degree being larger in the case of chromium than manganese. These results are consistent with the tendency of the steels examined in the present study to form less-tangled dislocation structures such as planar structures.

Mechanisms of Softening

Several mechanisms have been proposed to explain the cyclic softening of solution-treated metals and alloys. In the present study, the steels with higher nitrogen and carbon contents showed extensive softening after initial hardening at relatively low strain amplitudes, and small softening or a saturation stage following initial hardening at higher strain amplitudes.

It has also been suggested that slip bands are in the soft region and that softening is produced by the increase in the number of slip bands [24]. Figure 12 shows the surfaces of the specimens of 310L and 310N steels cyclically deformed at room temperature. Fewer slip bands are observed on the surface of the 310L steel.[2] However, the difference in the number of the slip bands is not so marked between these steels that the significant difference in their cyclic deformation behavior can be explained thereby. Hence the effect of the number of slip bands on softening is considered to be insignificant, and the difference in the degree of the softening of the slip bands or matrix may be rather more important.

On the other hand, ordered Ni_3Mn alloys show hardening and subsequent softening, which is interpreted as the breakdown of the long-range ordered structure [22]. Similar effects will be caused by short-range ordering [30]. Therefore, ordering between substitutional elements and interstitial atoms, which was mentioned before, is thought to introduce not only planar dislocation structures, but also cyclic deformation behavior as observed in austenitic steels with higher contents of nitrogen and carbon. Dyson et al [31] have suggested that such ordering might be one of the causes of solution hardening through nitrogen and carbon addition. Nevertheless, it is not evident that any ordering occurs in austenitic stainless steels and high-manganese steels. The mechanism of the solution hardening of austenitic steels by nitrogen and carbon should be investigated further.

Although destabilization of Stage I work hardening [22,23] and the Bauschinger effect [24] make a contribution, these factors do not alone suffice to

[2] Microcracks were observed more often along the slip bands of this steel.

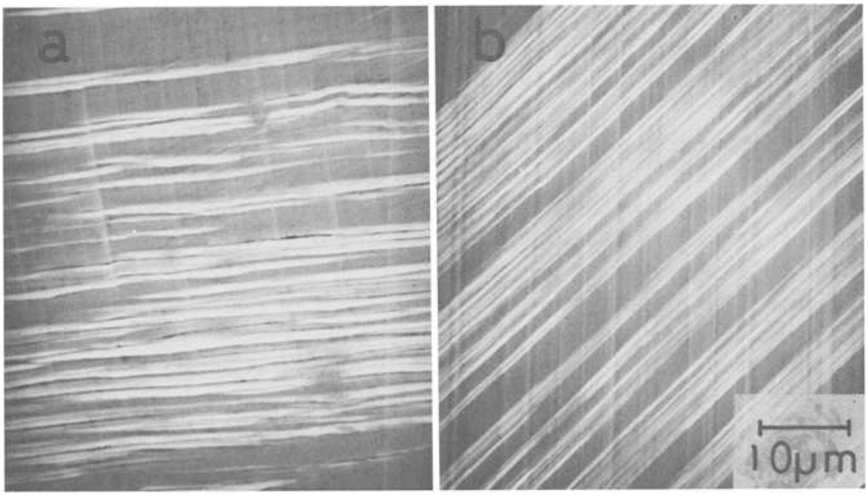

FIG. 12—*Slip bands on the surface of* (a) *310L and* (b) *310N steels cycled at a strain amplitude of 0.9 $\times$ 10^{-2} for 1000 cycles at room temperature.*

explain the remarkable softening observed in the present study, because a decrease in stress amplitude during constant-strain cyclic tests is not observed in annealed Cu-Al alloys [*23*]. This is significant since the destabilization of Stage I work hardening occurs easily [*23*] and the Bauschinger effect is appreciably large [*25*] because of the low SFE of such alloys.

Mild steel, with its distinct yield point, and pure bcc metals like molybdenum and pure iron exhibit a net softening at low strain amplitudes and a net hardening at high strain amplitudes. However, in these materials the softening occurs first, followed by hardening at low strain amplitudes. Published results have established that dislocation locking is broken down and Lüders strain, which is not observed in the steels investigated in the present study, disappears [*22,26,27*].

Frederic et al [*28*] have suggested that softening occurs by an increase in the number of mobile, fresh dislocations during cyclic strain of pure iron. Although the softening was also followed by hardening in this case, and the mechanism of the increase remains unclear in the present study, it is considered that an increase in the mobile dislocation density is attributable to the significant softening observed, since less tangled or planar dislocations, which are more mobile, are produced in steels showing the pronounced softening.

Lukás et al [*29*] proposed that the softening observed in pure iron occurred through rearrangement of dislocations into a cell structure. In the present study, however, it was observed that cell formation seemed to inhibit the softening (Figs. 6 and 10).

Several works [*22,32–34*] have related fatigue life to slip characters or cyclic strain hardening and softening behavior. Feltner et al [22] have shown that in the ordered alloys fatigue life increases because ordering results in a more planar slip character, which apparently outweighs any effect of strain concentration resulting from local softening. Table 2 shows fatigue life under strain-controlled conditions for 310L and 310N steels. The lives of the latter steel, which shows the pronounced softening, are longer than those of the former steel, which does not exhibit such softening. This is consistent with the results for ordered alloys [22]. In the case of stress-controlled tests, the lives of the steels showing the significant softening were also longer (Table 3), because of their higher yield and ultimate tensile strengths. The lives of these steels were shorter, however, when compared at the same strength ratio of applied stress to yield or ultimate tensile strength. It is considered that an increase in strain amplitude through softening is one of the reasons for this decrease in the fatigue life of steels showing the softening.

Conclusions

1. In all the austenitic stainless steels examined, cyclic softening following initial hardening was observed at lower strain amplitudes, and the softening was enhanced significantly by nitrogen addition. Solute carbon also produced fairly extensive softening, but to a lesser degree than nitrogen.
2. In the high-manganese steels, the amount of softening was significantly affected by the manganese content. The interstitial elements had an effect on softening, but it was not so marked in the 32% manganese series of steels as in the stainless steels.
3. A decrease in test temperature tended to enhance the softening.
4. Planar structures or less-tangled band structures of dislocations were produced, and cellular structures were scarcely observed in all the specimens showing the marked softening. On the other hand, dislocations tended to form cellular structures or tangled band structures in the specimens showing slight softening or a saturation stage.

TABLE 2—*Fatigue lives of 310L and 310N steels.*[a]

	Cycles to Failure	
Total Strain Amplitude	310L Steel[b]	310N Steel[c]
1.4×10^{-2}	2 280	4 410
1.4×10^{-2}	2 010	2 870
1.2×10^{-2}	3 760	5 170
1.2×10^{-2}	3 180	6 940
1.0×10^{-2}	7 160	9 940
0.7×10^{-2}	>13 000	>13 000

[a] The steels were solution-treated at 1323 K for 1 h and subjected to strain-controlled tests at room temperature.
[b] Tensile strength = 522 MPa; reduction of area = 82%.
[c] Tensile strength = 653 MPa; reduction of area = 79%.

TABLE 3—*Fatigue lives of 310S and 310SN steels.*[a]

Steels	0.2% Proof Stress ($\sigma_{0.2}$), MPa	Tensile Strength (σ_t), MPa	Stress Amplitude (σ_a), MPa	Stress Ratio $\sigma_a/\sigma_{0.2}$	Stress Ratio σ_a/σ_t	Cycles to Failure
310S	229	531	343	1.50	0.65	2910
			294	1.28	0.55	8800
310SN	340	691	490	1.44	0.71	910
			432	1.27	0.63	2440
			372	1.09	0.54	4100
			343	1.01	0.50	6590

[a] The steels were solution-treated at 1323 K for 1 h and subjected to stress-controlled tests.

5. The difference in the dislocation substructures produced during cyclic deformation, and the softening and hardening behavior of the steels investigated, especially the stainless steels, could not be explained by an SFE effect alone, but could be interpreted qualitatively by assuming some ordering between substitutional and interstitial atoms.

6. The significant softening observed in this study seemed to increase fatigue life under the total strain-controlled condition, which was consistent with the results reported for ordered alloys [*22*].

Acknowledgments

This research was financially supported by a Grant-in-Aid for Scientific Research from the Ministry of Education, Science, and Culture of Japan. The authors are grateful to Nippon Yakin Kogyo Company, the Japan Steel Works, Nippon Steel Corporation, and the National Research Institute for Metals for preparing the research steels. The authors also wish to thank Mr. Yoshinobu Kinoshita of Toshin Kogyo Company for assistance in designing the fatigue testing machine, and Dr. Masato Murakami for assistance in preparing the manuscript.

References

[*1*] Zeedijk, H. B., *Metals Science*, Vol. 11, May 1977, p. 171.
[*2*] Nagata, N., Furuya, K., and Watanabe, R., *Journal of Nuclear Materials*, Vol. 85–86, 1979, p. 839.
[*3*] Polak, J., Klesnil, M., and Lukás, P., *Materials Science and Engineering*, Vol. 15, No. 2/3, 1974, p. 231.
[*4*] Fickett, F. R. in *Advances in Cryogenic Engineering Materials*, Vol. 28, International Cryogenic Materials Conference, Plenum Press, New York and London, 1982, p. 1.
[*5*] Swann, P. R., *Corrosion*, Vol. 19, No. 3, 1963, p. 102.
[*6*] Kubin, L. P., Spieser, P., and Estrin, Y., *Acta Metallurgica*, Vol. 30, 1982, p. 385.
[*7*] Plumbridge, W. J. and Ryder, D. A., *Metallurgical Reviews*, Vol. 14, 1969, p. 119.
[*8*] Kocánda, S. in *Fatigue Failure of Metals*, Sijthoff & Noordhoff International Publishers, The Netherlands, 1978, p. 190.
[*9*] Stoltz, R. E. and Vander Sande, J. B., *Metallurgical Transactions*, Vol. 11A, June 1980, p. 1033.

[10] Fujikura, M., Tanaka, K., and Ishida, K., *Transactions of the Iron and Steel Institute of Japan,* Vol. 15, No. 9, 1975, p. 464.
[11] Schramm, R. E. and Peed, R. P., *Metallurgical Transactions,* Vol. 6A, July 1975, p. 1345.
[12] Lecroisey, F. and Pineau, A., *Metallurgical Transactions,* Vol. 3, Feb. 1972, p. 387.
[13] Latanision, R. M. and Ruff, A. W., Jr., *Metallurgical Transactions,* Vol. 2, Feb. 1971, p. 505.
[14] Volosevich, P. Y., Gridrev, V. N., and Petrov, Y. N., *Physics of Metals and Metallography,* Vol. 42, No. 2, 1976, p. 372.
[15] Brofman, P. J. and Ansell, G. S., *Metallurgical Transactions,* Vol. 9A, June 1978, p. 879.
[16] Rhodes, C. G. and Thompson, A. W., *Metallurgical Transactions,* Vol. 8A, Dec. 1977, p. 1901.
[17] Bampton, C. C., Jones, I. P., and Loretto, M. H., *Acta Metallurgica,* Vol. 26, No. 1, 1978, p. 39.
[18] Douglass, D. L., Thomas, G., and Roser, W. R., *Corrosion,* Vol. 20, No. 1, 1964, p. 15
[19] Mori, T. and Ichise, E., *Journal of the Institute of Metals,* Vol. 28, 1964, p. 145 (in Japanese).
[20] Nishizawa, T., "Thermodynamic Study of Fe-C-Mn, Fe-C-Cr, and Fe-C-Mo Systems," Report 4602, Swedish Board for Technical Development, 1967.
[21] Nishizawa, T., *Bulletin of the Japan Institute of Metals,* Vol. 12, No. 5, 1973, p. 401 (in Japanese).
[22] Feltner, C. E. and Beardmore, P. in *Achievement of High Fatigue Resistance in Metals and Alloys, ASTM STP 467,* American Society for Testing and Materials, Philadelphia, 1970, p. 77.
[23] Feltner, C. E. and Laird, C., *Acta Metallurgica,* Vol. 15, Oct. 1967, p. 1633.
[24] Ham, R. K. and Broom, T., *Philosophical Magazine,* Vol. 7, No. 73, 1962, p. 95.
[25] Abel, A. and Murr, H., *Philosophical Magazine,* Vol. 27, No. 3, 1973, p. 585.
[26] Klesnil, M., Holzmann, M., Lukás, P., and Rys, P., *Journal of the Iron and Steel Institute,* Vol. 203, Jan. 1965, p. 47.
[27] Klesnil, M. and Lukás, P., *Journal of the Iron and Steel Institute,* Vol. 205, July 1967, p. 746.
[28] Frederic, V. L. and Russel, C. J., *Metallurgical Transactions,* Vol. 1, Feb. 1970, p. 367.
[29] Lukás, P., Klesnil, M., and Rys, P., *Zeit Metallukunde,* Vol. 56, No. 2, 1965, p. 109.
[30] Kear, B. H. and Wilsdorf, H. G. F., *Transactions of the Metallurgical Society of AIME,* Vol. 224, No. 2, 1962, p. 382.
[31] Dyson, D. J. and Holmes, B., *Journal of the Iron and Steel Institute,* Vol. 208, May 1970, p. 469.
[32] Laird, C. and Feltner, C. E., *Transactions of the Metallurgical Society of AIME,* Vol. 239, July 1967, p. 1074.
[33] Grosskreutz, J. C., *Metallurgical Transactions,* Vol. 3, May 1972, p. 1255.
[34] Saxena, A. and Antolovich, S. D., *Metallurgical Transactions,* Vol. 6A, Sept. 1975, p. 1809.

DISCUSSION

R. W. Swindeman[1] (*written discussion*)—Often grain size, as well as short-range order, can affect the slip line spacing and strain-hardening characteristics of austenitic steels. Have you examined the effect of grain size on the cyclic softening behavior of your steels?

K. Shibata et al (*authors' closure*)—We have examined the effect of grain size by comparing cyclic softening and hardening behavior of steels heated at low temperatures and at high temperatures. It was concluded that the effect of grain size was small compared with that of the solution of precipitates.

[1] Nuclear Division, Union Carbide Corporation, Oak Ridge National Laboratory, Oak Ridge, TN 37830.

Rikuo Ogawa and J. W. Morris, Jr.

Fatigue Crack Growth Behavior in a Nitrogen-Strengthened High-Manganese Steel at Cryogenic Temperatures

REFERENCE: Ogawa, R. and Morris, J. W., Jr., "**Fatigue Crack Growth Behavior in a Nitrogen-Strengthened High-Manganese Steel at Cryogenic Temperatures,**" *Fatigue at Low Temperatures, ASTM STP 857,* R. I. Stephens, Ed., American Society for Testing and Materials, Philadelphia, 1985, pp. 47–59.

ABSTRACT: The fatigue crack growth rate (FCGR) of a nitrogen-strengthened high-manganese stainless steel of nominal composition 18Mn-5Ni-16Cr-0.02C-0.22N was determined in the intermediate stress-intensity factor range (20–70 MPa$\sqrt{m}$) at 77 and 4 K. Fractographic investigations were performed on the fracture surfaces. The FCGR at 4 K was very nearly the same as at 77 K and substantially below the FCGR for AISI 304LN steel. The fracture surfaces of both the high-manganese alloy and the 304LN showed a transgranular failure mode, but the detailed fractographic features varied with temperature and alloy type. The fractography was closely related to changes in the FCGR.

KEY WORDS: fatigue crack growth rates, nitrogen-strengthened high-manganese steel, 18Mn-5Ni-16Cr-0.02C-0.22N, intermediate stress intensity factor range, cryogenic temperatures, transgranular failure mode

AISI 304L and 316L stainless steels are common cryogenic alloys that have been widely used for 4 K service. They show excellent ductility and toughness at cryogenic temperatures but have relatively low yield strength. The recent development of large superconducting magnets, especially for fusion reactors, has created new needs for high structural alloys. Nitrogen-strengthened stainless steels such as AISI 304LN and 316LN were used for toroidal field coils for the Large Coil Project for fusion reactor research [*1*]. However, much stronger steels will be required for the next step in the test program because of planned increases in the size and electromagnetic force of the toroidal field coils. These new materials must also have good fatigue

Both authors are with the Department of Materials Science and Mineral Engineering and the Lawrence Berkeley Laboratory of the University of California, Berkeley, CA 94720. Mr. Ogawa was on leave from Kobe Steel Ltd., Asada Research Laboratory, Kobe, Japan.

resistance, since the toroidal field coils will be exposed to cyclic forces from the poloidal field coils [*1*].

Fatigue crack growth rates (FCGR) were measured in several austenitic stainless steels at cryogenic temperatures by Reed et al [*2*] and Tobler et al [*3*]. Tobler et al showed that the FCGR of the Type 304 stainless steels was increased at cryogenic temperatures by the addition of interstitial carbon and nitrogen; they also discussed the effect of stability of the austenite phase on the FCGR. However, the role of the strain-induced transformation (stability of austenite) remains unclear because both the stable Type 310 stainless steel and the least stable 304L steel show superior fatigue crack resistance at cryogenic temperatures [*3*].

In order to satisfy the need for new cryogenic structural alloys, a number of new high-manganese austenitic steels have been developed. These alloys offer low cost, stable austenite, and high strength. Previous research [*4*] has shown that promising cryogenic properties can be obtained in a modified 200 series high-manganese stainless steel having a nominal alloy composition of 18Mn-5Ni-16Cr-0.02C-0.22N. The present study was undertaken to evaluate the fatigue crack propagation behavior of this alloy at cryogenic temperatures.

Experimental Work

A 300-kg ingot of nominal composition 18Mn-5Ni-16Cr-0.02C-0.22N was prepared by vacuum-induction melting. The ingot was hot-forged to 80-mm-thick plate and then hot-rolled at 1523 K to 30-mm-thick plate. One part of the plate was solution-treated at 1323 K for 1800 s, followed by water quenching. Compact tenion (CT) specimens were cut from the center of the thickness of the hot-rolled and solution-treated plates. Specimens of AISI 304LN steel plate 76.2 mm thick were used to compare fatigue crack propagation behavior. The 304LN CT specimens were prepared in the as-hot-rolled condition. The measured alloy compositions are given in Table 1.

The CT specimen dimensions were width (w) = 50.8 mm and thickness (B) = 25.4 mm (B = 23.2 mm for 304LN). The original mechanical notch length was 15.88 mm and the direction of the notch was perpendicular to the plate rolling direction (LT orientation). The fatigue tests were carried out using an Instron servohydraulic machine and cryostat. The tests were run at

TABLE 1—*Alloy compositions (weight percent).*

Alloy	Mn	Ni	Cr	Si	P	S	C	N	C+N
18Mn-5Ni-16Cr-0.02C-0.22N	17.98	4.96	16.26	0.53	0.004	0.010	0.024	0.216	0.240
304LN	1.77	9.55	18.54	0.78	0.014	0.009	0.021	0.139	0.160

10 Hz in load control ($R = 0.125$) by using a sinusoidal tension stress waveform. The crack length was measured from the sample compliance. The FCGRs (da/dN) were obtained at intermediate ΔK (20 to 70 MPa$\sqrt{m}$). After testing, the fatigued specimens were broken or cut into two halves. The fracture surfaces were investigated by scanning electron microscopy. The fatigue crack paths were studied in an optical microscope by using either unbroken specimens or broken specimens whose surfaces were plated with nickel.

Results and Discussion

Cryogenic Mechanical Properties

The tensile and Charpy impact properties of 18Mn-5Ni-16Cr-0.02C-0.22N alloy are listed in Table 2. The yield (0.2% flow stress) and tensile strengths increased significantly as the deformation temperature was lowered from 293 to 77 and 4 K. The total elongation decreased as the temperature was lowered but remained over 35% at 4 K. The as-rolled plate had higher strength and ductility at 4 K than the solution-treated plate. The Charpy V-notch absorption energies decreased at cryogenic temperatures to approximately half their values at room temperature, but the absorbed energies at 4 K were comparable to those at 77 K, and ductile dimple fracture surfaces were observed. The alloys were metastable to transformation to either the hexagonal close-packed phase (ϵ) or body-centered-cubic (α') martensite phase during low-temperature deformation. Approximately 34% ϵ-phase and 6% α'-phase were found in the solution-treated tension specimen after it had been broken at 4 K. The specimen deformed up to 17% strain at 4 K showed 17% ϵ-phase and 0% α'-phase. Comparing the high-manganese alloy with the 304L and 304LN alloys, the austenite phase in this alloy is relatively unstable with respect to the austenite phase $\gamma \rightarrow \epsilon$ transformation during low-temperature deformation, but is relatively stable with respect to the $\gamma \rightarrow \alpha'$ (or $\gamma \rightarrow \epsilon \rightarrow \alpha'$) transformation [3].

TABLE 1—*Alloy compositions (weight percent).*

Specimen	Test Temperature, K	Yield Strength, MPa	Tensile Strength, MPa	Elongation, %[a]	Charpy Impact Values, J
As-rolled	293	323	662	74	300
	77	855	1319	54	174
	4	1144	1565	44	170
Solution-treated	293	338	656	81	302
	77	863	1298	64	168
	4	1074	1556	39	154

[a] Gage length = 20 mm.

Fatigue Crack Growth Rates

The FCGR of the experimental alloy is plotted as a function of ΔK at 77 and 4 K in Fig. 1. Data previously reported for 304 and 304LN [*2*] and data obtained in the present work for 304LN are included in Fig. 1. The data obey the Paris equation

$$da/dN = C\,(\Delta K)^n \tag{1}$$

where C and n are constants that depend on material and temperature. The values of C and n obtained from the data in Fig. 1 and reported in Ref *2* are given in Table 3.

The FCGR of the experimental alloy in both the as-rolled and the solution-treated conditions was substantially below that of 304LN steel but slightly higher than those reported for 304 [*2*] and 304L steels [*3*]. The experimental alloy also differed from 304LN in the temperature dependence of the fatigue crack growth rate. While 304LN exhibited a substantial increase in its FCGR as the temperature was reduced from 77 to 4 K, the FCGR in the experimental alloy was nearly the same at the two temperatures. The FCGR of the experimental alloy was slightly dependent on its heat treatment. The FCGR in the as-rolled plate was slightly below that of the solution-treated

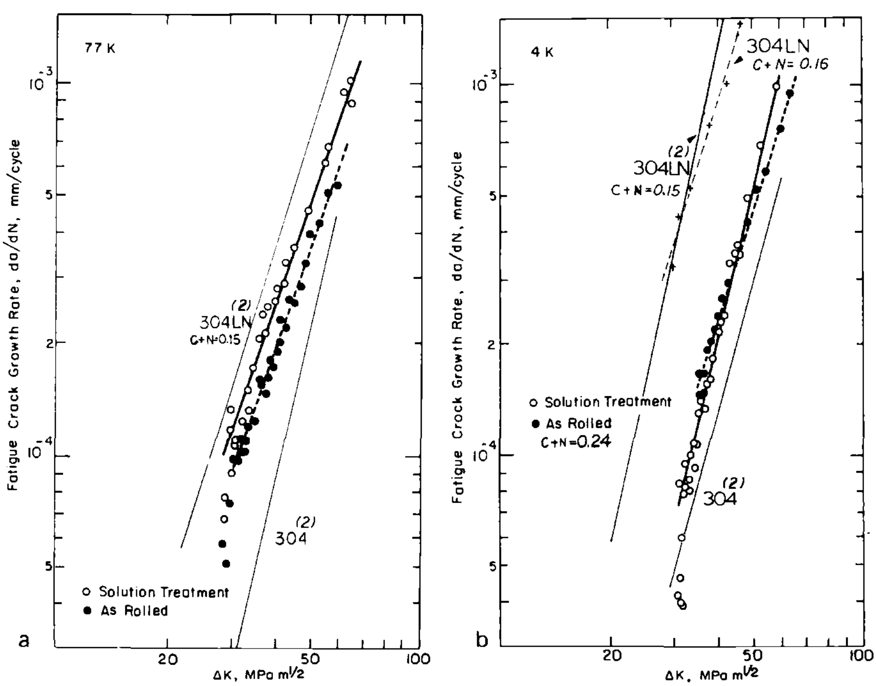

FIG. 1—*Fatigue crack growth rates as a function of* ΔK. (a) *77 K.* (b) *4 K.*

TABLE 3—*Paris equation parameters.*

Specimen	Test Temperature, K	n	C	K Region, MPa$\sqrt{m}$
18Mn-5Ni-16Cr-0.02C-0.22N				
As-rolled	77	2.71	9.8×10^{-9}	30 to 50
	4	3.16	1.95×10^{-9}	35 to 64
Solution-treated	77	2.77	8.03×10^{-9}	30 to 63
	4	4.18	3.98×10^{-11}	30 to 70
304 [2]	77	4.34	9.51×10^{-12}	[a]
	4	3.49	3.26×10^{-10}	18 to 50
304LN [2]	77	3.17	2.67×10^{-9}	[a]
	4	4.25	1.69×10^{-10}	25 to 75

[a] K regions at 77 K are not clear in Ref. 2.

plate at 77 K, and increased somewhat when the temperature was decreased from 77 to 4 K. The solution-treated plate exhibited a change in the slope of the Paris curve when the temperature was lowered to 4 K ($n = 2.8$ to 4.2). As a consequence of the slope change, the FCGR curves crossed; the FCGR at 4 K was less than at 77 K for ΔK less than about 50 MPa$\sqrt{m}$.

Metallography

Both optical fractography and scanning electron fractography showed that the fracture paths in the experimental alloy were transgranular at 77 K for both the as-rolled and the solution-treated conditions. Scanning electron fractographs of the 77 K fracture surfaces are shown in Fig. 2. The direction of crack propagation varied from grain to grain and sometimes changed within a grain. Well-defined striations and microcracks (short arrows) are visible on the fracture surface of the as-rolled plate (Fig. 2*a*). These are oriented almost perpendicularly to the direction of crack propagation (long arrow in Fig. 2*a*). The striations are poorly defined on the fracture surface of the solution-treated plate (Fig. 2*b*). They are feather-like and oriented differently in each grain.

The failure mode of the 304LN steel was also completely transgranular at 77 K. The direction of crack propagation was again found to change at the grain boundaries and occasionally inside the grains, but the fracture surface was flatter than in the experimental alloy (Fig. 3*a*). Each facet exposed exhibited a fine microstructure that was associated with the transformed martensite (Fig. 3*b*). The α'-martensite could be detected on the fracture surfaces of the 304LN steel with a Magnegage, though α'-martensite was not detected on the fracture surfaces of the experimental alloy.

Both optical and scanning electron fractographies of the fracture surface of the experimental alloy broken at 4 K showed that the fracture was again

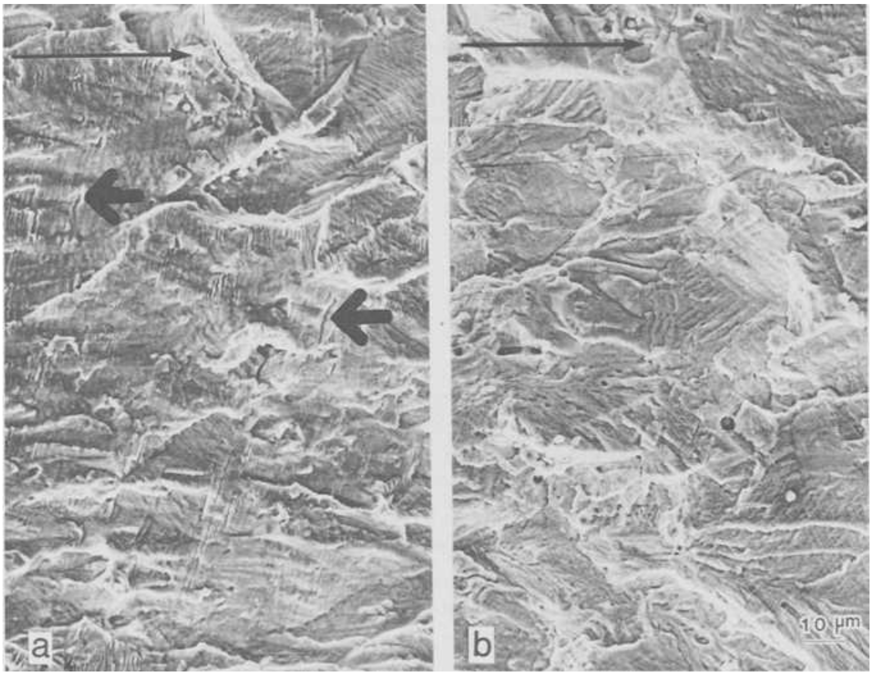

FIG. 2—*Fracture surfaces after fatigue cracking at 77 K* ($\Delta K = 35$ *MPa*$\sqrt{m}$). (a) *As-rolled.* (b) *Solution-treated. The long arrow shows the macrocrack growth direction* (da/dN); *the short arrows in* (a) *show the typical striations and the microcrack.*

transgranular. The crack propagation paths in the as-rolled plate are shown in Fig. 4. Many branches (secondary cracks) are seen in the intermediate and high ΔK range. The 4 K fracture surface is shown at 1000 × magnification in the scanning electron fractograph given in Fig. 5. The fracture surface of the as-rolled plate contained granular facets having feather-like striations that were oriented differently in each grain, together with slip markings and secondary cracks. The typical ductile striations that were seen on the fracture surfaces at 77 K disappeared at 4 K.

The fracture surfaces of the solution-treated plate also showed characteristic features. On the portion of the fracture surface that was created in the low ΔK range, some exposed grain facets exhibited striations that were oriented perpendicularly to the crack propagation direction, but did not cross a grain. On the surfaces created at the intermediate and high ΔK range, very smooth grain facets were exposed (A in Fig. 5*d*). These may have been due to intergranular failure. Crystallographic twins were also occasionally seen.

A typical transgranular failure mode was also observed in 304LN steel after fatigue cracking at 4 K (Fig. 6). However, the fracture surfaces differed qualitatively from those on the experimental alloy. Each grain facet displayed a fine lamellar structure that reflected the strain-induced martensite

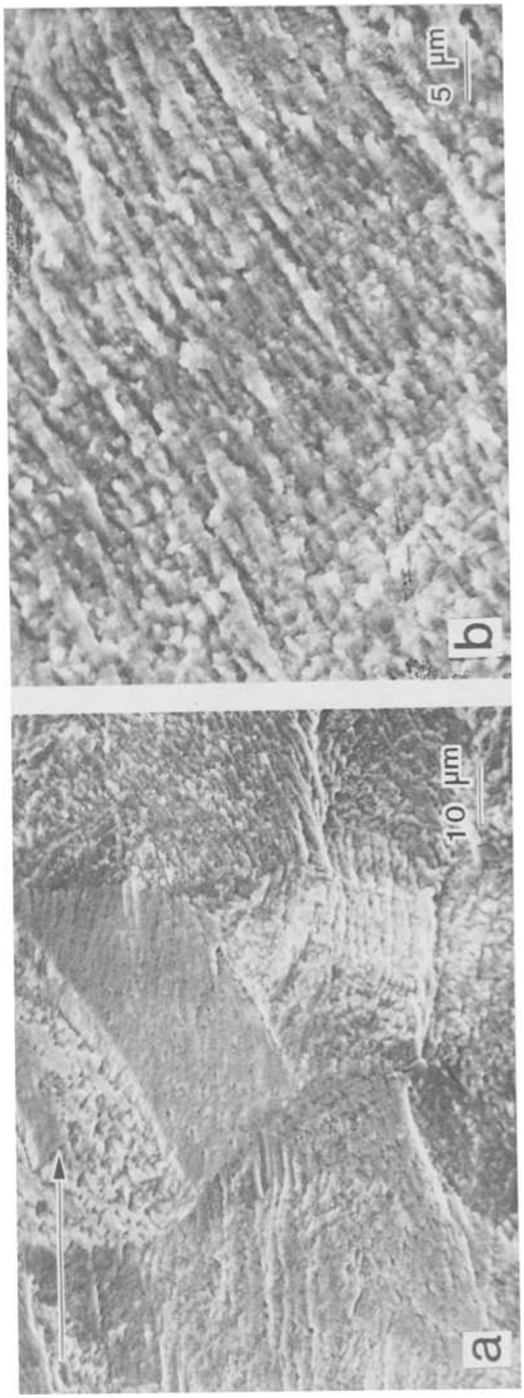

FIG. 3—*Fracture surfaces of 304LN steel after fatigue cracking at 77 K* ($\Delta K = 35$ *MPa*$\sqrt{m}$). (a) *Typical fracture feature.* (b) *Fracture lamellae associated with transformed martensite. The arrow indicates macrocrack growth direction* (da/dN).

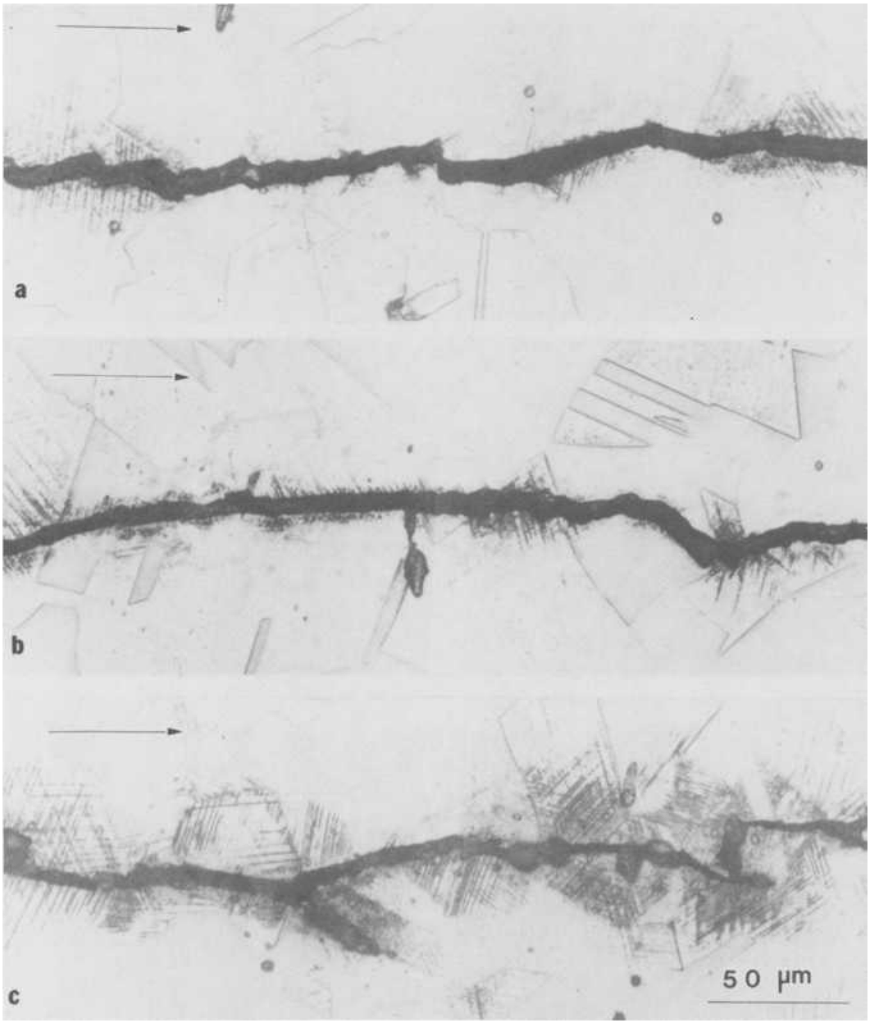

FIG. 4—*Crack propagation path of the as-rolled plate at 4 K.* (a) $\Delta K = 35$ *MPa$\sqrt{m}$.* (b) $\Delta K = 45$ *MPa$\sqrt{m}$.* (c) $\Delta K = 55$ *MPa$\sqrt{m}$. Arrows indicate macrocrack growth direction* (da/dN).

transformation (Fig. 7), but the lamellar structure was not as clearly defined on the 4 K specimen as it was on the 77 K specimen.

The metallographic investigation discussed above showed that the change in the FCGR of the experimental alloy with the testing temperature was closely related to the fractographic features on the fracture surface. The as-rolled plate, which had a low FCGR at 77 K, displayed fine striations that were typical of most ductile metals. This kind of striation was ill-defined on the 4 K fracture surface, and the FCGR was slightly higher at this tempera-

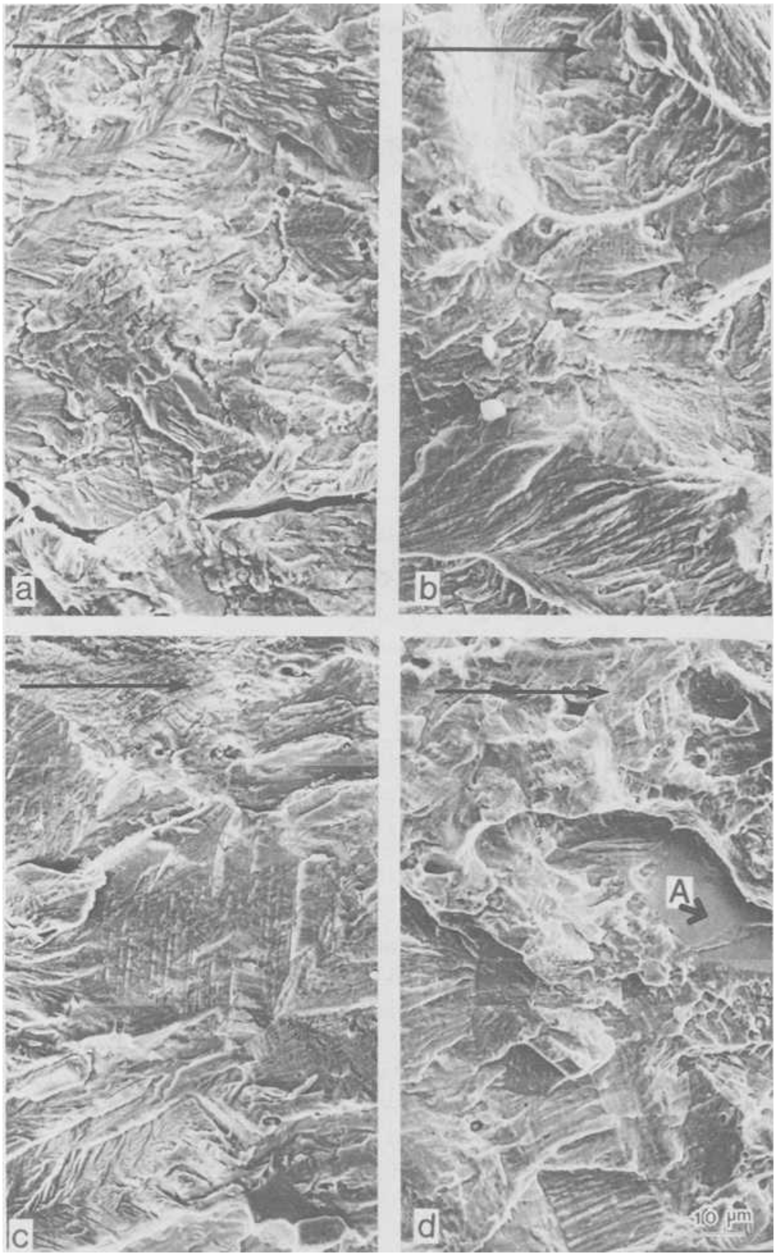

FIG. 5—*Fracture surfaces after fatigue cracking at 4 K.* (a) *As-rolled,* $\Delta K = 35\ MPa\sqrt{m}$. (b) *As-rolled,* $\Delta K = 45\ MPa\sqrt{m}$. (c) *Solution-treated,* $\Delta K = 35\ MPa\sqrt{m}$. (d) *Solution-treated,* $\Delta K = 45\ MPa\sqrt{m}$. *Arrows indicate macrocrack growth direction* (da/dN). (A) *indicates smooth grain facet.*

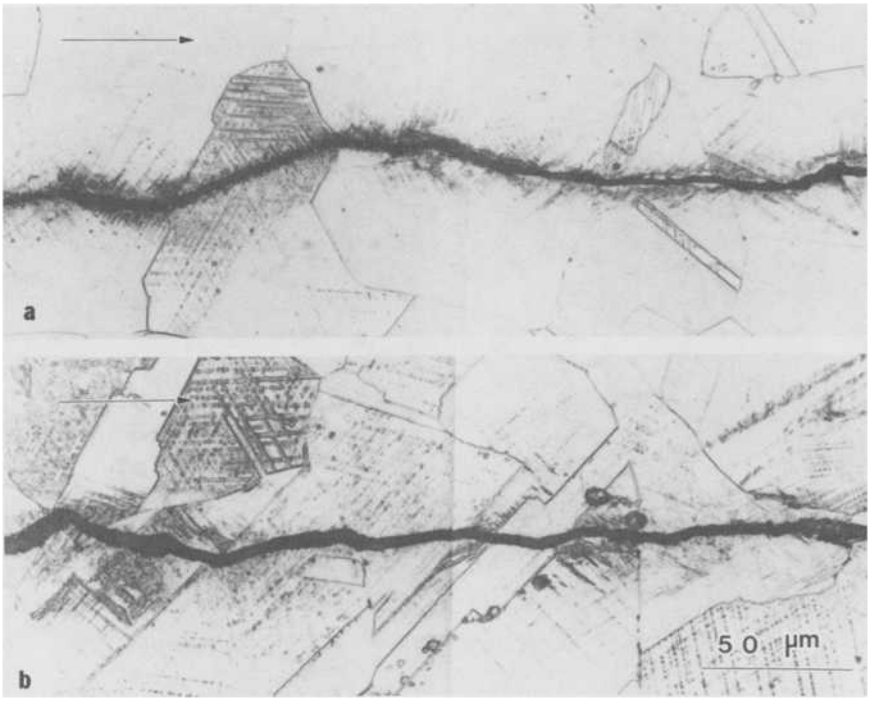

FIG. 6—*Crack propagation path of 304LN steel at 4 K.* (a) ΔK = *40 MPa$\sqrt{m}$.* (b) ΔK = *55 MPa$\sqrt{m}$. Arrows indicate macrocrack growth direction* (da/dN).

ture. The solution-treated plate was characterized by the increased slope of the logarithmic FCGR at 4 K and the cross-over between the fatigue crack growth rates at 4 and 77 K. The change in slope was coincident with a change in the fracture surface morphology. In the low ΔK range, where the FCGR at 4 K was lower than at 77 K, the grain facets exhibited ductile striations, while in the high ΔK range intergranular and twin-like facets were common. The similarity between the FCGR of the as-rolled plate at 4 K and that of the solution-treated plate at 77 K was also reasonable in light of the fractography. The two fracture surfaces showed similar features.

Fatigue cracks in the experimental alloy propagated mainly along slip planes. Figures 8*a* and 8*b* show examples of the crack path trace analysis using the slip marking ({111} plane traces). Fatigue cracks were also found to grow along the slip planes in the initial stages of fatigue crack propagation in ductile metals (Stage I [5]), but followed general planes at higher stress intensities (Stage II). The present alloy is interesting in that it showed crystallographic features in cryogenic fatigue in the Stage II as well.

Crystallographic crack growth was also found in 304LN steel after fatigue cracking at 4 K. Figure 8*b* shows an example of the 4 K crack trace of 304LN

FIG. 7—*Fracture surfaces of 304LN steel after fatigue cracking at 4 K, $\Delta K = 40$ MPa$\sqrt{m}$. Arrow indicates a fine lamellar structure that reflects α'-martensite.*

steel. In this case, the fatigue crack did not propagate along the {111} plane, but propagated along another plane, the trace of which was almost perpendicular to the slip markings. This local fracture surface was inferred to be the {110} plane from Fig. 8*b* and other analyses by using different grain orientations. As the fracture surface at 77 K showed noncrystallographic features, the increase in the FCGR at 4 K might be attributed to the crystallographic crack growth on the {110} plane. Crystallographic fractures have been observed in some aluminum alloys, in which case the fracture surface is (100) or (110) [*6,7*]. Crystallographic crack growth in aluminum alloys is believed to be enhanced by environmental contaminants that promote brittle fracture on the (110) plane [*7*]. In the present case, however, it is likely that the crystallographic fracture was associated with the transformation to martensite.

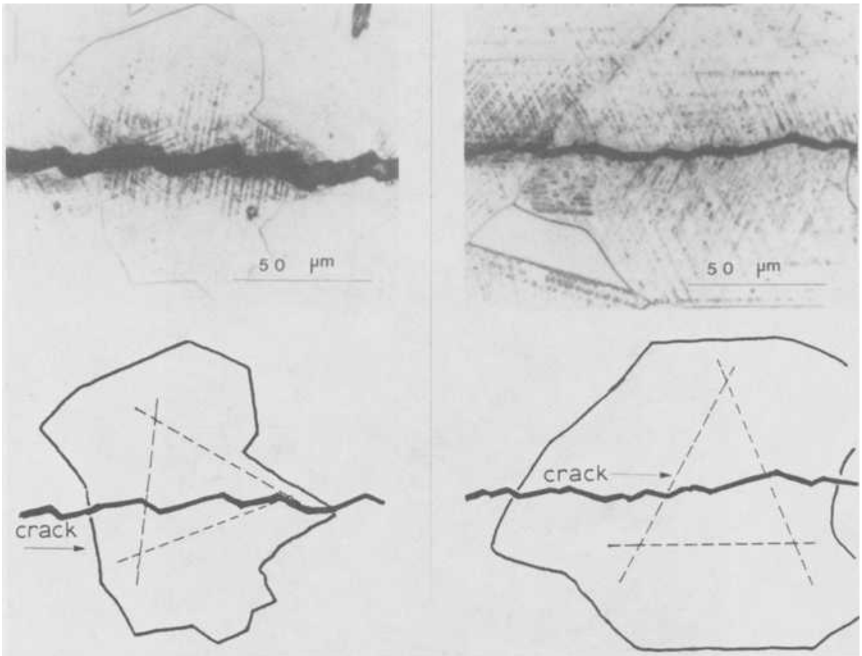

FIG. 8—*Examples of crack trace analysis after fatigue cracking at 4 K. Dashed line indicates* {111} *plane markings.* (a) *As-rolled plate.* (b) *304LN.*

Although α'-martensite was observed on the exposed grain facets at both 77 and 4 K, the matrix was still more than 50% austenite according to X-ray diffraction analysis. The martensite was almost certainly more brittle at 4 K than it was at 77 K. Brittle α'-martensite might have enhanced the {110} crystallographic crack growth of the matrix.

Conclusions

A nitrogen-strengthened high-manganese steel of nominal composition 18Mn-5Ni-16Cr-0.02C-0.22N showed promising fatigue resistance when compared with 304LN steel at cryogenic temperatures. The research described here found that:

1. The FCGR at 4 K was almost the same as at 77 K and was substantially below that of 304LN steel at 4 K.
2. The failure mode was transgranular in both the research alloy and 304LN at 77 and 4 K. Both alloys exhibited a pronounced crystallographic fracture under some conditions, which differed from that previously reported in structural steels in that it occurred in Region II of the crack growth behavior.

3. There was a reasonable correspondence between the fatigue crack growth behavior and the microstructural mechanisms of crack growth, as revealed by fractographic studies of the fatigue surface.

Acknowledgments

The alloys studied here were supplied by Kobe Steel Ltd., Kobe, Japan. This research was supported by the Director, Office of Energy Research, Office of Development and Technology, Magnetic Systems Division of the U.S. Department of Energy under Contract DE-AC03-76SF00098.

References

[1] Yoshida, K., Koizumi, K., Nakajima, H., Shimada, M., Sanada, Y., Takahashi, Y., Tada, E., Tsuji, H., and Shimamoto, S. in *Proceedings,* International Cryogenic Materials Conference, Butterworth, Surrey, U.K., 1982, p. 417.
[2] Reed, D. T. and Reed, R. P., "Materials Studies for Magnetic Fusion Energy Applications at Low Temperatures-II," NBSIR79-1609, National Bureau of Standards, Boulder, CO, 1979, p. 81.
[3] Tobler, R. L., Reed, D. T., and Reed, R. P., "Materials Studies for Magnetic Fusion Energy Applications at Low Temperatures-IV," NBSIR81-1645, National Bureau of Standards, Boulder, CO, 1981, p. 37.
[4] Ogawa, R. and Morris, J. W., Jr., in *Proceedings,* International Cryogenic Materials Conference, Butterworth, Surrey, U.K., 1982, p. 124.
[5] Forsyth, P. J. E., *Acta Metallurgica,* Vol. 11, No. 7, July 1963, p. 703.
[6] Garrett, G. G. and Knott, J. F., *Acta Metallurgica,* Vol. 23, No. 7, July 1976, p. 841.
[7] Nix, K. J. and Flower, H. M., *Acta Metallurgica,* Vol. 30, No. 8, Aug. 1982, p. 1549.

Mechanisms and Material Properties

Noncryogenic Temperatures

Khlefa A. Esaklul, Weikang Yu, and William W. Gerberich

Effect of Low Temperature on Apparent Fatigue Threshold Stress Intensity Factors

REFERENCE: Esaklul, K. A., Yu, W., and Gerberich, W. W., "**Effect of Low Temperature on Apparent Fatigue Threshold Stress Intensity Factors,**" *Fatigue at Low Temperatures, ASTM STP 857,* R. I. Stephens, Ed., American Society for Testing and Materials, Philadelphia, 1985, pp. 63–83.

ABSTRACT: Near-threshold fatigue crack growth in high-strength low-alloy (HSLA) steel, Fe, and Fe-Si alloys was found to depend on test temperature from room temperature down to 123 K. Near-threshold crack growth rates were lowered and threshold stress intensity factors increased with decreasing temperature. A "prominent" closure was observed for all test temperatures and materials and was further confirmed by the examination of fracture surfaces. The magnitude of closure increased with decreasing temperature, suggesting a dependence on yield strength and fracture morphology. The effects of R ratio were found to be closure-related for the same fracture processes. However, a change in the fracture process, (e.g., to cyclic cleavage) may lead to a $\Delta K_{th(eff)}$ dependence on load ratio even at very high R values. Hence mean stress may affect threshold independently of any closure-related phenomena. A reasonable correlation was obtained with a theoretical model for closure that could account for both geometrical and reversed plasticity phenomena.

KEY WORDS: closure, fatigue crack propagation, fatigue thresholds, fractography, HSLA steel, iron alloys, low temperatures, load ratio

The traditional approach to understanding low-temperature fatigue crack growth behavior, particularly threshold stress intensity factors and near-threshold crack growth, has been in terms of changes in yield strength [*1–9*] or the fracture process [*2,3,8,9*]. However, in view of the recent closure models proposed for threshold and near-threshold crack growth, namely re-

Drs. Esaklul and Yu are former research assistants and Dr. Gerberich is a professor in the Department of Chemical Engineering and Materials Science at the University of Minnesota, Minneapolis, MN 55455. Dr. Esaklul is currently an assistant professor in the Faculty of Engineering, Al-Fateh University, Tripoli, Libya. Dr. Yu is a postdoctoral associate in the Department of Materials Science and Mineral Engineering, University of California, Berkeley, CA 94720.

versed plasticity and oxide-induced or geometrically induced closure, it appears that competing or overlapping effects of closure versus changes in yield strength and the fracture process may be involved [*10*]. At low temperatures, the environmental effects diminish and the oxide-induced closure becomes less significant, leaving possible contributions of reversed plasticity and geometrically induced closure. Neumann et al [*11*] proposed that extrusion-intrusion pairs can develop during the fatigue process as a consequence of reversed slip around the crack tip when the crack was propagated near a threshold stress intensity factor for fatigue crack propagation.

This development, along with fracture surface roughness coupled with Mode I–Mode II displacement, can produce closure, as has been demonstrated by Minakawa and McEvily [*12*], Beevers [*13*], and Suresh and Ritchie [*14*]. A significant feature of this type of closure is that it is being controlled by the material properties as well as the fracture morphology. Closure also can be induced by a compressive stress acting at the crack tip because of residual plasticity generated by previous load cycles [*15*] and inherent residual stresses that are known to vary from grain to grain or from microstructural feature to feature. The consequence of these proposed closure mechanisms is a potential reduction in the effective stress intensity factor at the crack tip. Hence lower crack growth rates and a higher threshold stress intensity factor may result. Other microstructural and intrinsic material properties (e.g., dislocation substructure and dislocation dynamics) have been cited as significant factors in near-threshold crack growth [*4,7,8,16–18*], but they will not be considered fully in this study.

Previous results [*1,2,4–6,9,10*] for Mode I cracking indicate that, in general, fatigue crack growth rates (da/dN) decrease near the threshold and threshold stress intensity factors (ΔK_{th}) increase with decreasing temperature for both body-centered-cubic (bcc) and face-centered-cubic (fcc) materials. Whether the effect of temperature is purely an inherent material property or not is still unresolved; the question is further complicated by ignoring possible closure effects. For the limited data available, the thermal component of yield stress appears to be a controlling parameter in near-threshold crack growth [*4,9,10*]. However, a fracture process change at an intermediate cyclic stress intensity range (ΔK), such as static or cyclic cleavage, may offset any thermal stress effects [*2–5,9,10*]. A question then arises: If a decrease in temperature may raise the yield strength and change the fracture morphology, can closure, whether slip-induced or geometrically induced, be ignored? Further, which are more significant, extrinsic parameters such as closure, or intrinsic ones like the thermal component of the flow stress?

The present study was undertaken to separate the relative contribution of closure from other intrinsic parameters through controlled closure stress intensity measurements and fractographic analysis correlations.

Materials and Experimental Procedures

The materials used in this investigation included a fine grain high-strength low-alloy (HSLA) steel and a sequence of iron (Fe) and iron silicon (Fe-Si) alloys with different silicon contents. The HSLA steel was used in the as-received condition and heat-treated to obtain larger grain sizes. The heat treatment involved austenitizing the as-received 10-μm grain size material at 1473 K under vacuum of 10^{-5} torr for 30 min and then furnace cooling to obtain a grain size of 60 μm. The Fe and Fe-Si alloys were vacuum induction-melted and hot-rolled into plates 13 mm thick. The composition and properties of the alloys are listed in Tables 1 and 2. Note that atomic percent is used for the alloy designation for the Fe-Si alloys. The process history and heat treatment indicate that residual stress would be minimal except for the 10-μm HSLA steel.

All fatigue crack growth tests were performed by using standard Mode I compact tension (CT) specimens (except for the thickness) as described in ASTM Test for Constant-Load-Amplitude Fatigue Crack Growth Rates Above 10^{-8} m/Cycle (E 647). The specimen thickness varied because of the available plate thickness, from 6.5 mm for the HSLA steel to 12.3 mm for Fe and Fe-Si alloys. Cyclic loading was accomplished by using an electro-hydraulic-servocontrolled testing system in load control mode, with constant-amplitude tension-tension cycling at a frequency of 30 Hz. The load ratio (R) for the HSLA steel was controlled at 0.1, 0.35, or 0.7. For Fe-Si alloys, although the ratio varied slightly, it was on the order of 0.02 for all test conditions. The crack length was monitored by the compliance technique with a crack opening displacement gage clipped on the outer edge surface of the specimen. The loading sequence followed a "load shedding" scheme, with the cyclic stress intensity factor (ΔK) being started at a higher value and progressively decreased until the threshold stress intensity factor (ΔK_{th}) was reached. The fatigue threshold was taken as the cyclic stress intensity factor range at a fatigue crack growth rate (da/dN) equal to or less than 10^{-10} m/cycle. Intermittently, the experiment was interrupted for crack growth

TABLE 1—*Chemical composition (weight percent) of alloys tested.*

Alloy	Element								
	C	Mn	Si	P	S	Ti	Al	Nb	Fe
HSLA steel	0.070	0.51	0.03	0.01	0.01	...	0.01	0.014	balance
Fe	0.008	...	...	...	...	...	0.017	...	balance
Fe-1.0Si	0.011	0.01	0.45	0.005	0.005	0.09	0.021	...	balance
Fe-2.5Si	0.009	0.01	1.20	0.005	0.005	0.10	0.017	...	balance
Fe-4.0Si	0.020	0.01	1.90	0.005	0.005	0.12	0.018	...	balance

TABLE 2—*Grain size and yield strength of alloys tested.*[a]

Alloy	Average Grain Size, μm	Yield Strength, MPa, at Temperature Shown			
		300 K	233 K	173 K	123 K
HSLA steel	10	365	440	512	660
HSLA steel	60	230	300	350	535
Fe	103	122	230	345	477
Fe-1Si	73	158	192	287	444
Fe-2.5Si	63	195	217	275	368
Fe-4Si	93	218	302	322	423

[a] Yield strength is an average of two tests.

measurements by plotting compliance curves (load versus crack opening) on an *x-y* recorder with the frequency at 0.1 Hz. The closure load or, more precisely, the opening load was defined as the point on the unloading portion of the compliance curve where the curvature of the line started to go negative as defined by Elber [*19*]. After the threshold was established, the experiment was terminated on some specimens while others were pulled open for scanning electron microscopy (SEM) examination.

The fatigue testing environment used was either laboratory air with a relative humidity of about 50% or an open system of evaporated liquid nitrogen for low temperature. Four temperatures were used for all materials: 300, 233, 173, and 123 K. Low temperatures were attained by fan-forced mixing of evaporating liquid nitrogen with air compensated by an electric-resistance heater. With the heater connected to a feedback temperature controller, the specimen's temperature was maintained within 1 K of the specified value.

Results and Discussion

Near-threshold fatigue crack propagation decreased and threshold stress intensity factors increased with a decreasing temperature from 300 K down to 123 K for all materials used in this study.[1] This behavior is similar to that observed by others [*1,4–6,8*]. A prominent closure was observed for all test temperatures and materials. On the compliance curve, a significant deviation from linearity indicated that the crack surface was closed before the load reaching the minimum value of the loading waveform. Taking the first deviation of the unloading line as the opening stress intensity factor (K_{op}), the

[1] At higher values of ΔK a crossover in the crack growth curves can occur at low temperatures. The crossover is more pronounced in the Paris law regime. This behavior is due to the increase in yield strength and the onset of cyclic cleavage fracture [*3,4*].

value of the effective cyclic stress intensity factor (ΔK_{eff}) was determined from

$$\Delta K_{eff} = K_{max} - K_{op} \quad (1)$$

where K_{max} is the maximum stress intensity factor in the cycle [*5,6,10,12–14*]. Similarly, the K_{op} values were determined to obtain a curve for ΔK_{eff} versus da/dN. Both da/dN as a function of ΔK and ΔK_{eff} are shown in Fig. 1 for 10-μm grain size HSLA steel and 103-μm grain size iron at room temperature. Also shown are similar data for 60-μm HSLA steel and 103-μm Fe at 123 K. It is seen here that ΔK_{th} is near 5.0 MPa $\cdot$ m$^{1/2}$ and $\Delta K_{th(eff)}$ is near 3.8 MPa $\cdot$ m$^{1/2}$ for the 10-μm HSLA steel at room temperature. The corresponding values for iron are 9 and 6.5 MPa $\cdot$ m$^{1/2}$ at room temperature and 16 and 11.4 MPa $\cdot$ m$^{1/2}$ at 123 K, respectively. Figure 1*b* shows ΔK_{th} near 8.5 MPa $\cdot$ m$^{1/2}$ and $\Delta K_{th(eff)}$ near 5.9 MPa $\cdot$ m$^{1/2}$ for 60-μm HSLA steel tested at $R = 0.35$. The $\Delta K_{th(eff)}$ result indicates that closure at 123 K may remain substantial even at $R = 0.35$, as will be discussed further in the section on Load Ratio Effects. Both the apparent threshold stress intensity factor (ΔK_{th}) and the effective threshold stress intensity factor ($\Delta K_{th(eff)}$) are listed in Table 3 for the HSLA steel. Both follow a general trend of increasing with decreasing temperature. Similar trends are seen in the Fe and Fe-Si alloys, as depicted in Fig. 2 for Fe and Fe–2.5Si.

It is evident from the foregoing results that closure measured in terms of K_{op} increased with a decrease in test temperature, which suggests a strong dependence on yield strength and fracture mode. On the basis of closure induced by geometrical asperities, it has been shown that K_{op} depends on yield strength and grain size [*10*]. To evaluate this dependence, the opening stress intensity factor (K_{op}) was plotted as a function of $\sigma_{ys}d^{1/2}$, where σ_{ys} is the yield strength and d is the average grain diameter. A statistical analysis of the data shows a relation between K_{op} and $\sigma_{ys}d^{1/2}$ with a linear regression correlation coefficient of about 0.7 (Fig. 3). This suggests that surface roughness, which depends on the microstructure and the fracture process, may partially control the magnitude of closure, whether it is oxide-induced or geometrically induced. The yield strength contributes in terms of reversed plasticity-induced closure or through the relative change in strength and deformation of the asperities. The latter could effect a change in the oxide-induced and geometrically induced closure as well.

The magnitude of closure was further confirmed by the examination of fatigue fracture surfaces in some specimens as well as the crack path observation from various longitudinal sections in other unbroken specimens. The fatigue fracture surfaces of the HSLA steel were predominantly transgranular ductile fractures at 300 K and 233 K and transgranular ductile and cyclic cleavage at 173 K and 123 K, as was noted by Lucas and Gerberich [*4*]. The

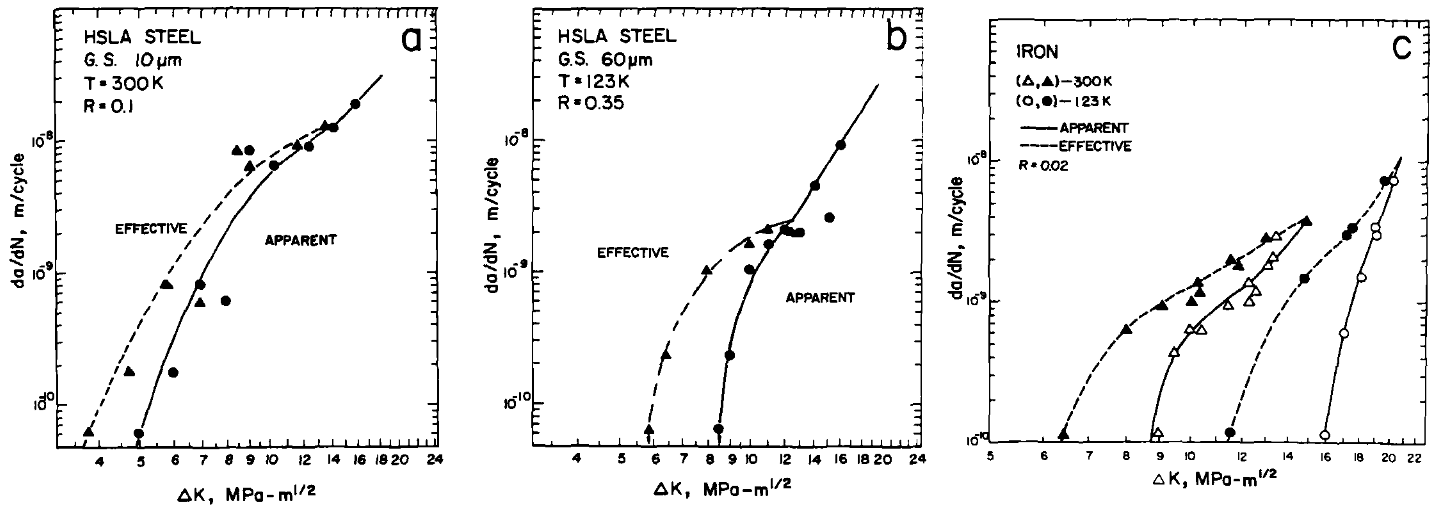

FIG. 1—*Crack growth rate as a function of apparent and effective stress intensity factor for HSLA steel and Fe.* (a) *HSLA steel, 10 μm, tested at 300 K with* R = *0.1.* (b) *HSLA steel, 60 μm, tested at 123 K with R = 0.35.* (c) *Fe tested at 300 and 123 K with* R = *0.02.*

TABLE 3—*Apparent and effective fatigue threshold stress intensities at four testing temperatures and three* R *ratios for HSLA steel.*

Grain Size (d), μm	Test Temperature K	ΔK_{th}, MPa · m$^{1/2}$, at R = 0.1	0.35	0.7	$\Delta K_{th(eff)}$, MPa · m$^{1/2}$, at R = 0.1	0.35	0.7
10	300	5.5	4.0	4.0	4.1	4.0	4.0
10	233	6.0	...	...	4.2	...	...
10	173	7.0	...	...	4.4	...	...
10	123	9.0	6.0	6.0	6.1	5.7	6.0
60	300	6.5	5.0	4.5	5.0	5.0	4.5
60	233	8.0	...	...	6.4	...	...
60	173	10.0	...	...	8.0	...	...
60	123	13.0	8.5	5.0	6.9	5.9	5.0

percentage of cyclic cleavage was much higher at 123 K for high mean stresses, as will be discussed further in the section on Load Ratio Effects. At threshold values with $R = 0.1$, the fracture surfaces were predominantly transgranular ductile fracture, even at 123 K. The highest percentage of cyclic cleavage was ~15% for the lower-strength material (60 μm) at 123 K tested at $R = 0.1$. Figure 4 illustrates the various fracture modes observed

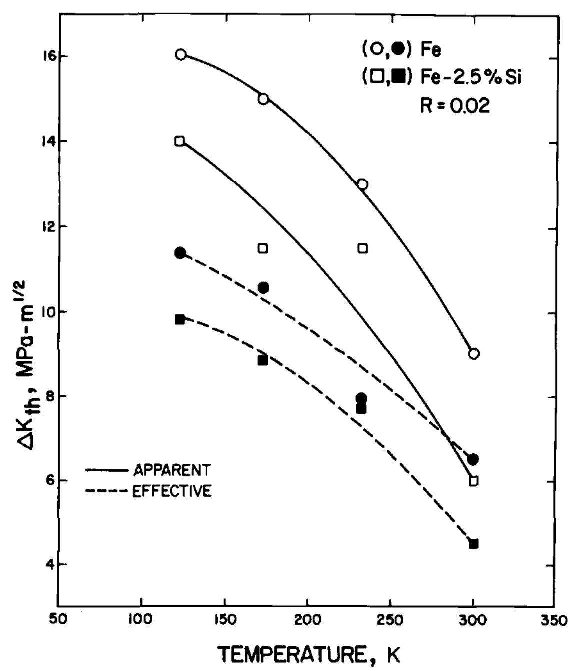

FIG. 2—*Comparison of* ΔK_{th} *and* $\Delta K_{th(eff)}$ *as a function of temperature for Fe and Fe-2.5Si.*

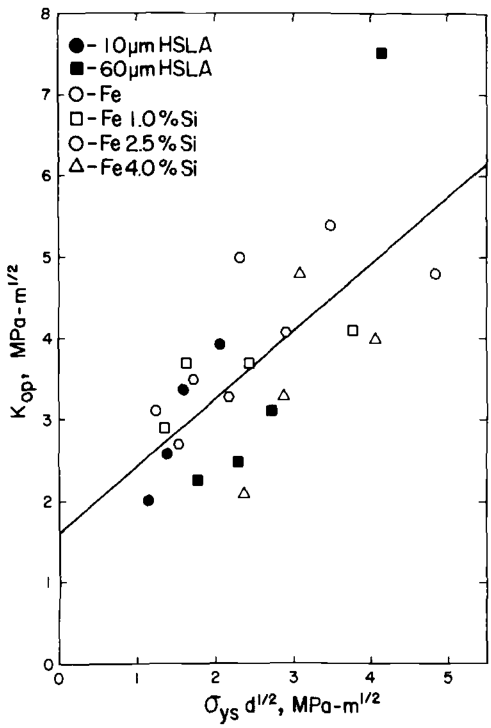

FIG. 3—*Correlation of opening stress intensity factor* (K_{op}) *to* $\sigma_{ys}d^{1/2}$ *for HSLA steel, Fe, and Fe-Si alloys.*

for the 60-μm material at room temperature and 173 K. It appears that the cyclic cleavage islands near threshold were increasing the degree of surface roughness and hence increased closure (i.e., higher K_{op}) as seen in the difference between the values of ΔK_{th} and $\Delta K_{th(eff)}$ listed in Table 3. The most severe case was the 60-μm material, where K_{op} increased from 2 MPa · m$^{1/2}$ at room temperature to 7.5 MPa · m$^{1/2}$ at 123 K.

The Fe and Fe-Si alloy fracture surfaces showed a similar transgranular ductile fracture process, with a few intergranular and cyclic cleavage facets, depending on the yield strength (i.e., alloy content). Transgranular ductile fracture was evident even at temperatures well below the ductile-brittle transition temperature and asperities could be readily found. Details of the fractography of each of these alloys are discussed elsewhere [*10,20*]. Examples of the various fracture processes are shown in Fig. 5 for Fe-2.5Si at room temperature and Fe-4Si at 123 K. The high percentage of cleavage can be seen in the Fe-4Si, and the combination of ductile and intergranular fracture can be seen in the Fe-2.5Si. At room temperature and 233 K an oxide could be seen covering mainly the transgranular ductile area. Evidence of an oxide over-layer could also be seen at $R = 0.1$ in the HSLA steel at room temperature and 233 K. The oxide was additional evidence of closure as observed in a separate investigation on AISI 4340 steel [*21*] and by others [*22–24*].

Load Ratio Effects

Results of tests on 10- and 60-μm grain size HSLA steel for $R = 0.1, 0.35$, and 0.7 at 300 K and 123 K are illustrated in Fig. 6. The near-threshold crack growth rate increased and the threshold stress intensity factor decreased with increasing load ratio; these effects have been observed by others [*12,22–24*]. A comparison of ΔK_{th} and $\Delta K_{th(eff)}$ is given in Table 3. It is evident that the effect of load ratio is due to closure alone in the 10-μm grain size material at 300 K, since data at $R = 0.35$ and $R = 0.7$ superimposed and $\Delta K_{th(eff)}$ values were equal for the three load ratios. This suggests that in terms of the effective stress intensity factor there is no mean stress effect. At 123 K, the *da/dN* versus ΔK curves did not coincide, but the $\Delta K_{th(eff)}$ values were the same again at low temperatures, indicating the absence of a mean stress effect. However, K_{op} values were higher at the low temperature, the difference being a result of the increase in yield strength and the change of the fracture morphology, as has been seen before [*10,20*].

The 60-μm material showed a behavior similar to the 10-μm material, with no dependence of $\Delta K_{th(eff)}$ on mean stress at room temperature. A comparison of the ΔK_{th} and $\Delta K_{th(eff)}$ values listed in Table 3 indicates that the effect of load ratio is also due to closure, since $\Delta K_{th(eff)}$ values are basically the same for the three load ratios. However, at 123 K the magnitude of closure is much higher, as may be seen in the spread of *da/dN* versus ΔK curves in Fig. 6*b*. The closure remained substantial even at $R = 0.35$, as shown in Figure 1*b*, where apparent and effective values for *da/dN* versus ΔK are split, up to a growth rate of 2×10^{-8} m/cycle. It is also seen that $\Delta K_{th(eff)}$ continuously decreased to $R = 0.7$, indicating a mean stress dependence at this temperature. Fractographic analysis showed that the percentage of cyclic cleavage fracture increased from 0 to 20% at $R = 0.1$, to 40 to 50% at $R = 0.35$, to 90% at $R = 0.7$, as qualitatively indicated in Fig. 7. Furthermore, a considerable number of twins observed on the cleavage facets also were dependent on the mean stress (i.e., R ratio). A sample of these twins, which were also seen in Fe-Si alloys [*20*], is shown in Fig. 7*d*. The percentage of the twinned cleavage facets ranged from about 20% at $R = 0.1$, to 50% at $R = 0.35$, to 80 to 90% at $R = 0.7$.

The increase in load ratio (i.e., mean stress) results in a higher maximum stress (σ_{max}) that seems to approach the critical stress for cyclic cleavage. The higher σ_{max} also could exceed the twinning stress, which will nucleate twins. These nucleated twins can act as nucleation sites for cyclic cleavage; hence higher cyclic cleavage results as the load ratio increases, in agreement with

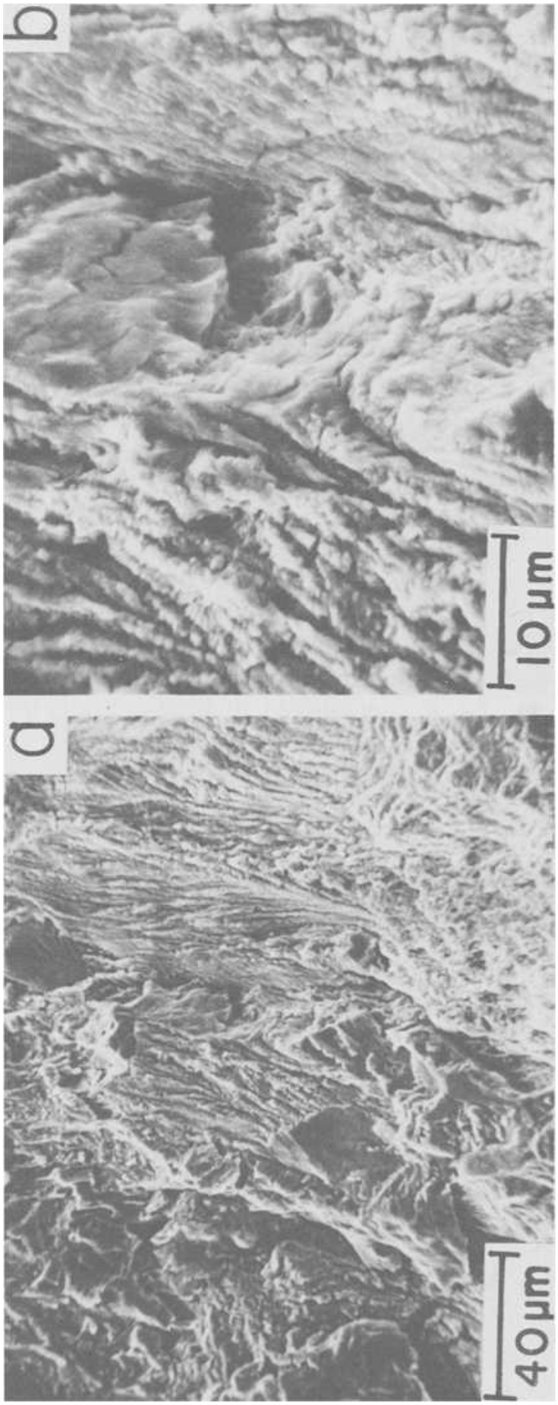
b
10 μm
a
40 μm

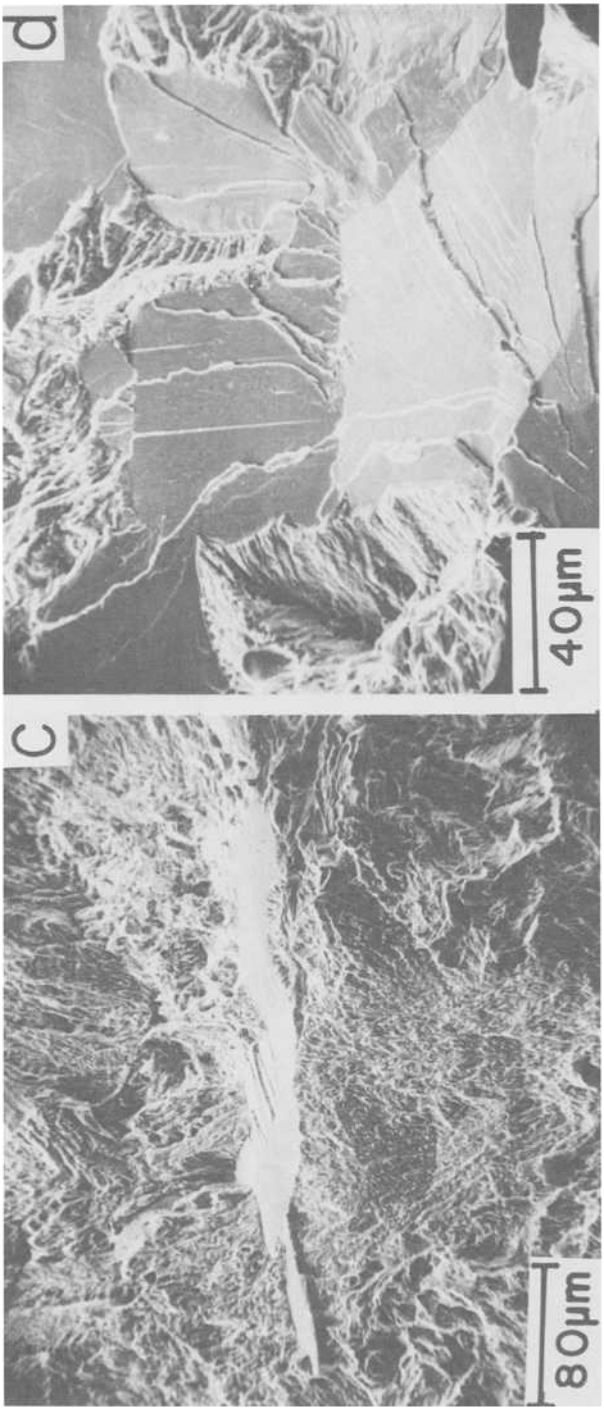

FIG. 4—*SEM micrographs showing the fracture morphology at threshold for 60-μm HSLA steel. Note transgranular ductile fracture at room temperature* (a,b) *and transgranular ductile fracture with a few cleavage facets at* 173 K (c,d). *Note the appearance of an oxide over-layer in* (b).

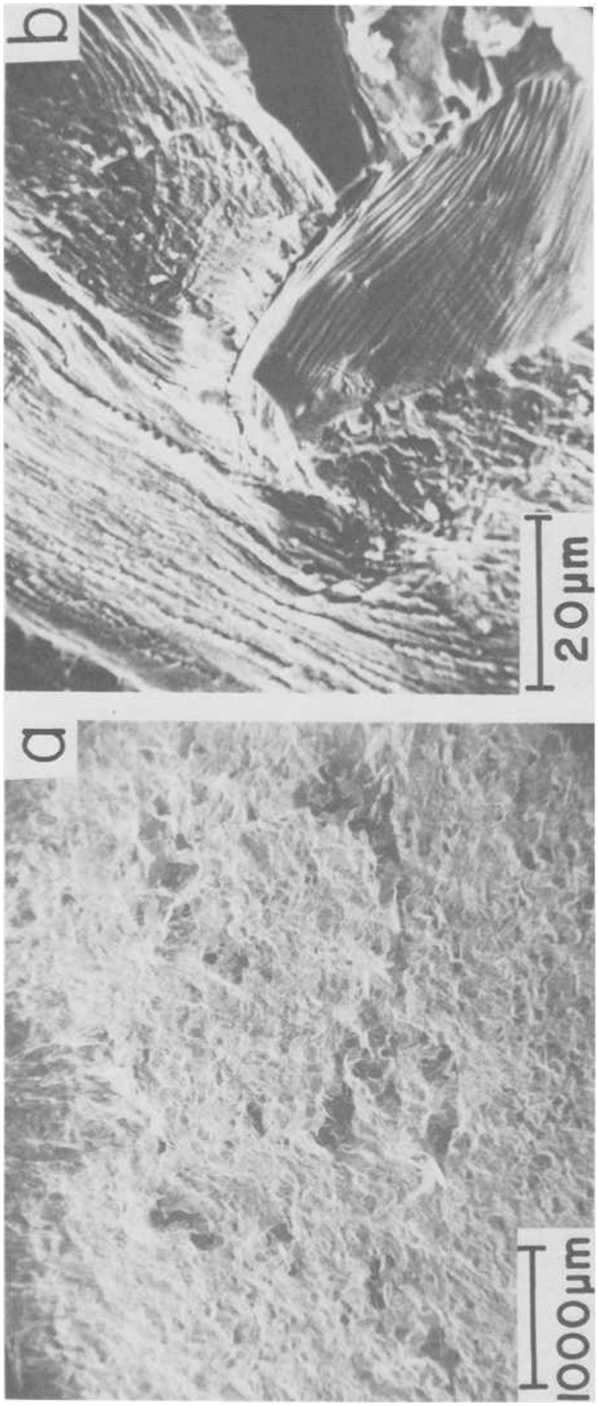
b
20µm
a
1000µm

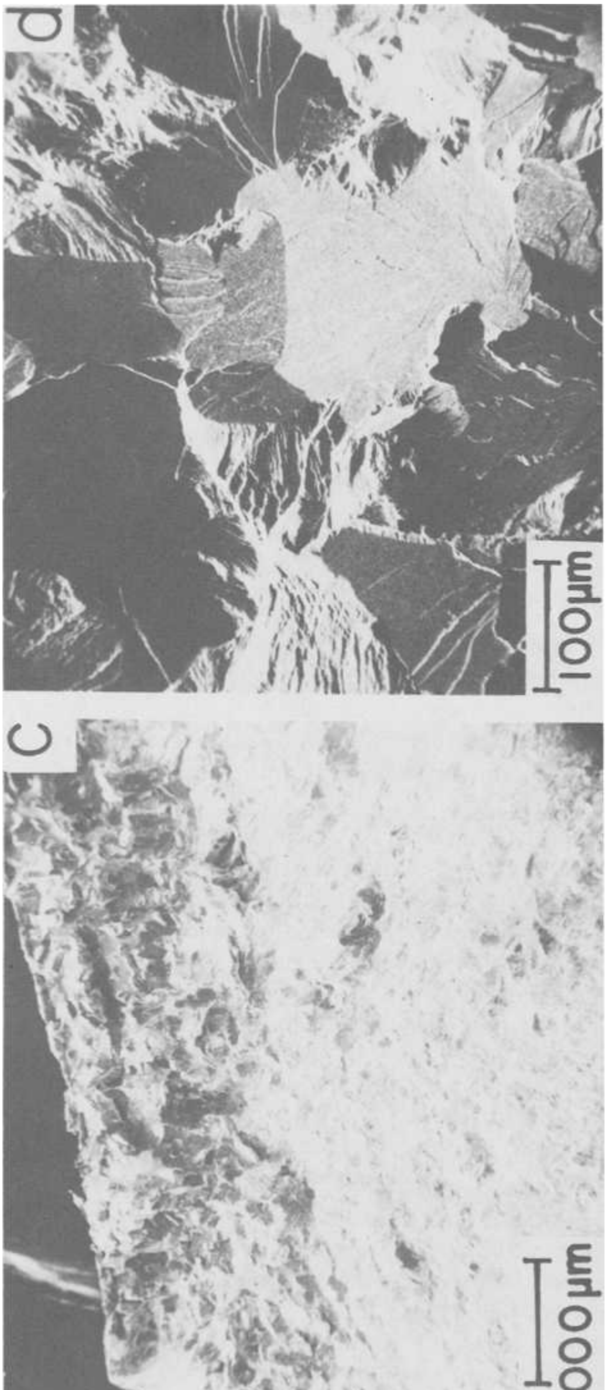

FIG. 5—*SEM micrographs showing the fracture morphology at threshold for Fe–2.5Si at room temperature* (a,b) *and Fe–4Si at 123 K* (c,d). *Note a mixture of intergranular and transgranular ductile fracture in the Fe–2.5Si and transgranular ductile cleavage in the Fe–4Si results. Note the degree of surface roughness in the low-magnification micrographs* (a,c).

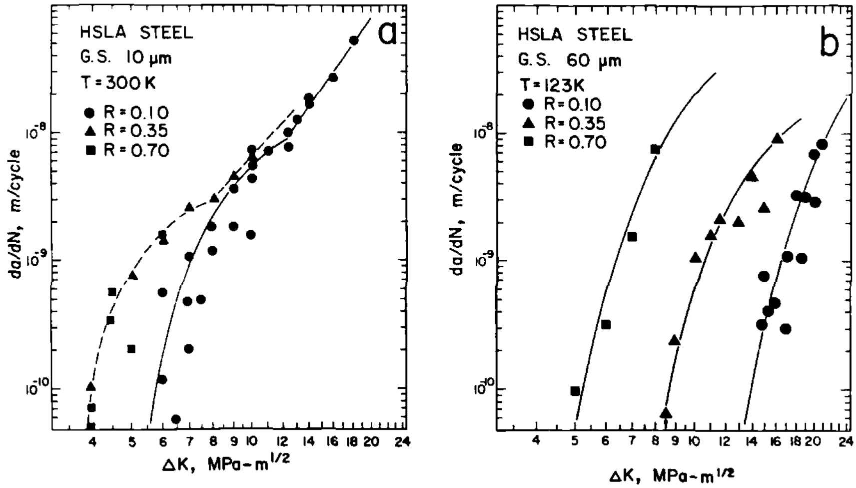

FIG. 6—*Comparison of crack growth rates as a function of stress intensity factor for HSLA steel at three* R *ratios.* (a) *10 μm tested at 300 K.* (b) *60 μm tested at 123 K.*

observations. The absence of mean stress effects at 123 K for the 10-μm grain size material could be a result of higher cleavage and twinning stresses as well as a lower slip-band concentration factor for the fine grain structure. This is in agreement with fractographic results at the three load ratios for the 10-μm material, which showed no significant difference in the amount of cleavage fracture at threshold.

The dependence of the fatigue threshold stress intensity factor on temperature considered here and in previous publications [*10,20*] appears to be controlled by the change in the material strength resulting from the temperature change, the change in the cracking mechanism, and the various operating closure forces that result. It has been concluded that closure alone cannot account for the dependence of ΔK_{th} on temperature. Once $\Delta K_{th(eff)}$ was considered separately, a strong correlation with the flow stress was observed [*20*]. However, to account for the overall dependence of ΔK_{th}, a better understanding of the closure mechanism is in order, particularly as it relates to changes in load ratio. It has been shown here that the effect of increasing the load ratio is generally closure-related, except for the cases where it alters the fracture processes involved, particularly near the threshold. Any theoretical consideration must account for these effects.

Several models have been proposed, generally based on such intrinsic material characteristics as dislocation dynamics [*4,7,8,16–18*] or closure-related phenomena, including oxide- [*22–24*], geometry- [*12–14*] or plasticity- [*11,13–15,19*] induced closure. The complexity of the parameters involved has hindered the incorporation of all these phenomena into a single model.

A recent attempt to combine such closure contributions into one model has been proposed in a current publication [*10*]. The model is based on incorporating the reverse slip, geometry, and oxide-induced closure in terms of the opening stress intensity factor. In the original form of Eq 19 in Ref *10*, based on $R = 0$, a good correlation was shown between calculated and measured values of K_{op} for the Fe and Fe-Si alloys. In the present study the load ratio (R) was included and the equation (Eq 19 in Ref *10*) takes the form

$$K_{op}^{2} = \frac{\alpha_0 \Delta K + \alpha_I r^{1/2} \Delta K^2 \dfrac{1}{(1-R)} + \phi_{oxide} E \Delta K}{(1-R)\left[(\Delta K/\sigma_{ys})^2 + \dfrac{24r}{\pi}\right]^{1/2}} \tag{2}$$

where the α_0 and α_I terms incorporate geometry and reversed plasticity, respectively. Here, r is the distance from the closure point to the crack tip, ϕ_{oxide} is the crack opening displacement caused by oxide wedging, E is the modulus of elasticity, and α_0 is a parameter that depends on the grain size, modulus, and deformation characteristics of the geometrical asperities. An estimate of α_0 was on the order of 0.007 MPa · m for the 10-μm and 0.042 MPa · m for the 60-μm HSLA steel. Note that it scales linearly with the grain size. The parameter α_I depends on the load ratio and is given by

$$\alpha_I = \beta \left(\frac{32}{\pi \lambda}\right)^{1/2} \tag{3}$$

where β and λ are two dimensionless parameters for the material. Based on Elber's [*19*] experimental results, $\lambda^{-1/2}$ is given by

$$\lambda^{-1/2} = (0.5 + 0.1R + 0.4R^2) \tag{4}$$

with R being the load ratio and β a fitting parameter in the range of 0.1 to 0.5 [*10*]. Taking $\beta \simeq 0.16$ and $r = 100$ μm for the 10-μm material and 300 μm for the 60-μm material, and assuming the oxide contribution to be zero at low temperatures, K_{op} at threshold can be calculated. It should be noted that the distance parameter is based partly on metallographic sectioning [*10*] and partly on Auger spectroscopy studies [*21*] previously used to identify closure distances. The results of these calculations are shown in Fig. 8 for the HSLA steel in terms of observed versus calculated K_{op}. Linear regression of the observed values onto the calculated ones showed a near one-to-one correspondence at both load ratios, 0.1 and 0.35. At $R = 0.7$ all the calculated K_{op} values were below the minimum stress intensity factor (K_{min}), which was expected since K_{min} is high and the crack remains open throughout the fatigue cycle.

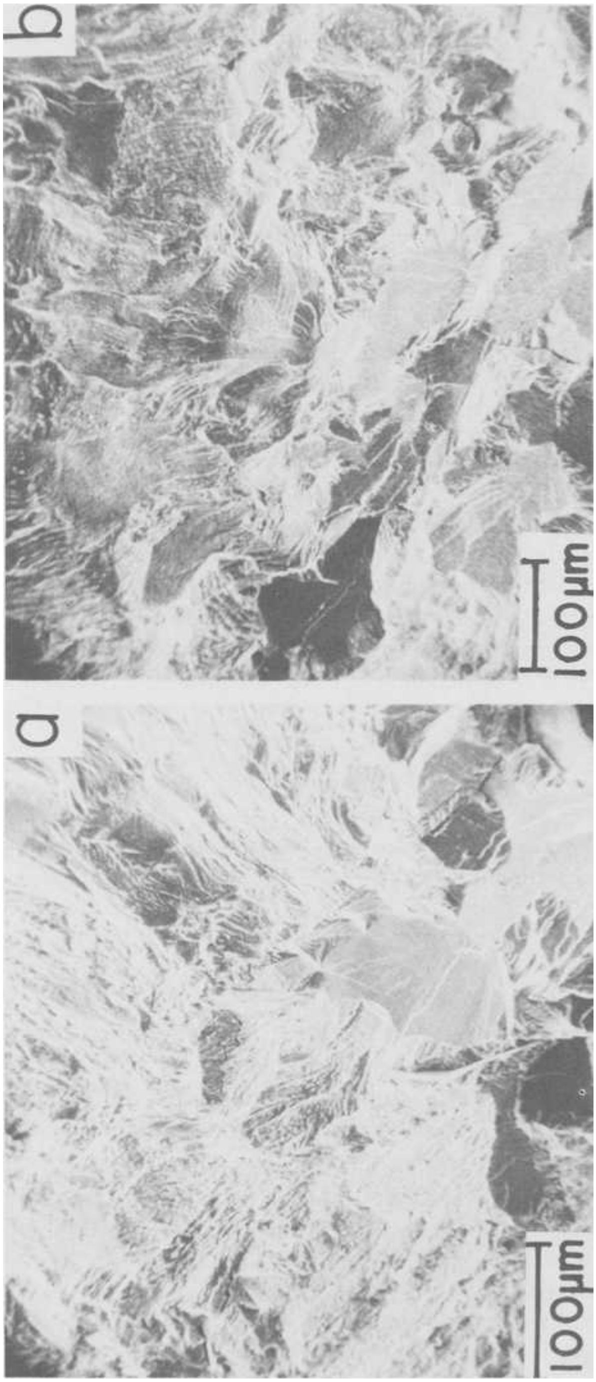
b
100μm
a
100μm

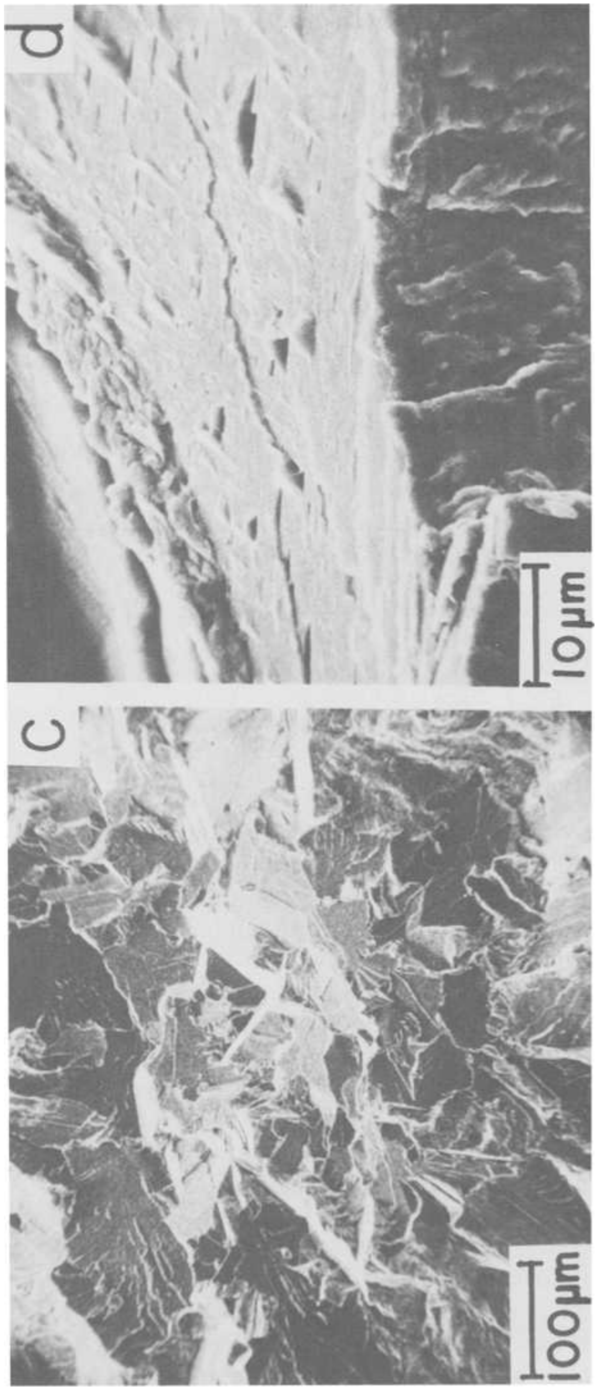

FIG. 7—*SEM micrographs showing the increase in the percentage of cleavage fracture with the increase in* R *ratio in the 60-μm HSLA steel tested at 123 K.* (a) R = *0.1.* (b) R = *0.35;* (c) R = *0.7;* (d) *Twin-related cleavage at* R = *0.7.*

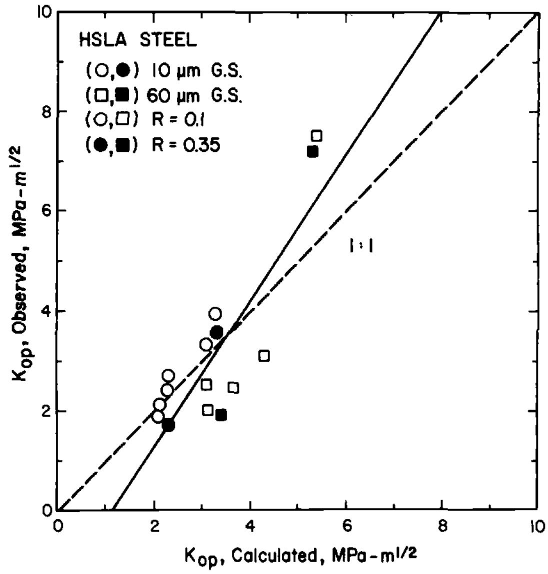

FIG. 8—*Comparison of observed and calculated opening stress intensity factor* (K_{op})*for HSLA steel.*

Summary and Conclusions

Based on the experimental work reported here on HSLA steel and Fe and Fe-Si alloys, the following conclusions are drawn:

1. Near-threshold crack growth and threshold stress intensity factor are dependent on test temperature.
2. Near-threshold crack growth rates are lowered and threshold stress intensity factors are increased with decreasing temperature, from 300 K down to 123 K.
3. Near-threshold fatigue crack growth at low test temperatures may produce large values of stress intensity for closure onset.
4. The dependence on temperature is a result of a change in strength and mechanism of cracking, both of which modify the closure force.
5. Increasing the load ratio increased the crack growth rate and lowered the apparent threshold.
6. The effects of load ratio are closure-related for the same fracture processes. A change in the fracture process (e.g., to cyclic cleavage) may lead to a dependence on the load ratio. At the lowest test temperature, increased mean stresses were seen to lower $\Delta K_{th(eff)}$ in the 60-μm grain size HSLA steel.

7. A correlation of K_{op} to $\sigma_{ys}d^{1/2}$, based upon geometrical asperity arguments, is found.

8. Calculated stress intensity factors for closure onset (K_{op}) at threshold, based on a model which simultaneously incorporates reversed slip, geometry, and oxide-induced closure, are in agreement with the observed values of this study.

Acknowledgments

The authors would like to thank Mr. Robert Ault of the Republic Steel Corp. and Mr. Ed Ryntz of General Motors Research Center for supplying the Fe and Fe-Si alloy laboratory heats and the HSLA steel used in this study. This work was supported by the Basic Energy Sciences Division of the Department of Energy under Contract DOE/DE-AC02-79ER10433.

References

[1] Burck, L. H. and Weertman, J., *Metallurgical Transactions A*, Vol. 7A, No. 2, Feb. 1976, pp. 257–264.
[2] Moody, N. R. and Gerberich, W. W., *Materials Science and Engineering*, Vol. 41, No. 2, Dec. 1979, pp. 271–280.
[3] Gerberich, W. W. and Moody, N. R., in *Fatigue Mechanisms, ASTM STP 675*, J. T. Fong, Ed., American Society for Testing and Materials, Philadelphia, 1979, pp. 292–341.
[4] Lucas, J. P. and Gerberich, W. W., *Materials Science and Engineering*, Vol. 51, No. 2, Dec. 1981, pp. 203–212.
[5] Tschegg, E. and Stanzl, S., *Acta Metallurgica*, Vol. 29, No. 1, Jan. 1981, pp. 33–40.
[6] Liaw, P. K. and Fine, M. E., *Metallurgical Transactions A*, Vol. 12A, No. 11, Nov. 1981, pp. 1927–1937.
[7] McKittrick, J., Liaw, P. K., and Fine, M. E., *Metallurgical Transactions A*, Vol. 12A, No. 8, Aug. 1981, pp. 1535–1539.
[8] Gerberich, W. W. and Jatavallabhula, K., *Acta Metallurgica*, Vol. 31, No. 2, Feb. 1983, pp. 241–255.
[9] Yu, W. and Gerberich, W. W., *Scripta Metallurgica*, Vol. 17, No. 1, Jan. 1983, pp. 105–110.
[10] Gerberich, W. W., Yu, W., and Esaklul, K. A., "Fatigue Threshold Studies in Fe, Fe-Si, and HSLA Steel. Part I: Effect of Strength and Surface Asperities on Closure," *Metallurgical Transactions A*, Vol. 15A, May 1984, pp. 875–888.
[11] Neumann, P., Fuhloff, H., and Vehoff, H., in *Fatigue Mechanisms, ASTM STP 675*, J. T. Fong, Ed., American Society for Testing and Materials, Philadelphia, 1979, pp. 371–395.
[12] Minakawa, M. and McEvily, A. J., *Scripta Metallurgica*, Vol. 15, No. 6, June 1981, pp. 633–636.
[13] Beevers, C. J., in *Advances in Fracture Research*, Vol. 3, D. Francois et al, Eds., Pergamon Press, New York, 1982, pp. 1335–1342.
[14] Suresh, S. and Ritchie, R. O., *Metallurgical Transactions A*, Vol. 13A, No. 9, Sept. 1982, pp. 1627–1631.
[15] Kanninen, M. F. and Atkinson, C., *International Journal of Fracture*, Vol. 16, No. 1, Feb. 1980, pp. 53–68.
[16] Smith, E., *International Journal of Fracture*, Vol. 17, No. 5, Oct. 1981, pp. 443–448.
[17] Yokobori, A. T., Jr., and Yokobori, T., in *Advances in Fracture Research*, Vol. 3, D. Francois et al, Eds., Pergamon Press, New York, 1982, pp. 1373–1380.

[18] Sadananda, K. and Shahinian, P., *International Journal of Fracture*, Vol. 13, No. 5, Oct. 1977, pp. 585–594.
[19] Elber, W. in *Damage Tolerance in Aircraft Structures, ASTM STP 486*, American Society for Testing and Materials, Philadelphia, 1971, pp. 230–242.
[20] Gerberich, W. W., Yu, W., and Esaklul, K. A., "Fatigue Threshold Studies in Fe, Fe-Si, and HSLA Steel. Part II: Thermally Activated Behavior of the Effective Stress Intensity at Threshold," *Metallurgical Transactions A*, Vol. 15A, May 1984, pp. 889-900.
[21] Esaklul, K. A., Wright, A. G., and Gerberich, W. W., "The Effect of Hydrogen-Induced Surface Asperities on Fatigue Crack Closure in Ultra-High Strength Steel," *Scripta Metallurgica*, Vol. 17, No. 9, Sept. 1983, pp. 1073–1078.
[22] Suresh, S., Zamiski, G. F., and Ritchie, R. O., *Metallurgical Transactions A*, Vol. 12A, No. 8, Aug. 1981, pp. 1435–1443.
[23] Liaw, P. K., Leax, T. R., Williams, R. S., and Peck, M. G., *Metallurgical Transactions A*, Vol. 13A, No. 9, Sept. 1982, pp. 1607-1618.
[24] Liaw, P. K., Leax, T. R., Williams, R. S., and Peck, M. G., *Acta Metallurgica*, Vol. 30, No. 12, Dec. 1982, pp. 2071-2078.

DISCUSSION

P. K. Liaw[1] *(written discussion)*—How does cleavage vary with ΔK? How does $K_{closure}$ vary with ΔK?

K. A. Esaklul et al (authors' closure)—The discusser poses two very important questions. At threshold, there was little cleavage observed in the 10-μm grain size material, even at 123 K. With increasing ΔK, and thus K_{max}, the amount of cleavage did increase. The amount of cleavage was quantified for the 60-μm grain size material to be 15% near threshold at $R = 0.1$. Although the cleavage percentage was not quantified for increasing ΔK, it was for increasing R values and thus increasing K_{max}. Here, as reported in the main body of the paper, it was found that the cyclic cleavage increased to 40–50% and 90% for $R = 0.35$ and 0.7, respectively. Taking the values of K_{th} at these three R values (Table 3), one finds that as K_{max} increased from 7.7 to 9.1 to 16.7 MPa $\cdot$ m$^{1/2}$, percent cleavage increased from 15 to 45 to 90% at 123 K.

With regard to $K_{closure}$, we did not report how $K_{closure}$ varies with ΔK except at threshold. From Fig. 2, one may infer that K_{op} (or $K_{closure}$) increases with ΔK at threshold. This has been shown and discussed in detail elsewhere [*10*]. On the other hand, for a given material and test temperature, as ΔK is increased away from threshold, there is a tendency for K_{op} to be nearly constant and then disappear. This is seen in Figs. 1*a* and 1*c*. For ΔK ranging from 5 to 10 MPa $\cdot$ m$^{1/2}$ in the first case and 9 to 13 MPa $\cdot$ m$^{1/2}$ in the second, K_{op} stayed near 1.5 MPa $\cdot$ m$^{1/2}$ in the former case and near 2 MPa $\cdot$ m$^{1/2}$ in the

[1] Westinghouse R&D Center, Pittsburgh, PA 15235.

latter. Above 15 $MPa \cdot m^{1/2}$, the closure disappeared, which is not surprising in the former case since $K_{min} > K_{op}$ for $R = 0.1$. For the tests at $R = 0.02$, however, this is not the case and the disappearance of closure must be attributed to a decreased time for fretting corrosion and hence less oxide-induced closure or proportionately less Mode II cracking and hence a smaller geometric closure contribution. Such effects need further investigation at low test temperatures.

Boris I. Verkin, Nataliya M. Grinberg, and Vladimir A. Serdyuk

Correlation of the Parameters of Fatigue Crack Growth with Plastic Zone Size and Fracture Micromechanisms in Vacuum and at Low Temperatures

REFERENCE: Verkin, B. I., Grinberg, N. M., and Serdyuk, V. A., "**Correlation of the Parameters of Fatigue Crack Growth with Plastic Zone Size and Fracture Micromechanisms in Vacuum and at Low Temperatures,**" *Fatigue at Low Temperatures, ASTM STP 857,* American Society for Testing and Materials, Philadelphia, 1985, pp. 84–100.

ABSTRACT: Much attention has been paid recently to the kinetics and micromechanisms of fatigue crack growth in various materials. Of particular interest are magnesium alloys, which find expanding applications in structures requiring high specific strength. This paper reports experimental results on Mg-Nd-Zr, Mg-Y-Cd, and Mg-Y-Cd-Zn alloys in different structural states. We measured the fatigue crack propagation rates and the values of the threshold point K_{th}, the transition points K_{1-2}, K^*, and K_{2-3}, and the critical point K_{fc} in air at 293 K and in a vacuum of 10^{-4} Pa at 293 and 140 K. The plastic zone size around a fatigue crack was studied by X-ray diffraction and the micromechanisms of its growth by electron fractography.

Vacuum is shown to produce a decrease in the rate of fatigue crack growth in the whole range of K_{max} values, while K_{th} and K_{fc} remain unchanged. The effect of vacuum was most prominent in thermally hardened alloys undergoing cyclic softening. A reduction in temperature from 293 to 140 K produced an increase in K_{th} and a decrease in the rate of fatigue crack growth in Region I and at the beginning of Region II for all alloys. In Region III, however, the rate of fatigue crack growth and K_{fc} changed ambiguously.

The plastic zone size was found to be larger in vacuum than in air; a reduction in temperature produced a decrease in its value regardless of the alloy structural state. The micromechanisms of fatigue crack growth were found to be dependent on composition and initial structural state of alloys, and variations in these parameters with low temperature correlated with the plastic zone size and the rate of fatigue crack growth. Our studies show the existence of certain structural and substructural criteria for the transition points K_{1-2}, K^*, and K_{2-3}.

KEY WORDS: fatigue crack growth, magnesium alloys, plastic zone size, vacuum, low temperatures, micromechanism, fatigue striations, transition points

The authors are with the Institute for Low-Temperature Physics and Engineering, Academy of Sciences of the Ukrainian SSR, Kharkov, USSR.

Through application of the principles of linear elastic fracture mechanics, considerable advances have recently been achieved in understanding the kinetics of fatigue crack growth. For all materials studied, the dependence of growth rate on the stress intensity factor may be expressed in terms of an S-like curve on log-log coordinates that shows three regions of crack growth and is limited by threshold (K_{th}) and critical (K_{fc}) values [*1*]. Most of the experiments on this problem were accompanied by electron fractography studies and, sometimes by investigations of plastic zone size and structure [*2,3*]. Nevertheless, up to now no clear idea has been obtained of the relation between microstructural peculiarities and microscopic regularities of growth in separate process regions. For instance, in titanium alloys the transition to Region II is considered to result from the cyclic plastic zone approaching the α-phase grain size [*4*]. Little attention has been directed to the question of whether other transition points in the growth rate curve depend on the plastic zone size. As for fatigue striations, it is believed that they are formed through Region II, but the correlation of the distance between striations with the macrocrack rate is not clearly understood [*5–8*].

The problem of correlation between macroscopic and microscopic parameters of crack growth has generally been investigated in air and at room temperature [*5,7*]. Considerably less work has been done on this problem for low temperatures and in vacuum [*9*], even though the effect of these factors of the kinetics of crack growth in various materials is well known. In this regard, magnesium alloys are of great interest; because of their high specific strength, these alloys find application in aerospace technology where these conditions exist.

This paper deals with the problems of the rate of fatigue crack growth in magnesium alloys of different structural states, the micromechanisms of the process in the whole range of K values, and the effect of vacuum and low temperature (140 K). An attempt is made to determine conditions corresponding to the transition points in the relation log dl/dN versus log K_{max}.

Materials and Experimental Procedure

Three types of magnesium alloys were investigated (compositions and mechanical properties are given in Tables 1 and 2). The IMV6 and VMD10 alloys of a magnesium-yttrium system were hot-rolled so that a certain thermal hardening took place [*10*]. The MA12 alloy was annealed (T2) and thermally hardened (quenching and aging, T6). Trapezoidal specimens with semicircular side notches (Fig. 1) were made of sheets and polished mechanically and electrolytically [*11*].

The test specimens were loaded by cyclic symmetrical ($R = -1$) cantilever bending at 12.5 Hz both for room temperature tests in air and in vacuum (1.33×10^{-4} Pa) and for low temperature (140 K) tests in a vacuum of the

TABLE 1—*Chemical composition (weight percent) of alloys.*

Alloy	Neodymium	Zirconium	Yttrium	Aluminum	Manganese	Cobalt	Cesium	Zinc	Cadmium	Magnesium
MA12 (T2 and T6)	2.9	0.44	...	...	...	...	...	...	...	balance
IMV6	...	...	7.8	0.12	0.55	0.49	0.11	...	...	balance
VMD10	...	0.5	7.0	...	...	...	...	1.85	1.73	balance

TABLE 2—*Mechanical properties of alloys.*

	σ_u, MPa		σ_y, MPa		δ, %		E, MPa		A in Eq 1		
									Air	Vacuum	
Alloy	293 K	140 K	293 K	140 K	293 K	140 K	293 K	140 K	293 K	293 K	140 K
MA12 (T2)	213	314	131	207	18.5	9.3	44 000	47 000	0.12	0.16	0.07
MA12 (T6)	270	320	198	195	8.5	7.5	43 500	46 500	0.07	0.09	0.05
IMV6	284	493	247	438	16.0	4.4	41 000	...	...	...	...
VMD10	293	312	220	298	12.8	0.35	...	...	...	...	...

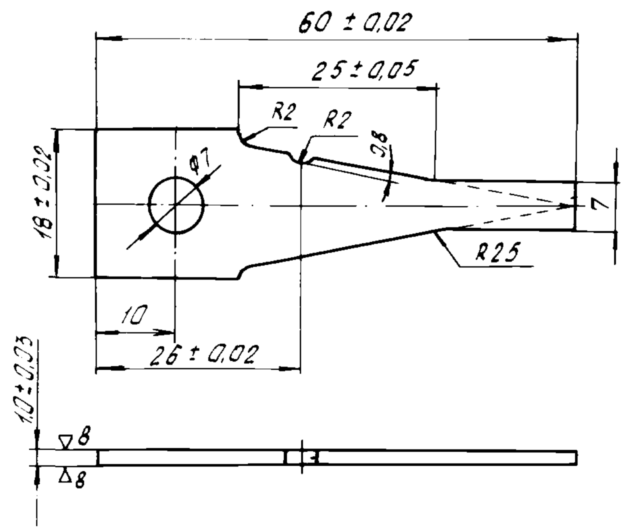

FIG. 1—*Specimen design.*

same value. The specimens were cooled through heat transfer to a liquid nitrogen vessel that was connected to the specimens by flexible copper heat conductors. During the growth of a crack, its length (l) was measured with an optical microscope at 0.5 ± 0.05 mm intervals. From the experimental results, the dependence of dl/dN on K_{max} was plotted, the K_{max} values being obtained by the compliance method [*12*]. The near-threshold fatigue crack growth rate and K_{th} were obtained by using a steplike reduction (within 3%) in the load corresponding to a given crack length.

The plastic zone formed during crack growth was investigated by X-ray diffraction analysis of the fracture surface and subsurface layers. The X-ray patterns were photographed by the Debye method on a URS-60 apparatus with chromium radiation and an 0.4-mm diameter pinhole (the depth of X-ray penetration was about 7 μm). The fractured surfaces were successively electropolished to remove the 10- to 15-μm thick layers so that the plastic zone size (h) could be found. Electropolishing was alternated with photographs of the X-ray patterns at fixed points along the crack length. The process was repeated as long as X-ray patterns typical of a given specimen were obtained. The total error in the h values did not exceed 10%.

Electron fractography studies of the fracture surfaces were performed by the platinum-carbon replica method on a UEMV-100L electron microscope. For the IMV6 alloy, the distance between striations (S) was measured for different strains and crack lengths; the data obtained were statistically analyzed. The experimental results were presented as plots of S versus K_{max} compared to dl/dN versus K_{max}.

Experimental Results

Let us consider the macroscopic behavior of fatigue crack growth and the effects of environment and temperature on the alloys tested. The kinetic diagrams of crack growth rate are S-shaped when each of three regions is distinguished by its peculiar slope to the axis (Figs. 2 to 4). The results obtained suggest that whatever the composition and structural state of an alloy, the crack growth rate is lower in vacuum than in air. The effect is most prominent in the near-threshold region, where in air the rate curve, when approaching K_{th}, changed its slope sharply; in vacuum the change was less pronounced. In this case the curve for vacuum approached the threshold value of K_{th} for air, which suggests that vacuum did not affect K_{th}. The effect of vacuum on both the crack growth rate in the near-threshold region and K_{th} has been studied in detail in Refs *13* and *14*. It follows from these papers that the effect of vacuum on K_{th} is related to the asymmetry coefficient R. The value of K_{th} has been shown [*13*] to be independent of R in vacuum and to decrease with increasing R from 0 to 0.7 in air. As R decreased, the difference in the K_{th} values in both environments became less pronounced; for $R = 0$ or 0.1 the K_{th} values in air and in vacuum were the same. Similar results were obtained in Ref *14*. It has also been shown [15] that for negative R ($-1 \leq R < 0$), the K_{th} value is highly insensitive to R. From these data one could expect that the effect of vacuum on K_{th} was small for these R values. The results of our work confirm this assumption. In Region II the crack growth rate was also lower in vacuum than in air. As K_{max} increased, the effect of vacuum diminished; for $K_{max} \rightarrow K_{fc}$ the crack growth rates in both environments became equal. Values of K_{fc} in air and in vacuum were essentially equivalent.

The reduction in temperature from 293 to 140 K produced an ambiguous change in the crack growth rate that is dependent on both alloy composition and structural state and the K_{max} value. For small K_{max}, the crack growth rate of all the alloys tested decreased and the K_{th} value increased with a reduction in temperature. As K_{max} rose, the variation in the crack growth rate in the Paris range was more intensive at the low temperature than at room temperature. Thus for the MA12 (T2) and VMD10 alloys, at low temperature and high K_{max} values the growth rate was higher than that at room temperature; additionally, K_{fc} decreased (Figs. 2*a* and 4). For the IMV6 and MA12 (T6) alloys, with an increase in K_{max} the crack growth rate also rose more rapidly at low temperature than at room temperature, remaining lower than the room temperature value, however (Figs. 2*b* and 3). For the IMV6 alloys, K_{fc} increased at lower temperatures within the range studied; for the MA12 (T6) alloys the K_{fc} values were equal for both temperatures.

Considering these results and the fact that the IMV6 and VMD10 alloys belong to the same magnesium-yttrium system, we suggest that crack growth resistance with reductions in temperature may be increased through alloying and thermal treatment.

The experimental dependence of plastic zone size (h) on K_{max} for the

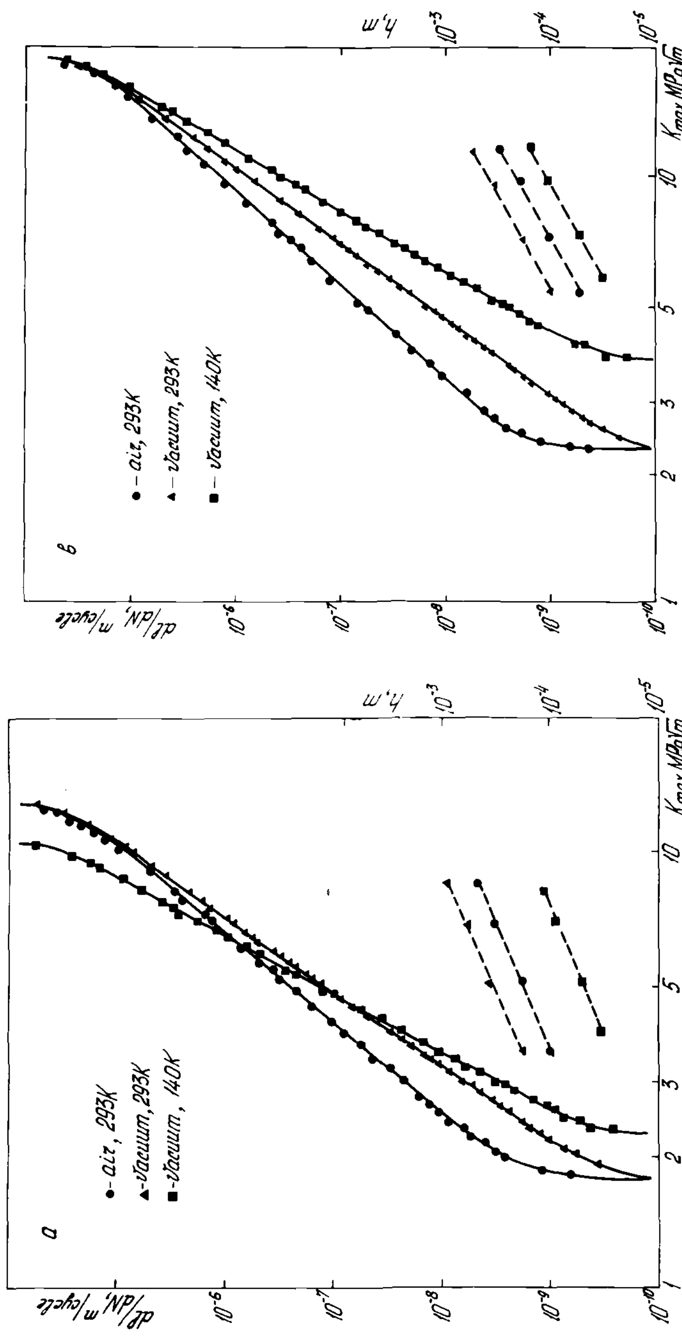

FIG. 2—*Rate of fatigue crack growth* (solid lines) *and the size of plastic zone* (dashed lines) *versus* K_{max} *in annealed* (a) *and thermally hardened* (b) *MA12 alloys* (R = −1).

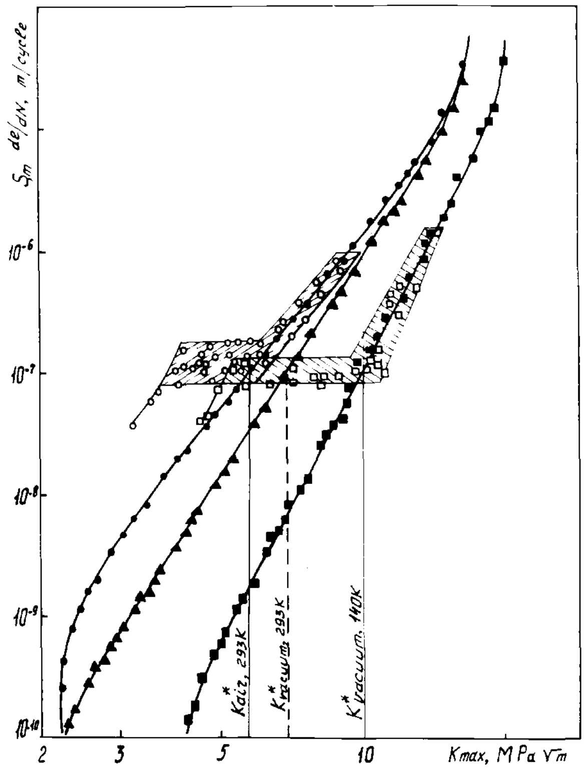

○ ● = Air, 293 K.
▲ = Vacuum, 293 K.
□ ■ = Vacuum, 140 K.

FIG. 3—*Rate of fatigue crack growth* (solid symbols) *and the distance between fatigue striations* (open symbols) *versus* K_{max} *in IMV6 alloys* (R = -1).

MA12 alloys are shown in Figs. *2a* and *2b*. For the same K_{max}, the plastic zone size was dependent on the alloy structural state. In the T2 case h was larger than in the T6 case, and the crack growth rate was also higher. Fatigue tests of MA12 alloys in vacuum at 293 K produced an increase in h compared to the value in air, while dl/dN decreased. This seems to be inconsistent with the concepts of linear fracture mechanics, according to which a larger plastic zone size should correspond to a higher crack growth rate. As may be seen from Figs. *2a* and *2b*, the conformity between the quantities h and dl/dN is valid for each environment taken separately, in air or vacuum. Apparently, this is because in vacuum a greater number of grains undergo plastic strain than in air, with a larger number of slip bands in every grain [*16*].

When the temperature fell from 293 to 140 K, in both structural conditions of the alloy the size h decreased for all K_{max}. Our attention is attracted to the disagreement between variations in the K_{max} dependence of h and

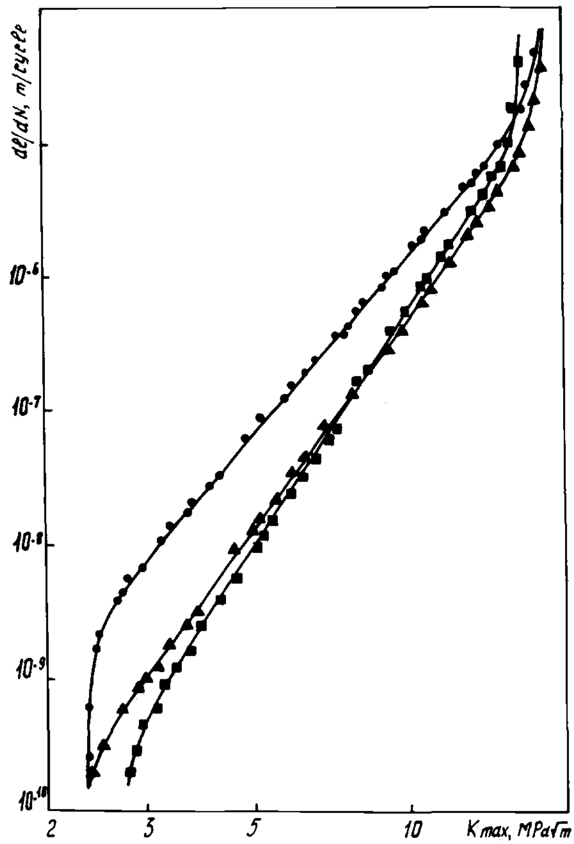

FIG. 4—*Rate of fatigue crack growth versus* K_{max} *for the VMD10 alloy* (R = −*1*). *Symbols as in Fig. 3.*

dl/dN in the MA12 (T2) alloy. For low and average values of K_{max}, a decrease in *h* was followed by a decrease in *dl/dN*, in good agreement with the mechanics of fracture. At the end of the Paris region, the crack growth rate was higher and *h* was smaller at low temperature than at room temperature. In this case the plastic zone size seemed to play no determining role in the crack growth process.

Let us now consider the morphology of the fractured surfaces of the specimens that were strained under the conditions described. At the beginning of Region II the fracture of each specimen was followed by the formation of quasicleavage (Fig. 5*a*). The formation of fatigue striations is known to be typical of Region II. In magnesium alloys their formation is not always dominant. For instance, in the MA12 (T2) and VMD10 alloys, fatigue striations occurred only on individual facets, even at room temperature in air (Fig. 5*b*). In this case crack growth was followed by the formation of transgranular

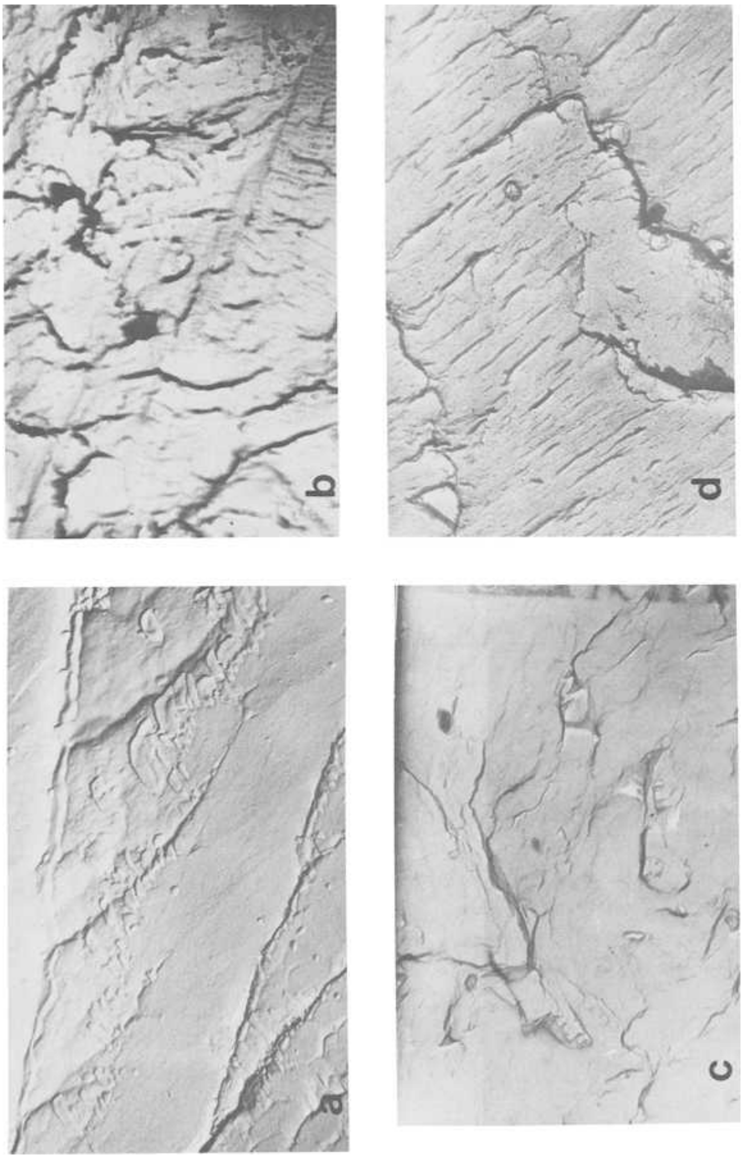
b
d
a
c

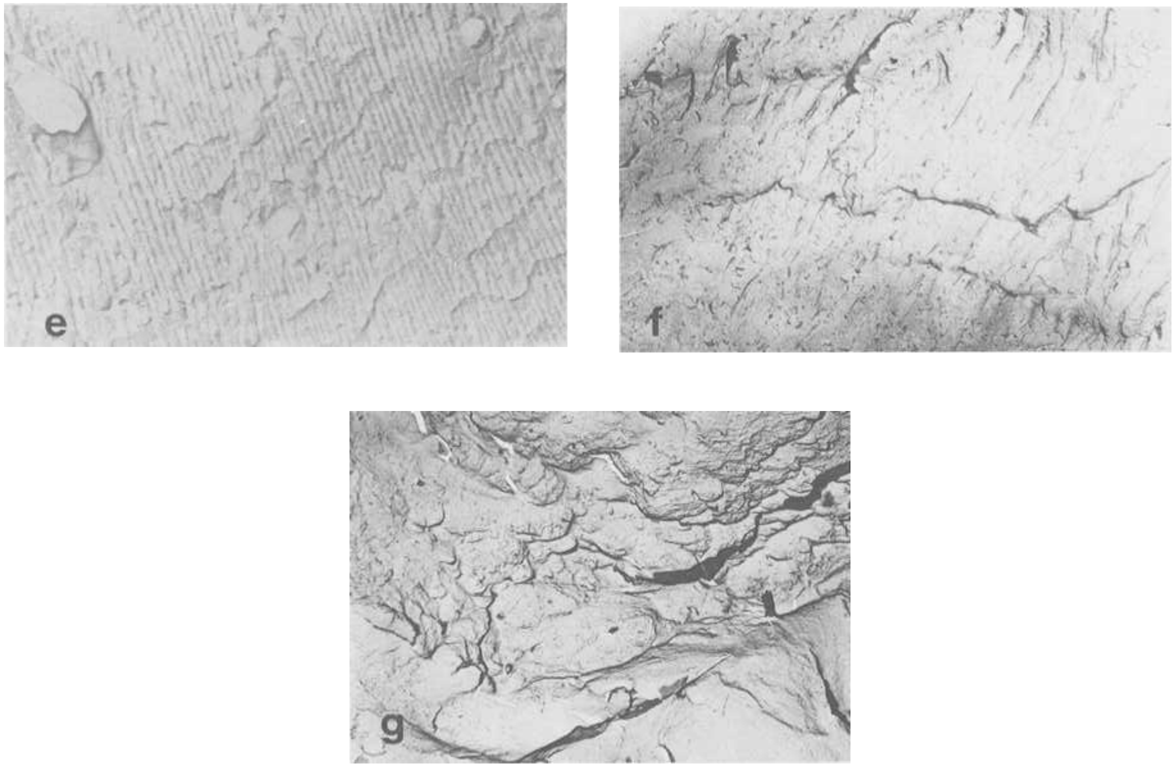

FIG. 5—*Micromorphology of fractured magnesium alloys taken at room temperature in air* (a to e) *and in vacuum* (f,g) (×7000). (a, e, f) *IMV6 alloy.* (b) *MA12(T2) alloy.* (c) *VMD10 alloy.* (d) *MA12 (T6) alloy.* (a to f) *correspond to Region II of the kinetic diagram.* (g) *corresponds to Region III of the kinetic diagram. In all cases the striations are perpendicular to the direction of crack propagation.*

quasicleavage (Fig. 5*c*). By contrast, in the MA12 (T6) and particularly in the IMV6 alloys the fracture in Region II was characterized by the formation of striations (Figs. 5*d* and 5*e*).

Under fatigue loading, the fracture within the Paris region at 293 K in vacuum was similar to that in air; in vacuum, however, the propagation of fatigue cracks was characterized by a higher degree of plasticity. A second distinguishing feature was that in the IMV6 and MA12 (T6) alloys, striations were smeared and indistinct in vacuum, while in air they were much more pronounced (Fig. 5*f*). However, in the same vacuum at low temperature striations were as distinct and prominent as in air (Figs. 6*a* to 6*c*). In Region III the micromechanism of fracture changed. At room temperature, facets of cleavage and dimple structures were formed, indicating the presence of ductile fracture (Fig. 5*g*). At the low temperature the MA12 (T6) and IMV6 alloys showed the same structures, but the MA12 (T2) and VMD10 alloys had cleavage and river structures, indicating brittle fracture (Fig. 6*d*).

Therefore a qualitative analysis of fracture surfaces suggests that the micromechanism of fatigue crack growth, which depends on alloy composition and structural state, varies during the transition from one region of the kinetic diagram to another. The formation of striations was sensitive to environment and temperature. In those alloys where the crack growth rate increased and h decreased with decreasing temperature, the micromechanism of fracture became more brittle than at room temperature (MA12 [T2] and VMD10).

Quantitative analysis of striation spacings in the IMV6 alloy (Fig. 3) indicates that for the K_{max} values that correspond to the first half of the Paris region, the separation between striations increased slightly initially (from 4×10^{-8} m to $1.0 \pm 0.08 \times 10^{-7}$ m in air at 293 K or $1.2 \pm 0.02 \times 10^{-7}$ m in vacuum at 140 K) and then remained unchanged up to a certain value of K_{max} that will be denoted by K^*. Under these conditions the macroscopic crack propagation per cycle was less than the striation spacing. Therefore in this region of crack growth (IIa) several cycles of loading were required for the microcrack to propagate by a distance equal to the striation spacing. The number of cycles was greater for lower K_{max}/K^*. Only for $K_{max}/K^* = 1$ was the crack growth rate coincident with the striation spacing [i.e., the microcrack propagated in each of the loading cycles (Region IIb)]. Not all of Region IIb was characterized by the formation of striations because for crack growth rates of 1 to 2×10^{-6} m/cycle there were no striations at all (Fig. 3).

It follows from the experimental results that K^* increased as the temperature decreased. The effect seems to be typical of some other alloys for which the low-temperature macroscopic curve of crack growth rate shifts to the right with respect to the room-temperature curve because the ordinate of the II*a*–II*b* region transition point is constant. When these macroscopic curves are crossed, K^* at low temperature can be lower than at room temperature if the crossover occurs at $dl/dN < 10^{-7}$ m/cycle.

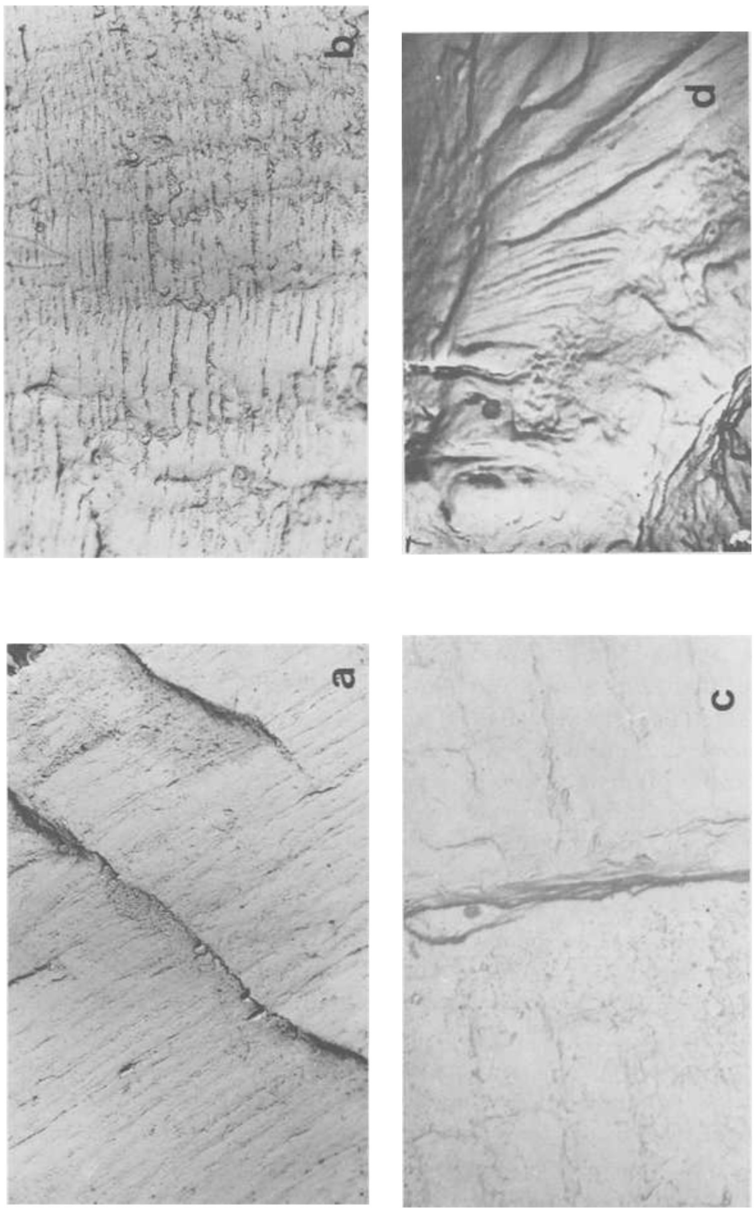

FIG. 6—*Micromorphology of fractured magnesium alloys taken in vacuum at 140 K (×7000). (a, b) IMV6, Region II. (c) IMV6, Region III. (d) MA12(T2), Region III. In all cases the striations are perpendicular to the direction of crack propagation.*

Discussion

Let us consider the conditions at the crack tip under which the micromechanism of fatigue crack growth varies through the whole process. Serdyuk and Grinberg [9] showed that for room temperature the cyclic plastic zone size at K_{max}, which corresponds to the Region I–Region II transition (K_{1-2}) and is denoted h_{1-2}, is comparable to the grain diameter (d) in the annealed MA12 alloy and to the distance between hardening particles in the thermally hardened MA12 specimen. As the temperature falls to 140 K, $h_{1-2} < d$, but for the thermally hardened alloy the relation remains unchanged. The Region I–Region II transition, therefore, occurs for a certain relation between the plastic zone size and the material structural parameters.

Such a correlation appears to be valid also for Region II, throughout which striations are formed. It has been suggested that striations appear only for a particular plastic zone size h [17]. We can estimate h by using the experimental data. From the data in Figs. 2*a* and 2*b*, we can suggest that the plastic zone size (h) obeys the known relation [18]

$$h = A\left(\frac{K_{max}}{\sigma_y}\right)^2 \quad (1)$$

where σ_y is yield strength and the coefficient A depends on structural state, environment, and temperature (Table 2). For the IMV6 alloy, the h value was not measured but calculated at point K^* by Eq 1, assuming that the values of the coefficient A were close to those for the thermally hardened MA12 specimens strained under the same conditions. In the IMV6 specimens the plastic zone sizes (h^*) were 42, 73, and 30 μm in air, in vacuum at 293 K, and in vacuum at 140 K, respectively. Considering that the average grain size in the IMV6 alloy is about 40 μm, we suggest that striations of the same spacing are formed when the plastic zone size in Region IIa does not exceed the grain size. In this case, the plastic zone structure [8,9] and hence the rigidity of its stressed state also changed, as indicated by the sensitivity of the A coefficient to environment and temperature.

In the thermally hardened alloy MA12 (T6), the plastic zone size was equal to 60, 170, and 75 μm in air, vacuum at 293 K, and vacuum at 140 K, respectively, for K_{max} corresponding to a $dl/dN \sim 1 \times 10^{-7}$ m/cycle (Fig. 2*b*). For an average grain diameter of about 80 μm, the plastic zone size in air at 293 K and in vacuum at 140 K (when striations are formed) was approximately of the same value as the grain diameter. In vacuum at 293 K, when there are no striations, it was twice this value.

The experimental data on the striation spacing provide support for Grinberg's hypothesis [8] on the difference in the micromechanisms of crack growth in Regions IIa and IIb. The data offer additional experimental evidence that the ordinate of the point 0 separating these regions is independent of temperature and environment, while its abscissa, K^*, varies in response to these factors.

It should be noted that the ordinate of the point corresponding to a constant separation between striations at Region IIa is almost the same for metals and different alloys, being within the limits of 0.8 to 4.0 $\times$ 10^{-7} m/cycle [*6,19*]. Such a constancy is natural, since it apparently takes account of the common character of the effects that occur in Region IIa in different materials. As indicated by an analysis of transmission electron microscopy and X-ray diffraction data [*8*], the value of $\sim 10^{-7}$ m corresponds to the diameter of a three-dimensional cellular structure which is formed at the tip of the fatigue crack in different metals and alloys. We can suggest then that the crack in Region II propagates in one loading cycle from one boundary of subgrain to the other and ceases its propagation for a certain number of cycles which depend on the K_{max}/K^* value. In Region IIb the fatigue crack propagation is not restricted by the dimensions of the dislocation cellular structure and occurs at each cycle of loading in accordance with K_{max} by the Paris formula.

Tanaka and his colleagues [*20,21*] concluded that for the crack growth rate of $\sim 10^{-7}$ m/cycle there is a so-called pivot point in the intermediate growth rate range which is common for alloys of the same base. Using the relation between parameters C and m in the Paris law, they obtained the expression:

$$dl/dN = B(\Delta K/K_0)^m \tag{2}$$

and showed that the constants B and K_0 were the coordinates of the pivot point at which the curves for all alloys of the same base were crossed. The constant B for steels was equal to 1.7 $\times$ 10^{-7} m/cycle and for aluminum and titanium alloys to 3.98 $\times$ 10^{-7} and 2.99 $\times$ 10^{-7} m/cycle, respectively [*21*]. Using these data, Tanaka and his colleagues proposed the following analytical expressions for the axial point coordinates:

$$K_0 = 10E\sqrt{b} \tag{3}$$

$$B = dl/dN = 10^3 b \tag{4}$$

where b is the Burgers vector and E is the elastic modulus of an alloy. Taking account of the fact that the striation spacing (S) is given by the formula

$$S = C'(\Delta K)^2 \tag{5}$$

they suggest that the plot log S versus log ΔK passes through the pivot point.

The coincidence of the pivot point ordinate, derived from the relation of the Paris equation parameters, and the point 0 obtained by the microfractography data, provides evidence in favor of the fact that in both cases the same point is meant which separates Regions IIa and IIb. Indeed, for the IMV6 alloy, estimation of the point abscissa by Eq 3 gives $K_0 = 7.4$ MPa m$^{1/2}$ ($b = 3.2 \times 10^{-10}$ m, $E = 41\,000$ MPa). As seen from Fig. 3, the K^* values are 6.0, 7.0, and 10.2 MPa m$^{1/2}$ in air and in vacuum at 293 K and in vacuum at 140 K, respectively. Taking account of the fact that the experimental data for steels, aluminum, and titanium alloys [*21*] are within a wide range of spread, we believe that for the magnesium alloy tested the agreement of the K^* values at room temperature with the K_0 values calculated by Eq 3 is rather good.

It should be mentioned that in the IMV6 alloy, the striations with a fairly small ($<10^{-7}$ m) and increasing spacing are observed for low K_{max} corresponding to the beginning of the Paris region. In the other alloys the minimum spacing between striations in Region IIa is constant and equals 10^{-7} m [*6,17,18*].

We believe that in this case the following two facts are of great importance. First, in Region IIa the striation spacing increases to $\sim 1 \times 10^{-7}$ m only and for all K_{max} remains considerably higher than the macrocrack rate. Secondly, the arrangement of striations and the relationship between their spacing and the macrocrack rate at low temperature are the same as those at room temperature. For the K_{max} values which slightly exceed $K_{1\text{-}2}$, the crack propagates in one cycle by a value smaller than the subgrain diameter with crack arrest for several tens or even hundreds of cycles. The distance for which the crack propagates with an increase in K_{max} at the beginning of Region IIa rises but only within the limit of the subgrain diameter. The microcrack rate also grows so that the number of cycles of crack arrest remains approximately the same. As K_{max} increases further through the whole Region IIa, the step of microcrack remains constant but the number of cycles of arrest decreases. The mechanism of crack growth is left the same at low temperature as well.

As indicated in Ref *22*, the condition for a fatigue-to-quasistatical fracture transition that occurs at K_{max}, corresponding to the Region II—Region III transition ($K_{2\text{-}3}$), is dependent on the micromechanism of fracture and, like the other transition point, is sensitive to the plastic zone size and structural parameters of a material. In the case of fatigue-to-brittle fracture transition (observed in the MA12 (T2) and VMD10 alloys at 140 K, see Fig. *6d*), the condition

$$\sigma_{2\text{-}3} > \sigma_{cr} \tag{6}$$

should be fulfilled at $K_{2\text{-}3}$. Then

$$\sigma_{2\text{-}3} = \sigma_y p \tag{7}$$

where p is the plastic constraint factor which is dependent on the alloy condition, environment, and temperature [9] and $p = (2\pi A)^{-1/2}$ where A is the coefficient from Eq 1.

According to the data obtained by Meshkov [23], the stress of brittle fracture is related to the grain diameter by

$$\sigma_{cr} = Kpd^{-1/2} \tag{8}$$

where $Kp = (300\gamma E/\pi)^{1/2}$, γ is a surface energy, and d is grain diameter. For the MA12 annealed alloy, the criterion of fatigue-to-ductile fracture transition is the equality [22,24]

$$\delta_{2\text{-}3} = d \tag{9}$$

where $\delta_{2\text{-}3}$ is the crack opening displacement at $K_{2\text{-}3}$ equal to

$$\delta_{2\text{-}3} = \frac{K_{2\text{-}3}^2}{E\sigma_y} \tag{10}$$

In the thermally hardened alloy, the critical crack opening displacement is smaller than the grain size, and the large intermetallic particles the sizes of which, as shown by the fractography data, are compared to the crack opening displacement found by Eq 10 may play the role of the material structural parameter which dictates the fatigue-to-ductile fracture transition [22].

Conclusions

1. Each of the transition points in the curve log (dl/dN) versus log K_{max} (i.e., $K_{1\text{-}2}$, K^* and $K_{2\text{-}3}$) corresponds to a particular relation between the plastic zone size and the structural parameters of the material. Different sizes of plastic zone and different degrees of plastic strain in it (which are sensitive to structural states, temperature, and environment) determine different micromechanisms of fatigue and crack growth rates during different stages of the process.
2. Cyclic straining in vacuum favors a decrease in the fatigue crack growth rate of magnesium alloys no matter what their composition and structural condition. The values of K_{th} and K_{fc} are similar in vacuum and in air. The failure in vacuum occurs with a larger degree of plastic strain than in air.
3. For small K_{max}, the rate of fatigue crack growth at 140 K decreases in all magnesium alloys and K_{th} increases. For large K_{max}, the crack growth rate at low temperature may decrease or increase depending on the alloy composition and structural condition and the K_{fc} values vary respectively. A decrease in K_{fc} and an increase in the crack growth rate correlate with an increase of brittle components in the fracture microstructure.

4. The plastic zone size formed in vacuum is larger than that in air at the same temperature. For the annealed and thermally hardened MA12 alloys, the reduction in temperature from 293 to 140 K causes a decrease in the plastic zone size within the K_{max} range studied.

5. The qualitative electron fractography analysis permits the Paris region to be separated into Regions IIa and IIb by the point 0 with the coordinates K^* and $dl/dN \sim 10^{-7}$ m/cycle. In the thermally hardened MA12 alloy, K^* corresponds to K_{max} at which the plastic zone size approaches the grain diameter both in air at 293 K and in vacuum at 140 K. The K^* value increases as the temperature decreases.

6. At the beginning of Region IIa the minimum distance between fatigue striations is 4×10^{-8} m, it rises to $\sim 1 \times 10^{-7}$ m with an increase in K_{max} and then for $K_{max} < K^*$ remains unchanged. In this case the distance between striations is larger than the crack growth macrocrack rate. The coincidence of the distance between striations with the macrocrack rate and the increase in the distance according to K_{max} is characteristic of the initial portion of Region IIb only, then striations vanish. These specific features are typical of crack growth at 293 K in air and at 140 K in vacuum.

References

[1] Beevers, C. J., "Fatigue Crack Growth Characteristics at Low Stress Intensities of Metals and Alloys," *Metal Sciences*, No. 8-9, 1977, pp. 362–367.

[2] Kotozi, A., Nobukazu, O., and Toshihiza, N., "Effect of Grain Size on Fatigue Fracture Toughness and Plastic Zone Size Attending Fatigue Crack Growth," in *Proceedings*, 2nd International Conference on the Mechanical Behavior of Materials, Boston, 1976, pp. 533–537.

[3] Stratmann, P., "Microstructure, Plastic Zone Size and Crack Propagation in Ni Steels," in *Advances in Research in Strength and Fracture of Materials*, 4th International Conference on Fracture, Waterloo, 1977, Vol. 2, New York, 1978, pp. 79–85.

[4] Yuen, A., Hopkins, S. W., Leverant, G. R., and Rau, C. A., "Correlations Between Fracture Surface Appearance and Fracture Mechanics Parameters for Stage II Fatigue Crack Propagation in Ti-6Al-4V," *Metallurgical Transactions*, Vol. 5, No. 8, 1974, pp. 1833–1842.

[5] Yokobori, T., Kawagishi, M., and Yoshimura, T., "Kinetic Aspects of Fatigue Crack Propagation," in *Proceedings*, 2nd International Conference on Fracture, Brighton, England, 1969, pp. 803–811.

[6] Grinberg, N. M., Ostapenko, I. L., and Alekseenko, E. N., "The Fractography of Fatigue Fracture of Silicon Iron in a Wide Range of Strain in Air and in Vacuum," *Problemy prochnosti*, No. 7, 1979, pp. 33–38 (in Russian).

[7] Ivanova, V. S., Maslov, L. I., and Bozrova, L. K., "About Regularities of Microfracture Under Stable Growth of Fatigue Crack," *Izvestiya AN SSSR Metally*, No. 5, 1981, pp. 144–149 (in Russian).

[8] Grinberg, N. M., "The Effect of Vacuum on Fatigue Crack Growth," *International Journal of Fatigue*, No. 4, 1982, pp. 83–95.

[9] Serdyuk, V. A., and Grinberg, N. M., "The Plastic Zone and Growth of Fatigue Crack in Magnesium MA12 Alloy at Room and Low Temperatures," *International Journal of Fatigue*, Vol. 5, No. 2, 1983, pp. 79–85.

[10] Grinberg, N. M., Serdyuk, V. A., "Softening of the IMV6 Magnesium Alloy Under Fatigue," *Problemy prochnosti*, No. 1, 1980, pp. 35–40 (in Russian).

[11] Grinberg, N. M., Serdyuk, V. A., Yakovenko, L. F., Malinkina, T. I., and Kamyshkov, A. S., "The Kinetics and Mechanics of Fatigue Fracture of MA2-1 and MA12 Magnesium Alloys," *Problemy prochnosti*, No. 8, 1977, pp. 40–45 (in Russian).

[12] Grinberg, N. M., and Serdyuk, V. A., "Parameters and Micromechanisms of the Fatigue Crack Growth in Sheet Magnesium Alloy Samples," *International Journal of Fatigue*, No. 7, 1981, pp. 143–148.

[13] Petit, J., and Maillard, J. L., "Environment and Load Ratio Effects on Fatigue Crack Propagation Near-Threshold Conditions," *Scripta Metallurgica*, Vol. 14, 1980, pp. 163–166.

[14] Cooke, R. J., Irwing, P. E., Booth, G. S., and Beevers, C. J., "The Slow Fatigue Crack Growth and Threshold Behavior of a Medium Carbon Alloy Steel in Air and Vacuum," *Engineering Fracture Mechanics*, Vol. 7, No. 1, 1975, pp. 69–77.

[15] Ohta, A. and Sasaki, E., "A Method of Determinating the Stress Intensity Threshold Level for Fatigue Crack Propagation," *Engineering Fracture Mechanics*, Vol. 9, No. 3, 1977, pp. 655–662.

[16] Grinberg, N. M., Serdyuk, V. A., Zmeevets, S. G., Ostapenko, I. L., Malinkina, T. I., and Kamyshkov, A. S., "Fatigue Crack Growth in the MA12 Magnesium Alloy in Air and in Vacuum," *Problemy prochnosti*, No. 3, 1978, pp. 12–16.

[17] Verkin, B. I. and Grinberg, N. M., "The Effect of Vacuum on Fatigue Behavior of Metals and Alloys," *Materials Science and Engineering*, Vol. 41, No. 2, 1979, pp. 149–181.

[18] Hahn, G., Hoagland, R. G., and Rosenfield, A. K., "Local Yielding Attending Fatigue Crack Growth," *Metallurgical Transactions*, Vol. 3, 1972, pp. 1189–1202.

[19] Grinberg, N. M., Gavrilyako, A. M., D'Yakonenko, N. L., Ostapenko, I. L., and Serdyuk, V. A., "Fatigue Crack Growth and Plastic Zone in Air and in Vacuum," *Problemy prochnosti*, No. 4, 1981, pp. 20–25 (in Russian).

[20] Tanaka, K. and Matsuka, S., "A Tentative Explanation for Two Parameters *C* and *m* in Paris's Equation of Fatigue Crack Growth," *International Journal of Fracture*, Vol. 13, No. 5, 1977, pp. 563–583.

[21] Tanaka, K., Masuda, S., and Nishijima, S., "The Generalized Relationship Between the Parameters *C* and *m* in Paris's Law for Fatigue Crack Growth," *Scripta Metallurgica*, Vol. 15, No. 3, 1981, pp. 259–264.

[22] Verkin, B. I., Grinberg, N. M., Serdyuk, V. A., and Yakovenko, L. F., "Low Temperature Fatigue of Metals and Alloys," *Materials Science and Engineering*, Vol. 58, No. 2, 1983, pp. 145–168.

[23] Meshkov, Y. Y., *Physical Basis of Steel Structure Fracture*, Naukova Dumka, Kiev, 1981, p. 239.

[24] Imhof, E. J. and Barsom, J. M., "Fatigue and Corrosion-Fatigue Crack Growth of 4340 Steel at Various Yield Strengths," in *Progress in Flaw Growth and Fracture Toughness Testing, ASTM STP 536*, American Society for Testing and Materials, Philadelphia, 1973, pp. 182–205.

Kumar V. Jata, William W. Gerberich, and C. J. Beevers

Low-Temperature Fatigue Crack Propagation in a β-Titanium Alloy

REFERENCE: Jata, K. V., Gerberich, W. W., and Beevers, C. J., "**Low-Temperature Fatigue Crack Propagation in a β-Titanium Alloy,**" *Fatigue at Low Temperatures, ASTM STP 857,* R. I. Stephens, Ed., American Society for Testing and Materials, Philadelphia, 1985, pp. 102–120.

ABSTRACT: Fatigue crack growth rates and crack closure have been examined for a body-centered-cubic (bcc) titanium alloy (Ti-30Mo) at five test temperatures ranging from 123 to 340 K. In the same temperature range the influence of internal hydrogen (as provided by gas phase charging) has been studied. Detailed fractographic analyses have been made to quantify the amount of cleavage fracture as a function of test temperature, hydrogen concentration, and stress intensity factor range. The extent of cleavage, both cyclic and static, increased with decreasing temperature. For the low-hydrogen content specimens the fatigue crack growth resistance increased with increasing cleavage over the temperature range from 340 to 190 K. The fatigue crack growth resistance for the high hydrogen alloy remained relatively insensitive to the increasing amounts of cleavage over the same temperature range. An examination of the fatigue crack growth rate data shows that the power exponent in the following expression is in the range of 2 to 2.5 for temperatures of 123 to 340 K:

$$\frac{da}{dn} = B(\Delta K^{i} - \Delta K^{i}_{th})^{n}$$

where $\Delta K = \Delta K^{i} + \Delta K^{c}$ and ΔK^{i} is the intrinsic component and ΔK^{c} is the closure component. These observations indicate that the factor dominating the fatigue crack growth rate and the resulting cyclic cleavage process is the reverse plasticity in the crack tip region. The increased resistance to fatigue crack growth in the temperature range from 340 to 190 K for the low hydrogen contents is attributed to the higher yield stresses in this region. The role of hydrogen in determining fatigue crack growth rates and fatigue thresholds (ΔK_{th}) is discussed in terms of its influence on both ΔK^{i} and ΔK^{c}.

KEY WORDS: fatigue crack propagation, low temperature, crack closure, hydrogen, fractography, static cleavage, cyclic cleavage, fatigue thresholds

In recent years there has been an increasing interest in investigating fatigue crack growth behavior at low temperatures in the near-threshold region (Re-

Dr. Jata (formerly Jatavallabhula) is with the Department of Materials Science, University of Virginia, Charlottesville, VA 22901; Dr. Gerberich is with the Department of Chemical Engineering and Materials Science of the University of Minnesota in Minneapolis, MN 55455; and Dr. Beevers is with the Department of Physical Metallurgy and Materials Science at the University of Birmingham, Birmingham, U.K.

gion I). The understanding of the mechanisms which control fatigue crack growth in Region I is complicated by several variables, such as microstructure, environment, and temperature, which play a dominant role in determining the fatigue threshold. Crack closure has been found to be of particular concern in the understanding of the fatigue thresholds and recent attention has been focused on the origin of fatigue crack closure and the ramifications of closure on the fatigue crack growth rate in Region I. The primary factor in the closure process is the creation of asperities in the crack tip region. These asperities can form as a result of out-of-plane crack trajectories associated with Mode II displacements, the presence of oxides, or other constituent particles on the crack faces, and localized plastic flow in the crack tip region [*1–5*]. The investigations examined the role of internal hydrogen content (22 and 1200 wt ppm) and test temperature on the fatigue crack growth and threshold response of the β-titanium alloy. The microstructure of the alloy is essentially single phase, with grains of the order of 80 to 100 μm in size. As reported previously [*6, 7*], the major effects of internal hydrogen and temperature on Ti-30Mo are to increase the yield stress (σ_{ys}) and internal stress (σ_i), while hydrogen alone increases the ductile-to-brittle transition temperature (DBTT). Although β-Ti alloys have higher hydrogen solubility limits than α- or α/β-Ti alloys, they still have been found to be affected by hydrogen or hydrogen-producing atmospheres. Furthermore, it has been found that for β-Ti alloys the effects of hydrogen are pronounced only if the starting microstructure enhances planar slip rather than multiple slip [*8*]. For example, the presence of coherent or semicoherent particles such as ω-phase particles satisfies this condition. On the other hand, hydrogen has been found to affect only certain regions of the fatigue crack propagation curve. As an example, Chakrabortty and Starke's work on Ti-27V [*9*] in a methanol/hydrochloric acid solution suggests that fatigue crack growth rates are affected only in the intermediate stress intensity factor range. Wilcox and Koss's [*8*] work on Ti-30V suggests that gaseous hydrogen affects fatigue crack propagation in all three regions of the fatigue crack propagation (fcp) curve. Results from previous work [*10–12*] show that at temperatures as low as 77 K, only a ductile transgranular mode of crack growth has been observed at near thresholds, including those alloy systems which otherwise exhibit extensive cyclic cleavage at higher stress intensity factors (in Region II).

Experimental Details

The nominal composition in weight percent of the as-received alloy is 0.02 carbon, 0.007 nitrogen, 0.02 iron, 0.007 oxygen, and 29.4 molybdenum. The as-received alloy was vacuum-annealed for 4 h at 100°C at 5×10^{-5} torr, which resulted in 22 wt ppm of hydrogen and an average grain size of 92 ± 10 μm. Hydrogen was introduced in the samples by gas phase charging in a Sieverts apparatus at 800°C. Hydrogen analysis on all samples was performed by the hot vacuum extraction technique. Fatigue crack propagation tests were performed on compact tension samples machined in the L-T orientation. In order to ensure plane strain conditions a thickness of 20 mm was used. Fatigue testing was performed on a servohydraulic closed-loop testing machine by using tension-tension sinusoidal loading at 20 Hz with a constant load ratio (R) of 0.05. Crack growth was monitored with a crack opening displacement (COD) gage. The COD gage measured the crack opening displacement (v), and the compliance (v/p) was determined from a corresponding load (p). The value of v/p is then used to calculate the crack length by using the calibration equation

$$v/p = \left(\frac{1}{BE}\right)[-2466.7 + 27078.2\,(a/w) - 115069(a/w)^2 + 24700(a/w)^3 - 248010(a/w)^4 + 101658(a/w)^5] \quad (1)$$

where w is the distance from the loading point to the edge of the sample, B is the thickness, and E is the elastic modulus. The stress intensities were calculated from

$$\Delta K = \frac{\Delta P}{Bw^{1/2}} f(a/w)$$

where ΔP is the cyclic load and

$$f(a/w) = 29.6(a/w)^{1/2} - 175.5(a/w)^{3/2} + 655.7(a/w)^{5/2} - 1017(a/w)^{7/2} + 639(a/w)^{9/2} \quad (2)$$

Fatigue testing was carried out in air; low-temperature conditions were controlled in an environmental chamber with evaporated liquid nitrogen as the coolant. A step-down procedure was used to obtain the fatigue thresholds.

Results and Discussion

Low Hydrogen Content (22 wt ppm)

The fcg curves in Region I, for 22 ppm level of hydrogen, are shown in Fig. 1*a*. As expected, the crack growth rates were observed to be highest at the maximum test temperature of 340 K. The crack growth rates decreased systematically from 340 to 233 K and reached a minimum at 190 K. At 123 K, a reversal in crack growth rates was observed. This is shown more clearly in Fig. 1*b* for a ΔK of 7 MPa m$^{1/2}$. Decreasing crack growth resistance at 123 K results in a lowering of the observed fatigue threshold at this temperature.[1]

[1] The authors recognize that ΔK_{th} is conventionally defined as the ΔK to sustain a growth rate of 10^{-10} m/cycle. In this instance the term *near-threshold* refers to growth rates of 6×10^{-10} m/cycle.

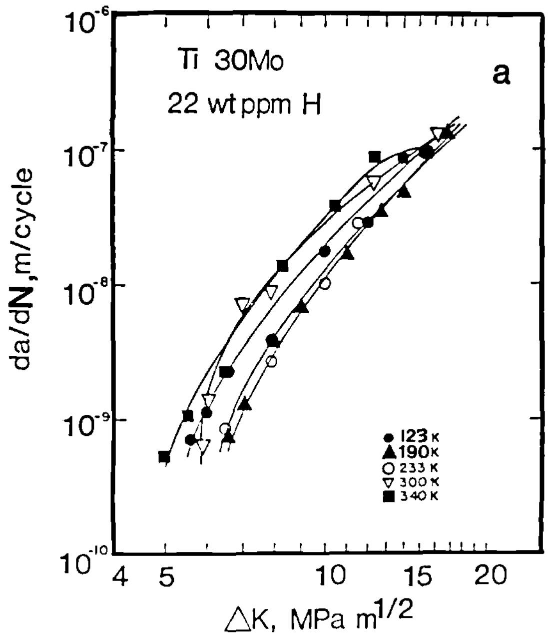

FIG. 1a.—*Comparison of observed* da/dN *versus* ΔK *for 22 wt ppm H.*

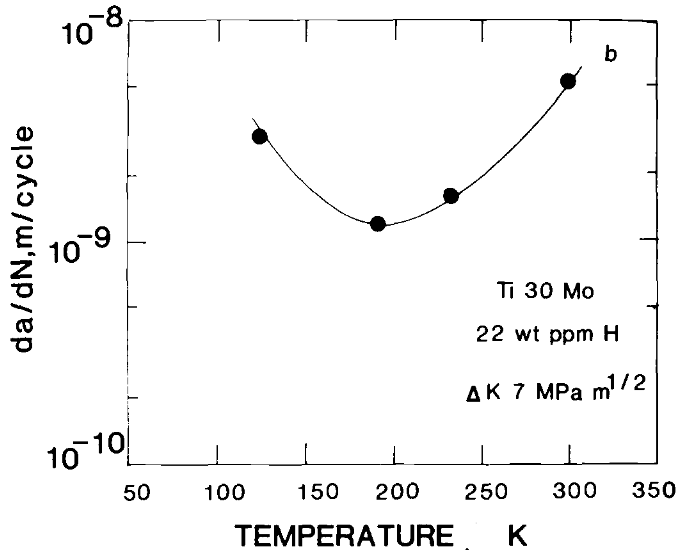

FIG. 1b.—*Effect of temperature on* da/dN *for 22 wt ppm H at* $\Delta K = 7$ *MPa* $m^{1/2}$.

The observed fatigue thresholds ΔK_{th}^{obs} are shown in Fig. 2 for all test temperatures. Previous work on Fe, Fe-Mo [*12*], mild steel [*11*], high-strength low-alloy steel [*10*], and Fe-Si alloys [*13*] indicates no crossover in fatigue crack growth rates in Region I at temperatures as low as 77 K. The fractography of these alloys as reported by the authors was characterized by a dominant ductile growth mechanism.

There are two main effects of temperature on body-centered-cubic (bcc) alloys: an elevation of the yield stress and a change in the ductile-to-brittle transition temperature (DBTT). Although an increase in yield stress should increase the fatigue crack growth resistance, the change in DBTT might decrease the fatigue crack growth resistance. This has been established both experimentally and analytically for Region II [*15*] for iron-base alloys. If the DBTT effects are encountered at low stress intensities and low temperatures then there would be two competing effects, namely yield stress and DBTT. At low stress intensities, in order for the crack to propagate by a brittle cleavage mode, a sufficient K_{max} value ($R = K_{min}/K_{max}$) has to be attained, or a dislocation dynamic controlled cyclic (cleavage) situation should exist [*14–16*]. In such an event, the fracture mode in Region I could be either brittle or a dual ductile/brittle mode which could dictate the rate of fatigue crack propagation.

Note that with decreasing temperature from 340 K in the 22 wt ppm alloy, the yield stress increased and the alloy exhibited a ductile-to-brittle transition. Both these factors contributed to the increase in fatigue crack growth resistance. The DBTT for Ti-30Mo was found to be 355 K in impact tests and 252 K in four-point slow bend tests [*6*]. The DBTT under impact conditions was higher because of the higher imposed strain rate of 200 s^{-1} as compared to 3×10^{-3} s^{-1} for four-point bend tests. If the dynamic strain rate [*16*] at the crack tip under fatigue is between the above two limits, then one might ex-

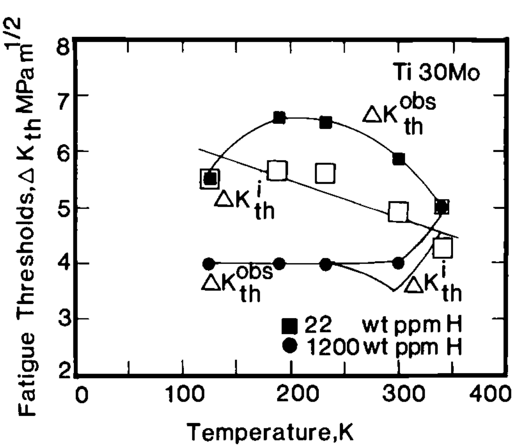

FIG. 2—*Comparison of fatigue thresholds* ΔK_{th} *versus* T.

pect the onset of brittleness at temperatures as high as 300 K in cracked fatigue samples under plane-strain conditions. Also, brittle conditions will be more likely at higher ΔK values where local stresses may be more easily raised to the cleavage stress. With this suggested importance of the DBTT, the discussion is directed to the fractography of the near-threshold region for the low-hydrogen samples.

In the present investigation of Ti-30Mo, fractography indicated that the fatigue crack propagation at test temperatures down to 190 K was predominantly ductile transgranular. At 123 K, a substantial number of cleavage facets were observed. To illustrate this, a few representative fractographs are presented. The fractographs shown in Fig. 3 correspond to near-threshold stress intensity at 300 K. At this temperature the area fraction of ductile growth was almost 0.8. Some of the facets (e.g., A in Fig. 3*a*) that appear smooth exhibited very fine ductile striations at higher magnification, as shown in Fig. 3*b*. In the fractograph shown in Fig. 3*a* there is also some evidence of monotonic cleavage. The overall amount of cleavage fracture increased at 123 K. At threshold, the area fraction of the fracture surface failed by cleavage was approximately 0.7. Figure 4 shows the variation in the amount of cleavage fracture as a function of stress intensity at 123 K. The results in Fig. 4 indicate that the amount of cleavage decreased with increasing ΔK from the near-threshold region to a ΔK of approximately 14 to 16 MPa $\cdot$ m$^{1/2}$ and subsequently increased above this ΔK. A tentative explanation for this behavior is given next.

Below a ΔK of 16 MPa m$^{1/2}$ the plastic zone size progressively decreased with decreasing ΔK. This would have the effect of reducing the extent of accommodation and associated ductile plasticity where cracks move from one grain to another along the crack front. For K_{max} greater than 16 MPa m$^{1/2}$, the increase in overall cleavage formation is attributed to the onset of static cleavage. A critical cleavage stress of 2000 MPa was exceeded ahead of the crack for K_{max} greater than 16 MPa m$^{1/2}$. From previous work [7] this would support the view that static cleavage was involved at the crack tip. Two fractographs at a stress intensity of 10 MPa m$^{1/2}$ are included in Fig. 5. The fractograph in Fig. 5*a* has been chosen to show the presence of ductile striated mode (in grain D) accompanying the cleavage mode. In the adjacent grain (S) the markings correspond to intersecting slip bands that are orthogonal to each other, which suggests that plasticity in that facet is concentrated along the two orthogonal slip systems. Evidence of cyclic cleavage at 123 K is shown in Fig. 5*b* (arrow). In the absence of higher magnification pictures, no attempt has been made to calculate the microscopic crack growth rate for the low-hydrogen case. Figure 5*c* shows the extensive cleavage that was observed at 123 K. The fine lines perpendicular to the macroscopic crack growth direction appear to be cyclic cleavage markings left behind by the advancing crack. However, the spacing of these ($\geq$1 μm apart) is much greater than the macroscopic growth rate of about 10^{-9} m/cycle at this stress intensity level.

FIG. 3—*Fractographs at near threshold; 22 wt ppm H at 300 K.*

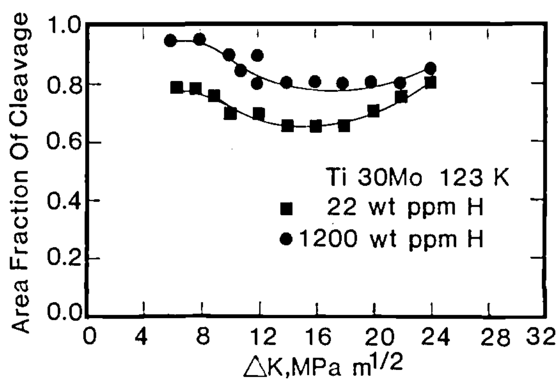

FIG. 4—*Variation in the area fraction of cleavage fracture with* ΔK *at 123 K.*

Since previous studies [*14,15*] demonstrated that local cyclic cleavage growth rates could be an order of magnitude greater than macroscopic growth rates in Fe-base systems, this result is consistent with those findings.

High-Hydrogen Content (1200 wt ppm)

For the high-hydrogen samples (1200 wt ppm), the lowest crack growth rates were observed at the highest test temperature, 340 K. Crack growth rates were little affected by lowering the temperature from 300 to 123 K. In Fig. 6, a comparison of the fcp curves at 340 and 123 K are shown. Here again the fatigue crack growth resistance decreases at lower temperatures, in spite of a twofold increase in yield stress. The DBTT for the 1200 wt ppm hydrogen was observed to be 375 K in four-point bend tests; thus the hydrogen raised the DBTT by more than 120 K. The lower thresholds obtained for the higher hydrogen content are shown in Fig. 2.

An examination of the fracture surfaces of the specimens showed substantial cleavage mode from 300 to 123 K. Particularly at 123 K, the fracture surface appeared 100% cleaved. Representative fractographs for the high hydrogen level are shown in Figs. 7 and 8. It is clear from these fractographs that the dominant mode of crack growth is cyclical cleavage. The microscopic crack growth rates were usually observed to be two orders of magnitude higher than the macroscopic values. At higher stress intensities the macroscopic and microscopic crack growth rates were found to be approximately the same. In addition, the cyclic cleavage crack growth was accompanied by some cyclic plasticity as shown in the fractography (Fig. 8*c*). The variation in the amount of cleavage fracture as a function of stress intensity is shown in Fig. 4.

Qualitatively, if the fatigue growth process were made up of brittle-type cleaved grains, one might expect the area fraction of cleaved grains to increase with increasing K_{max}. As the fraction of "cleaved" grains appears to go

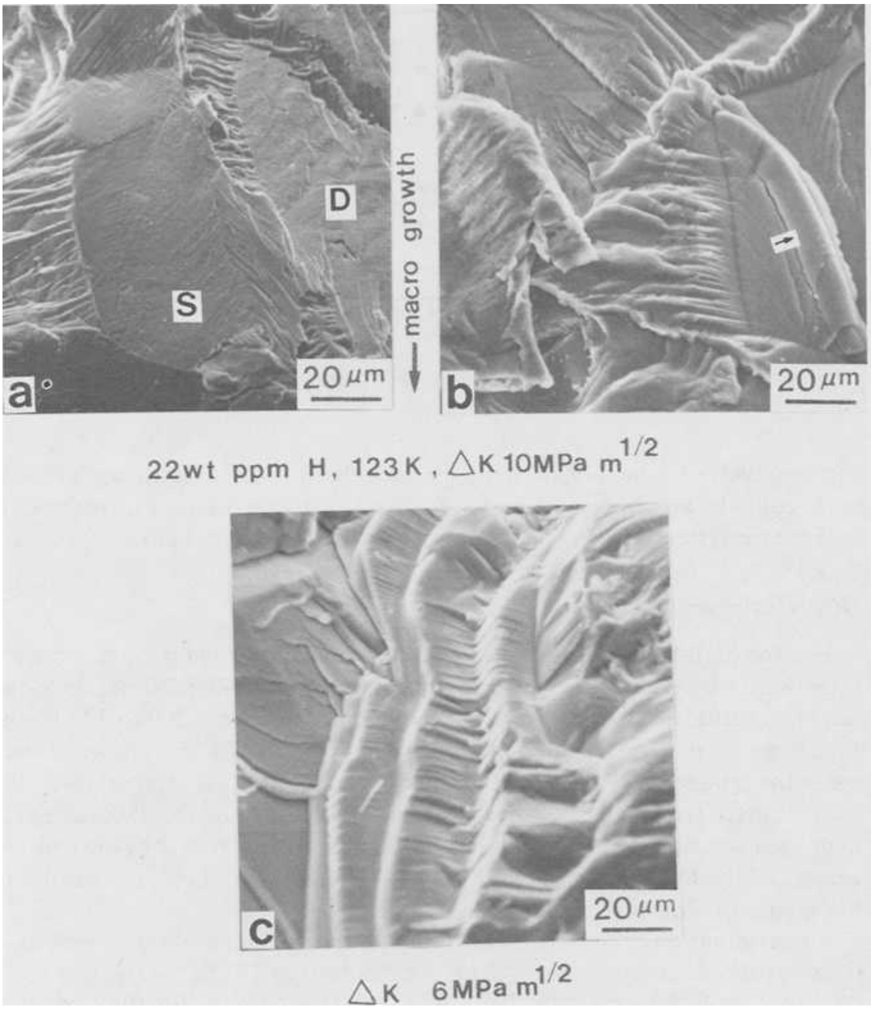

FIG. 5—*Fractographs at 10 and 6 MPa $m^{1/2}$ for 22 wt ppm H at 123 K.*

through a minimum, this probably represents competitive processes, with the cleavage fraction representing two distinct types of fracture micromechanisms. Again, this indicates a mixture of "brittle" and "ductile" types of cyclic decohesion.

Fatigue Crack Closure in Ti-30Mo

The crack closure data obtained from crack opening displacement gage measurements are shown in Table 1. These values, given as a percentage of K_{max}, correspond to the maximum amount of closure exhibited at the thresh-

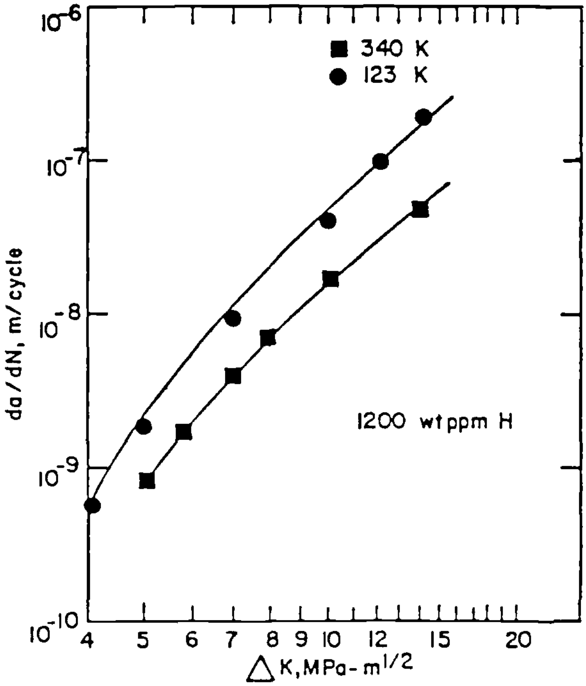

FIG. 6—*Comparison of observed* da/dN *versus* ΔK *for 1200 wt ppm H.*

old stress intensity (e.g., for 22 wt ppm hydrogen at 300 K, closure is 20%). This indicates that the fatigue crack remains closed until 20% of the maximum load is reached. Thus ΔK^i would be $K_{max} - 0.2\ K_{max}$, where ΔK is $K_{max} - K_{min}$ and $\Delta K^c = 0.2\,K_{max} - K_{min}$. The general observation is that the amount of crack closure decreased with decreasing temperature and increasing amounts of hydrogen content. It is to be noted that, firstly, all testing was performed at a constant R ratio (0.05) and under plane strain conditions. Secondly, for any given test temperature, the external environment test conditions were the same. Thus any oxide-induced closure that occurred should have resulted in equal amounts for any two different hydrogen contents at the same testing temperature. Table 1 shows, however, that for almost all temperatures the closure values decreased with increasing internal hydrogen contents. Therefore it is assumed that oxide-induced crack closure effects for Ti-30Mo played a secondary role in the closure levels observed.

It is well known that the near-threshold crack propagation is characterized by out-of-plane crack path trajectories, which results in considerable faceting. This tendency may be enhanced by active environmental species such as hydrogen. For Ti-30Mo, however, such faceting was observed for hydrogen levels as low as 22 ppm and at temperatures as high as 300 K. In addition, there were some important microscopic features of these facets that need to

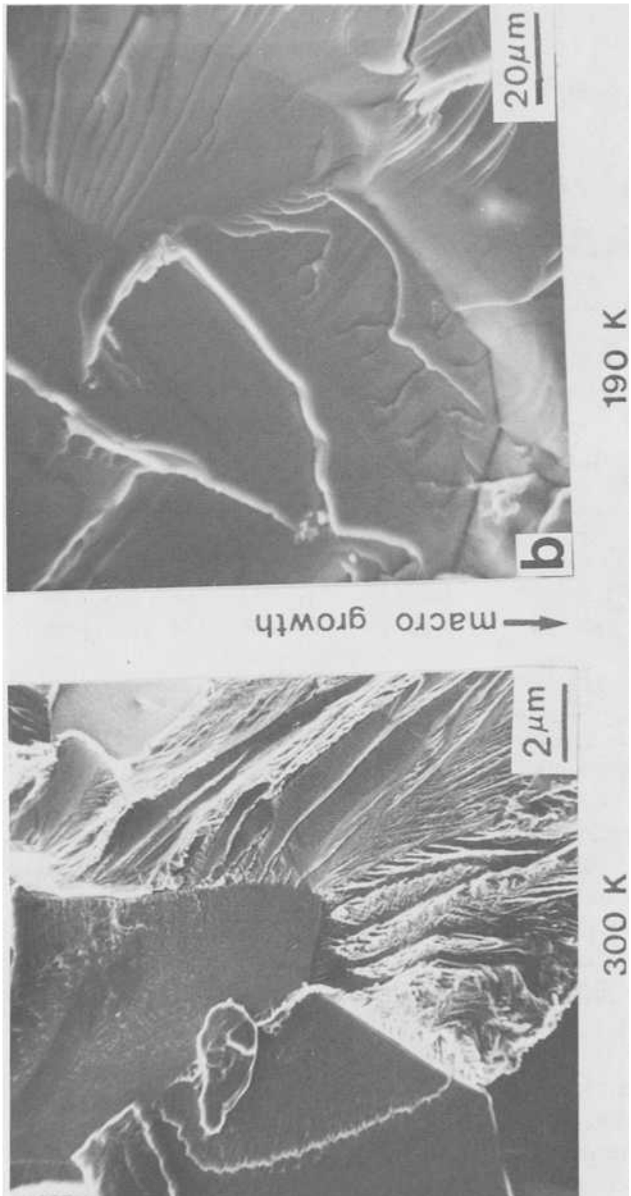

FIG. 7—Fractographs at near threshold for 1200 wt ppm H at 300 and 190 K.

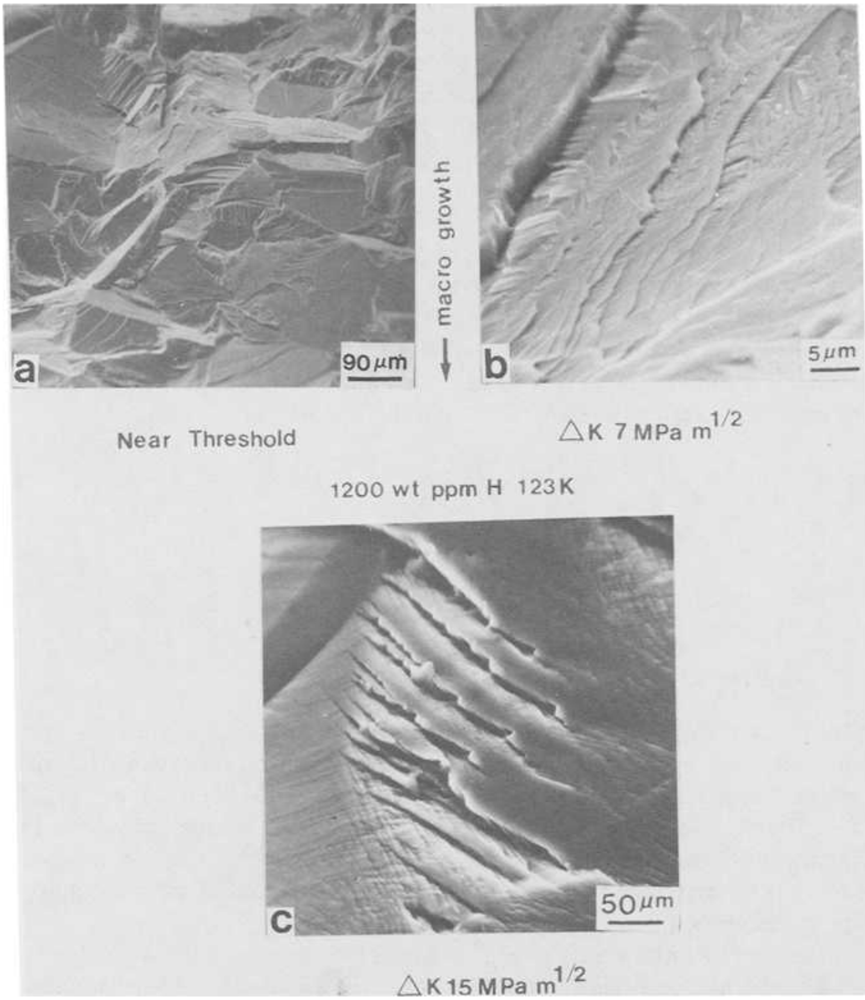

FIG. 8—*Fractographs at near threshold, 7 and 15 MPa $m^{1/2}$ for 1200 wt ppm H at 123 K.*

TABLE 1—*Crack closure values at threshold stress intensity for Ti-30Mo.*[a]

Temperature, K	22 wt ppm H	1200 wt ppm H
340	16%	7%
300	20%	13%
233	17.5%	0
190	18%	0
123	8%	0

[a] Crack closure values are as K^c/K_{max} in percentage.

be noted. As discussed previously, the facets exhibited slip bands that occasionally intersect orthogonally. At low temperatures and high hydrogen levels these facets transform more to cleavage or possibly Mode II cleavage along the active planes. Thus, although the Mode II (K_{II}) displacements at the crack tip that result in faceting were present in almost every testing condition, the overall effect on fractography was considerably different. The fractography suggests that with increasing hydrogen and decreasing temperature the slip offsets produced by shear or Mode II displacement decrease. Hence, less closure of the fatigue crack results in increasing cleavage.

In order to obtain an insight into the crossover of the fatigue crack growth curve for 22 wt ppm at 123 K in Region I, the closure values at each stress intensity level and the threshold values have been subtracted from the observed ΔK values. The data for Region I, Fig. 1, have been replotted in terms of an intrinsic effective stress intensity [17] defined as

$$\Delta K^{i}_{eff} = \Delta K^{i} - K^{i}_{th} \tag{3}$$

where

$$\Delta K^{i} = K^{obs} - \Delta K^{c}$$

and

$$K^{i}_{th} = \Delta K^{obs}_{th} - \Delta K^{c}_{th}$$

The plots of ΔK^{i}_{eff} versus da/dN shown in Fig. 9*a* suggest that the basic stress intensity (ΔK^{i}_{eff}) required to produce crack extension increases with yield stress. Furthermore, the slopes of da/dN versus ΔK^{i}_{eff} lie in a range of 2 to 2.8. These power exponents in Region I suggest that the crack growth in this region is controlled by the reverse plasticity at the crack tip, and the cyclic cleavage observed at low temperatures is thus attributed to the cyclic plasticity at the crack tip.

The experimental slopes in Fig. 9*a* are compared to the theoretical curves in Fig. 9*b* as described in the Appendix. The analysis is based upon the crack-tip driving force for dislocation motion on a cyclic-slip decohesion plane [18]. Comparison to the fatigue crack propagation data was made possible by recent measurements [19] of the cyclic strain-hardening exponent (β_c) and strain-rate sensitivity parameters (m and m^*). The latter were measured after the substructure had been cyclically stabilized in low-cycle fatigue tests. It is seen first in Fig. 9 that the predicted slopes at higher ΔK are in approximate accordance with the observed slopes. Also, at lower ΔK, the low test temperature data represented growth rates slower than the 300 K data by a factor of about 4 to 10. There was also a crossover point predicted near 8 MPa $m^{1/2}$, as was observed. Keeping in mind that the lower test temperature for predicted versus observed crack growth rates was different and that the

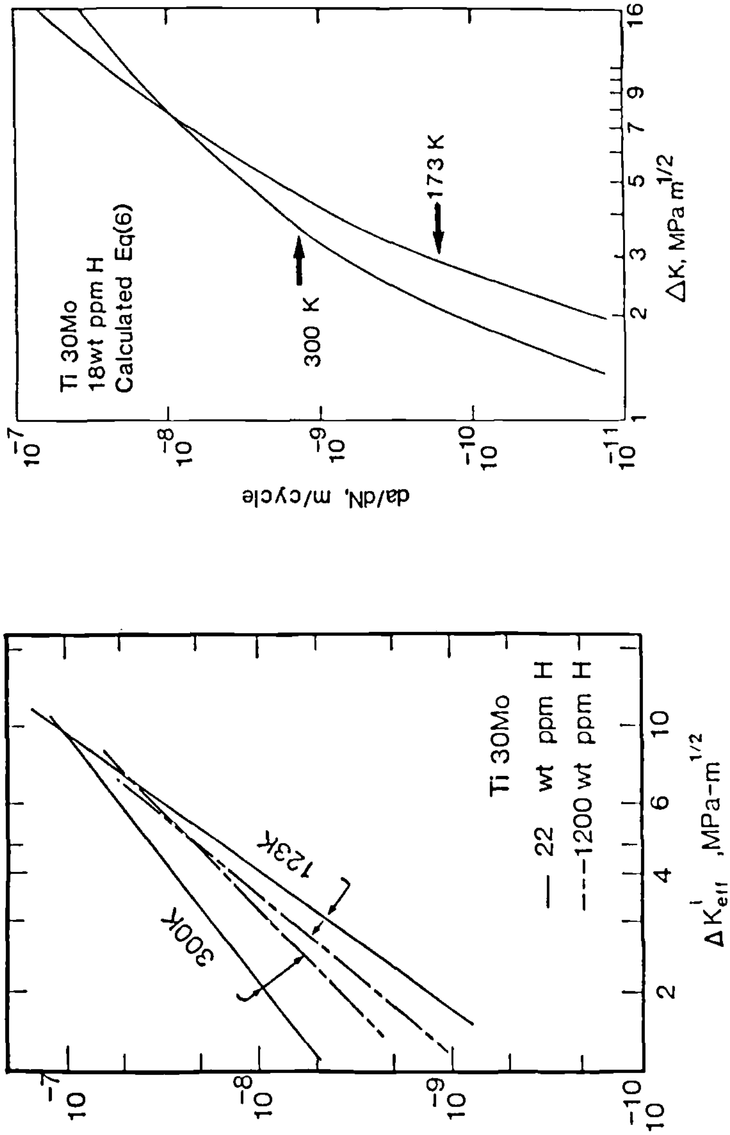

FIG. 9—*Comparison of observed* da/dN *versus* ΔK^{i}_{eff} *with predicted* da/dN *versus* ΔK *from Eq 6.*

analysis is for a single microfracture mechanism, the difference in the magnitude between prediction and observation is not significant.[2] The important point is that the general features are consistent, which suggests that dislocation dynamics controls the intrinsic growth process.

The presence of crack closure is known to raise the threshold stress intensity, and the stress intensity (ΔK^{c}_{th}) required to overcome closure becomes a significant part of ΔK^{obs}_{th}. In Fig. 2, the ΔK^{obs}_{th} values have also been replotted as ΔK^{i}_{th}:

$$\Delta K^{i}_{th} = \Delta K^{obs}_{th} - \Delta K^{c}_{th} \tag{4}$$

It is observed that the intrinsic threshold values (ΔK^{i}_{th}) fall approximately on a straight line, which indicates that the basic stress intensity range required to sustain crack growth increases with decreasing temperature or increasing yield stress. These observations are in accordance with a crack tip opening displacement criterion [*17*]

$$\Delta\text{CTOD} = \frac{(\Delta K^{i}_{th})^2}{4\sigma'_{ys}E} \tag{5}$$

where σ'_{ys} is the cyclic yield stress and E is Young's modulus (i.e., for a critical crack tip opening displacement, ΔK^{i}_{th} increases with σ'_{ys}. However, the higher hydrogen results do not seem to obey the above criterion, suggesting that for environmentally assisted crack growth a simple crack tip opening displacement criterion may not be applicable. The more important consideration appears to be the slip activity as is evidenced from the fractographic work. For a number of titanium alloys it has been shown that planar slip is enhanced by the presence of hydrogen; also, a change in the slip mechanism from cross slip to planar slip at low temperatures seems to be the cause of DBTT [*20*]. If this is true for Ti-30Mo, then the accumulated reverse plasticity at the crack tip would decrease with decreasing temperature and increasing hydrogen content. Thus increasing amounts of slip planarity would not only reduce closure but also promote cleavage. This model is consistent with the observations made here.

Looking again at Fig. 2, it can be seen that ΔK^{i}_{th}, the basic ΔK required to produce crack extension for 1200 wt ppm, slightly increases at 123 K compared with 300 K, in accordance with the increase in yield stress. Why the fa-

[2] It was difficult to perform tension-compression, low-cycle fatigue tests at 123 K in this coarse-grained material because of the tendency toward brittle fracture. Thus appropriate material constants could not be determined.

tigue thresholds at lower temperatures remain relatively constant is not yet known, but this phenomenon may be a result of increased cyclic slip resistance being offset by decreased cyclic cleavage resistance.

Summary and Conclusions

1. For low hydrogen contents, near-threshold crack propagation can best be described by an intrinsic stress intensity factor ΔK^{i}_{eff} rather than the usual ΔK. Such an approach leads to the conclusion that at very low temperatures, cyclic cleavage is dominated by reverse plasticity.
2. The fatigue threshold ΔK_{th} can be described by $\Delta K^{obs}_{th} = \Delta K^{c}_{th} + \Delta K^{i}_{th}$, where ΔK^{c}_{th} is the stress intensity needed to overcome closure and produce a fully opened crack, and ΔK^{i}_{th}, is the basic stress intensity needed to produce crack extension. It is found that ΔK^{i}_{th} decreases with increasing hydrogen content and increasing temperature. The effect of lowering temperature or increasing hydrogen content is to decrease ΔK^{c}_{th}.
3. Higher crack closure loads are accompanied by ductile-faceted crack growth and lower crack closure loads by cleavage-faceted monotonic or cyclic crack growth in Ti-30Mo.
4. A theoretical analysis of crack growth rates based on cyclically stabilized dislocation substructure has been obtained that shows good correlation with experimental observations. This analysis suggests that the intrinsic crack growth resistance (ΔK^{i}_{eff}) at low temperatures can be described by the dislocation dynamics at the crack tip.

Acknowledgments

The authors acknowledge the support of the Division of Materials Science, Basic Energy Sciences, Department of Energy, through Grant DOE-DE-AC02-79ER10433.

APPENDIX

Determination of Growth Rate by Cyclic Slip

From a previous analysis of cyclic slip along a slip-decohesion plane, it was shown that [*18*]

$$\left(\frac{da}{dN}\right)_D \simeq \Theta\Omega_1\Delta K\left[\frac{\sigma_{ys}}{\sigma_0}\left(\frac{\mathrm{Rp}_{\pm}}{L_s}\right)\beta'(\Omega_2)^{1/m} - \left(\frac{\sigma_i}{\sigma_o}\right)\right]^{m^*/2} \quad (6)$$

TABLE 2—*Some parameters appropriate to annealed Ti-30Mo (see Appendix).*

Parameter	Definition	At 300 K	At 173 K
σ^*	Thermal component of flow stress	34 MPa	78 MPa
m^*	Strain-rate sensitivity $(\partial ln\dot{\epsilon}/\partial ln\sigma^*)$	4	7.8
m	Strain-rate sensitivity $(\partial ln\dot{\epsilon}/\partial ln\sigma)$	63	83
ρ_m	Mobile dislocation density	$10^{14}/m^2$	$10^{14}/m^2$
σ_{ys}	Yield strength	710 MPa	960 MPa
σ_i	Internal stress	676 MPa	882 MPa
ω	Fatigue test frequency	20 Hz	20 Hz
$\dot{\epsilon}_s$	Tension test strain rate	$10^{-4}s^{-1}$	$10^{-4}s^{-1}$
Ω_1	$\left(\frac{1-\nu^2}{E}\right)\left[\frac{\nu_0}{2(m^*+1)\omega}\right]^{1/2}$	$6.43 \times 10^{-8} m^{1/2} MPa^{-1}$	$4.85 \times 10^{-8} m^{1/2} MPa^{-1}$
$(\Omega_1)^{1/m}$	$(\sigma_{ys}\omega/E_{\dot{\epsilon}_s})^{1/m}$	1.12	1.095
σ_0	Dislocation velocity stress constant	1350 MPa	516 MPa
β_c	Cyclic strain hardening exponent	0.049	0.043
β'	$(m\beta_c + 1)/m(1 + \beta_c)$	0.062	0.053
L_s	Subcell size	$1 \times 10^{-6}m$	$1 \times 10^{-6}m$

where

Θ = crystallographic orientation factor, $\simeq 1$ for polycrystalline materials,
$Rp_{\pm}$ = reverse plastic zone size, $\simeq \Delta K^2/12\pi\sigma_{ys}^2$,
σ_0 = dislocation stress constant, $\simeq \sigma^*(\dot{\epsilon}/\rho_{m}b\nu_0)^{-1/m^*}$, and
σ^* = thermal component of the flow stress, $\nu_0 = 0.01$ m/s.

The values of the other parameters appropriate to annealed Ti-30Mo are shown in Table 2.

The only parameters not fixed by either the cyclic stress-strain test data [19] or the input loading parameter for fracture mechanics testing were the mobile dislocation density (ρ_m) and the subcell size (L_s). To be consistent with other materials of this strength level and crystal structure the values chosen were 10^{10}/cm^2 and 1 μm, respectively. As is shown in the text, these parameters gave a reasonable representation of the test data.

References

[1] Suresh, S., Zamiski, G. F., and Ritchie, R. O., *Metallurgical Transactions*, Vol. 12A, No. 8, 1981, p. 1435.
[2] Beevers, C. J., "Threshold ΔK Values and Non-Closure of Fatigue Cracks," in *Advances in Fracture Research (ICF 5)*, Vol. 3, D. François, Ed., Pergamon Press, New York, 1980, p. 1335.
[3] Walker, N. and Beevers, C. J., *Fatigue of Engineering Materials and Structures*, Vol. 1, No. 2, 1979, p. 135.
[4] McEvily, A. J., *Metal Science*, Vol. 11, 1977, p. 274.
[5] Ritchie, R. O. and Suresh, S., *Metallurgical Transactions*, Vol. 13A, No. 5, 1982, p. 937.
[6] Gerberich, W. W., Jatavallabhula, K., Peterson, K. A., and Jensen, C. L., "Hydrogen-Induced Fracture Phenomena in a BCC Ti Alloy," in *Advances in Fracture Research (ICF 5)*, Vol. 2, D. François, Ed., Pergamon Press, New York, 1980, p. 989.
[7] Jatavallabhula, K. and Gerberich, W. W., *Fatigue of Engineering Materials and Structures*, Vol. 14, No. 2, 1982, p. 173.
[8] Wilcox, J. R. and Koss, D., "Crack Propagation Along Crystallographic Slip Bands and Hydrogen Embrittlement," in *Hydrogen in Metals*, AIME, New York, 1981, p. 203.
[9] Chakrabortty, S. B. and Starke, E. A., *Metallurgical Transactions*, Vol. 10A, No. 12, 1979, p. 1901.
[10] Lucas, J. P. and Gerberich, W. W., *Materials Science and Engineering*, Vol. 51, No. 2, 1981, p. 203.
[11] Tschegg, E. and Stanzl, S., *Acta Metallurgica*, Vol. 29, No. 1, 1981, p. 33.
[12] Burck, L. H. and Weertman, J., *Metallurgical Transactions*, Vol. 7A, No. 2, 1976, p. 257.
[13] Yu, W. and Gerberich, W. W., *Scripta Metallurgica*, Vol. 17, No. 1, 1983, p. 105.
[14] Gerberich, W. W. and Jatavallabhula, K., *Acta Metallurgica*, Vol. 31, No. 2, 1983, p. 241.
[15] Gerberich, W. W., Moody, N. R., and Jatavallabhula, K., *Scripta Metallurgica*, Vol. 14, No. 1, 1980, p. 113.
[16] Moody, N. R. and Gerberich, W. W., *Materials Science and Engineering*, Vol. 41, No. 2, 1979, p. 271.
[17] Beevers, C. J, "Some Aspects of the Influence of Microstructures and Environment and ΔK Thresholds," in *Fatigue Thresholds*, J. Backhund, A. F. Blum, and C. J. Beevers, Eds., EMAS, United Kingdom, 1982.
[18] Gerberich, W. W. and Peterson, K. A., "Micro and Macro Mechanics Aspect of Time Dependent Crack Growth," in *Micro and Macro Mechanics of Crack Growth*, E. Sadananda, Ed., TMS-AIME, New York, 1982, p. 1.
[19] Nayar, A., "Low-Cycle Fatigue of Ti-30Mo," M.S. thesis, University of Minnesota, Minneapolis, March 1983.
[20] Rack, H. J., *Scripta Metallurgica*, Vol. 10, No. 8, 1976, p. 239.

STP857-EB/Mar. 1985

DISCUSSION

Peter K. Liaw[1] (*written discussion*)—Do you think that oxide-induced crack closure is important in titanium alloys?

K. V. Jata (*author's closure*)—We have not performed any Auger analysis to show whether a sufficient thickness of oxide layers exists at the crack to promote oxide-induced crack closure.

[1] Dr. Liaw is with the Westinghouse R&D Center, Pittsburgh, PA 15236.

Takeo Yokobori, Ichiro Maekawa, Yuji Tanabe, Zhihao Jin, and Shin-Ichi Nishida

Fatigue Crack Propagation of 25Mn-5Cr-1Ni Austenitic Steel at Low Temperatures

REFERENCE: Yokobori, T., Maekawa, I., Tanabe, Y., Jin, Z., and Nishida, S.-I., **"Fatigue Crack Propagation of 25Mn-5Cr-1Ni Austenitic Steel at Low Temperatures,"** *Fatigue at Low Temperatures, ASTM STP 857,* R. I. Stephens, Ed., American Society for Testing and Materials, Philadelphia, 1985, pp. 121–139.

ABSTRACT: A study has been carrried out on the fatigue behavior of a newly developed high-manganese steel intended for low-temperature applications in the range from 0 to −174°C. As-rolled and solution-treated high-manganese steel were tested. The fatigue behavior of commercial austenitic steel was also presented for comparison.

The fatigue life of high-manganese steel was found to increase with decreasing temperature from 0 to −174°C. Crack growth rates were expressed in terms of the Paris relation $da/dN = C(\Delta K)^n$, and the power coefficient n was shown to depend on temperature. The temperature dependence of crack growth rate and n, as well as the linear dependence of apparent activation energy of the fatigue crack growth rate on the logarithm of the stress intensity factor range, are explained by the dynamic theory of fatigue crack growth.

Fatigue fracture toughness (K_{fc}) was found to increase with decreasing temperature. The effect of welding on K_{fc} is also shown.

KEY WORDS: fatigue, fracture, toughness, crack propagation, steel, manganese-containing alloy, solution treatment, welds, low temperature, rate process, dislocation

The development of structural steel for use at low temperatures is expected to affect a wide range of industrial applications, including nuclear fusion reactors, magnetohydrodynamic electric power generation, and the linear motor car. Several nickel alloys have been used for such purposes.

A 25Mn-5Cr-1Ni austenitic steel has also been developed [*1*]. This new high-manganese steel is nonmagnetic and shows high strength and toughness at low temperatures. These properties are desirable for applications like

Dr. Yokobori is Professor Emeritus, Dr. Maekawa is a professor, and Mr. Tanabe is a research associate in the Department of Mechanical Engineering II, Tohoku University, Sendai, Japan. Mr. Jin is a lecturer in the Department of Mechanical Engineering, Xian Jiaotong University, Xian, Shaanxi, People's Republic of China. Dr. Shin-Ichi Nishida is a senior researcher of the Technical Research Department at the Yawata Works of Nippon Steel Corp., Yawata, Japan.

those described above. Since this alloy contains a high concentration of manganese instead of nickel, it has an added advantage in that it uses ocean resources. Thus studies of the applicability of high-manganese steel as a structural material at low temperatures have an important practical significance. Therefore fracture properties were studied at 4 K [1,2]. Further study of fatigue properties at several temperature levels below room temperature also seemed necessary.

The purpose of the research described in this paper was to determine fatigue properties and the effect of welding for the high-manganese steel at low temperatures, comparing it with normal austenitic steel. Crack growth behavior, crack growth rate, fatigue fracture toughness, and fracture toughness were studied at 0, −120, −160, and −174°C or −178°C. This high-manganese steel showed ductility even at low temperatures. Therefore the fatigue crack growth rate was analyzed in terms of the rate process theory, taking into account a microscopic plastic model at the crack tip. The relation between fatigue fracture toughness and fracture toughness is discussed, as is the effect of heating during welding.

Specimens and Experimental Procedures

A newly developed 25Mn-5Cr-1Ni austenitic steel and SUS 304 steel, a commercial austenitic steel conforming to Japanese Industrial Standard for stainless steel (G 4303), were compared in this study. They were produced by Nippon Steel Corporation; their chemical compositions and mechanical properties are shown in Tables 1 and 2, respectively.

The high-manganese steel was supplied in the hot-rolled condition with a rolling ratio of 8 and in the solution-treated condition. The solution treatment consisted of heating at 900°C for 60 min and subsequently quenching in water. The solution treatment for the SUS 304 steel consisted of heating at 1040°C for 12 min and subsequently quenching in water.

Compact tension specimens with a notch perpendicular to the rolling direction were prepared as shown in Fig. 1*a* for both materials. Slightly different compact tension specimens, shown in Fig. 1*b*, were used to evaluate the elastic-plastic fracture toughness J_{Ic}. From the welded high-manganese steel, three series of specimens, designated WELD, BOND, and HAZ (for heat-affected zone), were sectioned as shown in Fig. 1*c*.

Fatigue experiments were performed at frequency of 3.3 Hz and load ratio (R) of 0.1 using a servohydraulic testing machine with a 98-kN capacity. A triangular loading wave was used. The maximum load (P_{max}) was 49 and 58.8 kN for the high-manganese and SUS 304 steel, respectively. Specimen temperature was measured by copper-constantan thermocouples attached to each specimen; temperature fluctuation was kept within 2°C at each temperature in a cooling box mounted on the testing machine. The box had a coiled copper pipe surrounding the specimen; the flow of liquid nitrogen in the pipe

TABLE 1—*Chemical composition (weight percent).*

Steel	C	Si	Mn	P	S	Ni	Cr	Nb	Al
25Mn-5Cr-1Ni steel (as-rolled)	0.18	0.20	24.42	0.024	0.005	1.07	4.96	0.05	. . .
SUS 304 steel	0.06	0.63	1.00	0.028	0.004	9.08	19.00	. . .	0.002

TABLE 2—*Mechanical properties.*

Steel	$\sigma_{0.2}$, MPa	σ_B, MPa	Elongation, % (Gage Length = 50 mm)	Reduction of Area, %
25Mn-5Cr-1Ni steel (as-rolled)	379.3	734.0	56.0	61.9
SUS 304 steel	263.6	619.4	58.8	73.1

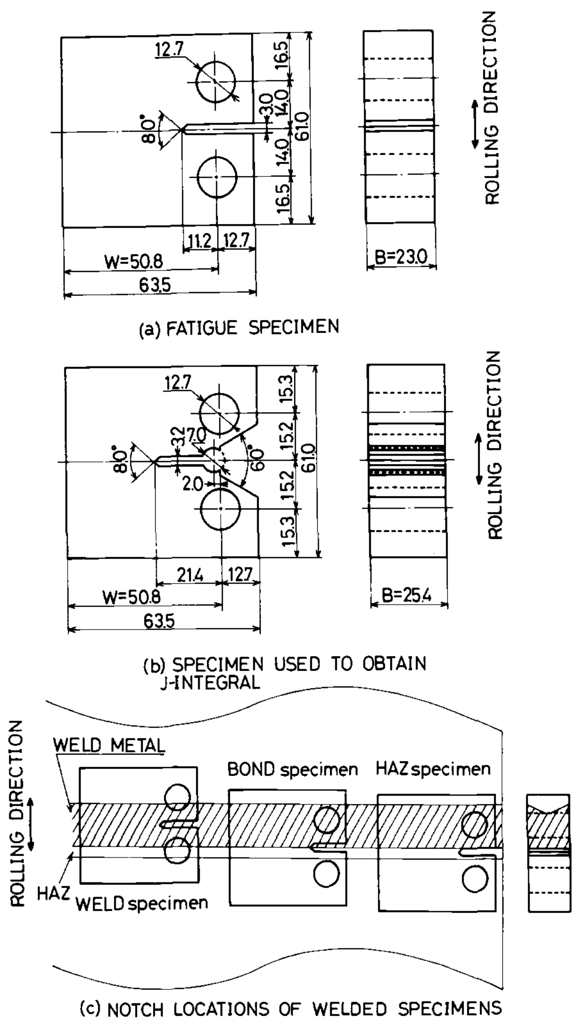

FIG. 1—*Compact tension specimens.*

was regulated by controlling the delivery of a plunger pump. Thus the specimens were cooled indirectly. The crack length (a)—that is, the distance between the crack tip and the artificial notch tip—was measured by using a traveling microscope through an observation window in the cooling box.

In order to evaluate J_{Ic}, several precracked specimens were used. Precracks were introduced by using the aforementioned testing machine at a frequency of 5 Hz at room temperature. The value of P_{max} was gradually decreased from 39.2 to 17.64 kN, keeping the load ratio at 0.1 until the crack length grew up to $0.6W$ (30.5 mm) in accordance with the Test for Elastic-Plastic Fracture Toughness J_{Ic} recommended by the Japan Society of Mechanical Engineering (JSME S001-1981). From this value of J_{Ic}, fracture toughness (K_c) was estimated and compared with fatigue fracture toughness (K_{fc}).

Experimental Results and Discussion

Fatigue Crack Growth Behavior

Crack length versus cycles for two series of high-manganese steel and SUS 304 steel are shown in Figs. 2*a* to 2*c*, respectively. The mean value of crack length for two specimens was used at each temperature level, except for −174°C in Fig. 2*b* and 0 and −178°C in Fig. 2*c*. Scatter for fatigue life is also shown in these figures. Figure 2*d* shows the experimental results for welded specimens. In Fig. 2, fatigue life to fracture increases with decreasing temperature. According to Figs. 2*a* to 2*c*, fatigue life was greater in SUS 304 than in high-manganese steel at low temperatures. The scatter of fatigue life for the high-manganese steel seems to be smaller than for SUS 304 steel, however. In Fig. 2*b*, fatigue life at −174°C lies within the range for −160 and −120°C. No significant difference between fatigue life at −160 and −174°C can be seen, and the existence of a reversal point for the temperature dependence of fatigue life is not clear. Similar trends that showed the existence of a reversal point for the temperature dependence of fatigue life at lower temperatures than those studied here have been observed for other materials [*3,4*]. A similar result can be seen in Fig. 2*c*. A comparison of Figs. 2*a* and 2*b* indicates that solution treatment had no significant effect on fatigue strength. From Figs. 2*a*, 2*b*, and 2*d* it can be seen that the fatigue life of the WELD specimens was comparable to that of as-rolled high-manganese steel at 0°C. The BOND and HAZ specimens were strongly affected by heating during welding, however. At −174°C, a similar result can be seen, except for the WELD specimens, for which fatigue life was a little shorter than that of the as-rolled specimens. Thus it appears that heating causes an increase in life. The WELD specimens frequently contained internal defects, however, and heating did not improve their life. Because the strength of a structural member depends on the weakest point, a welded structure may not have a superior strength even at low temperatures.

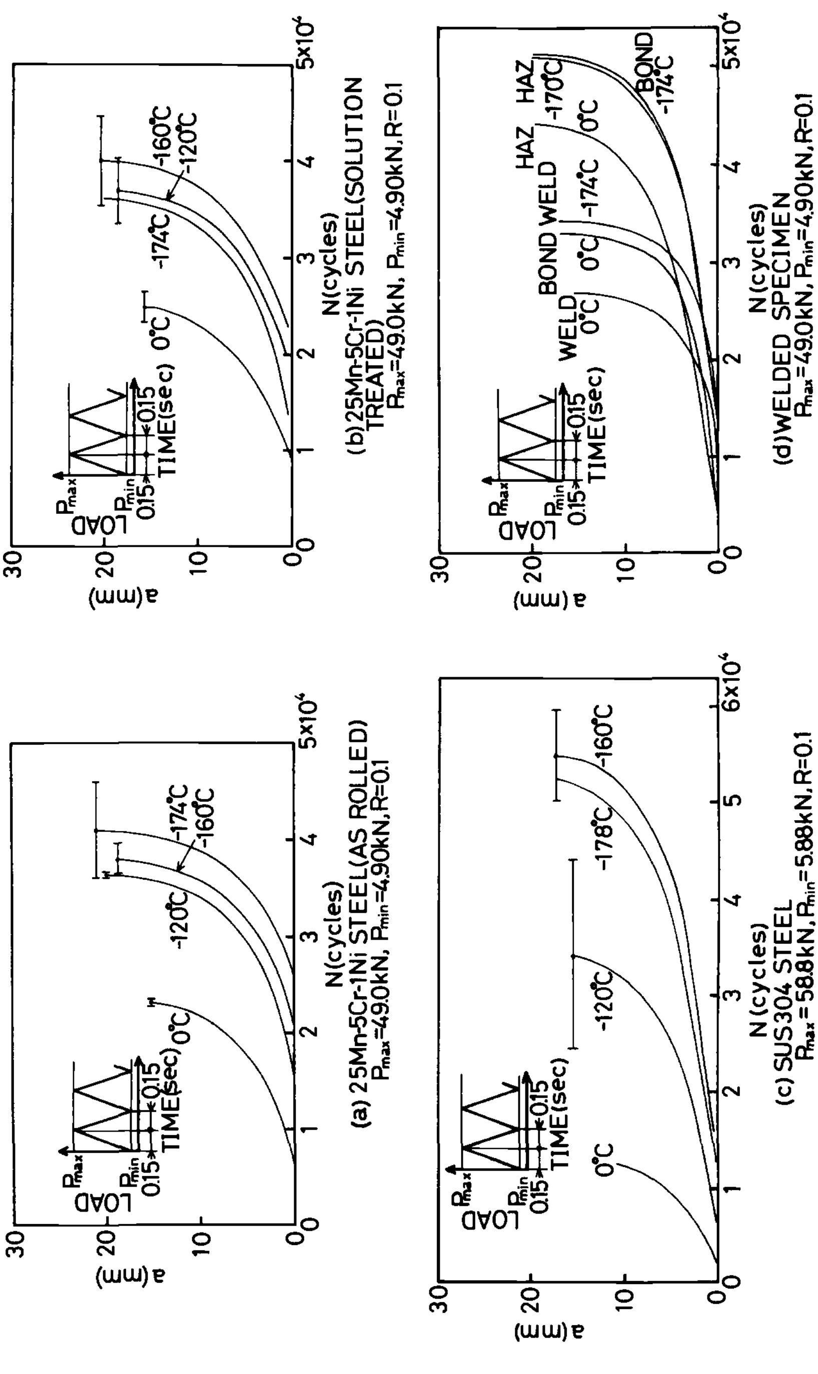

FIG. 2—*Crack length versus repeated cycle.*

The relation between cycles to fracture (N_f) and the inverse of absolute temperature (1/T) is shown in Figs. 3*a* and 3*b*. The increase in N_f was considerable in the case of the SUS 304 steel but moderate for the high-manganese steel. Thus the fatigue life of high-manganese steel is relatively stable over a wider range of temperatures than for the SUS 304 steel. This trend held true for welded specimens.

In this experiment, crack length and load were measured with a precision of ±0.002 mm and ±0.5 kN, respectively. Crack growth rate and ΔK value were then estimated within a relative error of ±1%. On the other hand, the scatter of fatigue life is not as small as in Fig. 2. Strictly speaking, the discussion should be based on a statistical treatment of experimental data, but this would require many specimens. For practical purposes, it is useful to know the trend in temperature dependence of fatigue behavior for 25Mn-5Cr-1Ni steel as compared with SUS steel. These limited results are also a first step towards understanding the fracture mechanism of steel at low temperatures.

Fatigue Crack Growth Rate

Fatigue crack growth rate (da/dN) is usually expressed as a function of the stress intensity factor range (ΔK); see Figs. 4*a* to 4*d*. The ΔK value is ob-

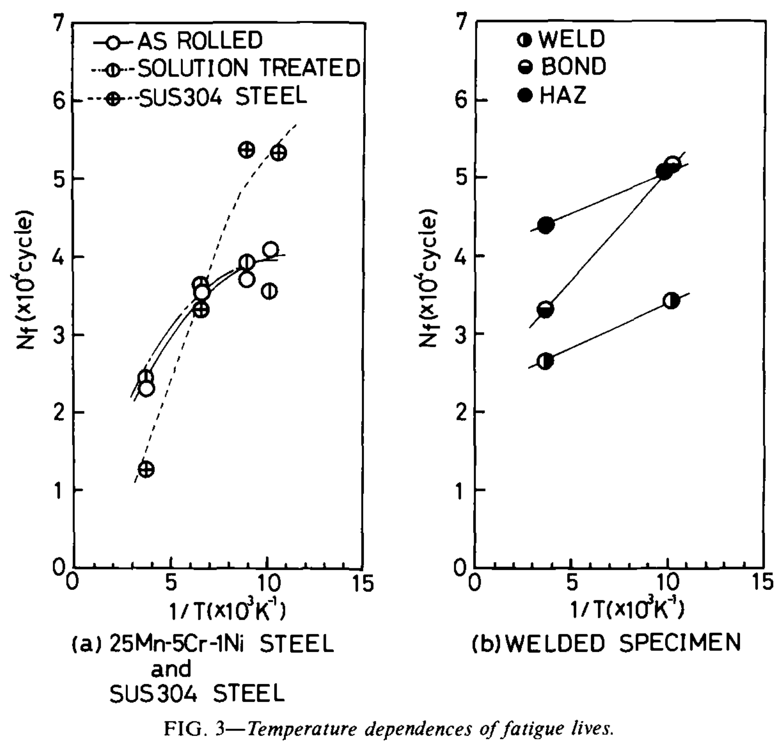

FIG. 3—*Temperature dependences of fatigue lives.*

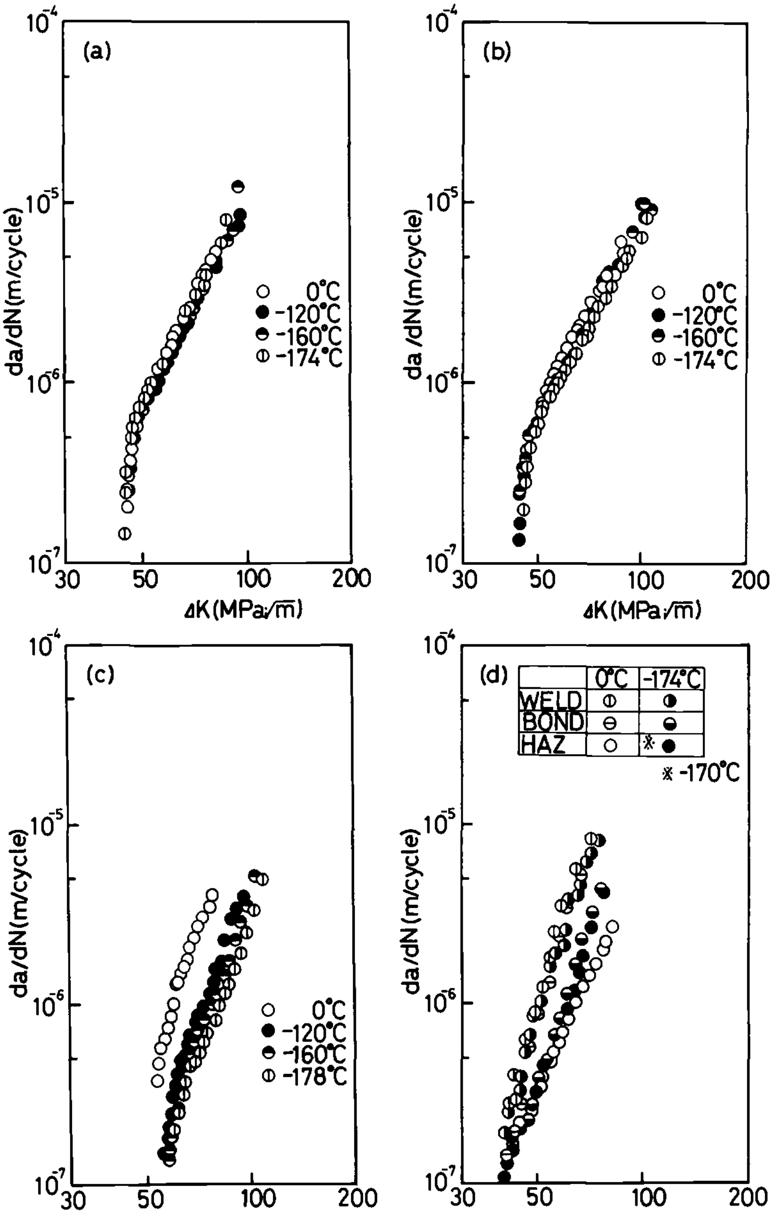

(a) 25Mn-5Cr-1Ni STEEL (AS ROLLED)
(b) 25Mn-5Cr-1Ni STEEL (SOLUTION TREATED)
(c) SUS 304 STEEL
(d) WELDED SPECIMEN

FIG. 4—*Fatigue crack growth rate versus* ΔK.

tained, substituting ΔP instead of P for K [5], by

$$\Delta K = \frac{\Delta P}{BW^{1/2}} f(a^*/W) \tag{1}$$

where

$$\begin{aligned} f(a^*/W) &= 29.6(a^*/W)^{1/2} - 185.5(a^*/W)^{3/2} + 655.7(a^*/W)^{5/2} \\ &\quad - 1017(a^*/W)^{7/2} + 638.9(a^*/W)^{9/2}, \\ \Delta P &= P_{max} - P_{min}, \text{ N}, \\ B &= \text{thickness of specimen, m, and} \\ a^* &= \text{distance between crack tip and loading line, m.} \end{aligned}$$

In Figs. 4*a* to 4*d* the linear dependence of crack growth rate on ΔK implies that fatigue crack growth obeys the Paris relation [6]

$$da/dN = C(\Delta K)^n \tag{2}$$

where C and n are numerical constants to be determined from crack propagation results.

Although the crack growth rate was lower at −174°C than at −160°C (Fig. 4*b*), the fatigue life was shorter at −174°C (Fig. 2*b*), because the number of cycles at which cracks start to grow was smaller at −174°C. Applying Eq 2 to these experimental results, numerical values for C and n were obtained (Table 3). In this table, the n value was about 3 or 4 in the case of high-manganese steel, almost the same values as reported in many other studies. But n took a slightly higher value in the case of SUS 304 steel. In Table 3, the value of n showed little increase with decreasing temperature. Thus da/dN depended on temperature; Figs. 5*a* to 5*f* show that da/dN generally decreased with decreasing temperature.

As mentioned above, the existence of a reversal point for the temperature dependence of da/dN at very low temperature range has been observed for other materials [3,4].

Because the fracture surface indicated that the high-manganese steel specimens were ductile even at low temperatures, it seems necessary to take into account the microscopic plastic mechanism as well as the macroscopic mechanical treatment in order to explain the temperature dependence of the crack growth rate. According to the dynamics of a crack propagation [7,8], the microscopic contribution from dislocations near a crack tip is expressed as

$$da/dN = n^*b \tag{3}$$

TABLE 3—*Values of* C *and* n *in the relation* $da/dN = C(\Delta K)^n$.[a]

	Temperature, °C	C	n
25Mn-5Cr-1Ni steel (as-rolled)	0	$10^{-12.72}$	3.90
	−120	$10^{-12.87}$	3.94
	−160	$10^{-12.84}$	3.95
	−174	$10^{-12.97}$	4.00
25Mn-5Cr-1Ni steel (solution-treated)	0	$10^{-12.37}$	3.68
	−120	$10^{-12.54}$	3.72
	−160	$10^{-12.61}$	3.77
	−174	$10^{-12.64}$	3.76
SUS 304 steel	0	$10^{-14.22}$	4.64
	−120	$10^{-14.95}$	4.80
	−160	$10^{-15.40}$	4.97
	−178	$10^{-15.48}$	4.97
Notch location			
Weld metal	0	$10^{-15.98}$	5.88
	−174	$10^{-16.17}$	5.97
Bond	0	$10^{-13.59}$	4.21
	−174	$10^{-14.36}$	4.64
HAZ	0	$10^{-12.97}$	3.82
	−170	$10^{-13.02}$	3.84

[a] *da/dN* is given in m/cycle; ΔK in $\text{MPa}\sqrt{\text{m}}$.

where

n^* = number of dislocations emitted from a crack tip until the time concerned, and
b = Burgers vector, m

In a previous paper [8], the final equation based on the rate process theory was obtained as

$$\ln (da/dN) = \ln A + b_1 \ln(\Delta K) - \frac{U_2 - a_1 \ln(\Delta K)}{kT} \tag{4}$$

where

A, a_1, b_1 and U_2 = material constants,
k = Boltzmann's constant, J/K, and
T = absolute temperature, K.

The numerator of the third term of the right-hand side in Eq 4 corresponds to the apparent activation energy (Q) of a crack growth and is written as

$$Q = U_2 - a_1 \ln(\Delta K) \tag{5}$$

In Eq 4, the temperature dependence of a crack growth rate is expressed in the form of an Arrhenius equation; the activation energy is a linear function

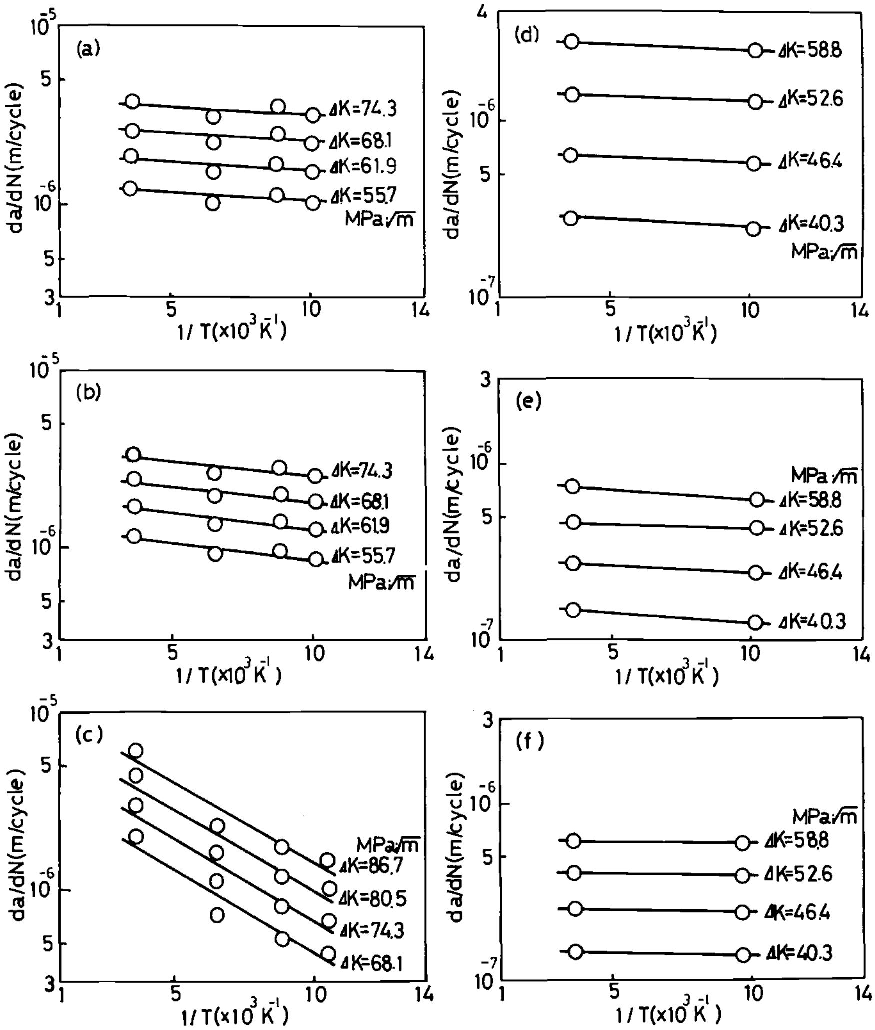

(a) 25Mn-5Cr-1Ni STEEL(AS ROLLED)
(b) 25Mn-5Cr-1Ni STEEL(SOLUTION TREATED)
(c) SUS304 STEEL
(d) WELDED SPECIMEN(WELD)
(e) WELDED SPECIMEN(BOND)
(f) WELDED SPECIMEN(HAZ)

FIG. 5—*Temperature dependence of crack growth rate.*

of $\ln(\Delta K)$ in Eq 5. The relationship between Q and $\ln(\Delta K)$ obtained from the experimental results is plotted in Figs. 6*a* and 6*b*. These experimental results agree with the qualitative theoretical description above. Further, it can be seen that the power coefficient of ΔK in Eq 4 corresponds to n in Eq 2. The numerical values of C and n were obtained as listed in Table 3. The value of n for high-manganese steel was slightly lower than for SUS 304 steel.

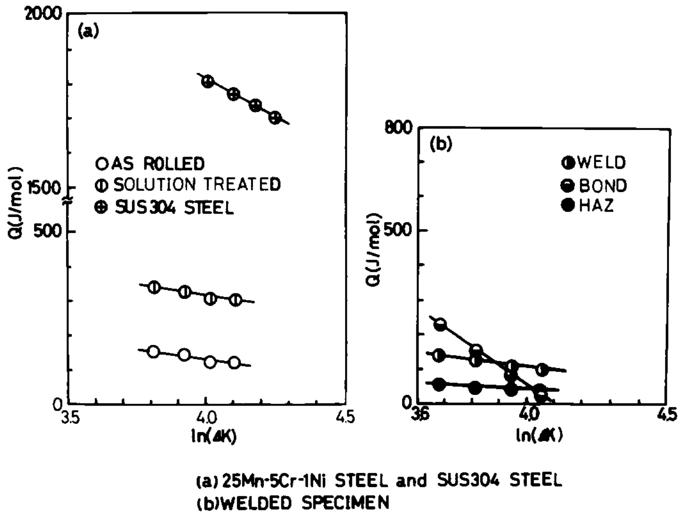

FIG. 6—*Apparent activation energy of crack growth versus logarithm of stress intensity factor range.*

It has been pointed out that for the same material, the activation energy model differs according to the temperature range [*9*]; in some materials, the activation energy model can be applied only within some range of temperatures [*3,4*]. Thus in the present article an attempt has been made to apply an activation energy model within the range studied. From the foregoing analysis, it was found that below about −174°C the same equation could not be valid for 25Mn-5Cr-1Ni austenitic steel. Thus below this temperature, *da/dN* may not obey the activation energy model, or may obey another activation model. Such trends were observed for 780-MPa-grade high-strength weldments [*3*] and 5.5% nickel steel weldments [*4*].

Since temperature effects are small in the present case, one might at first assume that they may be accounted for by the variation of elastic modulus with temperature. However, *da/dN* has not been definitely established as a function of elastic modulus, as shown in Table 1 of Ref *10*, although many formulas have been proposed. Based on rate process theory, *da/dN* is explicitly given in terms of elastic modulus; it is added as a logarithmic term [*7–9*] to activation energy and thus its effect may not be large. On the other hand, applying rate theory, experimentally obtained values of activation energy (Q) are found as a monotonically decreasing function of $\ln(\Delta K)$, which is in accordance with Eq 4.

Although the material constants in Eq 4 have not yet been obtained for the alloys used in this study, they are iron-based alloys. So we may try to estimate the crack growth rate for iron by using Eq 4 and substituting appropriate values for iron at $T = 273$ K, $f = 3.3$ Hz, $k = 1.38 \times 10^{-23}$ J/K, distance over which applied stress is averaged $\epsilon = 1.5 \times 10^{-7}$ m, and material constants $\mu = 80.3$ GPa, $a_1 = 9.04 \times 10^{-21}$ J, $b_1 = 0.8$, $U_2 = 1.58 \times 10^{-19}$ J. We obtain

$$da/dN = 1.51 \times 10^{-6} \text{ m/cycle}$$

for $\Delta K = 61.92 \text{ MPa}\sqrt{\text{m}}$. The details of the calculation are given in the Appendix. In contrast, experimental results are

$da/dN = 1.84 \times 10^{-6}$ m/cycle for high-manganese steel (as rolled)
$da/dN = 1.69 \times 10^{-6}$ m/cycle for high-manganese steel (solution treated)
$da/dN = 1.25 \times 10^{-6}$ m/cycle for SUS 304 steel

Thus the experimental results agree fairly well with the theoretical prediction. The differences among these materials may be attributed to the microscopic material constant b and m, which is included implicitly in Eq 4 as a power coefficient of stress dependence in dislocation velocity [7,8].

The numerical results for iron based on the rate theory showed fairly good agreement with the experimental results. This fact also shows the applicability of the rate theory in this case.

It should be noted that the temperature dependence of log (da/dN) for 25Mn-5Cr-1Ni austenitic steel is much smaller than for SUS 304 stainless steel and other materials [3,4]. This may mean that the term $a_1\ln(\Delta K)$ including activation volume in Eq 4 is much larger in this case.

Fatigue Fracture Toughness

The microscopic mechanical condition at a fatigue crack tip is supposed to be different from the condition at an internal crack already contained in a specimen. Accordingly fatigue fracture toughness (K_{fc}), which is defined in terms of final crack length and maximum load, is not always the same as usual fracture toughness (K_c) under monotonic load [11,12]. In this study, K_{fc} was calculated by substituting into Eq 1 the mean value of final crack length measured at three points on a fractured surface. The fatigue fracture toughness is plotted as a funciton of temperature in Figs. 7*a* and 7*b*; a linear relation between K_{fc} and $1/T$ can be seen for each material. The slope of the linear relation of high-manganese steel is slightly steeper than that of SUS 304 steel.

The difference between these slopes implies that the temperature dependence of final resistance to fracture is slightly more sensitive for high-manganese steel than for SUS 304 steel. This difference will be explained by studying the differences in the mechanical condition at the crack tip, including microscopic considerations. Although the temperature dependence of K_{fc} for HAZ specimens is similar to that of WELD and BOND specimens (Fig. 7*b*), their slopes are different. This may be attributed in part to experimental scat-

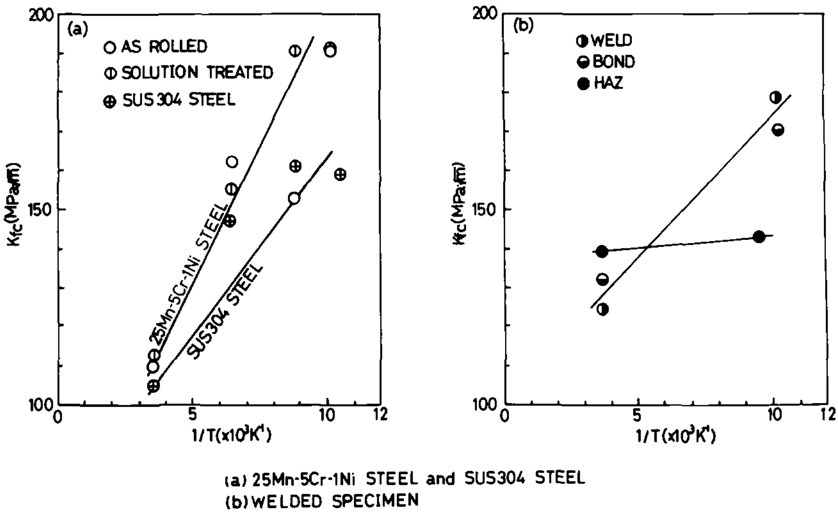

FIG. 7—*Temperature dependence of fatigue fracture toughness.*

ter. Also, the steepness of the slope corresponds to the severity of heating effects during welding. The reason for this will be left to future studies.

On the other hand, the slope is nearly horizontal for HAZ specimens. On the whole, K_{fc} values for high-manganese steel are higher than for SUS 304 steel. Since K_{fc} is a measure of the resistance of crack propagation to final fracture, it can be said that this resistance increases with decreasing temperature. Thus the resistance of high-manganese steel is a little higher than that of SUS 304 steel over the temperature range tested. In the case of welded specimens, the HAZ specimens did not show a distinct temperature dependence of this resistance.

Elastic-Plastic Fracture Toughness

It is interesting to study the relationship between K_{fc} and K_c, as it may be related to microscopic mechanisms at the crack tip and may provide some fundamental understanding. This relationship is also expected to offer a simple method of estimating K_{fc} by using K_c. Since the high-manganese steel used in this study was very ductile, the specimen thickness (B) did not satisfy the plane strain condition,

$$B \geqq 2.5 \left(\frac{K_{fc}}{\sigma_{ys}}\right)^2 \tag{6}$$

where σ_{ys} is yield strength. In such a case the use of elastic-plastic fracture toughness (J_{Ic}) is recommended by JSME standard S 001-1981, which corresponds to ASTM Test Method for J_{Ic}, a Measure of Fracture Toughness (E 813). According to the standard, the following condition must be satisfied:

$$B \geqq 25 \frac{J_{in}}{\sigma_{fs}} \tag{7}$$

where

J_{in} = J-integral when a crack starts to grow, J/m^2,
σ_{fs} = effective yielding point $\left(= \frac{\sigma_{ys} + \sigma_B}{2}\right)$, Pa, and
σ_B = tensile strength, Pa.

When Eq 7 is satisfied, J_{in} corresponds to J_{Ic}.

There are several methods for evaluating J_{in} at a crack tip. In this study, it was evaluated from the point of intersection of a blunting line and of a critical line. The former line was drawn through several points on a diagram of J versus stretched zone width (SZW) in which the J value was obtained by

$$J = \frac{A}{Bb_0} \times 2 \frac{1 + \beta}{1 + \beta^2} \tag{8}$$

where

$\beta = \left[\left(\frac{2a^*}{b_0}\right)^2 + 2\left(\frac{2a^*}{b_0}\right) + 2\right]^{1/2} - \left(\frac{2a^*}{b_0} + 1\right)$,
A = area surrounded by a load-displacement diagram, N·m, and
$b_0 = W - a^*$, m.

A critical line was drawn for the critical stretched zone width, which was measured on the surface after the fracture.

Figure 8 shows the temperature dependence of J_{Ic}, which was evaluated as described above. All these J_{Ic} values satisfied Eq 7. In principle, the following relation is not valid for these tests:

$$J = \frac{(1 - \nu^2)}{E} K^2 \tag{9}$$

where

ν = Poisson's ratio, and
E = Young's modulus, Pa.

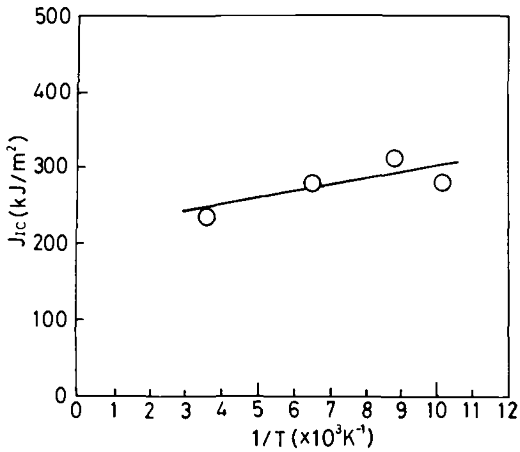

FIG. 8—*Temperature dependence of elastic-plastic fracture toughness.*

But we assume that Eq 9 is valid and calculate K_c using the J_{Ic} values in Eq 9, and compare the resulting values with K_{fc}. Figure 9 shows K_c as a function of temperature for as-rolled high-manganese steel. The linear relation between them can be seen, although there is some scatter at −175°C. This is similar to Fig. 7, but the K_c values are 1.5 times higher than the K_{fc} values. It is considered that this difference was caused by the plastic work which is included in K_c. Therefore the evaluation of K_c for K_{fc} will be an overestimation and is dangerous in practical engineering design.

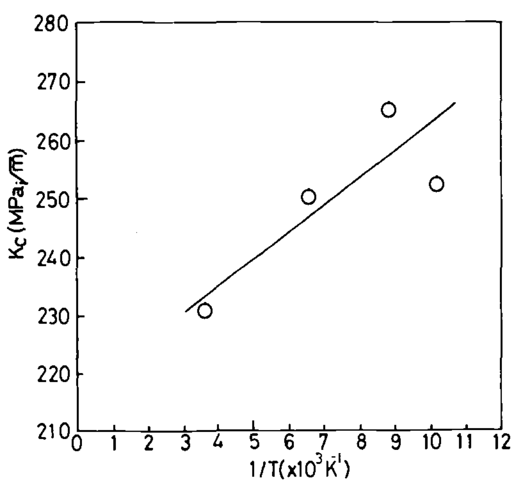

FIG. 9—*Temperature dependence of fracture toughness estimated from* J_{Ic}.

Conclusions

1. Fatigue life of the materials tested increases with decreasing test temperature from 0 to −174°C. Solution treatment seems not to have much effect on fatigue life.
2. The temperature dependence of the fatigue life of high-manganese steel is moderate within the range 0 to −174°C compared with that of SUS steel.
3. The fatigue life of welded specimens also increases at low temperatures.
4. When crack growth rate is expressed by the Paris relation [*6*], the power coefficient *n* of high-manganese steel is slightly lower than that of SUS steel and increases gradually with decreasing test temperature. The temperature dependence of the crack growth rate can be explained as a thermal activation process based on both microscopic and macroscopic treatment.
5. The linear dependence of the apparent activation energy of fatigue crack growth rate on the logarithm of the stress intensity factor range and the temperature dependence of *n* are also explained by dislocation dynamic theory of fatigue crack growth.
6. The fatigue fracture toughness of high-manganese steel is higher than that of SUS steel, especially at low temperature.
7. Elastic-plastic fracture toughness was evaluated by the *J*-integral. The estimated K_c from this *J*-integral is about 1.5 times higher than K_{fc} because plastic work is included in the former.

Acknowledgments

We gratefully acknowledge K. Suemune and H. Masumoto, Nippon Steel Corporation, for supplying materials and for their kind support.

APPENDIX

According to the theory described in the text [*7,8,13*], crack growth rate is expressed as

$$da/dN = 1.396\, m^{-1.45} b \left(\frac{A_1 \Delta K}{4\nu_0 f b \sqrt{\epsilon}\,\mu}\right)^{(m+1/m+2)} \exp\left[-\frac{\left[\dfrac{m+1}{m+2}\right] H_k \ln\left[\dfrac{\tau_{00}\sqrt{\epsilon}}{\Delta K}\right]}{4kT}\right] \tag{10}$$

Taking the logarithm of both sides of this equation,

$$\ln(da/dN) = \ln\left[1.396\, m^{-1.45} b \left(\frac{A_1}{4\nu_0 f b \sqrt{\epsilon}\,\mu}\right)^{(m+1/m+2)}\right] + \left(\frac{m+1}{m+2}\right) \ln(\Delta K)$$
$$-\frac{\dfrac{m+1}{4\,(m+2)} H_k \ln(\tau_{00}\sqrt{\epsilon}) - \dfrac{m+1}{4\,(m+2)} H_k \ln(\Delta K)}{kT} \tag{11}$$

where

$m = H_k/4kT$,
H_k = energy of kink,
$\tau_{00} = e^4\left[\frac{16}{\pi}\right]\tau_p{}^0$,
$\tau_p{}^0$ = Peierls force at 0 K,
μ = modulus of rigidity,
$\nu = A_1 \exp\left(-\frac{H}{kT}\right)$ = velocity of an isolated dislocation, and
$\nu_0 = 10^{-2}$ m/s.

Equation 4 is expressed more simply by using several constants, which are shown below:

$$a_1 = \frac{m+1}{4\,(m+2)} H_k$$

$$b_1 = \frac{m+1}{m+2}$$

$$A = 1.396\, m^{-1.45} b \left(\frac{A_1}{4\nu_0 f b\sqrt{\epsilon}\,\mu}\right)^{(m+1/m+2)}$$

$$U_2 = \frac{m+1}{4\,(m+2)} H_k \ln(\tau_{00}\sqrt{\epsilon})$$

Now, substituting

$T = 273$ K
$m = 3$ [13]
$H_k = 4.52 \times 10^{-20}$ J
$b = 2.48 \times 10^{-10}$ m
$\tau_{00} = 9.62 \times 10^{10}$ Pa
$f = 3.3$ Hz
$\epsilon = 1.5 \times 10^{-7}$ m
$\mu = 8.04 \times 10^{10}$ Pa

we obtain

$a_1 = 9.04 \times 10^{-21}$ J
$b_1 = 0.8$
$U_2 = 1.58 \times 10^{-19}$ J

These values are used in the calculation of *da/dN* in the text.

References

[1] Yoshimura, H., Masumoto, H., and Inoue, T., "Properties of Low-Carbon 25Mn-5Cr-1Ni Austenitic Steel for Cryogenic Use," *Advances in Cryogenic Engineering*, Vol. 28, Plenum Press, New York, 1982, pp. 115–125.

[2] McHenry, H. I. and Elmer, J. W., "Fracture Properties of a 25Mn Austenitic Steel and Its Welds at 4 K," *Austenitic Steels at Low Temperatures*, Plenum Press, New York, 1983, pp. 327–338.

[3] Sato, K., Yokobori, T., Igarashi, H., Nishida, S., and Masumoto, H., "Fatigue Crack Propagation Characteristic and Fatigue Fracture Toughness in 780-MPa Grade High-Strength Steel Weldments at Low Temperature," *Journal of the Japan Institute of Metals*, Vol. 47, No. 7, July 1983, pp. 596–602.

[4] Sato, K., Yokobori, T., Igarashi, H., Nishida, S., and Masumoto, H., "Fatigue Crack Propagation and Fatigue Fracture Toughness in 5.5%Ni Steel Weldments at Low Temperature," *Journal of the Japan Institute of Metals*, Vol. 47, No. 9, Sept. 1983, pp. 801–805.

[5] Brown, W. F., Jr. and Srawley, J. E. in *Plane-Strain Crack Toughness Testing of High-Strength Metallic Materials, ASTM STP 410*, American Society for Testing and Materials, Philadelphia, 1967, pp. 14–15.

[6] Paris, P. and Erdogan, F., *Transactions, Journal of Basic Engineering, Series D, American Society of Mechanical Engineering*, Vol. 85D, No. 4, Dec. 1963, pp. 528–534.

[7] Yokobori, T., Yokobori, A. T., Jr., and Kamei, A., "Dislocation Dynamics Theory for Fatigue Crack Growth," *International Journal of Fracture*, Vol. 11, 1975, pp. 781–788; Vol. 12, No. 4, Aug. 1976, pp. 519–520.

[8] Yokobori, T., Konosu, S., and Yokobori, A. T., Jr., "Micro and Macro Fracture Mechanics Approach to Brittle Fracture and Fatigue Crack Growth," *Proceedings*, International Conference of Fracture, Vol. 1, Pergamon Press, New York, 1978, pp. 665–682.

[9] Yokobori, T., "A Critical Evaluation of Mathematical Equations for Fatigue Crack Growth with Special Reference to Ferrite Grain Size and Monotonic Yield Strength Dependence," *Fatigue Mechanisms, ASTM STP 675*, American Society for Testing and Materials, Philadelphia, 1979, pp. 683–706.

[10] Yokobori, T. and Aizawa, T., "The Influence of Temperature and Stress Intensity Factor upon the Fatigue Crack Propagation Rate and the Striation Spacing in 304 Stainless Steel," *Journal of Japan Institute of Metals*, Vol. 39, No. 10, Oct. 1975, pp. 1003–1010.

[11] Yokobori, T. and Aizawa, T., "A Proposal for the Concept of Fatigue Fracture Toughness," *Reports of the Research Institute for Strength and Fracture of Materials*, Tohoku University, Vol. 6, No. 1, Nov. 1970, pp. 19–23.

[12] Kawasaki, T., Nakanishi, S., Sawaki, Y., Hatanaka, K., and Yokobori, T., "Fracture Toughness and Fatigue Crack Propagation in High Strength Steel from Room Temperature to −180°C," *Engineering Fracture Mechanics*, Vol. 7, No. 3, Sept. 1975, pp. 465–472.

[13] Yokobori, A. T., Jr., Yokobori, T., and Kamei, A., "Generalization of Computer Simulation of Dislocation Emission Under Constant Rate of Stress Application," *Journal of Applied Physics*, Vol. 46, No. 9, Sept. 1975, p. 3723.

R. I. Stephens, J. H. Chung, S. G. Lee, H. W. Lee, A. Fatemi, and C. Vacas-Oleas

Constant-Amplitude Fatigue Behavior of Five Carbon or Low-Alloy Cast Steels at Room Temperature and −45°C

REFERENCE: Stephens, R. I., Chung, J. H., Lee, S. G., Lee, H. W., Fatemi, A., and Vacas-Oleas, C., "**Constant-Amplitude Fatigue Behavior of Five Carbon or Low-Alloy Cast Steels at Room Temperature and −45°C,**" *Fatigue at Low Temperatures, ASTM STP 857,* R. I. Stephens, Ed., American Society for Testing and Materials, Philadelphia, 1985, pp. 140–160.

ABSTRACT: Five common carbon or low-alloy cast steels—SAE 0030, SAE 0050A, C-Mn, Mn-Mo and AISI 8630—were subjected to constant-amplitude fatigue tests at room temperature and at the common low climatic temperature of −45°C (−50°F). Tests included smooth specimen axial low and high cycle fatigue and compact type (CT) specimen crack growth behavior from 10^{-5} m/cycle (4×10^{-4} in./cycle) to threshold values at 10^{-10} m/cycle (4×10^{-9} in./cycle). Three of the five steels had nil ductility transition temperatures above the low test temperature. Despite this, all five cast steels showed equivalent or better fatigue resistance at the low temperature, except for some very short life low-cycle fatigue tests and for some very high fatigue crack growth rates where fracture was imminent. Scanning electron fractographic analysis indicated that ductile type fatigue crack growth mechanisms with or without striations occurred for all steels at both test temperatures except for a few interdispersed cleavage facets in 0050A steel at very high crack growth rates. At the low temperature, monotonic and cyclic stress-strain properties S_u, S_y, and S_y' increased by an average of about 10%, fatigue limits increased from 2 to 25%, and ΔK_{th} increased from 0 to 90%. No consistent correlations existed between fatigue and monotonic properties at either temperature. Mean stress effects at near ΔK_{th} levels appeared to be influenced by crack closure.

KEY WORDS: fatigue (materials), cast steel, low temperature, low and high cycle, crack growth, threshold, fractography, mechanisms, nil ductility transition

Nomenclature

a	Crack length, m
A	Coefficient for log-log linear da/dN-ΔK
da/dN	Crack growth rate, m/cycle

Dr. Stephens is a professor in the Mechanical Engineering Department of The University of Iowa in Iowa City, IA 52242. The other authors are all research assistants or former research assistants in the Materials Engineering Division, The University of Iowa.

b	Fatigue strength exponent
c	Fatigue ductility exponent
CVN	Charpy V-notch
CT	Compact type
E	Young's modulus, GPa
K	Stress intensity factor, MPa$\sqrt{m}$
ΔK	Stress intensity factor range, MPa$\sqrt{m}$
ΔK_{th}	Threshold stress intensity factor range, MPa$\sqrt{m}$
K'	Cyclic strain hardening coefficient
n	Exponent for log-log linear da/dN-ΔK
n'	Cyclic strain hardening exponent
N	Applied cycles
$2N_f$	Reversals to failure
NDT	Nil ductility transition
P_{min}	Minimum force, kN
P_{max}	Maximum force, kN
R	Load or stress ratio P_{min}/P_{max}
SEM	Scanning electron microscope
S_y	Yield strength, MPa
S_f	Fatigue limit, MPa
S_u	Ultimate tensile strength, MPa
S_y'	Cyclic yield strength, MPa
ϵ_f	True fracture strain
ϵ_f'	Fatigue ductility coefficient
$\Delta\epsilon_e$	Elastic strain range
$\Delta\epsilon_p$	Plastic strain range
$\Delta\epsilon$	Total strain range
σ_f	True fracture stress, MPa
σ_f'	Fatigue strength coefficient
σ_{max}	Maximum normal stress, MPa

Constant-amplitude low- and high-cycle fatigue behavior using smooth axial specimens and fatigue crack growth, and threshold behavior using compact type (CT) specimens were obtained for five carbon or low-alloy cast steels at room temperature and at the common low climatic temperature of −45°C (−50°F). The five cast steels were selected by the Carbon and Low Alloy Research Committee of the Steel Founders' Society of America, with the aid of input from about ten companies from the ground vehicle industry. The selected cast steels represent a wide range of steels commonly used in the ground vehicle industry.

Monotonic, cyclic, and fatigue behavior obtained at the two test temperatures were tensile stress-strain; Charpy V-notch impact energy; nil ductility transition (NDT) temperature; cyclic stress-strain; fully reversed low- and high-cycle fatigue in strain and load control, respectively, using smooth axial loaded specimens; and fatigue crack growth rate and threshold behavior with $R \approx 0$ and 0.5 using CT specimens. Both macrofractography and microfractography were used to contribute to a better understanding of low-temperature fatigue mechanisms.

Materials

The five cast steels chosen for this research were two normalized and tempered ferritic-pearlitic steels, SAE 0030 and SAE 0050A, and three normalized, quenched, and tempered martensitic steels, C-Mn, Mn-Mo, and AISI 8630. Heat treatment procedures are given in Table 1 and the resulting chemistry is given in Table 2. The cast steel microstructures are shown in Fig. 1. Both 0030 and 0050A steels have fine-grained (ASTM E 112, No. 8 or 9) microstructure, and all five cast steels contained normal inclusions and porosity and represent typical castings found in industry. All test specimens were machined from the castings. Additional details on pouring, heat treatment, microstructure, and machining can be found in Refs *1* to *3*.

The average monotonic tensile properties obtained from duplicate tests for each material are given in Table 3. Room temperature ultimate strengths for the five cast steels ranged from 496 to 1144 MPa. Thus the five cast steels investigated included a wide range of representative carbon and low-alloy cast steels. At −45°C, the yield strength (S_y) and the ultimate strength (S_u) increased on the average of 10%, while the true fracture ductility (ϵ_f) decreased from about 3 to 40%.

Standard Charpy V-notch (CVN) impact tests and standard drop weight tests were obtained for the five cast steels. The low test temperature, −45°C,

TABLE 1—*Cast steel heat treatment.*

Steel	Treatment	Time at Temperature, h	Temperature, °C
0030	normalize	0.5	900
	temper	1.5	677
0050A	normalize	4	900
	temper	4	650
C-Mn	normalize	3	900
	austenitize and water quench[a]	1	900
	temper	2.5	620
Mn-Mo	normalize	3	900
	austenitize and water quench	1	900
	temper[b]	2.5	682
8630	normalize	...	900
	austenitize and water quench	...	885
	temper	1.5	510

[a] Repeated twice to obtain complete austenitization.
[b] Four tempering temperatures between 552 and 682°C were used to avoid overtempering.

TABLE 2—*Cast steel chemistry (weight percent).*

Alloy	C	Mn	Si	S	P	Cr	Ni	Mo	Al
0030	0.24	0.71	0.44	0.026	0.015	0.10	0.10	0.08	0.06
0050A	0.49	0.93	0.61	0.023	0.024	0.11	0.08	0.04	0.08
C-Mn	0.23	1.25	0.39	0.028	0.036	0.10	0.09	0.04	0.02
Mn-Mo	0.34	1.32	0.40	0.035	0.024	0.11	0.11	0.22	0.06
8630	0.30	0.84	0.53	0.022	0.021	0.51	0.61	0.17	0.08

was in the lower shelf CVN region for 0030 and 0050A steels and in the low CVN transition region for C-Mn, Mn-Mo, and 8630 steels. The NDT temperatures are given in Table 3. The low test temperature was above the NDT temperature for C-Mn and Mn-Mo steels and below the NDT temperature for 0030, 0050A, and 8630 steels. The NDT temperature for 0050A was actually slightly above room temperature. Thus a wide range of NDT temperatures existed for these five cast steels. The greatest difference in the NDT temperatures existed between the ferritic-pearlitic 0050A steel and the tempered martensitic Mn-Mo steel. Hence the reports of most of the following low-temperature behavior and the ensuing discussion will focus on these two extreme cast steels.

Smooth Specimen Axial Fatigue

The specimen configuration used for the fully reversed low- and high-cycle axial fatigue tests is shown in Fig. 2. Specimens were polished with decreasing grades of emery cloth from 0 to 000 with final polishing scratches in the longitudinal direction. Tests were performed using an 89-kN closed-loop electrohydraulic test system. Low-temperature tests were conducted in an automated CO_2 temperature chamber. Low-cycle fatigue tests were performed in strain control with approximately 10^2 to 10^6 reversals to complete fracture. High-cycle fatigue tests were performed in load control with approximately 10^5 reversals to fracture and to run-outs at 2×10^7 reversals. Approximate half-life stable hysteresis loops were used to obtain the cyclic stress-strain curves, the steady-state elastic and plastic strain amplitudes, and the stress amplitudes. The elastic strain amplitude is

$$\frac{\Delta\epsilon_e}{2} = \frac{\Delta\sigma}{2E} \tag{1}$$

and the plastic strain amplitude is

$$\frac{\Delta\epsilon_p}{2} = \frac{\Delta\epsilon}{2} - \frac{\Delta\epsilon_e}{2} \tag{2}$$

where $\Delta\epsilon/2$ is the known controlled strain amplitude.

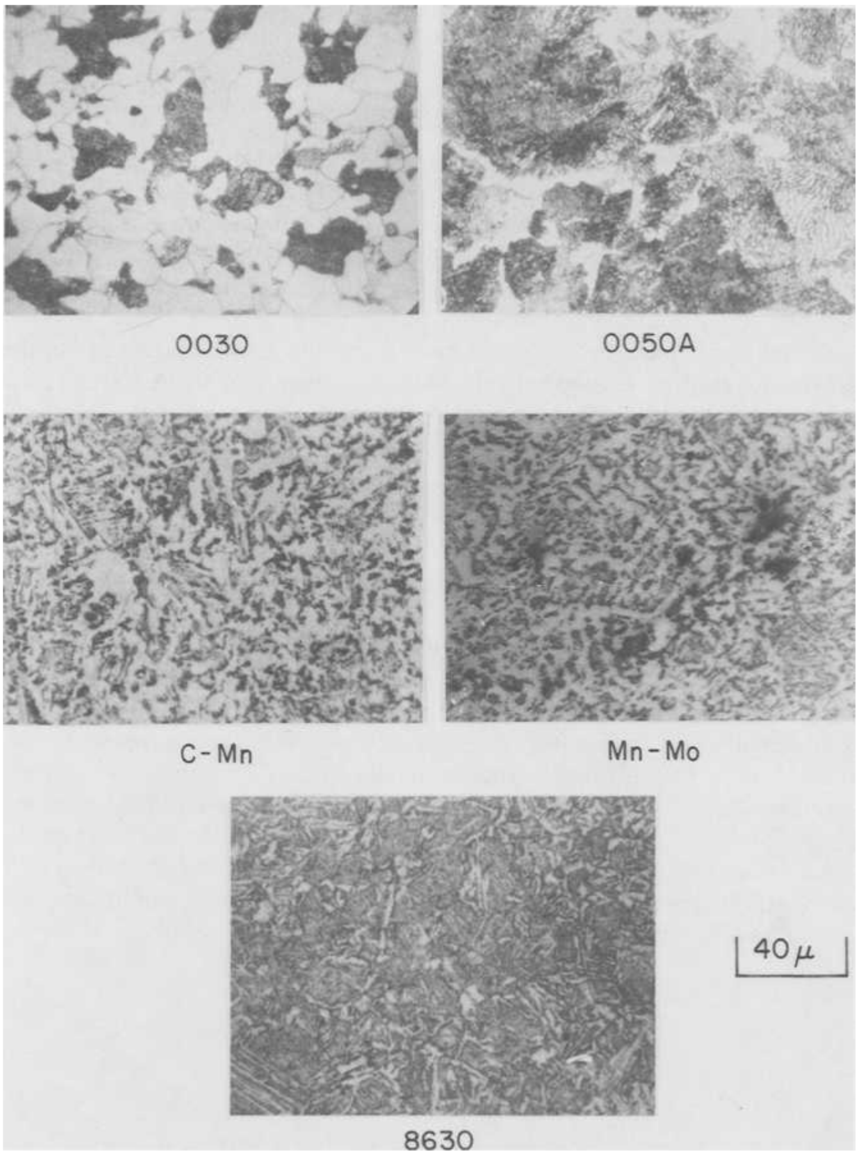

FIG. 1—*Cast steel microstructures* (×*500*).

TABLE 3—*Cast steel monotonic, cyclic, and axial fatigue properties.*

Parameter	0030 Steel (−29°C NDT)		0050A Steel (+27°C NDT)		C-Mn Steel (−57°C NDT)		Mn-Mo Steel (−62°C NDT)		8630 Steel (−29°C NDT)	
	R.T.[a]	−45°C	R.T.	−45°C	R.T.	−45°C	R.T.	−45°C	R.T.	−45°C
S_u, MPa	496	544	786	834	586	614	703	758	1144	1178
0.2% S_y, MPa	303	317	421	434	400	462	545	565	985	999
ϵ_f	0.62	0.36	0.21	0.17	0.34	0.26	0.38	0.36	0.35	0.33
0.2% S'_y, MPa	324	359	400	421	372	379	427	469	682	799
n'	0.136	0.116	0.171	0.117	0.141	0.139	0.096	0.105	0.122	0.095
K', MPa	738	731	1165	903	896	896	786	910	1502	1433
σ'_f, MPa	655	834	1338	1282	869	717	1117	1096	1936	1785
ϵ'_f	0.28	0.18	0.30	0.32	0.15	0.07	0.78	0.47	0.42	0.35
b	−0.083	−0.089	−0.127	−0.111	−0.101	−0.067	−0.101	−0.090	−0.121	−0.099
c	−0.552	−0.506	−0.569	−0.582	−0.514	−0.439	−0.729	−0.671	−0.693	−0.659
S_f, MPa	196	241	237	243	248	255	232	269	293	365
S_f/S_u	0.40	0.44	0.30	0.29	0.42	0.42	0.33	0.35	0.26	0.31

[a] Room temperature.

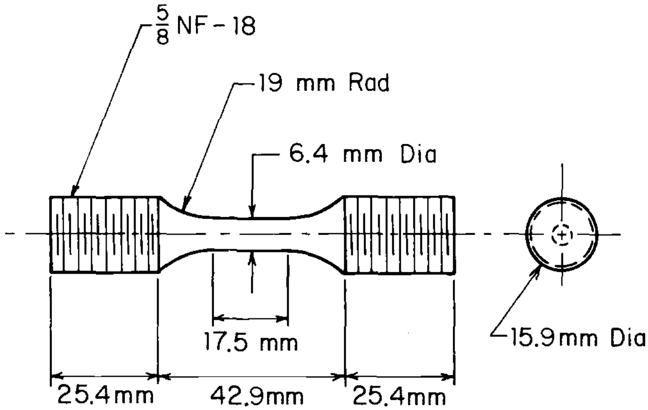

FIG. 2—*Axial fatigue specimen.*

Typical low-cycle fatigue hysteresis loops at −45°C are shown in Fig. 3 for 0030 cast steel. The first few cycles show the initial transient behavior (Fig. 3*a*), followed by a single steady-state hystersis loop (Fig. 3*b*), and then a series of transient hysteresis loops just before fracture (Fig. 3*c*). The results shown in Fig. 3 are typical of all low-cycle fatigue tests at both test temperatures. Figure 4 shows a plot of σ_{max} versus applied cycles at −45°C for 0050A and Mn-Mo steels under low-cycle fatigue conditions. Four or five representative continuous curves are shown for each steel with the strain amplitudes labeled on each curve. Additional data points indicate periodic readings taken from hysteresis loops or from the measurement amplitude panel. The results shown in Fig. 4 are typical for low-cycle fatigue tests at both test temperatures.

Cyclic stress-strain curves were obtained by connecting the tips of the strain-controlled hysteresis loops. These are superimposed on monotonic tensile stress-strain curves in the yield region in Fig. 5 for 0050A and Mn-Mo cast steels for both room temperature and −45°C. The upper yield point found in four of the five cast steels at both temperatures was eliminated under cyclic conditions (8630 has a continuous monotonic stress-strain curve). At larger strains, the cyclic curves intersect or tend to converge with the monotonic curves, except for 8630 steel. Thus 0030, and 0050A, and C-Mn cast steels cyclic strain–soften at the smaller strain levels and cyclic strain–harden at the larger strain levels for both test temperatures. For Mn-Mo and 8630 steels only cyclic softening existed. In general, the cyclic stress-strain curves were raised an average 10% at −45°C compared with room temperature; this increase is consistent with the monotonic stress-strain increases. The 0.2% cyclic yield strength (S_y'), the cyclic strain hardening exponent (n'), and the cyclic strain hardening coefficient (K') are given in Table 3 for both test temperatures.

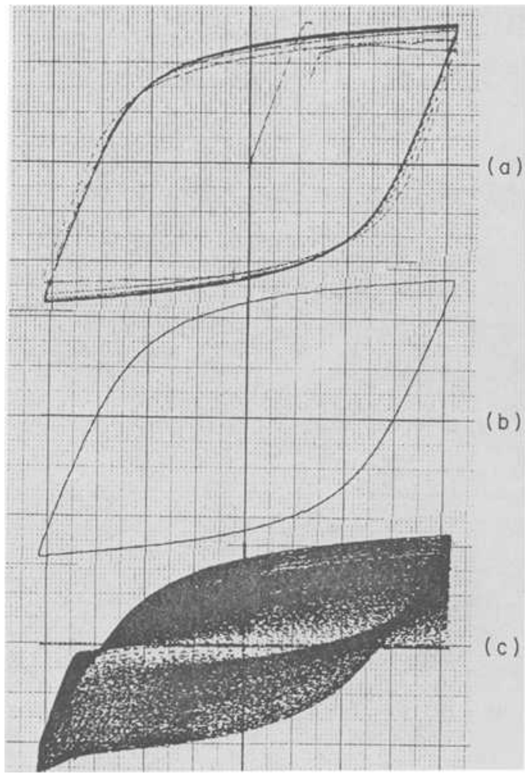

FIG. 3—*Low-cycle fatigue hysteresis loops at −45°C for 0030 cast steel.*

Both low- and high-cycle fatigue results are shown in Fig. 6 for 0050A and Mn-Mo steels at room temperature and −45°C. The low-cycle strain-control region includes the elastic, plastic, and total strain amplitudes, while the high-cycle load-control region (solid squares) includes only an elastic or total strain range obtained by dividing the controlled stress amplitude by Young's modulus (E). The low-cycle elastic and plastic components can be represented by straight line log-log equations as

$$\frac{\Delta\epsilon}{2} = \frac{\Delta\epsilon_e}{2} + \frac{\Delta\epsilon_p}{2} = \frac{\sigma_f'}{E}(2N_f)^b + \epsilon_f'(2N_f)^c \tag{3}$$

Values of σ_f', ϵ_f', b, and c were obtained with a least-square computer analysis and are given in Table 3 for the five cast steels at both test temperatures. All five cast steels exhibited typical fatigue limits around 5×10^6 to 10^7 reversals for both test temperatures. The fatigue limit (S_f) taken at 2×10^7 reversals and the fatigue ratio (S_f/S_u) are also given in Table 3 for both test temperatures.

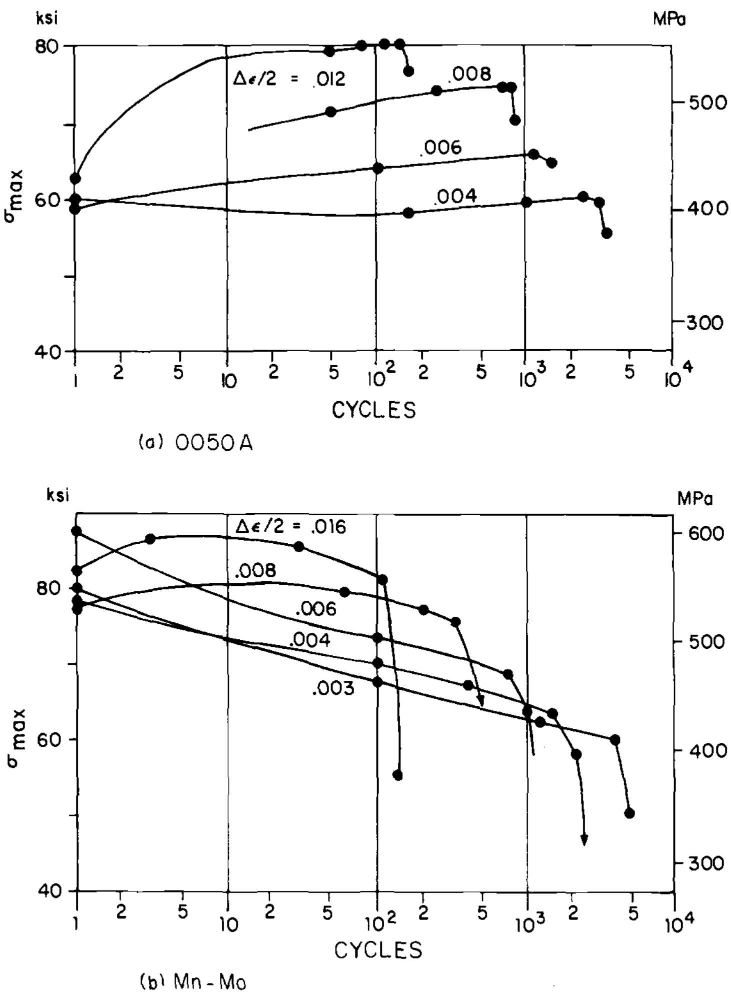

FIG. 4—σ_{max} *versus applied cycles at −45°C for 0050A and Mn-Mo cast steels.*

The fatigue curves of Fig. 6 and the data in Table 3 do not adequately show the low temperature effect on fatigue resistance of the five cast steels. The total strain versus life curves have thus been superimposed in Fig. 7 for each cast steel for proper comparison. The solid curves in Fig. 7 represent room temperature behavior and the dashed curves are for −45°C. Since these are log-log curves, differences in behavior are less evident. At longer lives ($>10^6$ reversals) the strain amplitudes and fatigue limits are between 2 and 25% higher at the low temperature for a given cast steel. This increase is in agreement with smooth specimen fatigue limits found by others for most wrought steels and other alloys [*4–7*]. At the shorter lives, mixed results occurred such that in some cases the low temperature was slightly beneficial,

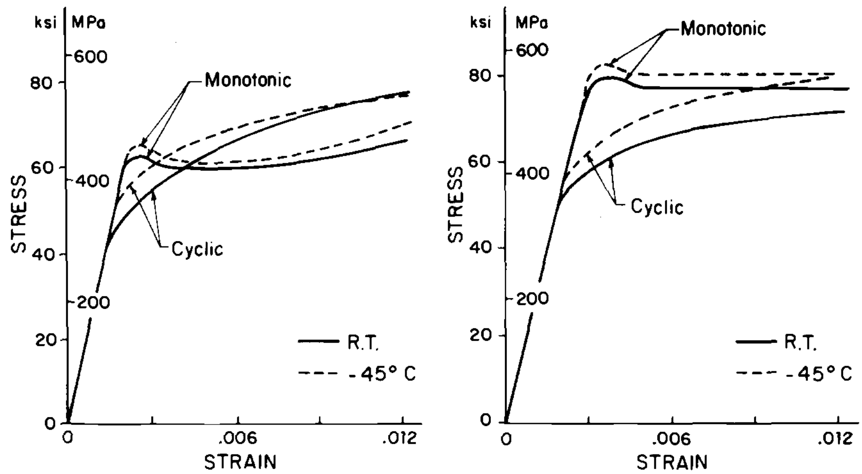

FIG. 5—*Monotonic and cyclic stress-strain behavior at room temperature and −45°C for 0050A and Mn-Mo cast steels.*

detrimental, or had little influence. This is also in agreement with the limmited data on low-temperature, low-cycle fatigue behavior available in the literature.

Fatigue Crack Growth and Thresholds

Compact type specimens (Fig. 8) were used for all fatigue crack growth tests. The three-hole configuration was used in conjunction with a monoball gripping system that allows only axial ram loading. Specimen thickness was 8.2 mm. ASTM Test for Constant-Load-Amplitude Fatigue Crack Growth Rates Above 10^{-8} m/Cycle (E 647) was followed for crack growth rates above about 10^{-8} m/cycle, while the proposed ASTM incremental load shedding procedure [*8*] was used as the principal guide for threshold and near-threshold tests. Tests were run with the load ratio $R = P_{min}/P_{max}$ set at approximately 0 (0.015 to 0.04) and 0.5 for high crack growth rate tests, and with R equal to 0.05 and 0.5 for threshold and near-threshold tests. Cracks were monitored using a ×33 magnification traveling telescope with a least reading of 0.01 mm (0.0004 in.). For low-temperature tests, the cracks were monitored through the glass window of the temperature chamber. Loads were applied using a sine wave with a frequency between 10 and 40 Hz depending upon load range and crack length. Two to four test specimens were run for each test condition for $da/dN \gtrsim 10^{-8}$ m/cycle, while a single specimen was sufficient to obtain threshold and near-threshold data for one or two test conditions. Incremental load shedding steps ranged from 2 to 10% reductions, with the smaller steps taken closer to the threshold levels. Crack extension for a given step was between 0.25 and 0.5 mm. To make sure fatigue crack growth retardation did not occur during the decreasing ΔK tests,

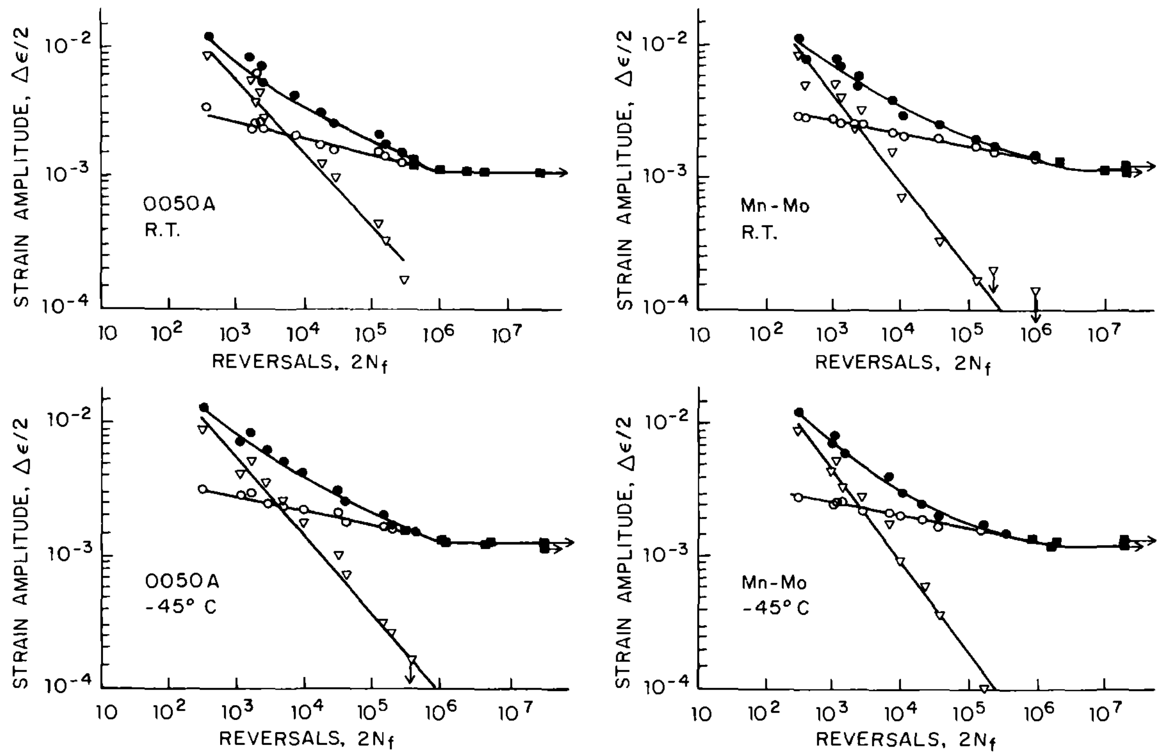

FIG. 6—*Axial fatigue behavior at room temperature and −45°C for 0050A and Mn-Mo cast steels.*

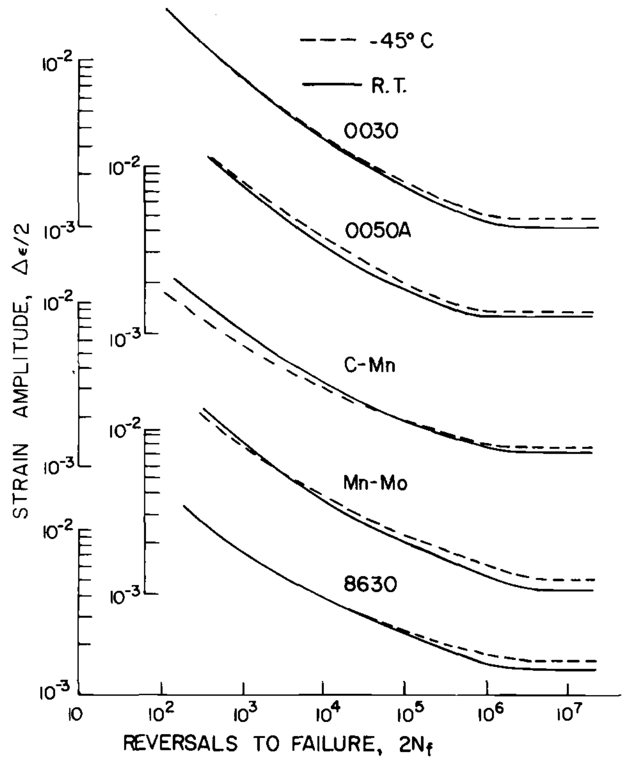

FIG. 7—*Composite strain versus life curves at room temperature and −45°C for five cast steels.*

an increasing ΔK test was often run after the required ΔK_{th} was obtained. These results were very consistent with decreasing ΔK results.

The crack growth rates for $da/dN \gtrsim 10^{-8}$ m/cycle were obtained using an incremental polynomial while near-threshold crack growth rates were obtained using the secant method and the crack extension per increment of applied cycles. The total data for a given material, R ratio, and temperature were reduced; typical results for 0050A and Mn-Mo cast steels are shown in Fig. 9. Both $R \approx 0$ and 0.5 are shown.

The da/dN versus ΔK data plotted on log-log coordinates have an approximate linear behavior above the threshold region, which can be represented by

$$\frac{da}{dN} = A(\Delta K)^n \tag{4}$$

Values of A and n along with ΔK_{th} are given in Table 4. From Fig. 9 and Table 4, it can be seen that the da/dN versus ΔK data for different R ratios and temperatures tend to converge and even overlap at the higher crack

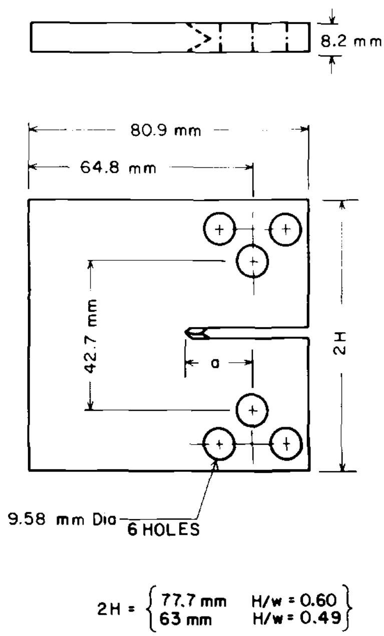

FIG. 8—*Compact type (CT) fatigue crack growth specimen.*

growth rates. For a given R ratio and material, values of n were always greater at low temperature compared to room temperature. At the lower crack growth rates and the threshold or near-threshold conditions, substantial divergence exists. Here it is seen that da/dN was generally lower and ΔK_{th} was generally higher at −45°C than at room temperature. At the low temperature, ΔK_{th} values increased 0 to 90% compared with room temperature. The two lower-strength cast steels, 0030 and C-Mn, showed the greatest increases in ΔK_{th} at −45°C, while the highest-strength cast steel, 8630, showed the smallest increase. These data indicate that a general improved fatigue crack growth resistance occurred at −45°C for these five cast steels; these data are consistent with the smooth specimen axial fatigue behavior.

For a given material, test temperature, and ΔK value, the crack growth rates for $R = 0.5$ were generally higher than for $R \approx 0$. The ΔK_{th} values at $R = 0.5$ were approximately one half the values for $R \approx 0$. This difference can be reasonably attributed to crack closure, since limited crack opening load measurements taken at near-threshold regions with $R \approx 0$ occurred at approximately $P_{max}/2$. This concept is also reinforced by the great amount of fretting often found in the near-threshold tests for $R \approx 0$. Insufficient crack closure loads were taken, however, to attribute the low-temperature crack growth resistance improvements solely to crack closure, as has been done by others [*9,10*].

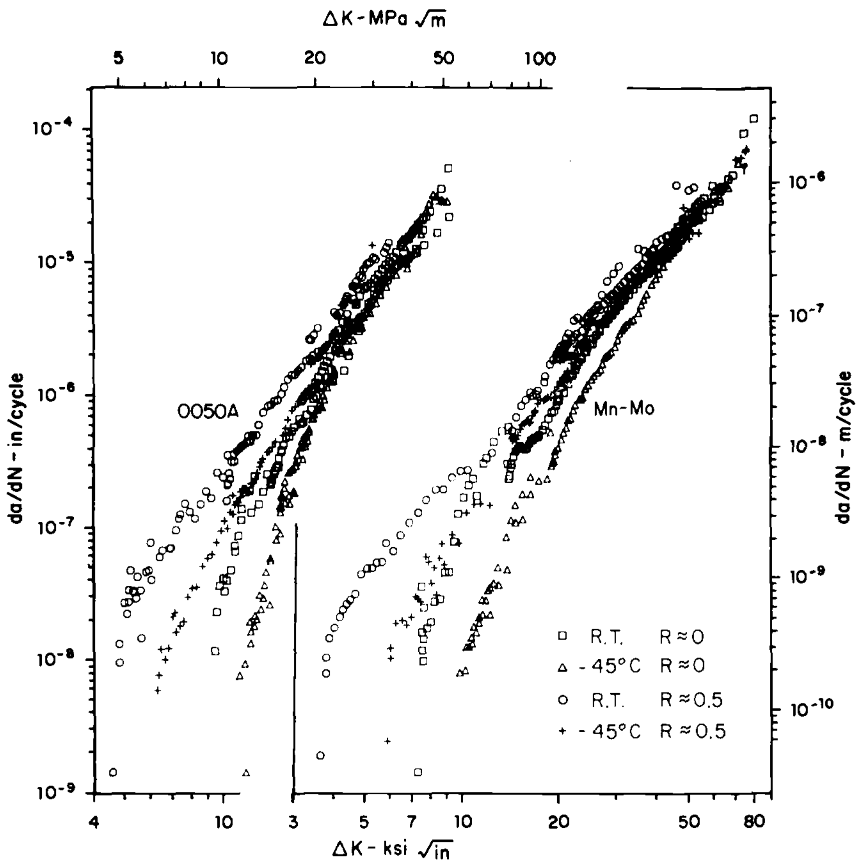

FIG. 9—*Composite* da/dN *versus* ΔK *at room temperature and −45°C for 0050A and Mn-Mo cast steels.*

Discussion

The low-temperature tests were performed below the NDT temperature for 0030, 0050A, and 8630 steels. The low temperature was also in the lower shelf CVN impact energy region for 0030 and 0050A steels and in the lower transition region for the other three steels. Nevertheless, the low-temperature constant-amplitude fatigue resistance of these five cast steels, as determined from smooth specimen axial low- and high-cycle fatigue tests and from complete *da/dN* versus ΔK curves, was generally either equivalent to or better than fatigue resistance at room temperature. The only decrease in fatigue resistance at low temperature occurred in a few of the very short low-cycle fatigue tests and with some of the very high fatigue crack growth rates where final fracture was essentially imminent. The above general behavior suggests that for these five cast steels the NDT temperature is not a possible fatigue

TABLE 4—*Fatigue crack growth,* $da/dN = A(\Delta K)^n$, *and threshold,* ΔK_{th}, *properties.*

Parameter	0030 R.T.[a]	0030 −45°C	0050A R.T.	0050A −45°C	C-Mn R.T.	C-Mn −45°C	Mn-Mo R.T.	Mn-Mo −45°C	8630 R.T.	8630 −45°C
					***R* ≈ 0**					
$A\left(\frac{m/cycle}{MPa\sqrt{m}}\right)$	3.34×10^{-14}	3.48×10^{-15}	2.24×10^{-13}	1.79×10^{-14}	7.74×10^{-13}	5.4×10^{-14}	1.12×10^{-12}	9.76×10^{-14}	2.63×10^{-12}	6.38×10^{-13}
n	4.33	4.72[b]	3.88	4.53	3.35	4.01	3.28	3.84	3.03	3.38
ΔK_{th}, MPa$\sqrt{m}$	9.1	14.2	10.2	12.3	8.3	14.4	8.1	10.7	9.4	9.4
					***R* ≈ 0.5**					
$A\left(\frac{m/cycle}{MPa\sqrt{m}}\right)$	...	...	1.99×10^{-12}	8.36×10^{-14}	2.34×10^{-12}	6.36×10^{-13}	7.15×10^{-12}	3.13×10^{-12}	1.39×10^{-11}	1.97×10^{-12}
n	...	...	3.40	4.30	3.21	3.52	2.89	3.04	2.67	3.22
ΔK_{th}, MPa$\sqrt{m}$	5.3	9.3	5.2	6.8	3.9	7.1	4.1	6.5	4.1	5.7

[a] Room temperature.
[b] −34°C for 0030 steel.

transition temperature; the NDT temperature can be considered as a conservative design temperature above which constant-amplitude fatigue resistance should be equal to or better than fatigue resistance at room temperature. A transition from beneficial to detrimental fatigue crack growth resistance, accompanied by a transition from ductile mechanisms to cleavage, appears to exist in steels significantly below the NDT temperature [*6,11–13*].

A macrofractographic and microfractographic analysis was made on the five cast steels for the smooth specimen axial tests and the CT specimen crack growth tests for both temperatures. The SEM analysis of the axial fatigue specimens showed substantial crack growth occurred before fracture. Many of the fracture surfaces exhibited severe rubbing damage and roughness because of the compressive loads. Multicrack initiation sites were often observed on specimens tested at low strain amplitudes, while crack origins were less clearly identifiable at the high strain amplitudes. Cracks initiated at or near the surface for both temperatures often involved inclusions or porosity.

The macrofractographic appearances for both $R \approx 0$ and 0.5 were similar for the $da/dN \gtrsim 10^{-8}$ m/cycle crack growth tests for a given material and temperature. For the threshold and near-threshold tests, however, the $R \approx 0$ surfaces often exhibited appreciable fretting damage, which indicates the greater importance of crack closure at these low ΔK values. In all tests, a flat Mode 1 fatigue crack growth region existed. In many cases the smooth fatigue crack growth region became rougher at longer crack lengths with high values of ΔK, but still remained essentially Mode 1 cracks. The final fracture regions showed:

1. Substantial necking and ductile fracture (dimples) at both temperatures for C-Mn and Mn-Mo steels.
2. Substantial necking, shear lips, and ductile fracture (dimples) at room temperature and brittle fracture (cleavage) at low temperature for 0030 and 8630 steels.
3. Brittle fracture (cleavage) at both temperatures for 0050A steel.

Representative fatigue crack growth SEM fractographs for 0050A and Mn-Mo steels are shown in Fig. 10 for $R \approx 0$ at both temperatures and for both higher da/dN values and near-threshold conditions. Cracks grew from the bottom to the top in Fig. 10. Fatigue striation bandings were readily found only in the log-log linear region for 0030 steel at both temperatures; this trend was somewhat true for the 0050A steel at both temperatures. For the other cast steels and for all near-threshold tests, very few distinct striations could be found. Some did exist, but in general the surfaces contained more of a ductile mode or quasistriation surface (Fig. 10). In all five cast steels, the SEM analysis revealed a ductile type transcrystalline fatigue crack growth behavior at both temperatures. However, some mixed ductile and

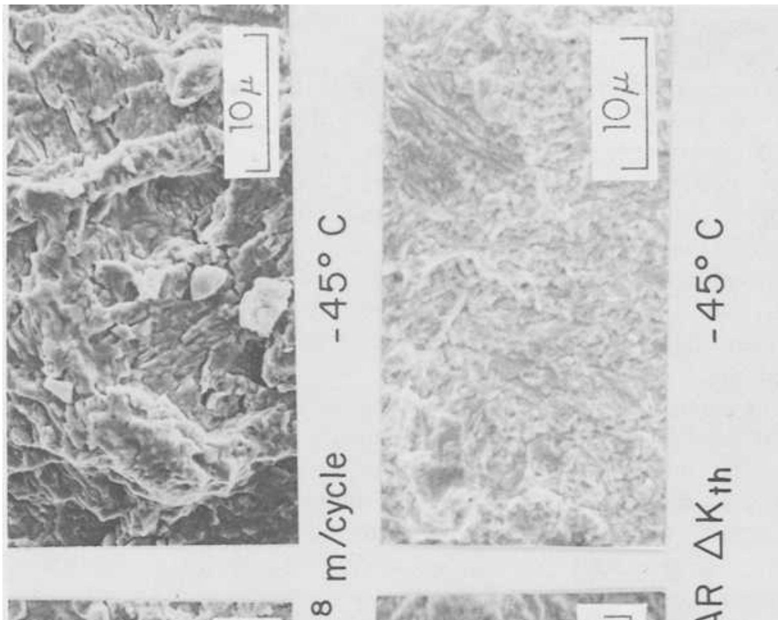

(a) 0050 A

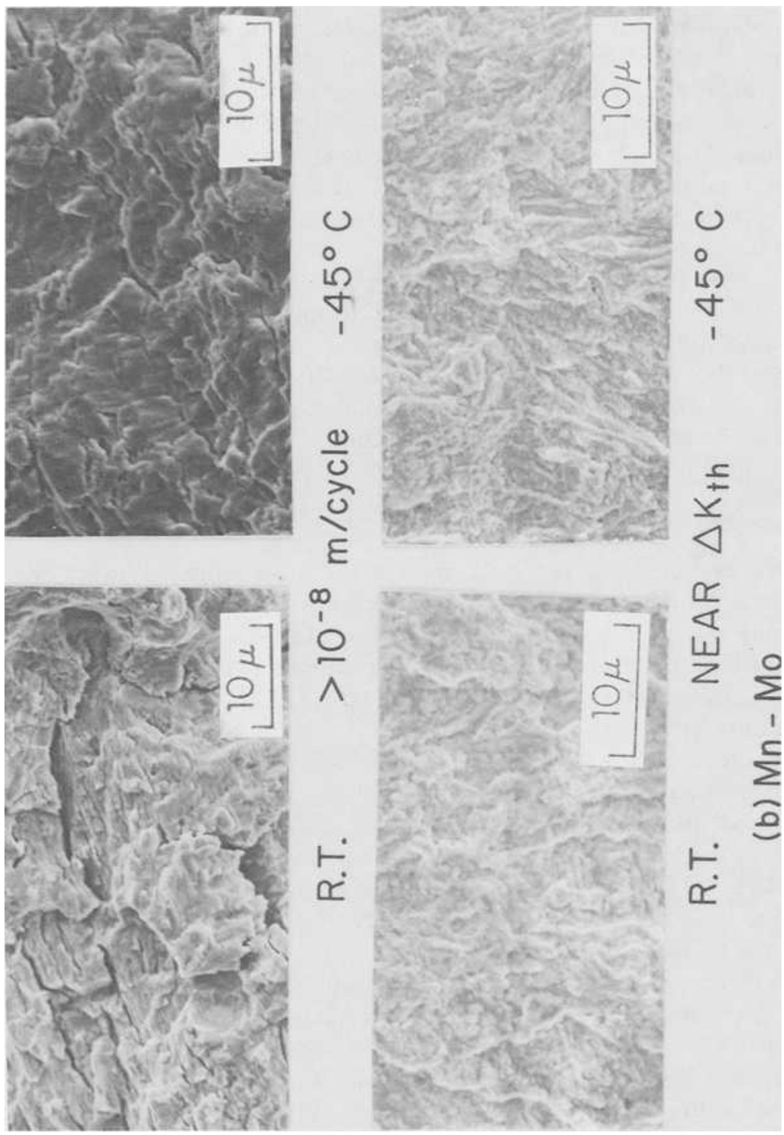

FIG. 10—*SEM fractographs with* da/dN > 10^{-8} *m/cycle and at near thresholds at room temperature and* $-45°C$ *for 0050A and Mn-Mo cast steels.*

cleavage regions became evident in 0050A steel at the low temperature at the long crack lengths and hence at the highest ΔK values. Secondary microcracking, voids, and inclusions were common for all test conditions. In general, however, the fatigue crack growth mechanisms for each cast steel were essentially the same at both temperatures. No brittle microscopic growth behavior was observed at either temperature except for 0050A steel at −45°C with longer crack lengths approaching final fracture. The similarity of the fractographic results indicate why the low temperature was not detrimental to the constant-amplitude fatigue crack growth behavior. Under variable-amplitude loading, however, the −45°C temperature was shown to be detrimental to fatigue crack growth life [*3,14*]. Thus constant-amplitude testing may not indicate the entire effect of low temperature on fatigue crack growth behavior.

The fatigue properties obtained in this research (i.e., σ_f', ϵ_f', b, c, S_f, da/dN versus ΔK, and ΔK_{th}) could not be related to specific monotonic properties such as S_y, S_u, σ_f and ϵ_f. For steels, ΔK_{th} has often been shown to vary inversely with S_f, S_y or S_u [*15*], while S_f has often been shown to increase with S_u [*4,5,7*]. None of these generalizations were evident in this research for these five cast steels at either temperature.

Summary and Conclusions

1. The monotonic upper yield point stress was eliminated under cyclic stress-strain conditions at both test temperatures. Cyclic softening and/or hardening existed at both room temperature and −45°C.

2. The monotonic and cyclic stress-strain curves, and thus S_y, S_u and S_y', increased by an average of about 10% at −45°C compared with room temperature.

3. In the low-cycle fatigue region, the fatigue curves at the two test temperatures tended to converge or intersect at large strain amplitudes, thus giving small mixed fatigue life differences in this region. At the longer lives the curves tended to diverge resulting in 2 to 25% increases in the fatigue limit (S_f) at −45°C. The fatigue ratio (S_f/S_u) increased slightly from a range of 0.26 to 0.42 at room temperature to 0.29 to 0.44 at −45°C.

4. Fatigue crack growth rates for both $R \approx 0$ and 0.5 at −45°C were equivalent to or lower than those at room temperature for a given ΔK, except for very high crack growth rates near imminent fracture. Thus the log-log linear exponent (n) was always greater at the low temperature compared to its value at room temperature. At −45°C, ΔK_{th} values increased from 0 to 90% compared with room temperature values, with the two lower-strength steels showing the greatest improvement.

5. The value of ΔK_{th} at $R = 0.5$ was approximately 50% of ΔK_{th} at $R \approx 0$. This mean stress effect in these cast steels appears to be related to crack closure.

6. Ductile type transcrystalline fatigue crack growth occurred for all five cast steels at both test temperatures. Fatigue striations, however, were only appreciably evident in the ferritic-pearlitic 0030 and 0050A steels at both temperatures with $da/dN \gtrsim 10^{-8}$ m/cycle. No striations were commonly evident in the near-threshold regions for all tests.

7. Ductile type transcrystalline fatigue crack growth behavior and generally improved fatigue resistance occurred at the low temperature, even though three of the five cast steels had NDT temperatures above the low test temperature, and the low test temperature was in the lower shelf CVN impact energy region for two steels and in the lower transition CVN region for the other three steels. Thus the NDT temperature and the CVN ductile-brittle transition temperature does not predict possible ductile-brittle transitions in constant-amplitude fatigue crack growth behavior for these five cast steels. The NDT temperature, however, can be used as a conservative criterion in design for fatigue ductile-brittle transitions.

8. Final fracture regions at −45°C showed that cleavage fracture for 0030, 0050A, and 8630 cast steels and hence low-temperature fatigue crack growth mechanisms can differ significantly from final fracture mechanisms.

Acknowledgments

The authors would like to thank the Steel Founders' Society of America, The University of Iowa, and contributing companies who financially sponsored this research.

References

[1] Stephens, R. I., "Fatigue and Fracture Toughness of Five Carbon or Low Alloy Cast Steels at Room and Low Climatic Temperatures," Research Report 94A, Steel Founders' Society of America, Des Plaines, IL, Oct. 1982.

[2] Stephens, R. I., "Fatigue and Fracture Toughness of Five Carbon or Low Alloy Cast Steels at Room and Low Climatic Temperatures," Research Report 94B, Steel Founders' Society of America, Des Plaines, IL, May 1983.

[3] Stephens, R. I., Chung, J. H., Fatemi, A., Lee, H. W., Lee, S. G., Vacas-Oleas, C., and Wang, C. M., "Constant- and Variable-Amplitude Fatigue Behavior of Five Cast Steels at Room Temperature and −45°C," *ASME Journal of Materials and Technology*, Vol. 106, No. 1, Jan. 1984, p. 25.

[4] Forrest, P. G., *Fatigue of Metals*, Pergamon Press, New York, 1962.

[5] Mann, J. Y., *Fatigue of Materials*, Melbourne University Press, Melbourne, Australia, 1967.

[6] Stephens, R. I., Chung, J. H., and Glinka, G., "Low Temperature Fatigue Behavior of Steels—A Review", Paper 790517, *SAE Transactions*, Vol. 88, 1980, p. 1982.

[7] Fuchs, H. O. and Stephens, R. I., *Metal Fatigue in Engineering*, Wiley Interscience, New York, 1980.

[8] Bucci, R. J., "Development of a Proposed Standard Practice for Near Threshold Fatigue Crack Growth Measurement," in *Fatigue Crack Growth Measurement and Data Analysis, ASTM STP 738*, American Society for Testing and Materials, Philadelphia, 1981, p. 5.

[9] Esaklul, K. A., Yu, W., and Gerberich, W. W., "The Effect of Geometric Closure on Threshold Stress Intensities at Low Temperatures," in *Fatigue at Low Temperatures, ASTM STP 857*, R. I. Stephens, Ed., American Society for Testing and Materials, Philadelphia, 1985, p. 63.

[10] Jata, K. V., Gerberich, W. W., and Beevers, C. J., "Low-Temperature Fatigue Crack Propagation in a β-Ti Alloy," in *Fatigue at Low Temperatures, ASTM STP 857*, R. I. Stephens, Ed., American Society for Testing and Materials, Philadelphia, 1985, p. 102.
[11] Gerberich, W. W. and Moody, N. R., "A Review of Fatigue Fracture Topology Effects on Threshold and Kinetic Mechanism," in *Fatigue Mechanisms, ASTM STP 675*, J. Fong, Ed., American Society for Testing and Materials, Philadelphia, 1979, p. 292.
[12] Tobler, R. L. and Reed, R. P., "Fatigue Crack Growth Resistance of Structural Alloys at Cryogenic Temperatures," in *Advances in Cryogenic Engineering*, Vol. 24, K. D. Timmerhaus, R. P. Reed, and A. F. Clark, Eds., Plenum Press, New York, 1978, p. 82.
[13] Kawasaki, T., Yokobori, T., Sawaki, Y., Nakanishi, S., and Izumi, H., "Fatigue Fracture Toughness and Fatigue Crack Propagation in 5.5% Ni Steel at Low Temperature," in *Fracture 1977, ICF-4*, Vol. 3, University of Waterloo Press, Waterloo, Ont., Canada, June 1977, p. 857.
[14] Stephens, R. I., Fatemi, A., Lee, H. W., Lee, S. G., Vacas-Oleas, C., and Wang, C. M., "Variable-Amplitude Fatigue Crack Initiation and Growth of Five Carbon or Low-Alloy Cast Steels at Room and Low Climatic Temperatures," in *Fatigue at Low Temperatures, ASTM STP 857*, R. I. Stephens, Ed., American Society for Testing and Materials, Philadelphia, 1985, p. 293.
[15] Bäcklund, J., Blom, A. F., and Beevers, C. J., Eds., *Fatigue Thresholds Fundamentals and Engineering Applications*, Engineering Materials Advisory Services Ltd., U.K., 1982.

Spectrum Loading, Structures, and Applications

Cryogenic Temperatures

J. M. Toth, Jr., W. J. Bailey, and D. A. Boyce

Fiberglass Epoxy Laminate Fatigue Properties at 300 and 20 K

REFERENCE: Toth, J. M., Jr., Bailey, W. J., and Boyce, D. A., "**Fiberglass Epoxy Laminate Fatigue Properties at 300 and 20 K**," *Fatigue at Low Temperatures, ASTM STP 857*, R. I. Stephens, Ed., American Society for Testing and Materials, Philadelphia, 1985, pp. 163–172.

ABSTRACT: A subcritical liquid hydrogen orbital storage and supply experiment is being designed for flight in the Space Shuttle cargo bay. The Cryogenic Fluid Management Experiment (CFME) includes a liquid hydrogen tank supported in a vacuum jacket by two fiberglass epoxy composite trunnion mounts. The ability of the CFME to last for the required seven missions depends primarily on the fatigue life of the composite trunnions at cryogenic temperatures. To verify the trunnion design and test the performance of the composite material, fatigue property data at 300 and 20 K were obtained for the specific E-glass fabric/S-glass unidirectional laminate that will be used for the CFME trunnions. The fatigue life of this laminate was greater at 20 K than at 300 K, and was satisfactory for the intended application.

KEY WORDS: composite materials, glass fiber, epoxy resin, room temperature properties, cryogenic properties, fatigue

Future space missions will require the use of cryogenic liquids for propulsion, life support, power generation, sensor cooling, and thermal control, and reactants for experiment or process consumables. Storing and supplying subcritical (liquid) rather than supercritical (gaseous) cryogens offer advantages in weight savings. These savings result from the lower pressures associated with subcritical storage, which are reflected in thinner gage tanks and plumbing. Reduced weight and resulting loads and stress require lighter weight support mounts, leading to trade-offs between structural safety factors and thermal heat leak considerations. These trade-offs multiply as support cross-sectional areas increase. The Cryogenic Fluid Management Experiment (CFME), shown in Fig. 1, is such a system. The low heat-leak requirement, as part of the thermal control design, led to the use of fiberglass/epoxy trunnions as structural supports for the tank.

The ability of the CFME to last for the required seven missions depends

Mr. Toth is the manager of composites technology, Mr. Bailey a staff engineer, and Mr. Boyce a senior engineer with Martin Marietta Corp., Denver, CO 80201.

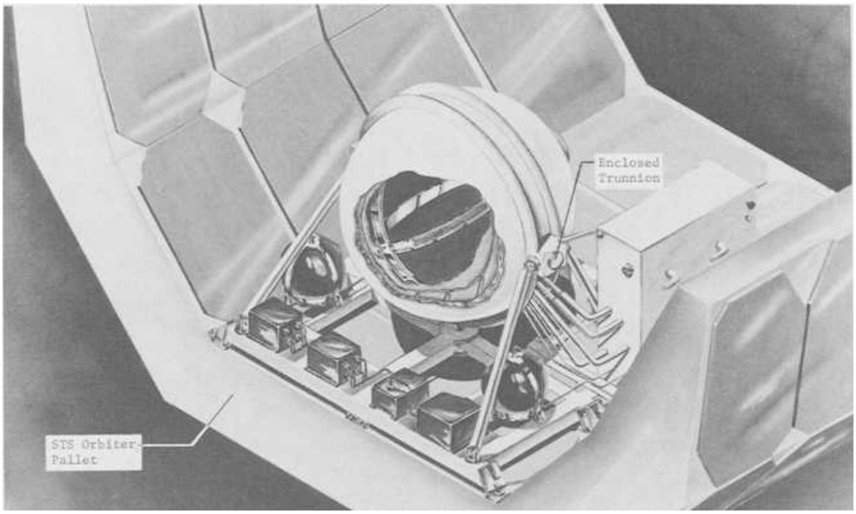

FIG. 1—*Cryogenic Fluid Management Experiment.*

primarily on the fatigue life of the composite trunnions at cryogenic temperatures. Because of the limited availability of analytical or experimental treatments of the fatigue life of composites at cryogenic temperatures [*1*], an experimental program was initiated to verify the trunnion design and to determine the performance characteristics of the composite material. A full description of the trunnion design and test program is provided in Ref *2*. The fatigue testing of the selected fiberglass laminate is discussed here.

Laminate Design

The design of the laminate was based on thermal, stiffness, and strength requirements. The laminate design selected was ($-45°/0°_3/+45°/0°_3/+45°/-45°/0°_3/+45°/0°_3/-45°$), where the 45°-material is Style No. 1581 E-glass fabric at a cured thickness of 0.023 cm/ply and the 0°-material is S2 unidirectional glass fibers at a cured thickness of 0.030 cm/ply. The epoxy matrix was Fiberite Corporation's 934 resin system. Fiber volume and void content of the laminate test panel, based on five test samples, were 61% and 2.2%, respectively. The laminate was balanced to avoid inplane coupling effects. The laminate was not symmetrical, but because the Style No. 1581 fabric was only slightly unbalanced with respect to warp and fill modulus (i.e., $E_{\text{fill direction}} = 95\% \, E_{\text{warp direction}}$), and the asymmetric plies were grouped about the centerline, the coupling between inplane and bending response was minimized. The coupling in the fabricated trunnion would be less significant because of the closed, cylindrical section.

Test Specimen Design

The design of fatigue test specimens in a flat configuration was a complex issue and underwent several modifications before an acceptable configuration was established. Little information was available in the literature on fiberglass epoxy composite fatigue specimen designs suitable for use at both 300 and 20 K with fully reversed ($R = -1.0$) tension-compression loading. The proposed design evolved from the following considerations or criteria:

- The specimen/test machine interface had to be compatible to minimize buckling on the compression part of the cycle.
- The specimen gage section cross-sectional area had to be compatible with the existing liquid hydrogen cryostat and fatigue fixture capacities.
- The specimen end configuration and machine attaching had to minimize alignment complexities.

Figure 2 shows the selected configuration of the test specimen. Fiberglass tabs, fabricated of $(0/90)_s$ laminates of unidirectional S2-glass, were bonded to the ends of the specimens with American Cyanamid Corporation FM-1000 adhesive. The 0°-orientation laminae were aligned with the x-direction of the test specimen laminate. The overall specimen length and gage section were minimized to prevent buckling during specimen compression. A four-bolt attachment interfaced with the test fixture and aligned the centerline of the coupon with the load line of the test machine.

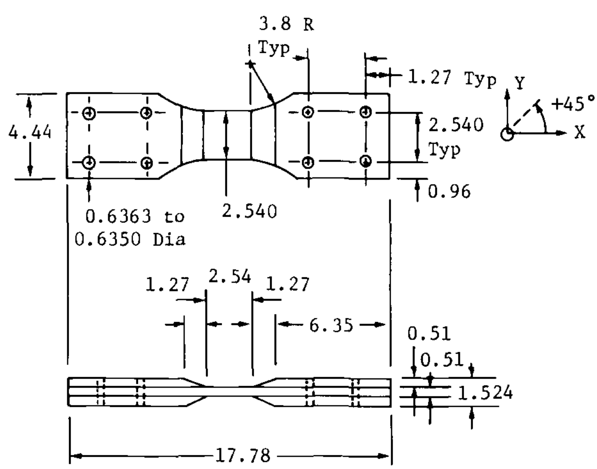

FIG. 2—*Test specimen (all dimensions in centimetres).*

Test Setup

Figure 3 shows the test specimen installed in the test fixture, which was an integral part of the lid of a liquid hydrogen cryostat. For the 300 K tests, the cryostat reservoir was not installed. Tests were performed with the test specimen completely immersed in liquid hydrogen and at 300 K. Loads were transferred to the specimen through a loading rod attached to the top of the specimen by a mating clevis. The rod was flange-mounted to a load cell and hydraulic actuator that were mounted on top of the fixture (Fig. 4). The lower end of the specimen was rigidly fixed to a similar mating clevis bolted to the bottom of the test fixture.

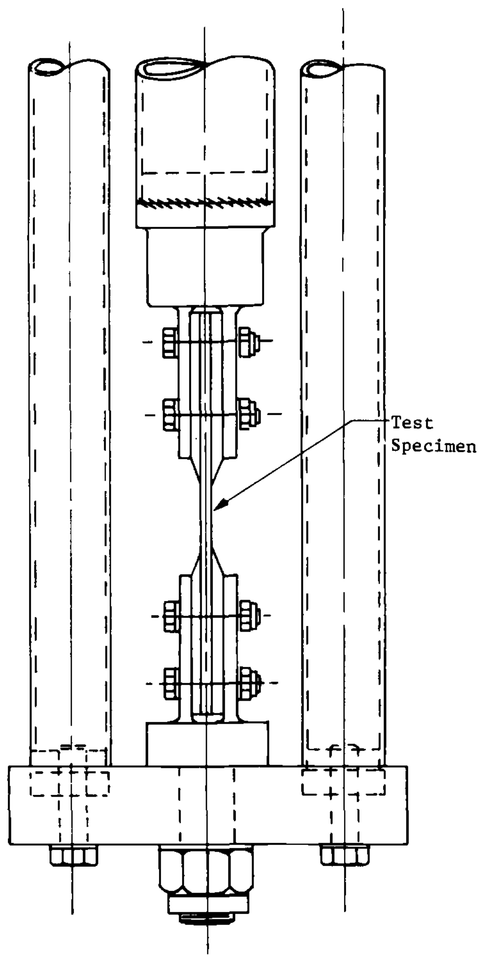

FIG. 3—*Load fixture for cryogenic testing.*

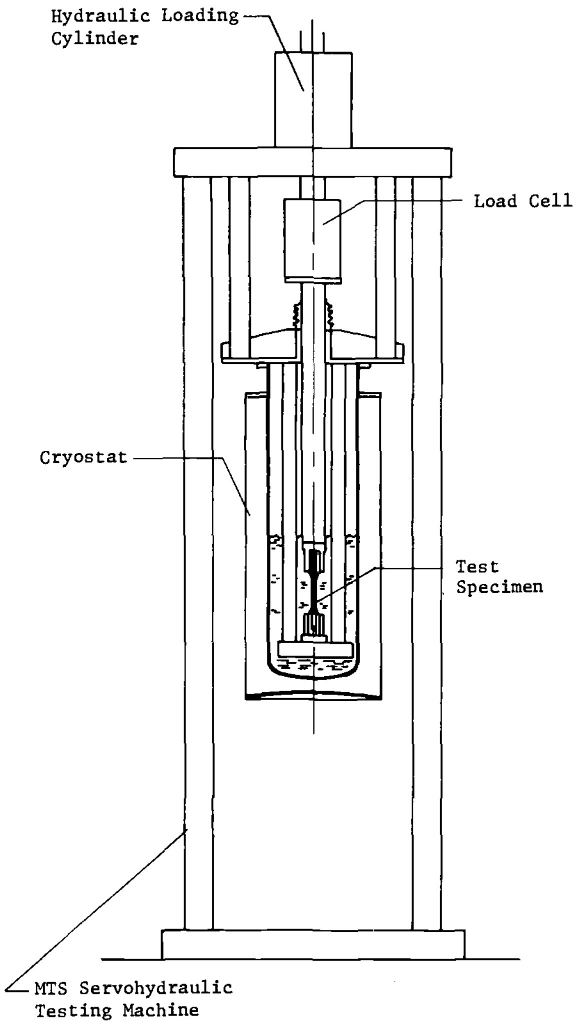

FIG. 4—*Test fixture configuration.*

Test Description and Results

Tension-compression loads were applied sinusoidally to the specimens with $R = -1.0$. Testing was conducted at frequencies of $\frac{1}{2}$ to 4 Hz depending on the magnitude of the maximum load; that is, higher loads were applied at lower frequencies to reduce heating of the specimens.

Results of the fatigue testing at 300 K of seven specimens is shown in Fig. 5. A failed specimen tested at 300 K is shown in Fig. 6. Failure initiation ap-

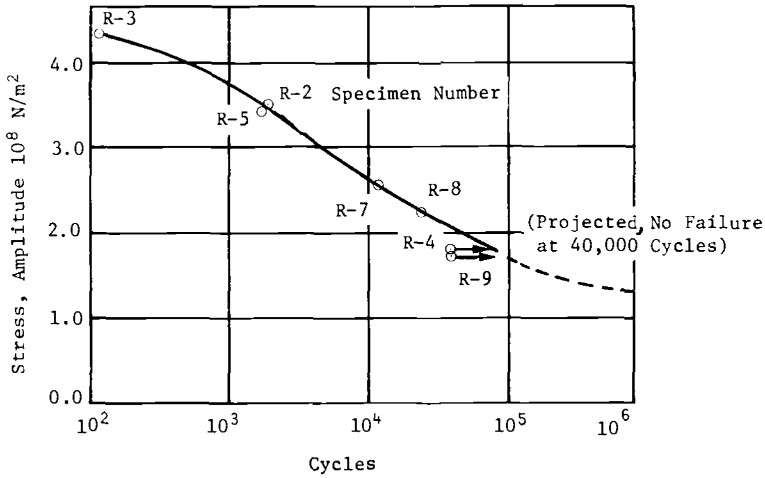

Note:

Specimen R_2 and R_5 Tested at 1 Hz
Specimen R_3 Tested at 1/2 Hz
Specimen R_4 and R_9 Tested at 4 Hz
Specimen R_7 and R_8 Tested at 3 Hz

FIG. 5—*S/N curve for ambient temperature.*

peared to have occurred in all cases in the transition region between the straight-sided gage section and the end-tab section. The same failure initiation mode occurred for the static test specimens. Laminate static strength at 300 K was determined to be 13.24×10^8 Pa from an average of three specimens.

Results of the fatigue testing at 20 K of four specimens is shown in Fig. 7. A failed specimen tested at 20 K is shown in Fig. 8. As with the 300 K tests, failure initiation appeared to have occurred in the transition region between the straight-sided gage section and the end-tab section. The static strength of the laminate was not determined at 20 K because the strength of the laminate exceeded the load-carrying capacity of the test system, which was 66 720 N.

Also shown in Fig. 7 is a comparison between the 300 and 20 K fatigue data. The results demonstrate the improved fatigue resistance at cryogenic temperatures of the fiberglass composite laminate. The static strength of filament-wound fiberglass (0/90) laminate composites at 20 K, compared with strength at 300 K, has been shown to be approximately 20% to 30% greater [*3*]. The limited fatigue test data included here indicate that cryogenic temperatures increase the fatigue life of fiberglass composites by about 10% at the stress level corresponding to 1000 cycles in Fig. 7 and by more than 38% at the stress level corresponding to 40 000 cycles, as indicated by the

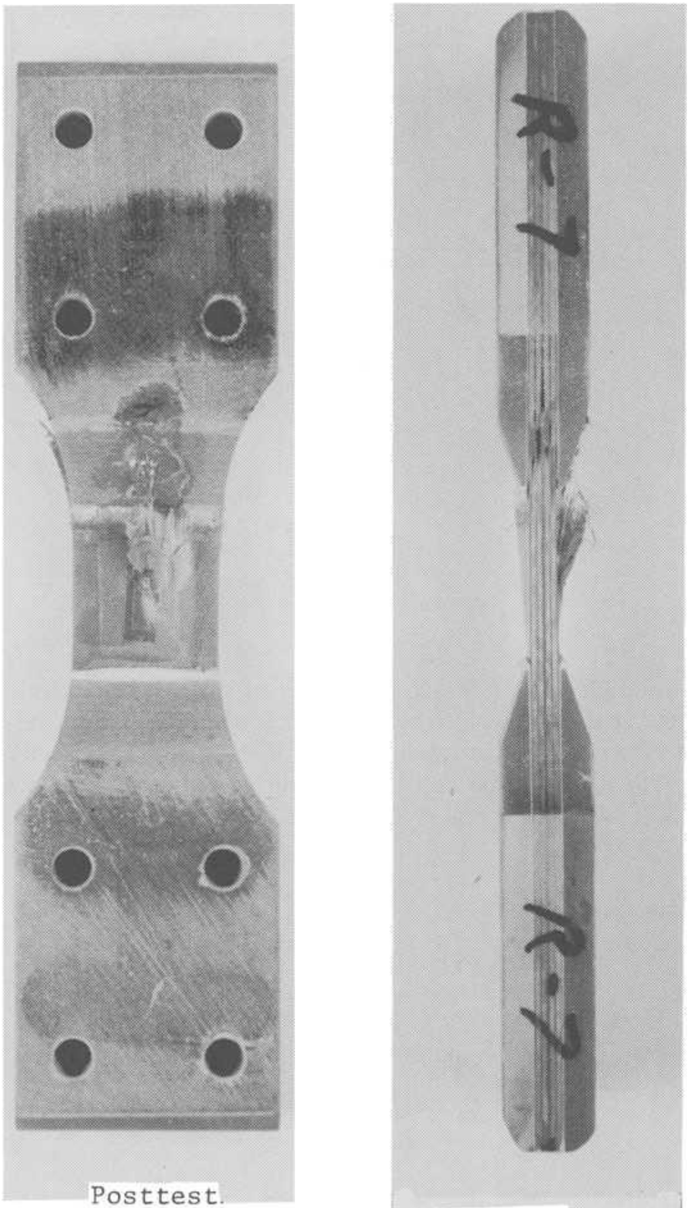

FIG. 6—*Specimen R-7 tested at 300 K.*

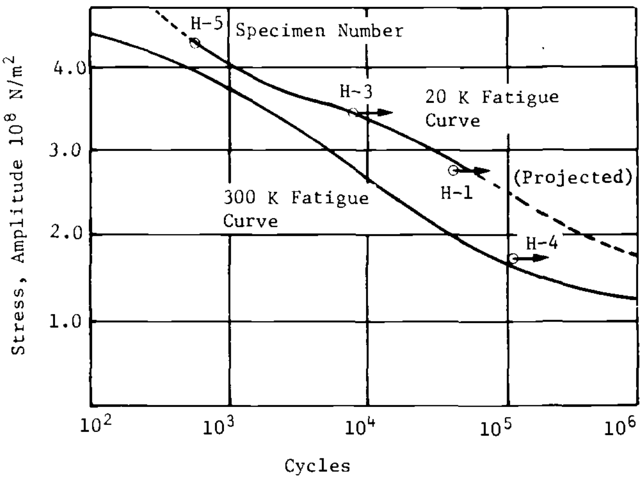

Note:

Specimen H1 Tested at 3 Hz
Specimen H3 Tested at 1 Hz
Specimen H4 Tested at 4 Hz
Specimen H5 Tested at 1/2 Hz

FIG. 7—*S/N curve for liquid hydrogen temperature.*

lack of failure of Specimen H1 at that stress level. These results follow the same trend as those described by Morris [*4*], where unidirectional fiberglass composites were tested in tensile fatigue at $R = 0.1$. There, stress level increases of the order of 200% were found for the temperature reduction from 300 to 20 K for the less severe $R = 0.1$ condition.

Conclusion

Fiberglass laminates can be designed and fabricated for effective use as combination thermostructural components at cryogenic temperatures. Fatigue life at 20 K apparently exceeds that at 300 K for the range of applied stress and cyclic loading conditions studied.

Acknowledgments

The results described here were generated as part of a NASA Lewis Research Center sponsored program: Cryogenic Fluid Management Experiment, Trunnion Verification Test Program, Contract NAS3-23245. Harold J. Kasper was the program monitor.

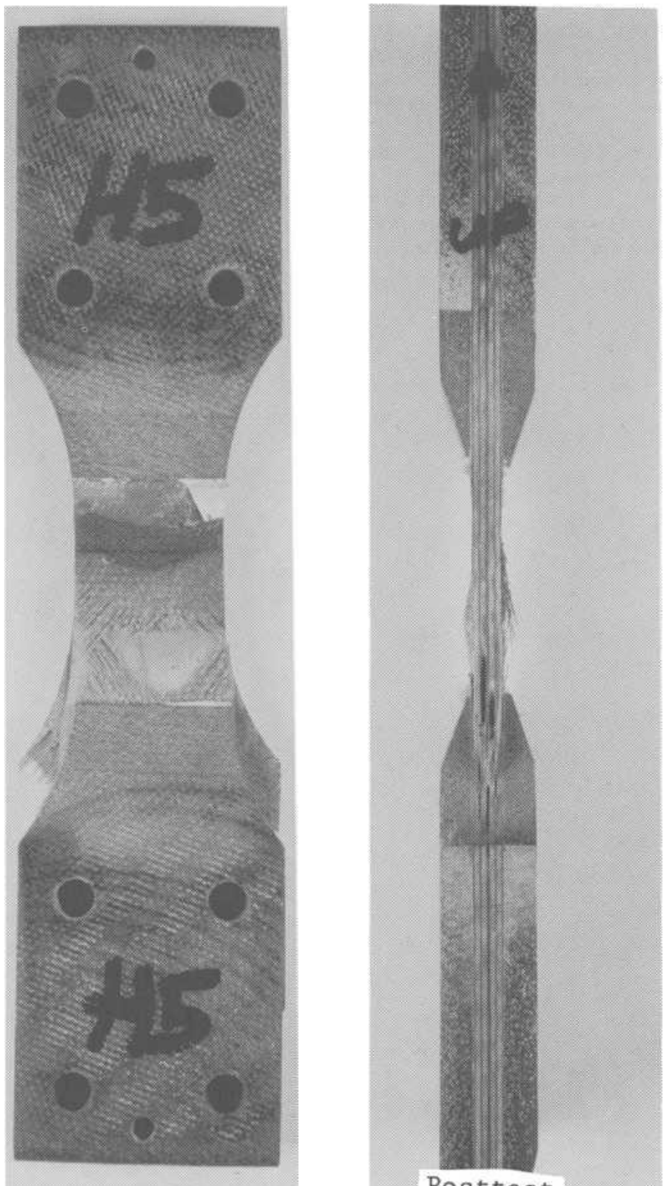

(a) Posttest Plan View

(b) Posttest Side View

FIG. 8—*Specimen H-5 tested at 200 K.*

References

[1] Kasen, M. B., *Cryogenics*, Vol. 15, No. 6, June 1975, p. 327.
[2] Fester, D. A., Bailey, W. J., Toth, J. M., Jr., and Kasper, H. J., "Cryogenic Fluid Management Experiment Trunnion Fatigue Verification," presented at AIAA/ASME/AHS Structures, Structural Dynamics, and Materials Conference, Lake Tahoe, NV, 2-4 May 1983, published by American Institute of Aeronautics and Astronautics, New York, 1983.
[3] Toth, J. M., Jr., and Soltysiak, D. J., "Investigation of Smooth-Bonded Metal Liners for Glass Fiber Filament-Wound Pressure Vessels," Final Report, Contract NAS 3-6293, McDonnell Douglas Corp., Huntington Beach, CA, May 1967.
[4] Morris, E. E., "Filament-Wound Composite Thermal Isolator Structures for Cryogenic Dewars and Instruments," in *Composites for Extreme Environments, ASTM STP 768*, American Society for Testing and Materials, Philadelphia, 1982, pp. 95–109.

Peter K. Liaw, William A. Logsdon, and Mustan H. Attaar

Computerized Near-Threshold Fatigue Crack Growth Rate Testing at Cryogenic Temperatures: Technique and Results

REFERENCE: Liaw, P. K., Logsdon, W. A., and Attaar, M. H., "**Computerized Near-Threshold Fatigue Crack Growth Rate Testing at Cryogenic Temperatures: Technique and Results,**" *Fatigue at Low Temperatures, ASTM STP 857,* R. I. Stephens, Ed., American Society for Testing and Materials, Philadelphia, 1985, pp. 173–190.

ABSTRACT: A computerized near-threshold fatigue crack growth rate (FCGR) test method has been applied at cryogenic temperatures. Near-threshold FCGR tests were conducted at room and cryogenic temperatures as low as 4.2 K (−452°F) on JBK-75 (modified A-286) stainless steel (base and autogenous gas-tungsten arc weld metal). Near-threshold crack growth rates in both the base and weld metal tended to decrease with decreasing temperatures from 297 to 4.2 K (75 to −452°F). At each temperature, the JBK-75 base material typically demonstrated a higher threshold stress intensity range than the weld material. Unlike the room temperature results, at 77 and 4.2 K (−320 and −452°F) near-threshold crack propagation rates were insensitive to load ratio ($R = P_{min}/P_{max}$). The decreased dependence of near-threshold FCGR data on load ratio at low temperatures appears to be in agreement with a crack closure model.

KEY WORDS: fatigue tests, near-threshold tests, computerized tests, cryogenic tests

The fatigue crack propagation threshold (ΔK_{th}) of a material is defined as the value of the stress intensity range (ΔK) below which an existing crack will not propagate (or will grow only at an extremely small rate) under fatigue loading. The value of ΔK_{th} is a function of load ratio (R), the ratio of minimum to maximum load in a fatigue cycle, environment, and microstructure [*1–6*]. Load-bearing members of machines or structures frequently have low-level cyclic loads superimposed on the static loads. In most cases, the presence of pre-existing cracks cannot be ruled out. Given some assumed maximum crack length, generally taken to be the sensitivity of the inspection technique used, the fatigue crack propagation threshold then gives the maxi-

Dr. Liaw and Mr. Logsdon are with the Metallurgy Department of the Westinghouse R&D Center in Pittsburgh, PA 15235. Mr. Attaar is with the Nuclear Services Integration Division (NSID) of the Westinghouse R&D Center in Pittsburgh, PA 15235.

mum cyclic load range for which the pre-existing cracks will not grow at an appreciable rate. The fatigue threshold is thus an important design parameter when one is considering the effect of low-amplitude, high-cycle loading.

Near-threshold fatigue crack growth rate (FCGR) data were formerly developed by using a manual load-shedding technique [1–3,5,6]. As the fatigue crack extended, the applied loads were manually reduced to obtain a lower stress intensity range. This process was continued until the rate of crack propagation reached the threshold. Since near-threshold crack propagation rates were relatively slow, the manual load-shedding technique was a time-consuming scheme for generating near-threshold crack growth rate results. Combined with the high cost of cryogenic coolants, manual near-threshold fatigue crack propagation testing at low temperatures proved very tedious and expensive.

In this investigation, an automated technique was employed to conduct near-threshold FCGR tests at cryogenic temperatures. Moreover, the effects of temperature and load ratio on the near-threshold crack propagation behavior of JBK-75 (modified A-286) stainless steel base plate and autogenous gas tungsten arc weld metal were examined.

Decreasing Stress Intensity FCGR Tests

In order to develop ΔK_{th} parameters, FCGR measurements must be taken at relatively low values of ΔK, where the growth rates are very slow. For a conventional FCGR test, maintaining a constant load during crack propagation typically increases ΔK (depending on the specimen geometry), while maintaining a constant deflection progressively decreases ΔK [7]. The moderate decreases in K-level and the large amount of time and consequent use of enormous quantities of liquid helium combine to make it very unattractive to conduct a threshold FCGR test under decreasing ΔK conditions using a constant displacement criterion. Load shedding can be accelerated by manual adjustments but this approach requires an operator's constant supervision. Therefore, a completely automated FCGR data acquisition and load control system was used to measure crack length and also shed the applied cyclic load during a decreasing ΔK test. Following the suggestion of Saxena et al [7] the load-shedding schedule was controlled to satisfy the relationship

$$\Delta K = \Delta K_0 \exp[c(a - a_0)]$$

where a is the instantaneous crack length, ΔK_0 is the stress intensity range corresponding to the starting crack length of a_0, and c is an experimental constant. In this investigation the value of c was chosen to be -0.098 mm^{-1}. Previously, it has been shown that decreasing ΔK testing with $c = -0.098$ mm^{-1} gives consistent crack propagation rate data, as compared to increasing ΔK (constant-load-range) testing [7,8].

The austenitic stainless steel JBK-75 was developed by Sandia Laboratories as a special chemical modification to A-286 in order to control the propensity for hot cracking in heavy-section A-286 welds. The chemical composition of the JBK-75 tested in this investigation (Heat 85422, Ingot 2) is summarized in Table 1. Compared with A-286, JBK-75 places tighter chemical controls on manganese, silicon, and boron, and increases the nickel level from approximately 24 to 30 weight-percent.

In actual production, JBK-75 plate is solution-annealed at 900°C (1650°F), cold rolled 5%, formed into a square cross-section, and autogenously gas-tungsten arc welded. Subsequently, the JBK-75 is cold worked an additional 10% during the conductor sheath–forming operation and heat-treated for 30 h at 700°C (1292°F) to react the superconductor. To simulate this production process, the JBK-75 sheet examined in this investigation was subjected to a standard mill production solution annealing treatment at 900°C (1650°F); autogenously gas-tungsten arc welded (GTAW) by using argon shielding gas at 50 A, 8.5 V, and a 10.2 cm/min (4 in./min) travel speed; cold-worked 15%; and reaction-annealed in an argon atmosphere for 30 h at 700°C (1292°F). Final sheet thickness was 3.56 mm (0.140 in.). The grain size of JBK-75 steel was ~25 μm.

The ambient and cryogenic tensile properties of JBK-75 are summarized in Table 2. Sheet tensile specimens 1.3 mm (0.050 in.) thick with either a 25.4 mm (1.0 in.) (base material) or 6.35 mm (0.25 in.) (weld metal) gage length were used to generate these tensile properties. The loading orientation for each specimen was transverse to the plate rolling direction; the direction of welding was identical to the plate rolling direction. The reduced specimen gage length in the weldment tensile specimens completely spanned the weld fusion zone and was primarily made up of weld metal. As such, this specimen geometry provides a very accurate measure of weldment yield and ultimate strength. On the other hand, care should be used in comparing total elongation values for the base and weld metal, since they were measured with specimens of different gage lengths. To help in this comparison, uniform elongation (deformation to the point of maximum load), a measurement that is independent of specimen gage length, is also reported in Table 2.

With one exception (GTAW room temperature reduction in area) the yield and ultimate strengths as well as the ductility of both the base and weld metal increased with decreasing temperature. Further, with the exception of the liquid helium temperature yield strength, the JBK-75 base material yield and ultimate strengths, elongation (both uniform and total), and reduction in area were all superior to those of the gas-tungsten arc weld metal.

The near-threshold FCGR data were generated by using 2.5 mm (0.10 in.) thick (B) and 51 mm (2.0 in.) wide (W) compact specimens ($H/W = 0.6$, where H is half of the specimen height) machined so that the specimen crack opening displacement could be measured at the centerline of loading. The notch orientation in the base material specimens was in the direction of cold

TABLE 1—*Chemical composition of JBK-75 (Heat 85422, Ingot 2).*

Heat/Ingot Identity	Chemical Composition, wt%														
	C	Mn	P	S	Si	Ni	Cr	Mo	V	Ti	Al	B	O	N	Fe
85422-2	0.014	0.02	0.009	0.001	0.08	29.33	13.91	1.24	0.28	2.11	0.29	0.0013	0.0016	0.0019	bal.

TABLE 2—*Tensile properties of fully processed JBK-75 base material and autogenous gas-tungsten arc weld metal.*[a]

Base or Weld	Temperature		0.2% Yield Strength		Ultimate Strength		Uniform Elongation, %	Total Elongation, %	Reduction in Area, %
	K	°F	MPa	ksi	MPa	ksi			
Base	297	75	1031	149.6	1251	181.5	[b]	[b]	31.6
	77	−320	1182	171.4	1478	214.3	15.6	17.8	32.1
	4.2	−452	1253	181.7	1585	229.9	18.4	21.4	34.3
GTAW	297	75	1009	146.4	1056	153.1	4.8	9.2	24.5
	77	−320	1115	161.7	1444	209.4	14.3	14.3	15.0
	4.2	−452	1338	194.1	1529	221.7	15.1	15.1	19.4

[a] "Fully processed" indicates standard mill production; solution-annealed at 900°C (1650°F); autogenously gas-tungsten arc welded (where applicable); cold worked, 15%; and reaction-annealed, 30 h at 700°C (1292°F). The loading orientation for all tests was transverse.

[b] Elongations not available because of slippage.

rolling or *T-L* per ASTM Test for Plane-Strain Fracture Toughness of Metallic Materials (E 399). The notch orientation in the weld specimens was parallel to the direction of welding. The load ratios (R) were 0.1 and 0.8; tests at $R = 0.8$ were conducted only for base metal.

Experimental Test System

An experimental setup was required to cool the specimens to 4.2 K (−452°F), apply the loads on the specimen while it was maintained at liquid helium temperature, sense and record the load and displacement signals continuously throughout the test, and control the loads automatically. Previously, an electrohydraulic fatigue machine was interfaced with a PDP 11/34 A computer to conduct air environment near-threshold fatigue crack growth rate tests [*8*]. In this investigation, the same automated technique was applied to study the cryogenic temperature near-threshold crack propagation behavior of JBK-75 stainless steel. The test frequency was 85 to 100 Hz. Displacement is sensed by a double-cantilever cryogenic service extensometer that is balanced on a thick blade knife-edge attached to the specimen at the load line.

The cryostat with the specimen mounted in the load train is illustrated in Fig. 1. The refrigeration techniques and apparatus for extremely low temperature testing have been previously described [*9,10*]. Briefly, the cryostat is a multilayer Dewar flask made up of a primary container and a liquid nitrogen chamber that are separated by two styrofoam chambers (Fig. 1). For 4.2 K (−452°F) testing, the cryostat was precooled with liquid nitrogen before establishing a liquid helium flow rate. The helium coolant dispenser served as a helium distributor and temperature stabilizer. Cold helium gas surrounded the specimen to provide the desired 4.2 K (−452°F) test temperature. For 77 K (−320°F) testing, the specimen was directly immersed in liquid nitrogen. Thermocouples mounted on the specimen constantly monitored the cryogenic temperatures [*11,12*].

Results and Discussion

The near-threshold FCGR properties of JBK-75 base material and autogenous gas-tungsten arc weld metal at three temperatures (4.2, 77 and 297 K [−452, −320 and 75°F]) are illustrated in Figs. 2 to 4. The near-threshold fatigue crack growth rates of JBK-75 base and weld metal both tend to decrease with decreasing temperature. In addition, as the applied alternating stress intensity (ΔK) is decreased, the difference between room and liquid helium temperature fatigue crack growth rates becomes increasingly pronounced. Similar results were also found in aluminum alloys [*13*] and other steels [*14–18*].

The values of threshold stress intensity range (ΔK_{th}) are listed in Table 3. At $R = 0.1$, decreasing the temperature from 297 to 4.2 K (75 to −452°F)

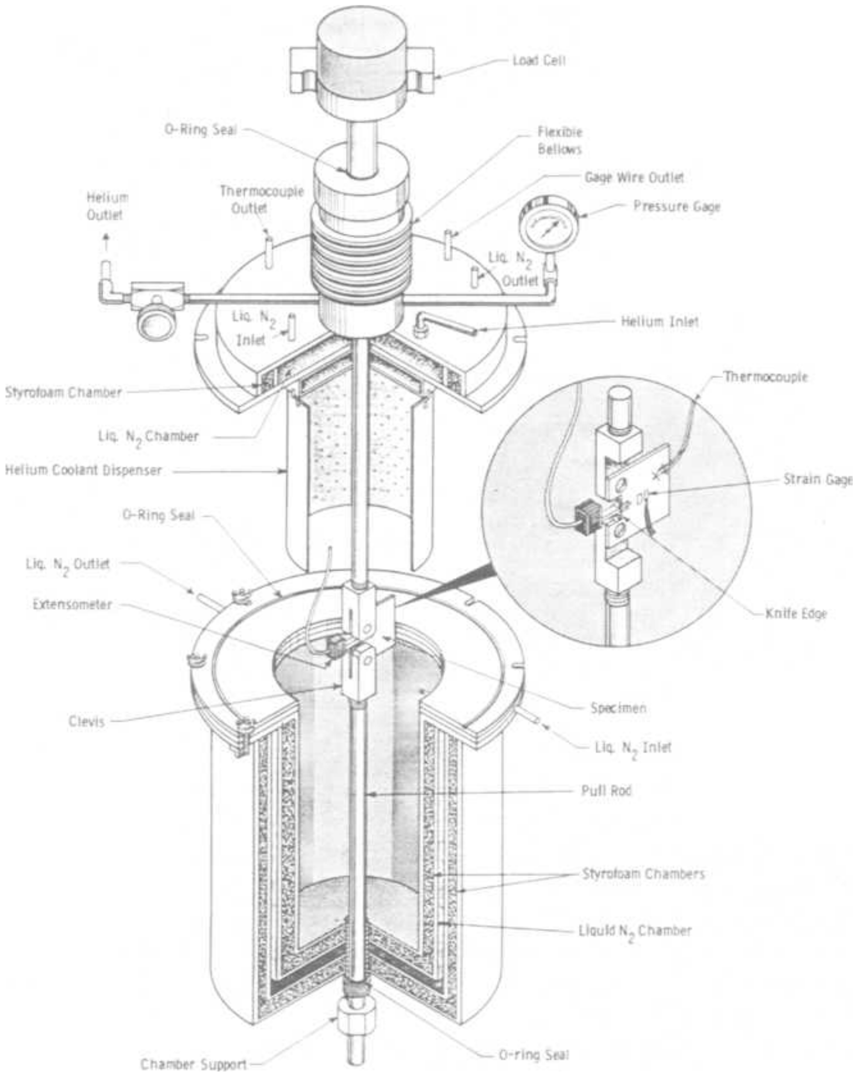

FIG. 1—*Cryostat for low-temperature testing.*

generally increases ΔK_{th} in both base and weld metals. The same trend was observed at $R = 0.8$ in base metal.

The near-threshold crack growth rate properties at $R = 0.1$ in base and weld materials are compared in Figs. 5 to 7. At all three temperatures, crack propagation rates in the base metal are slower than those in the weld metal. As shown in Table 3, the values of ΔK_{th} at $R = 0.1$ in the base metal are larger than those in the weld metal, independent of test temperature.

Thus far, little information exists regarding the influence of welds on

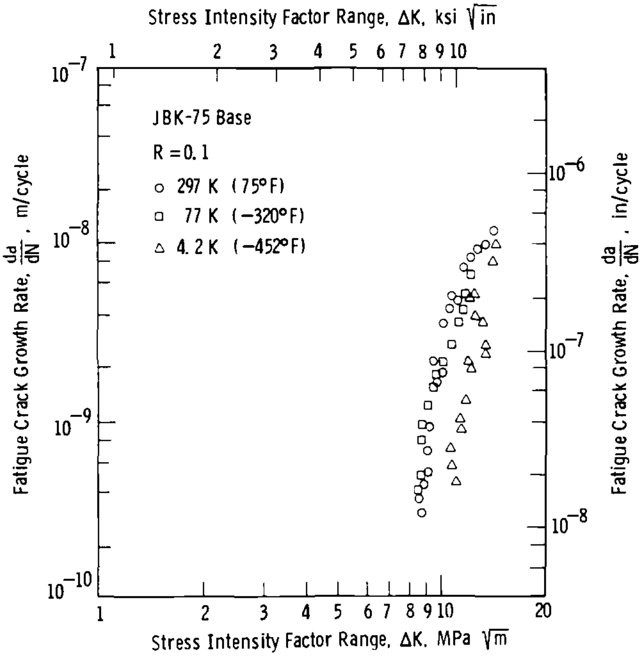

FIG. 2—*Effect of temperature on the near-threshold fatigue crack growth rate properties of JBK-75 stainless steel at* R = *0.1.*

threshold crack propagation rate performance, except for a few investigations of steels [*3,19–24*]. In other stainless steels [*21–24*], the rates of near-threshold crack growth in weldments are faster than those in the corresponding parent metals; this behavior is consistent with current observations. Results in mild steels [*19,20*], however, demonstrate no apparent variation in ΔK_{th} for base versus weld materials. Several factors, such as residual stress or crack closure, may cause different near-threshold crack propagation behavior in base and weld materials. Consequently, further research is required to understand crack propagation performance in base metals and their corresponding weldments.

The effect of load ratio on the near-threshold FCGR properties of JBK-75 base metal at 297, 77, and 4.2 K (75, −320, and −452°F) is presented in Figs. 8, 9, and 10, respectively. At 297 K (75°F), increasing the load ratio from 0.1 to 0.8 increases the near-threshold fatigue crack growth rates. Furthermore, the influence of load ratio on crack propagation rate increases with decreasing ΔK. This behavior is characteristic of room temperature, air-environment near-threshold crack growth performance in structural alloys. It is interesting to note, however, that at 77 and 4.2 K (−320 and −452°F) (Figs. 9 and 10) the effect of load ratio on the rate of near-threshold crack propagation is significantly reduced compared with that of 297 K (75°F). Further, at 77 and

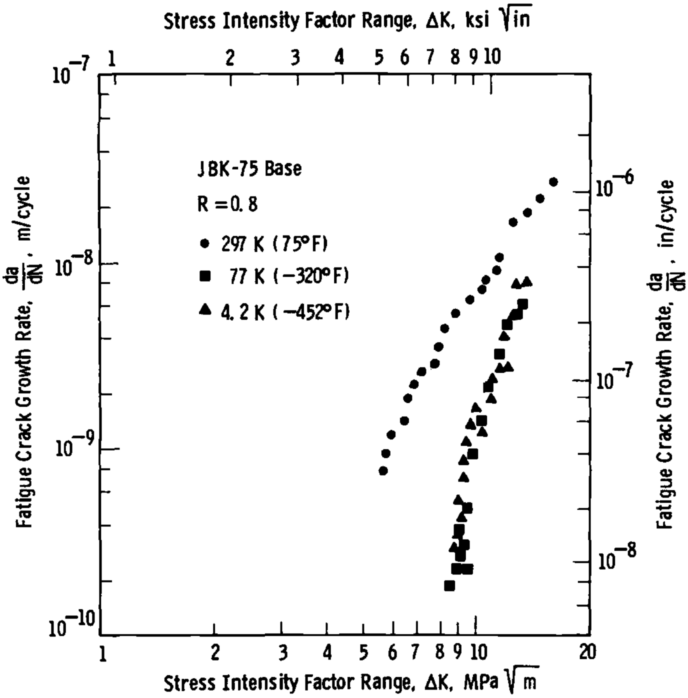

FIG. 3—*Effect of temperature on the near-threshold fatigue crack growth rate properties of JBK-75 stainless steel at* R = *0.8.*

4.2 K (−320 and −452°F) the crack growth rates at $R = 0.1$ and $R = 0.8$ are nearly identical.

It has been suggested that the dependence of near-threshold FCGR behavior on load ratio may be due to oxide-induced crack closure [*4,5,25–27*]. At 297 K (75°F), oxide deposits form at low ΔK levels because of fretting oxidation [*28*]. Decreasing the R value increases the thickness of the oxide layer at the threshold because of increased plasticity-induced crack closure and increased Mode II displacements, which enhance fretting oxidation [*4,5,25–31*]. At low R values ($\leq$0.5), the thicknesses of the oxide deposits at the threshold are typically comparable to the cyclic crack opening displacements in steels and copper [*4,25,27*]. The sizable oxide layers at low R values wedge the crack tip, increase the crack closure level (oxide-induced crack closure), and decrease the effective stress intensity range ($\Delta K_{\text{eff}} - K_{\max} - K_{\text{closure}}$, where $K_{\max}$ and K_{closure} are the stress intensities that correspond to the maximum and crack closure loads, respectively). The result is slower near-threshold crack propagation rates relative to those at high R values. At 77 and 4.2 K (−320 and −452°F), fretting oxidation does not tend to occur because of the low temperature and lack of moisture or oxygen. Consequently, oxide-induced crack closure is minimal at low temperatures; this effect in turn

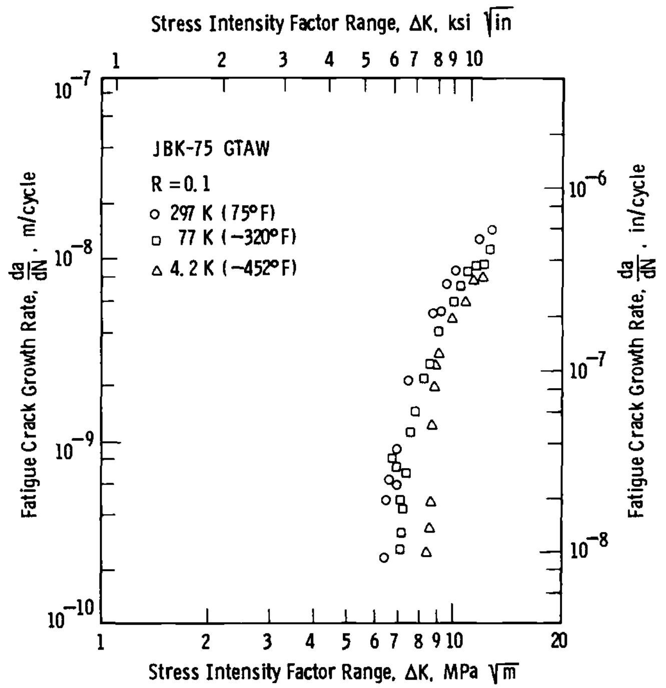

FIG. 4—*Effect of temperature on the near-threshold fatigue crack growth rate properties of JBK-75 gas-tungsten arc weld metal at* R = *0.1.*

yields a decreased dependence of near-threshold crack growth rates on R values.

In a similar vein, load ratio has a smaller influence on near-threshold crack growth behavior in inert as compared with moisture-containing environments. Data taken from the literature support the above statement. For example, it has been reported that near-threshold growth rates in vacuum are independent of R values in aluminum [*32*], titanium alloys [*33*], and steels

TABLE 3—*Values of threshold stress intensity range for JBK-75 base and autogenous gas-tungsten arc weld metal.*

Material	Temperature		R Ratio	ΔK_{th}	
	K	°F		MPa$\sqrt{m}$	ksi$\sqrt{in.}$
Base	297	75	0.1	8.5	7.7
Base	77	−320	0.1	8.5	7.7
Base	4.2	−452	0.1	11.0	9.9
Base	297	75	0.8	5.7	5.1
Base	77	−320	0.8	9.0	8.1
Base	4.2	−452	0.8	9.0	8.1
GTAW	297	75	0.1	6.4	5.8
GTAW	77	−320	0.1	7.2	6.5
GTAW	4.2	−452	0.1	8.5	7.7

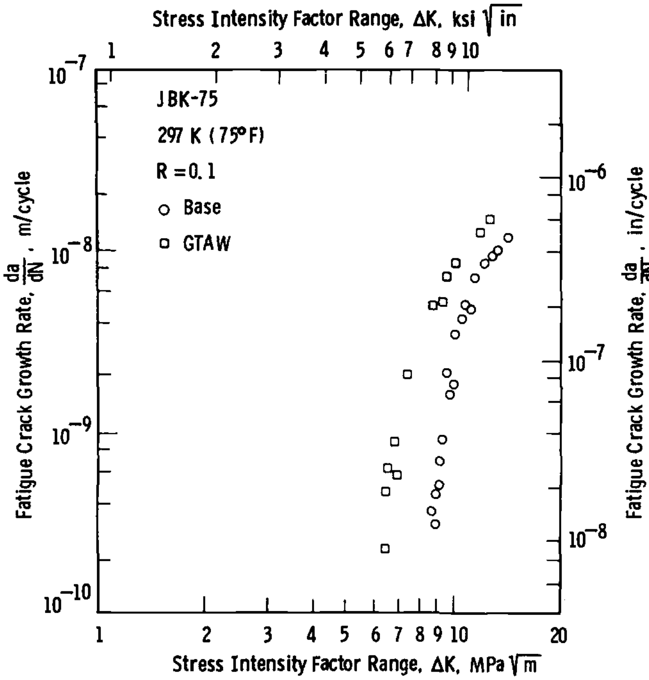

FIG. 5—*Comparison of the near-threshold fatigue crack growth rate properties of JBK-75 base and gas-tungsten arc weld metals at 297 K (75°F).*

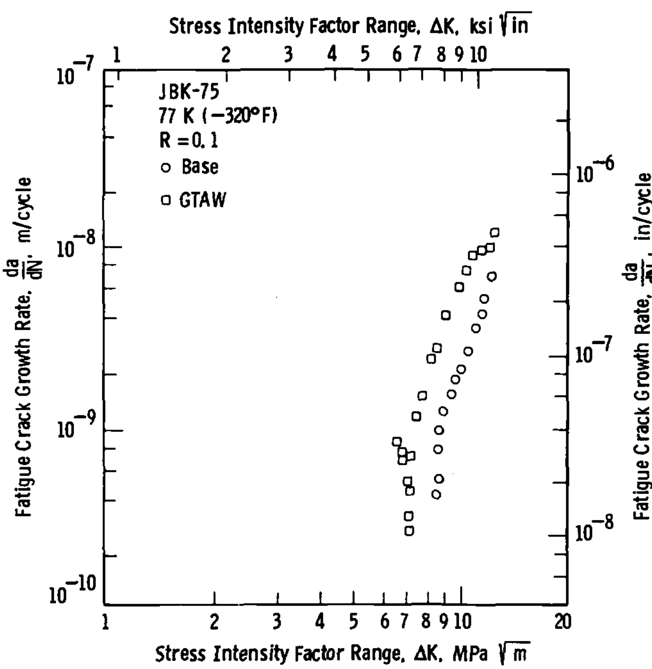

FIG. 6—*Comparison of the near-threshold fatigue crack growth rate properties of JBK-75 base and gas-tungsten arc weld metals at 77 K (−320°F).*

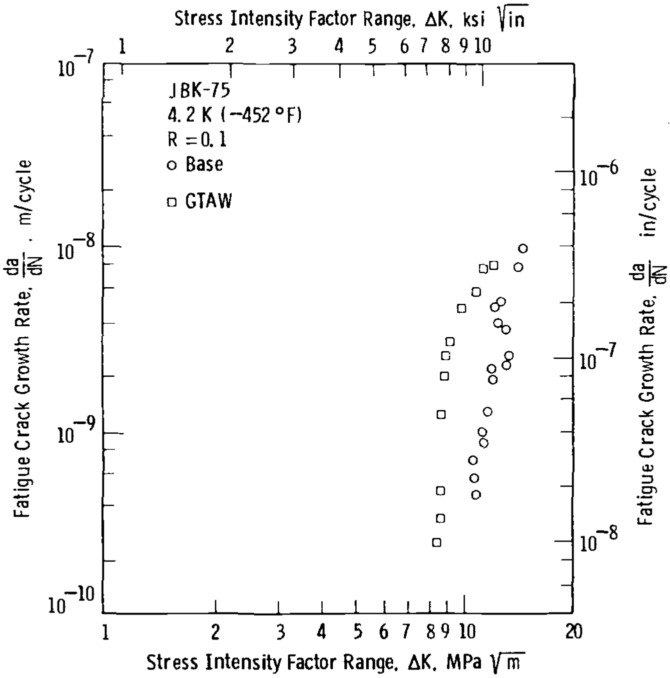

FIG. 7—*Comparison of the near-threshold fatigue crack growth rate properties of JBK-75 base and gas-tungsten arc weld metals at 4.2 K (−452°F).*

[*6,34,35*]. Further, the near-threshold crack growth rates in inert gas are less sensitive to R values than those in air for various steels [*5,25*]. Consequently, the decreased influence of load ratio on near-threshold crack growth behavior at cryogenic temperatures and in inert environments appears to be related to the lack of oxide-induced crack closure. Moreover, it was observed that the fracture surfaces appeared to be smoother at 4.2 K than at 297 K in JBK-75 stainless steel [*36*]. At cryogenic temperatures, the decreased surface roughness-induced crack closure resulting from mismatch of the fracture surfaces [*30,37–40*] may also contribute to the decreased effect of load ratio on ΔK_{th} at lower temperatures.

In Figs. 2 and 3, decreasing the temperature generally increases resistance to near-threshold crack growth, as mentioned before. If crack closure could rationalize the influence of temperature on crack propagation behavior, a minimum temperature effect would be observed at high load ratios, since the extent of crack closure decreases with increasing load ratio. In Fig. 3, at a high load ratio of 0.8, however, there is a significant temperature effect on cooling from 297 to 4.2 K. Thus, crack closure cannot be used to explain the influence of temperature on crack growth rates in the temperature range of 297 to 4.2 K. The same conclusion has also been reported by other investigators [*41,42*]. It has been suggested that Young's modulus (E) may reconcile near-threshold crack propagation behavior for materials of various E values

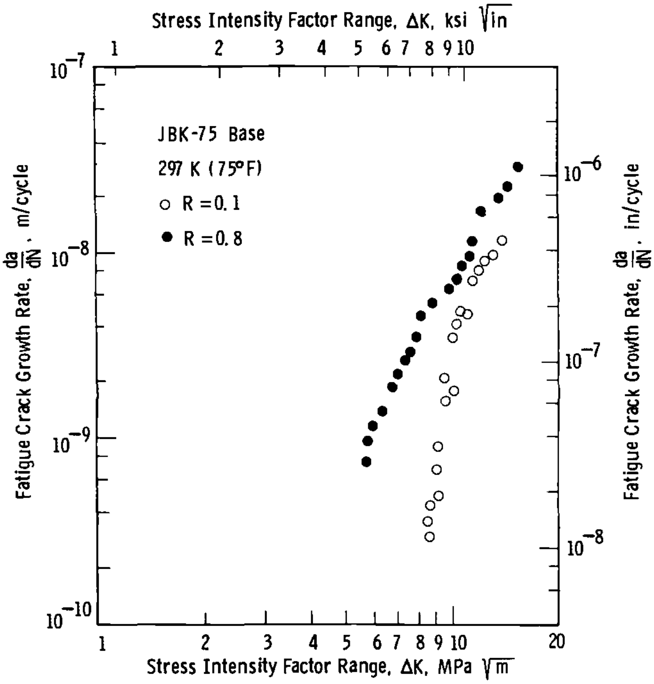

FIG. 8—*Effect of load ratio on the near-threshold fatigue crack growth rate properties of JBK-75 stainless steel at 297 K (75°F).*

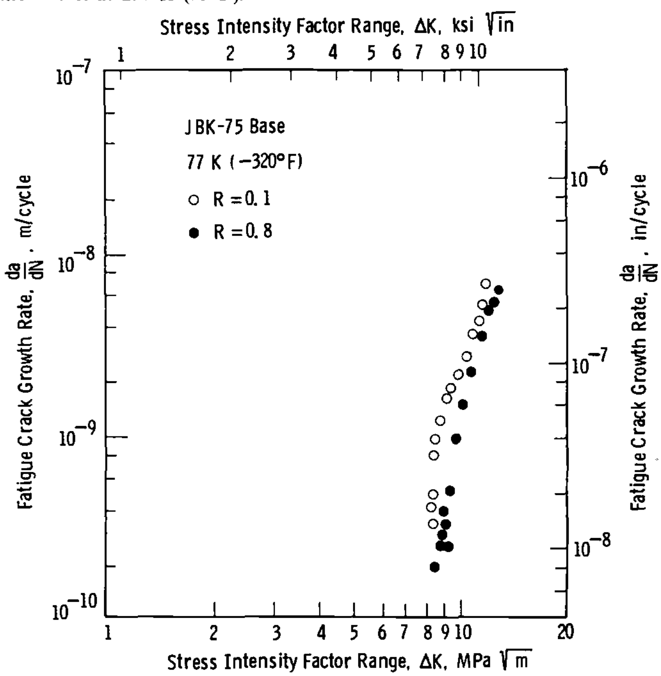

FIG. 9—*Effect of load ratio on the near-threshold fatigue crack growth rate properties of JBK-75 stainless steel at 77 K (−320°F).*

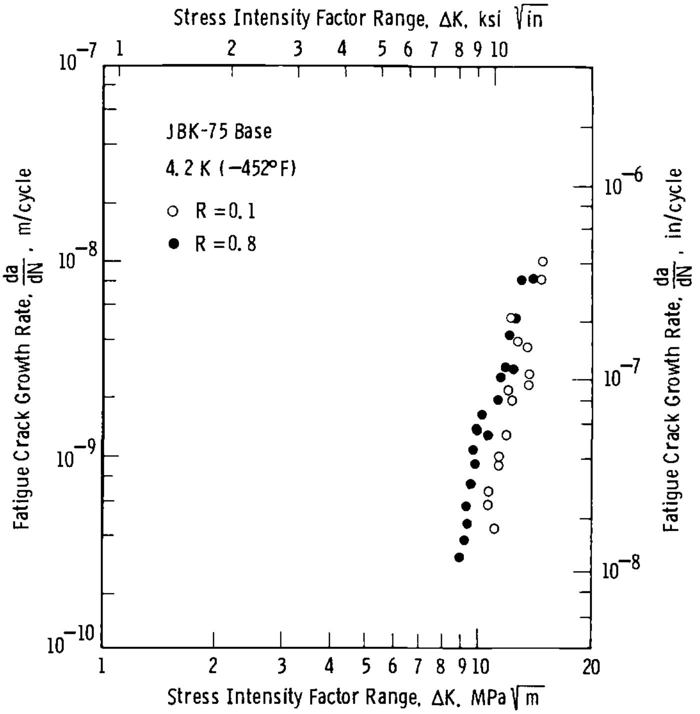

FIG. 10—*Effect of load ratio on the near-threshold fatigue crack growth rate properties of JBK-75 stainless steel at 4.2 K (−452°F).*

[*43*]. In the present steel, decreasing the temperature from 297 to 4.2 K increases E by approximately 10%, which cannot totally account for the change of nearly 40% in ΔK_{th} on cooling at load ratios of 0.1 and 0.8 (Table 3). It appears that dislocation dynamics offers a possible explanation for the effect of temperature on near-threshold crack propagation rates [*41,42,44,45*]. In other words, the lower activation energy at cryogenic temperatures restricts the dislocation motion at the crack tip, which in turn results in higher resistance to crack growth at lower temperatures.

Finally, these JBK-75 near-threshold FCGR results demonstrate the successful automation of a decreasing stress intensity FCGR threshold test at cryogenic temperatures. During these tests, the computer constantly monitored crack lengths and adjusted applied loads instantaneously so that the decrease of ΔK (load shedding) was essentially continuous. Compared with manual threshold FCGR testing and its associated discrete steps of load shedding, the continuously decreasing ΔK technique minimizes the transient effects associated with manual load shedding. Using this computerized near-threshold crack growth technique, it takes one or two days to complete one test at a low load ratio ($\leq$0.5), which takes about one week with the manual load shedding method. Therefore, the present automated technique saves considerable testing time, and excellent near-threshold FCGR data can now be developed at extremely low temperatures with relative ease.

Conclusions

1. Near-threshold fatigue crack growth rate (FCGR) data have been developed at room and cryogenic temperatures as low as 4.2 K (−452°F) on JBK-75 (modified A-286) base and autogenous gas-tungsten arc weld metal by using a completely automated FCGR data acquisition and load control system. Computer-controlled load shedding substantially reduced testing time in these low-temperature thershold FCGR tests.
2. The near-threshold fatigue crack growth rates of JBK-75 base and autogenous gas-tungsten arc weld metal tended to decrease with decreasing temperature over the temperature range 297 to 4.2 K (75 to −452°F).
3. At a given temperature, JBK-75 base material typically demonstrated a higher level of threshold stress intensity range (ΔK_{th}) than weld metal.
4. At 297 K (75°F), increasing the load ratio from 0.1 to 0.8 increased the rates of near-threshold fatigue crack propagation in JBK-75 base metal. At 77 and 4.2 K (−320 and −452°F), however, the near-threshold FCGR properties were insensitive to load ratio.
5. The decreased dependence of near-threshold FCGR data on load ratio at 77 and 4.2 K (−320 and −452°F) relative to 297 K (75°F) appears to be in agreement with a crack closure model.

Acknowledgments

The authors wish to gratefully acknowledge R. E. Gainer, E. J. Helm, R. R. Hovan, G. McFetridge, and M. G. Peck of the Mechanics of Materials Laboratory, Westinghouse R&D Center, for supervising and conducting all the experiments. The major contribution of R. S. Williams towards computerizing the test facility is also acknowledged. Financial support for this program was provided by the Advanced Programs Department, Westinghouse Steam Turbine Generator Division.

References

[*1*] Paris, P. C., Bucci, R. J., Wessel, E. T., Clark, W. G., and Mager, T. R., "Extensive Study of Low Fatigue Crack Growth Rates in A 533 and A 508 Steels," *Stress Analysis and Growth of Cracks, ASTM STP 513,* American Society for Testing and Materials, Philadelphia, 1972, pp. 141–176.

[*2*] Bucci, R. J., Clark, W. G., Jr., and Paris, P. C., "Fatigue Crack Propagation Growth Rates Under a Wide Variation of ΔK for an ASTM A 517 Grade F (*T*-1) Steel," *Stress Analysis and Growth of Cracks, ASTM STP 513,* American Society for Testing and Materials, Philadelphia, 1972, pp. 177–195.

[*3*] Ritchie, R. O., "Near-Threshold Fatigue-Crack Propagation in Steels," *International Metals Reviews,* Nos. 5 and 6, 1979, pp. 205–230.

[*4*] Liaw, P. K., Leax, T. R., Williams, R. S., and Peck, M. G., "Near-Threshold Fatigue Crack Growth Behavior in Copper," *Metallurgical Transactions A,* Vol. 13A, Sept. 1982, pp. 1607–1618.

[5] Stewart, A. T., "The Influence of Environment and Stress Ratio on Fatigue Crack Growth at Near-Threshold Stress Intensities in Low-Alloy Steels," *Engineering Fracture Mechanics*, Vol. 13, 1980, pp. 463–478.
[6] Cooke, R. J. and Beevers, C. J., "The Effect of Load Ratio on the Threshold Stresses for Fatigue Crack Growth in Medium Carbon Steels," *Engineering Fracture Mechanics*, Vol. 5, 1973, pp. 1061–1071.
[7] Saxena, A., Hudak, S. J., Donald, J. K., and Schmidt, D. W., "Computer-Controlled Decreasing Stress Intensity Technique for Low Rate Fatigue Crack Growth Rate Testing," *Journal of Testing and Evaluation*, Vol. 6, No. 3, 1978, pp. 167–174.
[8] Williams, R. S., Liaw, P. K., Peck, M. G., and Leax, T. R., "Computer Controlled Decreasing ΔK Fatigue Threshold Test," *Engineering Fracture Mechanics*, Vol. 18, No. 5, 1983, pp. 953–964.
[9] Wessel, E. T., "Refrigeration Techniques and Apparatus for Very Low Temperatures to 4.2 K," *Refrigeration Engineering*, Vol. 65, 1957, pp. 37–45.
[10] Fox, D. K. and Pryle, W. H., "Test Apparatus and Tensile Properties of N6-ZR Superconductor Alloy Wire in the Temperature Range 300 to 4.2 K," Westinghouse Corp., Pittsburgh, PA, 1963.
[11] Aston, J. G., "The Use of Copper-Constantan Thermocouples for Measurement of Low Temperatures, Particularly in Calorimetry," *Temperature, Its Measurement and Control in Science and Industry*, American Institute of Physics, Reinhold, New York, 1941, p. 219.
[12] Dauphince, T. M., MacDonald, D. K. C., and Pearson, W. B., "The Use of Thermocouples for Measuring Temperatures below 70 K, A New Type of Low-Temperature Thermocouple," *Journal of Scientific Instruments*, Vol. 30, No. 11, 1953, pp. 399–400.
[13] McKittrick, J., Liaw, P. K., Kwun, S. I., and Fine, M. E., "Threshold for Fatigue Macrocrack Propagation in Some Aluminum Alloys," *Metallurgical Transactions A*, Vol. 12A, Aug. 1981, pp. 1535–1539.
[14] Tschegg, E. and Stanzl, S., "Fatigue Crack Propagation and Threshold in bcc and fcc Metals at 77 and 293 K," *Acta Metallurgica*, Vol. 29, 1981, pp. 30–40.
[15] Lucas, J. P. and Gerberich, W. W., "Low Temperature and Grain Size Effects on Threshold and Fatigue Crack Propagation in a High Strength Low Alloy Steel," *Materials Science and Engineering*, Vol. 51, 1981, pp. 203–212.
[16] Gerberich, W. W., Yu, W., and Esaklul, K. A., "Fatigue Threshold Studies in Fe, Fe-Si, and HSLA Steel. Part I: Effect of Strength and Surface Asperities on Closure," *Metallurgical Transactions A*, Vol. 15A, May 1984, pp. 875–888.
[17] Esaklul, K. A., Yu, W., and Gerberich, W. W., "The Effect of Low Temperature on Apparent Fatigue Threshold Stress Intensity Factors," *Fatigue at Low Temperatures, ASTM STP 857*, R. I. Stephens, Ed., American Society for Testing and Materials, Philadelphia, 1985, pp. 63–83.
[18] Stephens, R. I., Fatemi, A., Lee, H. W., Lee, S. B., Vacas-Oleas, C., and Wang, C. M., "Variable-Amplitude Fatigue Crack Initiation and Growth of Five Carbon or Low-Alloy Cast Steels at Room and Low Climatic Temperatures," *Fatigue at Low Temperatures, ASTM STP 857*, R. I. Stephens, Ed., American Society for Testing and Materials, Philadelphia, 1985, pp. 293–312.
[19] Pook, L. P. and Greenham, A. F., in *Proceedings*, Fatigue Testing and Design Conference, Vol. 2, Society of Environmental Engineers, London, England, 1976, p. 301.
[20] Priddle, E. K., "Some Effects of Temperature, Vacuum, and CO_2 Environments on Fatigue Crack Growth and Threshold for EN3A Mild Steel and a Weld Metal," Report RD/B/4990N81, Central Electricity Generating Board, London, England, April 1981.
[21] Pickard, A. C., Ritchie, R. O., and Knott, J. F., "Fatigue Crack Propagation in a Type 316 Stainless Steel Weldment," *Metals Technology*, Vol. 2, 1975, pp. 253–263.
[22] Shahinian, P., Smith, H. H., and Hawthorne, J. R., "Fatigue Crack Propagation in Stainless Steel Weldments at High Temperature," *Welding Research Supplement*, Vol. 51, 1972, pp. 527–532.
[23] Tschegg, E. K., Tauschitz, C., and Stanzl, S. E., "The Fatigue Crack Growth Behavior of Electron-Beam-Welded A 286 Superalloy," *Metallurgical Transactions A*, Vol. 13A, Aug. 1982, pp. 1483–1489.
[24] Liaw, P. K., Logsdon, W. A., and Attaar, M. H., "Automated Near-Threshold Fatigue Crack Growth Rate Testing of JBK-75 Stainless Steel at Cryogenic Temperatures," *Aus-*

tenitic Steels at Low Temperatures, R. P. Reed and T. Horiuchi, Eds., Plenum Press, 1982, pp. 171–185.
[25] Suresh, S., Zamiski, G. F., and Ritchie, R. O., "Oxide-Induced Crack Closure: An Explanation for Near-Threshold Corrosion Fatigue Crack Growth Behavior," *Metallurgical Transactions A,* Vol. 12A, Aug. 1981, pp. 1435–1443.
[26] Liaw, P. K., Swaminathan, V. P., Leax, T. R., and Donald, J. K., "Influence of Load Ratio on Near-Threshold Fatigue Crack Propagation Behavior," *Scripta Metallurgica,* Vol. 16, 1982, pp. 871–876.
[27] Liaw, P. K., Leax, T. R., Williams, R. S., and Peck, M. G., "Influence of Oxide-Induced Crack Closure on Near-Threshold Fatigue Crack Growth Behavior," *Acta Metallurgica,* Vol. 30, 1982, pp. 2071–2078.
[28] Benoit, D., Namdar-Irani, R., and Tixier, R., "Oxidation of Fatigue Fracture Surfaces at Low Crack Growth Rates," *Materials Science and Engineering,* Vol. 45, 1980, pp. 1–7.
[29] Davidson, D. L., "Incorporating Threshold and Environmental Effects into the Damage Accumulation Model for Fatigue Crack Growth," *Fatigue of Engineering Materials and Structures,* Vol. 3, 1981, pp. 229–236.
[30] Minakawa, K. and McEvily, A. J., "On Crack Closure in the Near-Threshold Region," *Scripta Metallurgica,* Vol. 15, 1981, pp. 633–636.
[31] Otsuka, A., Mori, K., and Miyata, T., "The Condition of Fatigue Crack Growth in Mixed Mode Condition," *Engineering Fracture Mechanics,* Vol. 7, 1975, pp. 429–439.
[32] Petit, J. and Maillard, J. L., "Environment and Load Ratio Effects on Fatigue Crack Propagation Near Threshold Conditions," *Scripta Metallurgica,* Vol. 14, 1980, pp. 163–166.
[33] Irving, P. E. and Beevers, C. J., "The Effect of Air and Vacuum Environments on Fatigue Crack Growth Rates in Ti-6Al-4V," *Metallurgical Transactions A,* Vol. 5A, Feb. 1974, pp. 391–398.
[34] Irving, P. E. and Kurzfeld, A., "Measurements of Intergranular Failure Produced During Fatigue Crack Growth in Quenched and Tempered Steels," *Metal Science,* Nov. 1978, pp. 495–502.
[35] Priddle, E. K., Walker, F., and Wiltshire, C., *Proceedings,* Conference on the Influence of Environment on Fatigue, Institute of Mechanical Engineering, London, England, 1977, p. 137.
[36] Liaw, P. K. and Logsdon, W. A., unpublished research.
[37] Walk, N. and Beevers, C. J., "A Fatigue Crack Closure Mechanism in Titanium," *Fatigue of Engineering Materials and Structures,* Vol. 1, 1979, p. 135.
[38] Minakawa, K. and McEvily, A. J., "On Near-Threshold Fatigue Crack Growth in Steels and Aluminum Alloys," *Fatigue Thresholds,* J. Backlund, A. Blom, and C. J. Beevers, Eds., EMAS Publishers, Warley, England, 1981, p. 373.
[39] Ritchie, R. O. and Suresh, S., "Some Considerations on Fatigue Crack Closure at Near-Threshold Stress Intensities Due to Fracture Surface Morphology," *Metallurgical Transactions A,* Vol. 13A, May 1982, p. 937.
[40] Liaw, P. K., Saxena, A., Swaminathan, V. P., and Shih, T. T., "Effects of Load Ratio and Temperature on the Near-Threshold Fatigue Crack Propagation Behavior in a CrMoV Steel," *Metallurgical Transactions A,* Vol. 14A, Aug. 1983, p. 1631.
[41] Yu, W., Esaklul, K., and Gerberich, W. W., "Fatigue Threshold Studies in Fe, Fe-Si, and HSLA Steel. Part II: Thermally Activated Behavior of the Effective Stress Intensity at Threshold," *Metallurgical Transactions A,* Vol. 15A, May 1984, pp. 889–900.
[42] Park, D. H. and Fine, M. E., "Near-Threshold Fatigue Crack Propagation in Fe and Al-3% Mg," in *Proceedings,* Symposium on Fatigue Crack Growth Threshold Concepts, TMS-AIME, Philadelphia, Oct. 1983, D. L. Davidson and S. Suresh, Eds., pp. 145–161.
[43] Liaw, P. K., Leax, T. R., and Logsdon, W. A., "Near-Threshold Fatigue Crack Growth Behavior in Metals," *Acta Metallurgica,* Vol. 31, 1983, p. 1581–1587.
[44] Fine, M. E., *Bulletin of the Japan Institute of Metals,* Vol. 20, 1981, p. 668.
[45] Liaw, P. K. and Logsdon, W. A., "Fatigue Crack Growth Threshold at Cryogenic Temperatures: A Review," *Engineering Fracture Mechanics,* in press.

STP857-EB/Mar. 1985

DISCUSSION

L. D. Roth[1] (*written discussion*)—Could you distinguish between the effect of temperature and that of environment in liquid nitrogen and liquid helium? That is, would you not expect to see the R ratio effect at 77 and 4.2 K if the specimen were tested in air in a refrigerated system at 77 and 4.2 K? I would assume that the liquid nitrogen and liquid helium have a very low solubility of oxygen and hence very little oxide should form. In refrigerated air at the same temperature, however, oxides might form, which would mean this is an environmental effect and not just a temperature effect. Have any tests been performed in oxygenated liquid nitrogen?

P. K. Liaw et al (authors' closure)—At 77 or 4.2 K the lesser effect of load ratio on ΔK_{th} than at 297 K is related to the decreased extent of oxide and roughness-induced crack closure. Even though oxygen is present in a refrigerated air system at 77 or 4.2 K, it is expected that fretting oxidation during near-threshold crack propagation would have difficulty in occurring because of the low diffusion rate of oxygen at cryogenic temperatures. The fracture surfaces in refrigerated air at 77 or 4.2 K may be smoother than those in room temperature air, as observed by the present authors with liquid nitrogen and liquid helium (unpublished work). Therefore, the near-threshold fatigue crack growth rates may be insensitive to load ratio in refrigerated air because of the decreased oxide and roughness-induced crack closure.

The solubility of oxygen is low in liquid nitrogen and liquid helium. However, there is a difference in near-threshold fatigue crack growth rates at 77 and 4.2 K. This behavior suggests that there exists an intrinsic temperature effect on fatigue crack propagation rates.

We did not conduct tests in oxygenated liquid nitrogen.

[1] Westinghouse R&D Center, Pittsburgh, PA 15235.

Yosef Katz, Arieh Bussiba, and Haim Mathias

Effect of Warm Prestressing on Fatigue Crack Growth Curves at Low Temperatures

REFERENCE: Katz, Y., Bussiba, A., and Mathias, H., "**Effect of Warm Prestressing on Fatigue Crack Growth Curves at Low Temperatures,**" *Fatigue at Low Temperatures, ASTM STP 857,* R. I. Stephens, Ed., American Society for Testing and Materials, Philadelphia, 1985, pp. 191–209.

ABSTRACT: Low-temperature fatigue crack extension is studied in precracked single-edge-notched specimens of AISI 4340 steel. Steady-state crack extension in tension-tension fatigue and cyclic loading in conjunction with warm prestressing (WPS) are particularly emphasized. Effects of WPS on the fatigue crack growth curve are demonstrated and discussed. Special attention is given to the cleavage fracture mode, which dominates the features of the fatigue crack growth curve below the ductile-brittle transition (DBT) temperature. In AISI 4340 steel, which is characterized by DBT, WPS affects the alternative fracture mode and therefore alters the lower and upper bound values K_{th} and K_{Ifc}, respectively. For a more complete view, the behavior of AISI 304 stainless steel is discussed. The experimental results at low temperatures are mainly interpreted in terms of a transition in the cumulative crack tip damage process, induced by characteristic values of the stress intensity range amplitudes (ΔK).

KEY WORDS: fatigue crack propagation rates, threshold, effective stress intensity factor, warm prestressing, ductile-brittle transition, cleavage, frequency effect, steel

Thermal effects on plastic flow behavior clearly influence fatigue crack propagation rates (FCPR) at low temperatures. However, there exist two additional events that are very typical of the low-temperature environment and might dominate the peculiar nature of the FCPR curve: first, the ductile-brittle transition (DBT) phenomenon in body-centered-cubic (BCC) and hexagonal-close-packed (HCP) systems, which introduces a fracture mode transition, and second, the possible formation of martensitic phases with high volume concentrations in metastable austenitic materials [*1,2*]. The latter is associated with some further complexity, since the stress level for irreversible deformation is altered and the intrinsic fatigue resistance might be changed because of microstructural transformations.

All three authors are research scientists at the Nuclear Research Center–Negev, Beer-Sheva, Israel.

The events mentioned above are probably the cause of the dispute in the literature regarding the differences in fatigue crack growth rates between 77 K and ambient temperatures. For example, Bucci et al [3] have obtained small changes in the crack growth rates of 9-Ni steel measured at 77 K and room temperature. On the other hand, Moody and Gerberich [4] have found an increase in FCPR in Fe, Fe-Si, and Fe-Ni binary alloys below the DBT temperature. Moreover, it appears that not enough has been done in exploring such differences along the entire fatigue curve, namely from the near threshold value up to the critical value of the applied stress intensity factor. Thus a clear distinction between the tested materials in terms of the DBT, as well as a clearer indication of the relevant fatigue crack curve region, is necessary in order to explain some of the conclusions that have been derived by several investigators in the field of fatigue at low temperatures [3–7].

For the case of crack extension enhanced by an alternative mode, Gerberich and Moody [8] have pointed out the restriction of the dislocation dynamic theory proposed by Yokobori [9]. Consequently, for materials below the DBT they suggested a cyclic cleavage model in order to explain the high value of the cyclic exponents obtained at low temperatures.

Based on recent research in AISI 4340 steel [10], austenitic stainless steels [1,2], and Zn-22Al superplastic alloy [11], a consistent trend has been established in fatigue at low temperature, as compared to ambient temperature. This tendency applies to materials that are characterized by DBT phenomenon. First, a shift in the threshold stress intensity factor K_{th} to higher values occurs. Additionally, the FCPR decreases only along Stage I. Secondly, there is some fatigue life at low temperatures that is due to the absence of a discrete critical stress intensity value below the DBT temperature. The fatigue curve is approaching such a critical value, in terms of a drastic degeneration of Stage II as the temperature goes down. Thirdly, below the DBT temperature the upper asymptotic bound of the degenerated sigmoidal fatigue curve is the fatigue-critical plane-strain fracture toughness (K_{Ifc}) rather than plane-strain fracture toughness (K_{Ic}) ($K_{Ifc} < K_{Ic}$). This final point was addressed in the work of Yokobori [12] and has been recently reconfirmed [10].

For materials not characterized by DBT, the fatigue behavior at low temperatures is completely different. In AISI 304 stainless steel, at temperatures down to 77 K, a consistent decrease of the FCPR was obtained along the whole fatigue curve up to the fatigue-critical plane-stress fracture toughness (K_{fc}), which is nearly equal to the plane-stress fracture toughness (K_c) [10]. This behavior was mainly attributed to the increase of the flow stress caused by its thermal dependency.

The peculiar behavior of Stage I below the DBT temperature introduces the problem of cleavage processes in terms of nucleation and propagation. Moreover, this behavior also introduces the question of cleavage criteria in the case of a steep stress gradient, as occurs in fatigue crack extension initiated by sharp flaws.

The present investigation is centered on the typical features of the FCPR curve at low temperatures in AISI 4340 steel with and without warm prestressing (WPS). For a comparative study some attention is given to experimental results in 304 stainless steel in order to demonstrate the dominating role of the DBT in fatigue processes. Two issues are particularly treated: fatigue behavior at Stage I and the significant decrease of the upper bound K_{Ifc} relative to K_{Ic} below the DBT temperature. For the latter, the experimental program has been extended to include the effects of WPS on the low-temperature FCPR curve. The knowledge of such interactive effects is important in order to deal with some of the basic issues already mentioned.

The WPS phenomenon has been reviewed by Nichols [*13*] and was investigated recently by Chell et al [*14*] and Curry [*15*]. Generally, WPS improves the resistance of BCC and HCP systems to brittle fracture. Specifically, loading-unloading tensile cycling of precracked specimens above the DBT temperature results in higher values of the critical stress intensity factor, as compared to the normally obtained values below the DBT temperature. There have been several attempts to explain these effects of WPS in terms of work hardening, crack tip blunting effects, and possible effects of the effective stress intensity and its variation after a WPS cycle.

So far the effects of WPS have been established in monotonic loading, but no research activity has explored WPS effects in cyclic loading. The present study emphasizes the effects of WPS on fatigue crack extension curves at low temperatures, attempting to use this information to explain some of the basic problems of fatigue below DBT temperatures.

Experimental Procedure

The material studied was AISI 4340 steel; its composition in weight percent was carbon, 0.38; nickel, 1.9; chromium, 0.85; manganese, 0.80; molybdenum, 0.25; silicon, 0.2; copper, 0.13; aluminum, 0.05; sulfur, 0.004; phosphorus, 0.006; and iron for the balance. This steel was tested in different metallurgical states after selected heat treatments. Standard mechanical properties were established, including the critical fracture toughness parameters at 77 and 296 K. These parameters were determined in accordance with ASTM Test for Plane-Strain Fracture Toughness of Metallic Materials (E 399). In addition, impact testing was performed in order to determine the DBT temperature and its variation with microstructure.

Fatigue tests were carried out by using an electrohydraulic closed loop system with a load amplitude control device. Compact precracked single-edge-notched specimens 12 mm in thickness were used under controlled ΔK cycling with a sinusoidal waveform at 77 and 296 K. A range of different frequencies (0.1 to 80 Hz) was applied with $R \simeq 0$ to minimize load-ratio effects. Crack length was measured by direct tracking observations and by an electropotential technique that yielded complete curves of the steady-state FCPR versus the nominal ΔK. The FCPR dependency on the nominal ΔK was obtained according to the relation

$$\Delta K = \frac{\Delta P Y}{B W^{1/2}}$$

where

$$Y = 29.6\,(\bar{a}/W)^{1/2} - 185.5\,(\bar{a}/W)^{3/2} + 655.7\,(\bar{a}/W)^{5/2} - 1017\,(\bar{a}/W)^{7/2} + 638.9\,(\bar{a}/W)^{9/2}$$

and ΔP is the applied cycling load, $\bar{a}$ is the crack length, and B and W are the specimen thickness and width, respectively.

This experimental procedure enabled us to calculate the asymptotic values for the lower limit (ΔK_{th}) and the upper limit (K_{Ifc}) from the FCPR curves. An additional section of the experimental scheme was WPS in monotonic loading and during cyclic conditions. Generally, WPS was performed by a single load cycle of $K^{WPS} = \beta K_{Ic}$ at 296 K (with the constant $\beta < 1$), while subsequent monotonic or cyclic loading was carried out at 77 K, as schematically illustrated in Figs. 1 and 2, respectively.

In fact, WPS at 296 K was first performed after interrupting the 77 K steady-state fatigue crack extension of nearly 10^{-5} mm/cycle. Since the WPS resulted in crack arrest, the subsequent 77 K cyclic loading was applied at a higher ΔK than before the WPS. Keeping ΔK constant, the cycling was con-

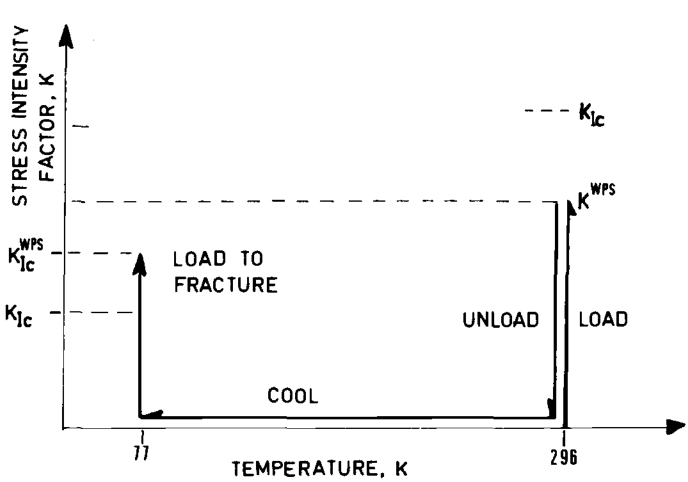

FIG. 1—*Monotonic loading after warm prestressing.*

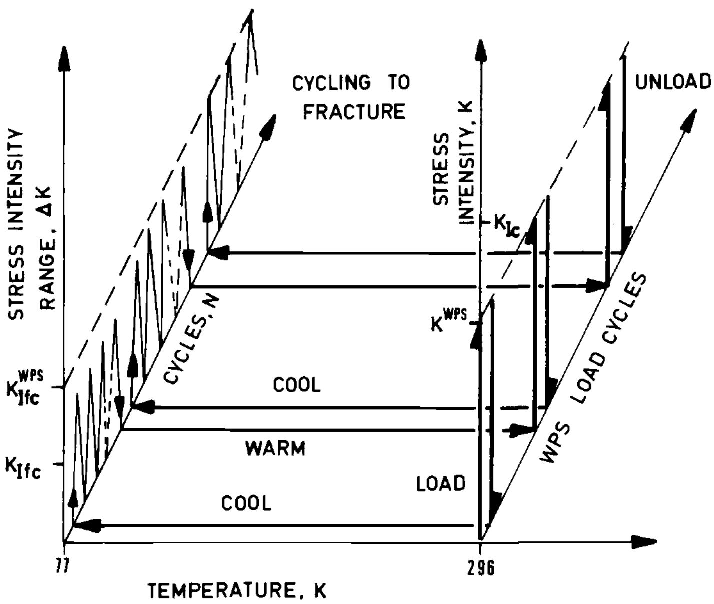

FIG. 2—*Cyclic loading interrupted by warm prestressing.*

tinued until the FCPR approached the former steady-state value. This procedure of WPS and subsequent cyclic loading at stepwise enlarged ΔK values was repeatedly applied until unstable crack growth occurred. The corresponding stress intensity upper limit was designated by $K_{\rm Ifc}^{\rm WPS}$. Similarly, the critical stress intensity factor obtained after WPS for monotonic loading was designated $K_{\rm Ic}^{\rm WPS}$.

During the WPS, particular attention was given to acoustic emission (AE) activity. Following cyclic loading at 77 K, comparative AE signals were recorded during two successive load cycles at 296 K.

Fractographic studies were performed for steady-state fatigue crack propagation by tracking the modes at different stages along the fatigue crack extension curves at 296 and 77 K. Special emphasis was given to fracture surface studies at the early stages of fatigue crack growth, as well as during crack extension following WPS.

For comparison, steady-state fatigue tests were performed on AISI 304 stainless steel whose composition in weight percent was carbon, 0.05; nickel, 9.5; chromium, 18.6; manganese, 1.2; molybdenum, 0.23; copper, 0.25; silicon, 0.44; sulfur, 0.016; phosphorus, 0.033; and iron for the balance. Although the martensitic transformation occurred, namely the $\gamma \rightarrow \epsilon' + \alpha'$ transformation [*1,2*] (where γ is the face-centered austenitic phase and ϵ' and α' are the close-packed hexagonal and the body-centered martensitic phases, respectively), this material is not characterized by DBT down to 77 K. Typical fatigue curves were obtained for AISI 304 steels, for contrast with the behavior of AISI 4340 steel, which is a BCC system dominated by the fracture transition at low temperature.

Experimental Results

The various heat treatments and corresponding mechanical properties of AISI 4340 steel are summarized in Table 1. Notice that the three metallurgical states are designated H0, H1, and H2. While the H0 consisted of proeutectoid ferrite and pearlite phases, the H1 and the H2 were tempered martensite at two different strength levels. As revealed by impact testing, the 296 and 77 K temperatures are above and below the DBT temperature. A complete cleavage mode occurred at 77 K. For the AISI 304 stainless steel the yield stress (0.2% offset) was 260 and 510 MPa at 296 and 77 K, respectively, while the ultimate tensile stress was 590 and 1350 MPa at 296 and 77 K, respectively.

Figure 3 shows FCPR curves in AISI 4340 at 77 and 296 K for the H0, H1, and H2 heat treatments. For comparison, the fatigue curve for the 304 stainless steel is given in Fig. 4. For AISI 304 the regular shape of the FCPR curve is preserved at 77 K, but with a consistent shift to the right relative to the 296 K curve for the entire range of the applied ΔK values.

As previously mentioned, the Stage II region in 77 K fatigue of AISI 4340 is degenerated, and the two critical limits are altered. Values for ΔK_{th} are shifted to the right and Region I is associated with decreased fatigue crack growth rates da/dN, up to nearly $(da/dN)_{eq}$, defined at ΔK where ambient and low temperature rates are equal. Above this value a dramatic increase of the crack growth occurred with an upper critical limit $K_{Ifc} < K_{Ic}$. This relationship is typical of fatigue below the DBT temperature, while at room temperature $K_{Ifc} \simeq K_{Ic}$, as was also found for the Type 304 stainless steel at 77 K.

Figure 5 illustrates the fatigue crack extension curve for Type 4340 steel at 77 K for two frequencies. Here, a decrease of the FCPR was obtained for cyclic loading at the higher frequency.

Some of the fractographical findings are particularly interesting. For type 4340 H0 condition, Fig. 6 demonstrates mode changes in fatigue fracture from the near-threshold value and later stages associated with increasing ΔK. It should be mentioned that for early stages of crack extension no striations were observed. This is typical for the tested material even at room temperature. Nevertheless, the important point is that there was no cleavage mode but rather a relatively high-energy mixed mode (Fig. 6*a*).

Figures 6*b* and 6*c* show the mixed fracture mode at increased ΔK for the H0 and H1 conditions, respectively. Notice the start of a mode transition associated with "static" cleavage, still isolated but readily observed.

Figure 6*d* illustrates the fatigue fracture surface at a further increased ΔK,

TABLE 1—*Heat treatments and mechanical properties of AISI 4340 steel.*

Heat Treatment Conditions and Designation	Yield Stress, 0.2% Offset, ($\sigma_{0.2}$), MPa		Ultimate Tensile Stress (σ_{UTS}), MPa		Elongation (e), %		Critical Fracture Toughness (K_{Ic}) MPa·m$^{1/2}$		Rockwell C Hardness	Grain Size, μm
	296 K	77 K	296 K	77 K	296 K	77 K	296 K	77 K		
As-received (HO)	350	680	680	935	18.0	0.4	100	30	22	25
Austenitized at 850°C for ½ h and tempered at 480°C for 4 h (H1)	1100	1325	1225	1410	10.8	4.8	110	42	38	12–15
Austenitized at 850°C for ½ h and tempered at 280°C for 4 h (H2)	1520	1810	1760	1810	5.2	0.6	75	36	48	12–15

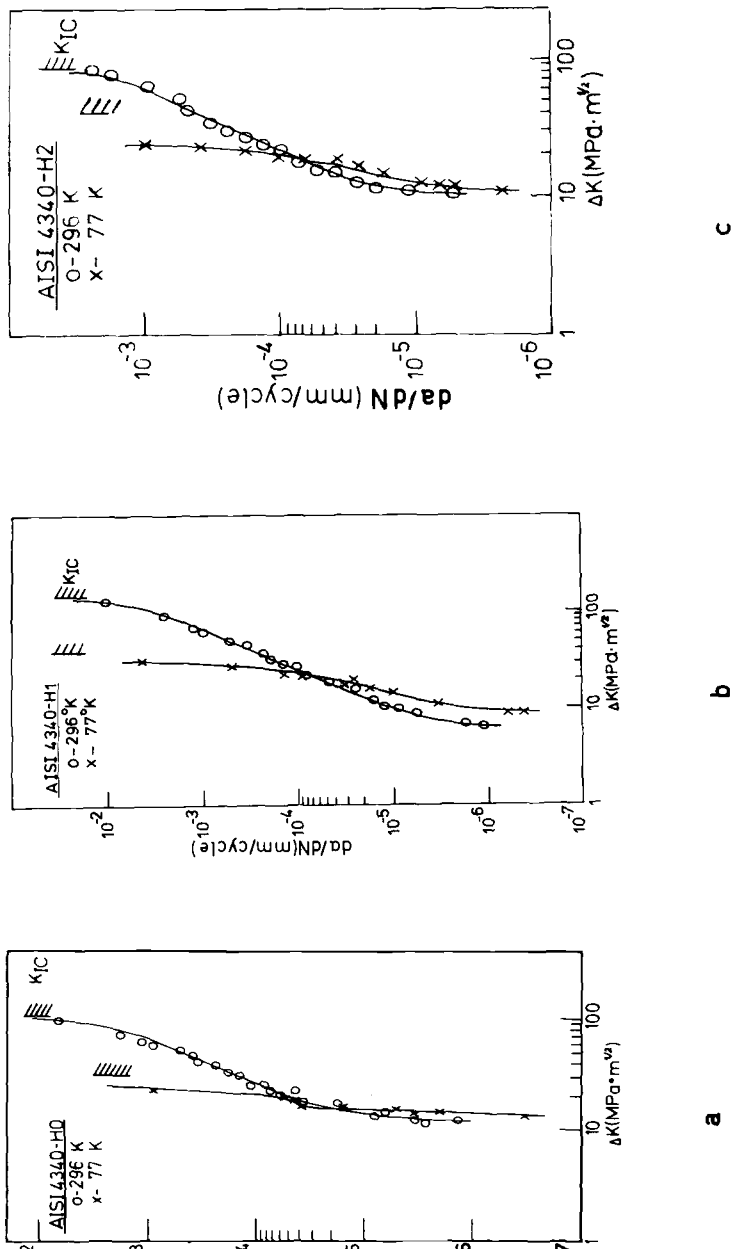

FIG. 3—*Fatigue crack propagation rate versus ΔK curves in AISI 4340 steel after (a) HO, (b) H1, and (c) H2 heat treatments.*

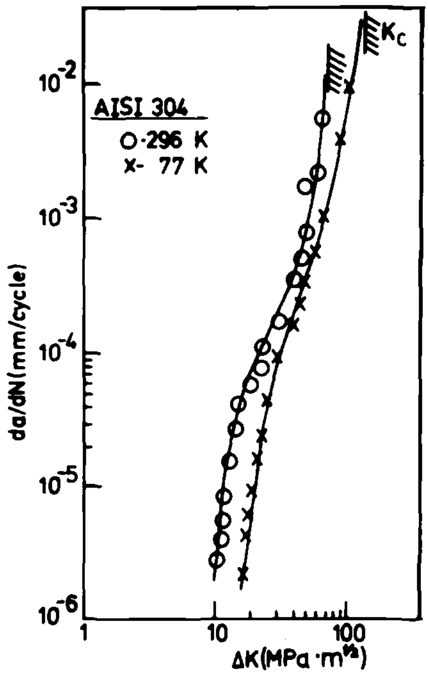

FIG. 4—*Fatigue crack propagation rate versus* ΔK *curves in austenitic (296 K) and microduplex (77 K) Type 304 steel.*

or higher crack extension rate, showing a complete cleavage mode, which dominates the fracture process under cyclic loading conditions. In contrast, ductile striations were detected at Stages II and III in the AISI 304 stainless steel (Fig. 7). Although some second interphase decohesion was observed at 77 K, the basic ductile striation mode was preserved.

The experimental results for WPS in AISI 4340 can be summarized as follows. For the H1 heat treatment and for $\beta = 0.75$, WPS in monotonic loading resulted in a ratio $K_{Ic}^{WPS}/K_{Ic} = 1.3$. This is the ratio between fracture toughness at 77 K after WPS and without it. Similar tests for H0 heat treatment provided a ratio of $K_{Ic}^{WPS}/K_{Ic} = 1.52$. Clearly, a significant effect of WPS in monotonic loading was measured for both microstructures.

With respect to the interaction of WPS with fatigue crack extension, the procedure and results are briefly described. For example, the steady-state fatigue crack extension at 77 K was interrupted at a crack extension rate of 1.3×10^{-5} mm/cycle, which corresponded to the stress intensity range of $\Delta K = 13.2$ MPa·m$^{1/2}$ for the H1 treatment. Here WPS was performed for $\beta = 0.75$, and crack arrest was experienced for more than 3×10^4 cycles. After this stage, cycling at a progressively increasing ΔK was repeatedly interrupted by additional WPS of double load cycles for $\beta = 0.65$ with simultaneous tracking of AE spectra after each cycling block. Figure 8*a* shows the

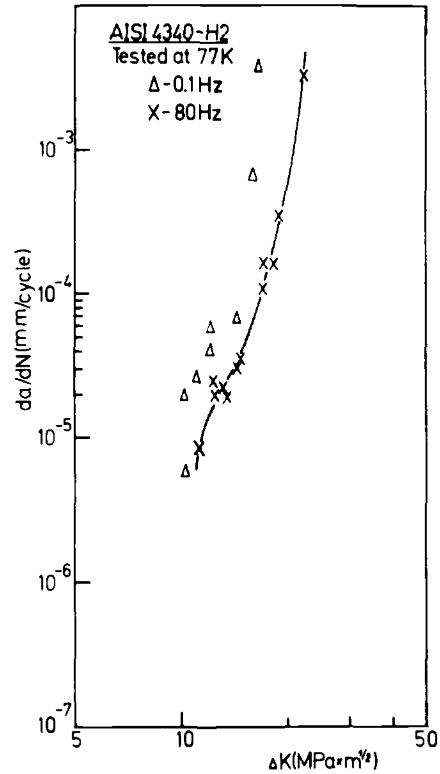

FIG. 5—*Frequency effects below the DBT temperature.*

massive activity of high-intensity AE waves associated with the first WPS cycle.

In contrast, a significant decrease of AE activity was obtained during the second WPS cycle (Fig. 8*b*). After each WPS the crack extension rate at preselected ΔK values was limited to the velocity range of 2×10^{-5} to 1×10^{-4} mm/cycle. This procedure enabled us to extend the applicable ΔK range and to determine the correspondingly higher K_{Ifc}^{WPS} value.

For the H1 treatment, $K_{\text{Ifc}}/K_{\text{Ic}}$ with no WPS process yielded a ratio of 0.65, while in the case of WPS the corresponding ratio, $K_{\text{Ifc}}^{\text{WPS}}/K_{\text{Ic}}^{\text{WPS}}$, increased to 0.73. This clearly indicated that $K_{\text{Ifc}}^{\text{WPS}}$ exceeded the upper conventional limit (K_{Ifc}) and almost approached the value of the conventional K_{Ic}, as expressed by the ratio $K_{\text{Ifc}}^{\text{WPS}}/K_{\text{Ic}} \simeq 1$.

As already shown, the effect of WPS on the final critical stress in monotonic loading was more evident in the H0 than in the H1 material. A similar tendency was obtained in the case of cyclic loading. Here, double WPS cycles were applied after the FCPR reached the value of 9×10^{-6} mm/cycle. At this stage the amplitude range (ΔK) was increased stepwise, and WPS was re-

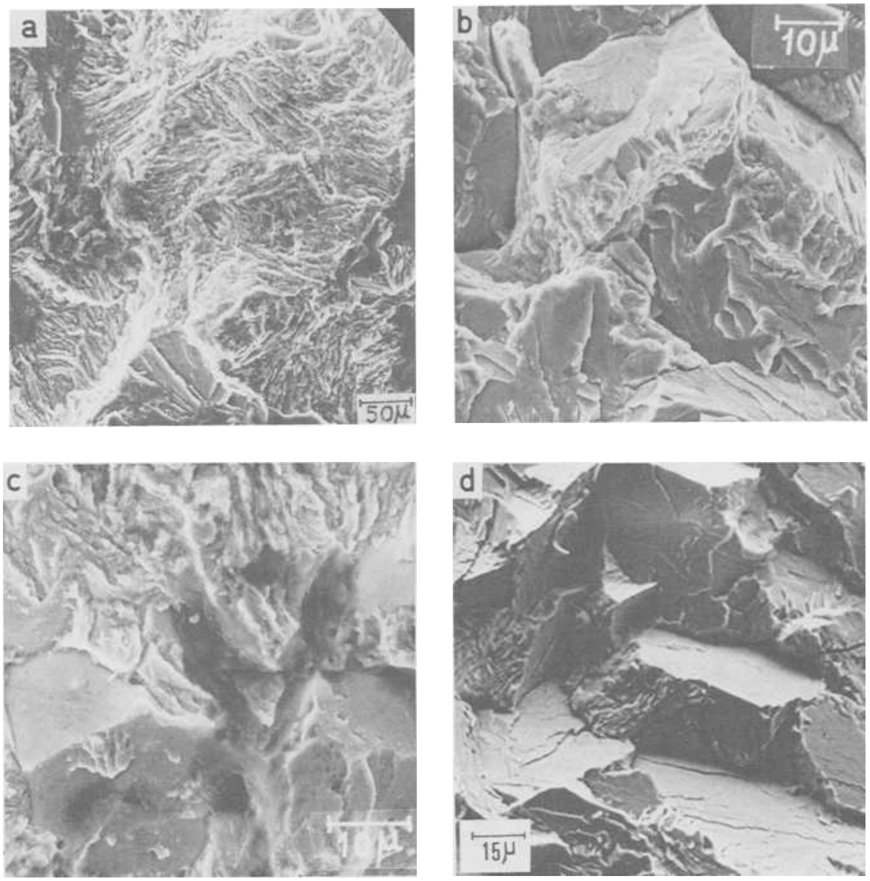

FIG. 6—*Fatigue fracture modes in AISI 4340 steel for 77 K cycling at 10 Hz.* (a) *Ductile mode at Stage I for HO;* $\Delta K = 14\ MPa \cdot m^{1/2}$. (b) *Mixed ductile-cleavage mode at Stage II for HO;* $\Delta K = 18\ MPa \cdot m^{1/2}$. (c) *Mixed ductile-cleavage mode at Stage II for HI;* $\Delta K = 19\ MPa \cdot m^{1/2}$. (d) *Cleavage mode at Stage III for HO;* $\Delta K = 21\ MPa \cdot m^{1/2}$.

peated after each fatigue run. Significant AE activity was observed during the first WPS cycle and higher values were obtained for the upper critical limit. For this material it was found that the ratio K_{Ifc}/K_{Ic} equalled 0.72, while in the case of warm prestressing a ratio of $K_{Ifc}^{WPS}/K_{Ic}^{WPS} = 0.94$ was obtained. Additionally, it was found that $K_{Ifc}^{WPS}/K_{fc} = 2$, whereas in monotonic loading the corresponding ratio was only 1.52.

Fractographic observations of the region affected by WPS revealed a fracture mode transition. For example, Fig. 9*a* illustrates the occurrence of a mixed mode fracture at a ΔK value for which a complete cleavage mode was usually observed without WPS. Figure 9*b* demonstrates the appearance of an apparent ductile mode at a ΔK value that generally resulted in a mixed-mode fracture during 77 K steady-state fatigue.

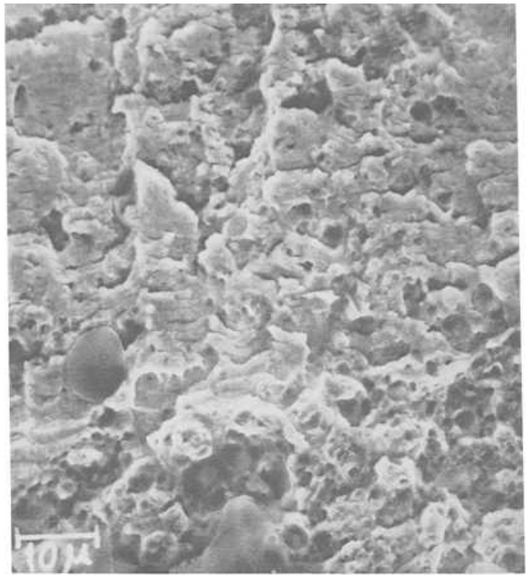

FIG. 7—*Ductile striations in Type 304 stainless steel for 77 K cycling at 10 Hz during stage II;* $\Delta K = 44\ MPa \cdot m^{1/2}$.

Discussion

The current experimental results indicate that WPS influences are not exclusive to monotonic loading. At low temperatures, the FCPR versus ΔK curve, including the upper limit K_{Ifc} values, are in fact sensitive to the WPS process and are strongly influenced by variations of the localized stress distribution field at the vicinity of the crack tip.

Furthermore, the dominating factor in shaping the FCPR curve below the DBT temperature is attributed to crack extension enhanced by the cleavage mode. Therefore WPS, which affects the necessary conditions needed to satisfy the cleavage criteria, should be reflected in the FCPR curves. This has been confirmed experimentally in the present study.

In the case of monotonic loading, WPS results in an apparent increase of the critical fracture toughness parameters. Clearly, this influence relates to a modification of the critical conditions for cleavage, since cleavage is the dominating fracture mode below the DBT temperature. Consequently, it is believed that in cyclic loading also WPS effects should be examined in terms of a possible hindrance of the microscopic cleavage mode.

While referring to the problem of WPS in ferritic steels under monotonic loading conditions, Curry [*15*] proposed a prediction method for the final fracture load after the WPS. His predictions, as well as predictions by Chell et al [*14*], have been shown to be in very good agreement with experimental results. In fact, Chell et al used a completely different approach, one based

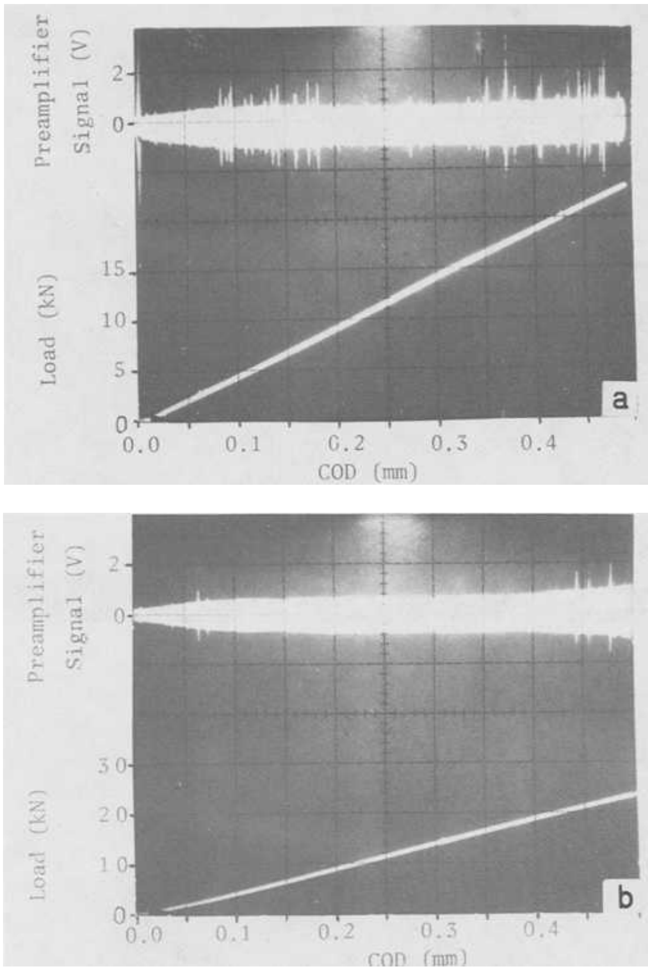

FIG. 8—*Acoustic emission activity in AISI 4340 steel during warm prestressing after* 2×10^4 *fatigue cycles at 77 K;* $\Delta K = 16\ MPa \cdot m^{1/2}$. *Upper and lower traces represent AE activity and loading respectively versus crack opening displacement for the first* (a) *and second* (b) *WPS cycle.*

on the *J*-integral, not on the main argument which is based on the cleavage fracture criteria of Ritchie et al [*16*]. According to these criteria, cleavage fracture will occur only when the local stress exceeds the cleavage fracture stress over some microstructurally determined characteristic distance. It is realized that in cyclic loading dynamic factors are involved, but the main idea of a characteristic distance remains as a central feature that might propose a proper explanation of fatigue behavior below the DBT temperature. For example, the FCPR curves at 77 and 296 K indicate a peculiar behavior in Stage I (Fig. 3). As shown, during this stage the fracture is not enhanced by microcleavage and the thermal effects on FCPR are preserved.

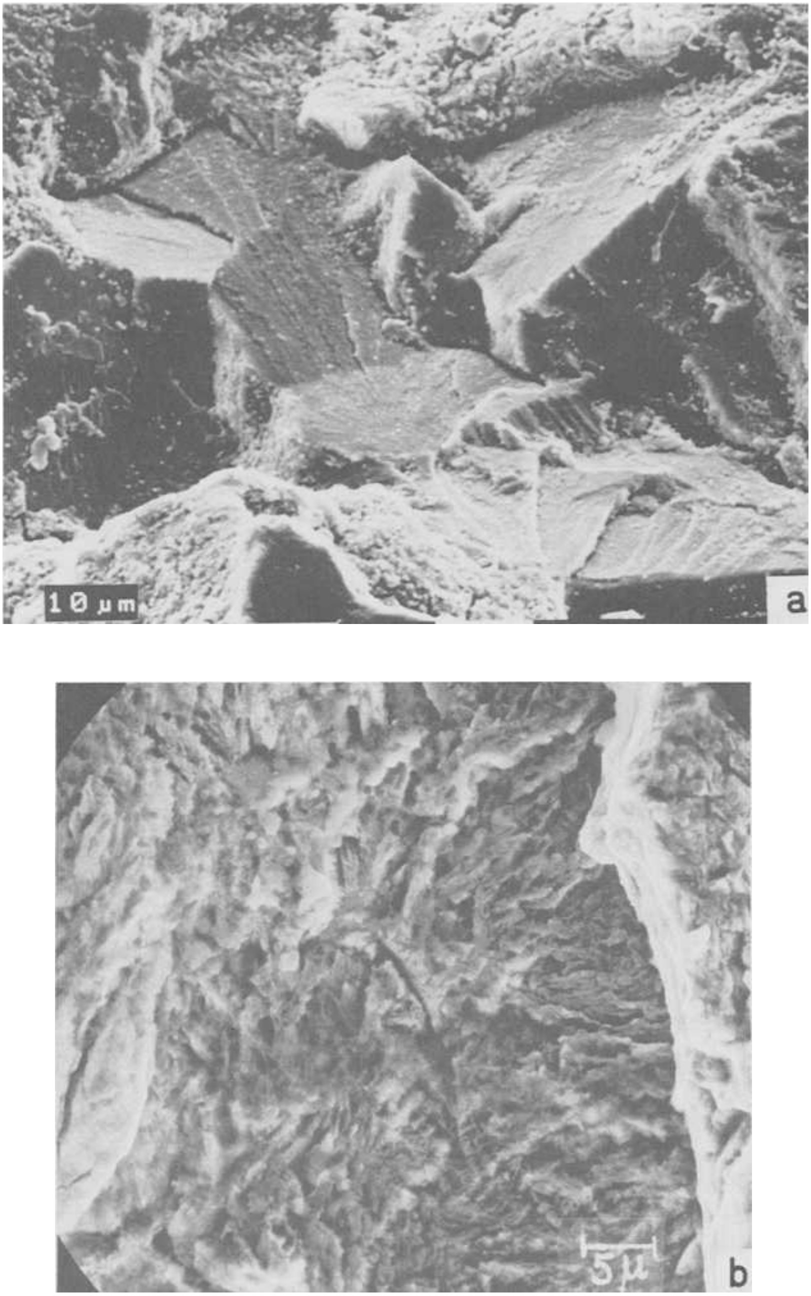

FIG. 9—*77K fatigue fracture in AISI 4340 steel after WPS.* (a) *Mixed mode in HO material for* $\Delta K = 30$ *MPa·m*$^{1/2}$ *and* $\beta = 0.75$. (b) *Ductile mode in H1 material for* $\Delta K = 28$ *MPa·m*$^{1/2}$ *and* $\beta = 0.65$.

Only during Stage I is the behavior similar to that of materials that are not characterized by a DBT (Fig. 4), where the FCPR values increase with temperature elevation. The dislocation group theory [9] trend prevails along Stage I even below the DBT temperature. This behavior can be attributed to the characteristic distance (S_0) that is not satisfied near the threshold values (although the localized fracture stress is exceeded), resulting in a regular fatigue initiation process even at low temperature.

Figure *6a* strongly supports this explanation, since mixed-mode fracture or a complete cleavage mode with a significant increase of the FCPR values develops only at a later stage (Figs. *6b* to *6d*). It appears that the main difference between AISI 4340, which is basically a body-centered-cubic system, and the austenitic AISI 304 lies in the DBT phenomenon.

Notice that in the Type 304 stainless steel the flow stress at 77 K increases significantly because of the martensitic phase formation. However, the absence of DBT is apparently the major factor that keeps the FCPR curve in the more familiar and regular behavior, even with the formation of the martensitic α' phase. The ductile fatigue processes of crack tip blunting and resharpening control the crack extension from near threshold up to the critical value. This comparative study clarifies the role of the microcleavage mode and its reflection on the fatigue curve, thus making the domination of the DBT more evident.

Referring back to the WPS in cyclic loading, two major reasons for the crack growth behavior at low temperatures can be identified. These reasons relate to the flow stress elevation and the decrease of the effective cyclic stress intensity factor (ΔK_{eff}). Curry [15] estimated the characteristic distance for slip-induced cleavage fracture by using the finite element crack tip distribution analysis in plane strain and small-scale yielding developed by Tracey [17] and by Ostergren [18]. For this purpose the cleavage and yield stress as well as the applied stresses and the theoretical stress intensity parameters were measured. Following this approach it can be seen that if the flow stress is raised by thermal effects and ΔK_{eff} decreases because of WPS, then the critical characteristic distance necessary for cleavage is no longer satisfied. Clearly, these circumstances result in the prevention of the cleavage mode, so that crack extension can occur only by ductile fatigue and by the conventional cumulative damage processes (Fig. *9b*).

As ΔK is raised, cleavage might occur, increasing the crack extension rate (Fig. *9a*). This trend has been demonstrated in the present study by the experimental results. According to these findings, the following modified view on the role of cumulative damage below the DBT temperature is proposed.

Let us consider the ductile steady-state fatigue crack propagation process. Here, cumulative damage is localized at the process zone, which is smaller than the dynamic plastic zone. Because of the extremely steep damage accumulation gradient at the vicinity of the crack tip, the prior cyclic history is relatively masked during an incremental crack growth.

In contrast, fatigue crack growth below the DBT temperature and above a critical value of ΔK can be viewed by cumulative damage in terms of microcleavage events that develop beyond the process zone. These discrete events are pronounced during high rates of crack extension. Thus cyclic loading at low temperature above Stage I can be associated with a crack tip damaging mechanism highly dependent on ΔK amplitudes.

The formation of this kind of damage zone seems to be responsible for the reduction of the upper bound limit, namely $K_{Ifc} < K_{Ic}$. Consequently, warm prestressing, which affects the cleavage mode, should result in a higher value of K_{Ifc} and even close the gap between K_{Ifc} and K_{Ic}.

At a certain stage of the present investigation it was assumed that lower K_{Ifc} values below the DBT temperature are related to dynamic aspects. It was hypothesized that K_{Ifc} might be connected to critical dynamic or crack arrest values. This idea was investigated by cyclic loading in the range of frequencies between 0.1 and 80 Hz (Fig. 5). The results showed a tendency toward frequency-dependent FCPR changes, as has already been indicated by Gerberich et al [*19*]. Actually, the effects obtained were significantly smaller than expected. With respect to the K_{Ic} value, however, the aforementioned dynamic approach was not confirmed at the frequency range tested.

Figures 10 and 11 show schematically the nature of fatigue curves in materials that are characterized by DBT. With respect to life predictions at low temperatures, the shape of this curve has to be considered by including the typical elements that become more and more evident at low temperatures.

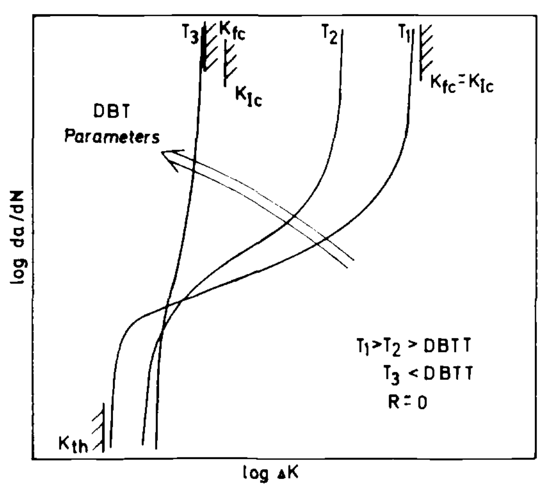

FIG. 10—*Schematic fatigue curves above and below the DBT temperature.*

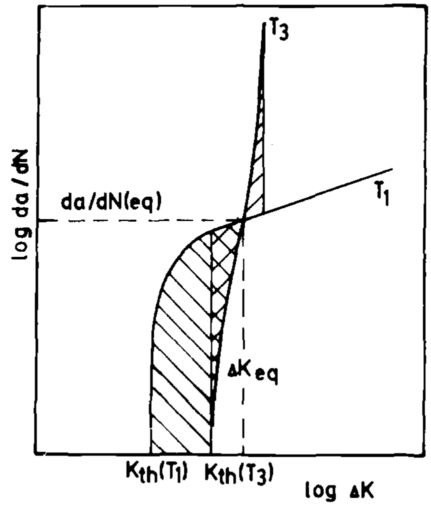

FIG. 11—*Schematic fatigue curves with emphasis on typical features at low temperature.*

As shown in Fig. 11, a higher value for ΔK_{th} is obtained at a low temperature (T_3). Only in the limited range between ΔK_{th} (T_3) and ΔK_{eq} are the FCPR values lower for T_3, which is below the DBT temperature.

Finally, tests of WPS in Type 304 stainless steel and fatigue at low temperatures is being carried out in our laboratory. At this stage no significant effect has been observed in austenitic steel. It appears that in the absence of the microcleavage fracture mode sensitivity to WPS is drastically reduced, which emphasizes again the major role of the alternative brittle mode in fatigue processes at low temperatures.

Conclusions

1. DBT phenomena and microcleavage fracture are major events in shaping the typical FCPR curve at low temperatures.
2. Comparisons between AISI 4340 and 304 stainless steel at 77 and 296 K demonstrate the dominating role of the microcleavage fracture mode in fatigue crack extension processes. With regard to the FCPR curve tendencies, the high concentration of martensitic phases in Type 304 stainless steel plays a minor role.
3. In materials characterized by DBT, WPS strongly affects the FCPR curve at low temperatures.
4. The characteristic distance necessary to satisfy cleavage criteria is a central feature in fatigue crack extension below the DBT temperature, with and without WPS.

5. The upper limit K_{Ifc} is sensitive to WPS; its dependency can be explained in terms of a cumulative damage mechanism at the vicinity of the crack tip.

6. Frequency effects in AISI 4340 at 77 K indicate tendencies similar to those proposed by a cyclic cleavage crack growth model. Quantitatively, the FCPR dependency on frequency is less than has been proposed by the mentioned model.

Acknowledgments

The authors wish to thank Mr. M. Kupiec of the Nuclear Research Center-Negev for experimental assistance during the present investigation.

References

[1] Katz, Y., Bussiba, A., and Mathias, H. in *Materials Experimentation and Design in Fatigue*, F. Sherratt and J. B. Sturges, Eds., IPC Press, Guildford, Westbury House, England, 1981, pp. 147–158.
[2] Katz Y., Bussiba, A., and Mathias, H. in *Proceedings*, 4th European Conference on Fracture, Vol. 2, K. L. Maurer and F. E. Matzer, Eds., Engineering Materials Advisory Services, Warley, West Midlands, England, 1982, pp. 503–511.
[3] Bucci, R. J., Greene, B. N., and Paris, P. C. in *Progress in Flaw Growth and Fracture Toughness Testing, ASTM STP 536*, American Society for Testing and Materials, Philadelphia, 1973, p. 206.
[4] Moody, N. R. and Gerberich, W. W., *Material Science and Engineering*, Vol. 41, 1976, pp. 271–280.
[5] Burck, L. H. and Weertman, J., *Metallurgical Transactions*, Vol. 7A, Feb. 1976, pp. 257–264.
[6] Stonesifer, F. R., *Engineering Fracture Mechanics*, Vol. 10, 1978, p. 305.
[7] Tschegg, E. and Stanzl, S., *Acta Metallurgica*, Vol. 29, 1981, pp. 33–40.
[8] Gerberich, W. W. and Moody, N. R. in *Proceedings*, Fourth International Conference on Fracture, Vol. 3, D. M. R. Taplin, Ed., Solid Mechanics Division, Waterloo, Canada, 1977, pp. 829–838.
[9] Yokobori, T., Yokobori, A. T., Jr., and Kamei, A., *International Journal of Fracture*, Vol. 11, No. 5, Oct. 1975, pp. 781–788.
[10] Bussiba, A., Katz, Y., and Mathias, H. in *Proceedings*, Materials Engineering Conference, I. Minkoff, Ed., Freund Publishing House, Tel-Aviv, 1981, pp. 123–126.
[11] Katz, Y., Bussiba, A., and Mathias, H., "Fatigue in Rate-Dependent Alloy," to be published.
[12] Kawasaki, T., Nakanishi, S., Sawaki Y., Hatanaka, K., and Yokobori, T., *Engineering Fracture Mechanics*, Vol. 7, No. 3, 1975, pp. 465–472.
[13] Nichols, R. W., *British Welding Journal*, Vol. 15, 1968, Jan., pp. 21–42, Feb., pp. 75–84.
[14] Chell, G. G., Haigh, J. R., and Vitek, V., *International Journal of Fracture*, Vol. 17, No. 1, Feb. 1981, pp. 61–81.
[15] Curry, D. A., *International Journal of Fracture*, Vol. 17, No. 3, June 1981, pp. 335–343.
[16] Ritchie, R. O., Knott, J. F., and Rice, J. R., *Journal of the Mechanics and Physics of Solids*, Vol. 21, Nov. 1973, pp. 395–410.
[17] Tracey, D. M., *Journal of Engineering Materials and Technology, Transactions of ASME*, Vol. 98, April 1976, pp. 146–151.
[18] Ostergren, W. I., Master's thesis, Brown University, Providence, RI, March 1969.
[19] Gerberich, W. W., Moody, N. R., and Jatavallabhula, K., *Scripta Metallurgica*, Vol. 14, No. 1, 1980, pp. 113–118.

STP857-EB/Mar. 1985

DISCUSSION

P. K. Liaw[1] (*written discussion*)—Why are crack growth rates at 77 K faster at 0.1 Hz than at 10 Hz?

Y. Katz et al (*authors' closure*)—The effect of frequency on the FCPR has been addressed by Yokobori et al [*9*],[2] who propose a kinetic model that is associated with dislocation generation and activation processes. Accordingly, FCPR is expected to be lower at higher frequencies. Clearly, the case of fatigue crack propagation below the DBT temperature, where the cleavage mode takes place, requires a modified view and explanation. Moody and Gerberich [*4, 19*] attempted a dislocation dynamics model based on cleavage growths steps. They assumed that the dislocations along the rivers of a propagating crack control cyclic cleavage. Here also, the frequency is introduced and results in a similar trend, namely that high frequency is associated with relatively lower FCPR values.

During the present work frequency effects have been studied experimentally at low temperatures (Fig. 5). According to our knowledge, these data are not available in the literature. It should be emphasized that although the general trend which has been suggested by Moody and Gerberich [*4, 19*] was confirmed, there are still difficulties in verifying their proposed relationship quantitatively. We believe that the whole issue is more complex below the DBT. There are several variables that have to be considered (e.g., adiabatic heat, strain rate effects and, mainly, the role of the characteristic distance needed for cleavage). These variables are competitive and therefore some of the expected frequency effects might be reduced even at low temperatures.

[1] Westinghouse R&D Center, Pittsburgh, PA 15235.
[2] Citations of references and figures refer to the main body of the paper.

James T. Ryder and William E. Witzell

Effect of Low Temperature on Fatigue and Fracture Properties of Ti-5Al-2.5Sn(ELI) for Use in Engine Components

REFERENCE: Ryder, J. T. and Witzell, W. E., "**Effect of Low Temperature on Fatigue and Fracture Properties of Ti-5Al-2.5Sn (ELI) for Use in Engine Components,**" *Fatigue at Low Temperatures, ASTM STP 857,* R. I. Stephens, Ed., American Society for Testing and Materials, Philadelphia, 1985, pp. 210–237.

ABSTRACT: The results of an experimental investigation designed to obtain the material property data necessary to establish the salient characteristics of a Ti-5Al-2.5Sn(ELI) alloy for use in a fuel pump impellor at cryogenic temperatures are described. Tension, fracture toughness, and fatigue crack propagation data were obtained from pancake forgings at room temperature in laboratory air and at 20 K (−423°F) in liquid hydrogen. Experiments were performed on coupons of three different orientations, from different forgings, and from different forging lots. The effect of frequency (0.1 and 10 Hz) and R ratio (+0.05 and +0.5) on crack propagation was evaluated.

Tensile strength significantly increased at cryogenic temperatures compared to room temperature, percent elongation had a minor reduction, percent reduction in area significantly decreased, and modulus increased approximately 8%. Fracture toughness showed a significant reduction at cryogenic temperatures, as expected. A difference in toughness caused by orientation of as much as 25% was observed, despite the lack of any significant differences in material texture. The fatigue crack growth rate of this alloy showed a remarkable lack of sensitivity to the various experimental conditions. Crack orientation effects were minimal, although there were some small shifts in threshold. The two different forging lots resulted in a small shift in growth rate. No effect of frequency was found at any combination of R ratio and temperature. A load ratio effect was observed, but this expected result was manifested only by a small shift to higher rates at $R = 0.5$. No effect of temperature on fatigue crack propagation was observed from threshold ($\sim 10^{-8}$ m/cycle [$\sim 4 \times 10^{-7}$ in./cycle]) to 44 MPa $\sqrt{m}$ (40 ksi $\sqrt{in.}$) ($\sim 1 \times 10^{-6}$ m/cycle [$\sim 4 \times 10^{-5}$ in./cycle]). Above this level the observed difference in growth rate was due to the lower fracture toughness at 20 K (−423°F).

KEY WORDS: mechanical properties (tensile strength, fracture toughness, fatigue crack growth), low temperature properties (titanium)

Dr. Ryder is a senior research scientist with the Lockheed-California Co. in Burbank, CA 91520; Mr. Witzell is a group engineer with the General Dynamics Convair Division in San Diego, CA 92138.

The recent development of reuseable upper stage spacecraft, high pressure rocket engines for such applications as the space shuttle, and space tugs represents a significant extension of previous propulsion component design. The reuseable nature of such components has necessitated careful consideration of procedures for ensuring design life. The development of adequate procedures is severely influenced by the fact that these high-pressure components must be of small size and weight; these can only be achieved by employing high-tip speed turbines and accepting the concomitant highly stressed impeller and turbine disks. The problem is aggravated for fuel pump impellers because of the high stresses that exist in rotor disks operated in the low temperatures of liquid hydrogen or oxygen. At such high stresses and in the cryogenic environments of interest, titanium alloys such as Ti-5Al-2.5Sn(ELI) are used because of their low density and high strength. However, also because of the high stresses, rotor disks can be extremely sensitive to small initial defects. This problem is intensified by the reduction of an alloy's fracture toughness at cryogenic temperatures [*1*].

The research effort described in this paper was directed towards providing material characterization data, tensile and fracture toughness data, and fatigue crack propagation data necessary to establish the salient characteristics of a Ti-5Al-2.5Sn(ELI) alloy to be used in a fuel pump impeller in a cryogenic environment. The data were used in a research program sponsored by the NASA/Lewis Research Center [*2*] to correlate crack propagation data from conventional laboratory coupons with data from a parallel sided rotating disk used to model the rotor stresses. A key question concerning the use of such a material was whether rotating disk experiments conducted at room temperature could be correlated to potential experiments conducted at cryogenic temperatures. The data obtained in this program were reviewed to help answer that question and thereby possibly avoid expensive cryogenic rotating disk experiments.

Material Characterization

The Ti-5Al-2.5Sn(ELI) alloy is nearly an all-alpha phase alloy with excellent weldability. The presence of small beta stabilizer content (iron and manganese) as an impurity can be detrimental to extreme low-temperature properties. The beta content in the alloy is therefore kept small. Enough beta stabilization is seen metallographically in the standard grade, but it is not visible metallographically in the extra-low interstitial (ELI) grade. This alloy is a non-heat treatable material and the ELI grade has somewhat lower tensile strength properties than the standard grade [*1,3*]. The microstructure at room temperature is in the alpha phase, with traces of beta phase from the residual iron content in the sponge. The alpha phase can be produced in an equiaxed form by mechanical working and annealing at temperatures in the alpha phase field, while an acicular structure results when cooling from the beta phase field. Detrimental presence of ordered phases, such as the hexagonal close-packed order compound Ti_3Al in the Ti-5Al-2.5Sn alloy, is usually minimal [*4*].

Two lots of Ti-5Al-2.5Sn(ELI) were purchased from the Rocketdyne Division of Rockwell International. Both lots were from Reactive Metals Incorporated (RMI) Heat 891389 and were purchased to the ELI requirements of Aerospace Material Specification (AMS) 4924B as well as appropriate Rocketdyne specifications. Lot 1 was a 3567 N (802-lb) billet, 1090 mm (43 in.) long and 305 mm (12 in.) in diameter, while Lot 2 was a 2002 N (450-lb) billet, 610 mm (24 in.) long and 305 mm (12 in.) in diameter.

Results of a chemical analysis of the two lots of material are shown in Table 1. As can be seen in this table, both lots of material met both specifications. An element not listed in Table 1 is yttrium. Conversations with Rocketdyne personnel confirmed that this RMI Heat of Ti-5Al-2.5Sn(ELI) was one of numerous heats of titanium produced by RMI to which yttrium was added during the melt. Yttrium in small amounts and finely distributed can be used to reduce grain size and improve the forgeability of titanium and other alloys [*5*]. An analysis[1] of available data [*6–8*] on the effect of yttrium on the mechanical properties of titanium alloys indicated for Ti-5Al-4V somewhat lower longitudinal and short transverse tensile properties and a decrease in resistance to stress corrosion cracking. For Ti-5Al-2.5Sn, the addition of yttrium appeared to result in a reduction of K_c by 13.2 to 22 MPa $\sqrt{m}$ (12 to 20 ksi $\sqrt{in.}$).[2] These reductions in mechanical properties were apparently due to both the addition and poor segregation of the yttrium [*6–8*].[2] The amount of segregation of yttrium in this alloy is unknown and thus its effects on properties are also unknown. Future users of this alloy must consider this potential problem.

The Ladish Company, Cudahy, Wisconsin, prepared 20 press-forged pancake disks from a first billet of material and twelve from a second lot. Each pancake was approximately 457 mm (18 in.) in diameter and 76 mm (3 in.) thick. Specimens were drawn from sections of the first 18 pancakes for tensile, fracture toughness, and fatigue crack propagation behavior characterization. From the remaining pancakes of Lot 1 and those of Lot 2, disks were machined for an investigation [*2*] into material response under centrifigual loads induced by rotation. In addition, coupons were manufactured for tensile, fracture toughness and fatigue crack propagation characterization.

The starting stock material of Lot 1 was cut into two pieces labeled 1-Top and 2-Bottom; these two pieces received Ladish Lot Nos. H4-2046 and H4-2180. Lot 2 of the starting stock material received Ladish Lot No. H5-834. All three pieces were drawn down to 152-mm (6-in) diameter billets, after

[1] Private communication from J. Van Orden, Lockheed-California Co., Burbank, CA, 12 March 1975, on analysis of reactive metals.

[2] Private communication from J. Van Orden, Lockheed-California Co., Burbank, CA, 12 March 1975, on analysis of data supplied to G. Wald obtained from Reactive Metals Inc.

TABLE 1—*Chemical composition (weight percent) of Ti-5Al-2.5Sn(ELI).*[a]

Chemical	Lot 1 (H4-2046, H4-2180)	Lot 2 (H5-834)	AMS4924 Specification		RB0170-152[b] Specification	
			Minimum	Maximum	Minimum	Maximum
Aluminum (Al)	5.08	5.08	4.70	5.60	4.60	5.60
Tin (Sn)	2.37	2.37	2.00	3.00	2.00	3.00
Carbon (C)	0.01	0.02	...	0.08	...	0.05
Iron (Fe)	0.07	0.06	...	0.25	...	0.20
Hydrogen (H)	0.006	0.005	...	0.0125	...	0.010
Manganese (Mn)	<0.01	<0.01	...	0.10	...	0.030
Nitrogen (N)	0.01	0.01	...	0.07	...	0.04
Oxygen (O)	0.08	0.07	...	0.12	...	0.10
Other elements, each	<0.01	<0.01	...	0.05	...	0.05
Other elements, total	<0.15	<0.15	...	0.40	...	0.20
Titanium	remainder	remainder	remainder	remainder	remainder	remainder

[a] Heat 891389.
[b] Rocketdyne Specification.

which 152-mm (6-in.)-long pieces were cut off for the pancake forgings. The Lot 1 billet yielded approximately 3025 N (680 lb) of material after draw-down, while Lot 2 yielded approximately 1846 N (415 lb) after draw-down.

Forging reductions, to a total of 50%, were started above the beta transus temperature (T_β) determined to be 1283 K (1850°F), and finished in the alpha field. The billets were upset twice during forging. Forgings were annealed at 1061 ± 14 K (1450 ± 25°F) for 2 h and furnace cooled. The 152-mm (6-in.)-diameter billets after draw-down were found acceptable to Level 30, according to Fig. 3 of AMS Specification 2380. Sonic testing per AMS 2631 showed no apparent defects or flaws. The aluminum rating was met. While no specific AMS specification for microcleanliness is known to exist for this material, Ladish examination of the forged microstructure showed the material to be apparently free of microstructural segregation, porosity, or material nonuniformities.

From Lot 1, ten pancakes from each piece were produced numbered 1 to 20 from the top down, the first ten from piece 1-Top. Lot 2 produced twelve pancakes numbered 21 to 32. The finished pancake weight was approximately 151 N (34 lb); the dimensions were nominally 203-mm (8-in.) diameter and 76-mm (3-in.) thickness. Pancake 11 was slightly underweight, while Pancakes 15 and 18 were discovered by sonic inspection to have small center cracks. During machining, Pancake 16 was also discovered to have a small crack at the location of the two tensile blanks.

Macrostructures of Pancakes 1, 9, and 16 were obtained by taking a diametrical cut. Grain size appeared to be uniform. The photomacrographs showed that their macroetch grain size was acceptable according to Fig. 15 of AMS 2380. The etchant used was Kroll's: 10% nitric and 8% hydrofluoric acid in water. Some indication of grain flow was evident, but this did not become pronounced until the higher serial numbered pancakes, numbers 15 through 18.

Hardness readings were taken on the top surface of each pancake, at three locations, 120 deg apart at the midradius. All hardness readings were taken by using a standard 29.42-kN (in old units, 3000-kgf) load and a standard 10-mm-diameter steel ball. All pancake surface readings were taken at small polished areas. Brinell hardness was obtained because titanium sticks to the diamond tip used in Rockwell C hardness testing, often resulting in false readings. In addition, although this is not a serious problem for Ti-5Al-2.5Sn, which is an all-alpha alloy, Brinell hardness is an average over a large area, as opposed to the small diamond tip of Rockwell C testing, which would detect differences in the two phases of titanium platelets, alpha and beta. This is not always desirable. The Brinell Hardness Number (BHN) was 269 for each reading.

Two texture examinations (pole figures) were performed on Pancake 1, one at midradius, center position, and one at 90 deg from the initial position, but at one-quarter radius from the pancake center. Both examinations showed no evidence of preferred orientation.

Although the standard does not actually apply to titanium alloys, ASTM E 112 was used to estimate the average grain size for the microstructures. Three micrographs for Pancakes 1, 9, 16, and 18 were taken from the same radial-thickness plane cut along the pancake diameter as used to obtain the macrographs. Pancake 1 exhibited an estimated average grain size of 6 at ×100, while Pancakes 9, 16, and 18 exhibited a grain size of 7 at ×100. The microstructure in all four pancakes was similar. However, there appeared to be somewhat more oriented grain flow in Pancakes 9, 16, and 18 than in Pancake 1, as well as more secondary particle segregation.

The tension specimen coupons were 6.25 mm (0.250 in.) in diameter with a 25.4 mm (1.00 in.) gage length. These coupons were machined and tested according to ASTM Tension Testing of Metallic Materials (E 8). Seventy-four tensile coupons were obtained from 18 different pancakes. Of these coupons, 66 were circumferentially (C) oriented near the outer edge of the pancake, half surface and half center location, and four each were oriented in the radial (R) and thickness (L) directions of Pancake 16. Fracture toughness and fatigue crack growth coupons were of the Manjoine wedge-opening-loaded (WOL) type compact tension specimens with a specimen width W of 50.8 mm (2.00 in.) and a thickness of 19.0 mm (0.750 in.). From 17 pancakes, 138 compact (WOL) specimens were obtained, 48 circumferential orientation (26 CR, 22 CL), 45 radial orientation (23 RC, 22 RL), and 45 thickness orientation (23 LR, 22 LC). These orientations are as per ASTM Test for Plane-Strain Fracture Toughness of Metallic Materials (E 399).

Hardness readings were taken of tension, fracture toughness, and fatigue crack propagation test coupons. The hardness survey results varied over a small range, from 3.60 Brinell Hardness Diameter (BHD) (285 BHN) to 3.90 BHD (241 BHN) with only one reading above 3.80 BHD and only five below 3.70 BHD out of 265 readings. According to approximate tensile ultimate strength tables and Rockwell C conversion tables, these results convert to tensile ultimate strengths from 800 to 896 MPa (116 to 130 ksi) and Rockwell C Hardness (R_c) values from 30 to 23. The results were somewhat higher than actual tensile ultimate strengths, which varied from 800 to 841 MPa (112 to 116 ksi).

Experimental Procedures

Tension tests at 20 K (−423°F) were conducted in liquid hydrogen cryostats installed in the test machines. Extensometers used with liquid hydrogen testing consisted of rod-in-tube extensions that transmitted the strain from the specimen test section to a transducer located outside of the liquid hydrogen cryostat. The output of the transducer was transmitted to the drum recorder of the test machine in a conventional manner. Machine controls and readout equipment for the LH_2 tests were located in another room completely isolated from the area in which LH_2 was used, so that accidental arcing from electrical equipment could not pose a safety problem. The LH_2 was transferred from a storage tank outside of the test building by means of a double-walled, evacuated pipe to the cryostat on the test frame and vented to the atmosphere. The test facility was subjected to continual monitoring for the presence of H_2 gas during any H_2 test.

All fracture toughness specimens were precracked at room temperature in a Baldwin SF-1N fatigue machines by using a three-step fatigue loading sequence to ensure that the final load was equivalent to a stress intensity less than 60% of the expected K_Q value. All cyclic precracking was performed by using a stress ratio (R) of 0.1 at a constant frequency of 30 Hz. Specimens were instrumented with an ASTM E 399 type crack opening displacement (COD) gage and a monotonic tensile load was applied to produce failure. The resulting load-displacement curves were analyzed to determine plane strain fracture toughness values. If any of the K_{Ic} validity criteria were not met, appropriate K_Q values and residual strength ratios (R_{SC}) were calculated for each specimen per ASTM E 399 requirements.

Compliance calibration was obtained by using the procedures of Ref *9*, at room temperature in laboratory air for three samples and at 20 K (−423°F) in LH_2 for one sample. For room temperature tests the compliance measurement was the average of five readings taken at each a/W value. Compliance curve readings were made approximately every 1.3 mm (0.050 in.). At low temperatures, multiple compliance readings were taken at less regular intervals. Results were analyzed so that they could be used to interpret the compliance data obtained from the fatigue crack propagation tests as well as to obtain an experimental compliance calibration. The primary purpose of the experimental compliance calibration was to determine if the compliance calibration of the material changed as a function of temperature.

The compliance calibration showed excellent agreement (less than a 1% difference) between optical and compliance a/W data, both at room temperature and at 20 K (−423°F). Both optical and compliance readings were, however, used for subsequent low-temperature experimentation. In addition, compliance calibration was shown not to be affected by temperature, except for allowance of a modulus change. Hence the practice of precracking coupons in room temperature and subsequently testing them at low temperature was assumed not to affect their toughness or fatigue crack growth properties.

Precracking of fatigue crack propagation specimens was accomplished in the same manner as for static fracture toughness specimens. Generally, 20 data points were obtained over a spread of ΔK values for each specimen. Experiments were conducted at $R = 0.05$ and 0.5, $F = 10$ and 0.1 Hz, and at room temperature (RT) and 20 K (−423°F). Tests at room temperature were conducted in laboratory air by using a closed-loop electrohydraulic testing machine. Coupons were tested at 20 K (−423°F) in a Tatnal servo-controlled test system equipped with a liquid hydrogen cryostat containing a clear plastic window. Loads were applied in three steps, with each load larger than the previous one. Initially, marker bands were induced in the specimen for the purpose of enhancing posttest fractography. However, the data reduction technique was adequate for accurate growth readings to be produced without the marker bands; thus they were discontinued.

The crack length of coupons tested at room temperature was measured optically on both sides of the room temperature coupons. The two surface measurements were averaged. For tests in LH_2, optical readings could be taken on only one side, but this was not a critical omission because the crack front remained symmetrical throughout the tests, as shown by posttest observation of the fracture surface. A check of the crack length was obtained from COD data by expressing a/W as a function of normalized compliance, and comparing the results to those obtained optically. The optical crack length measurements, after adjustment for crack bowing, agreed closely with compliance-based measurements. An adjustment length of 1.27 mm (0.050 in.) was added to each average optical surface crack length measurement to account for the bow in subsurface crack extension. This was justified by posttest observation of coupon fracture surfaces, which showed that the crack length based on the two surface readings and three subsurface measurements (¼, ½, and ¾ thickness) was 1.01 to 1.52 mm (0.040 to 0.060 in.) longer than the average of the two surface measurements. The adjustment in crack length resulted in less than a 1% change in ΔK. Crack growth rate (da/dN) was defined simply as the change in crack length (Δa) divided by the change in cycles (ΔN). Crack length intervals were usually maintained between 0.6 and 1.9 mm (0.025 and 0.075 in.), with no readings less than 0.33 mm (0.013 in.) considered acceptable. At higher ΔK levels, the shorter crack length intervals were used, if at all possible. Stress intensity was calculated by using the experimentally based compliance curve.

All fatigue crack propagation data discussed in subsequent sections are presented in a graphic format. Plotted data are shown along with statistically based 2σ curve fit scatter bands where σ is standard deviation. The crack growth data taken at one test condition were combined and empirically fitted by using the following expression developed by Sandifer and Bowie [*10*], after the well-known form of Gumbel double exponential distribution [*11*].

$$da/dN = \exp\{u - \ell n\,[- \ell n(1 - \Delta K/K_d)]/\alpha\} - 1$$

where α and u are constants for a particular data set and K_d is the K_{max} value at fracture of a crack growth coupon. Based on this equation, a median crack growth curve was defined as that corresponding to the α and u values found by linear regression. A curve suggested by Bowie [*10*] as a useful design curve to give a conservative life estimate was defined by the left side 1σ scatter band curve. Figure 1 shows the 2σ scatter bands, median curve, and suggested design curve.

Tension and Fracture Toughness Results

Tension test results are summarized in Table 2. Included in Table 2 are the minimum properties from two standards, AMS4924B (dated 1 November

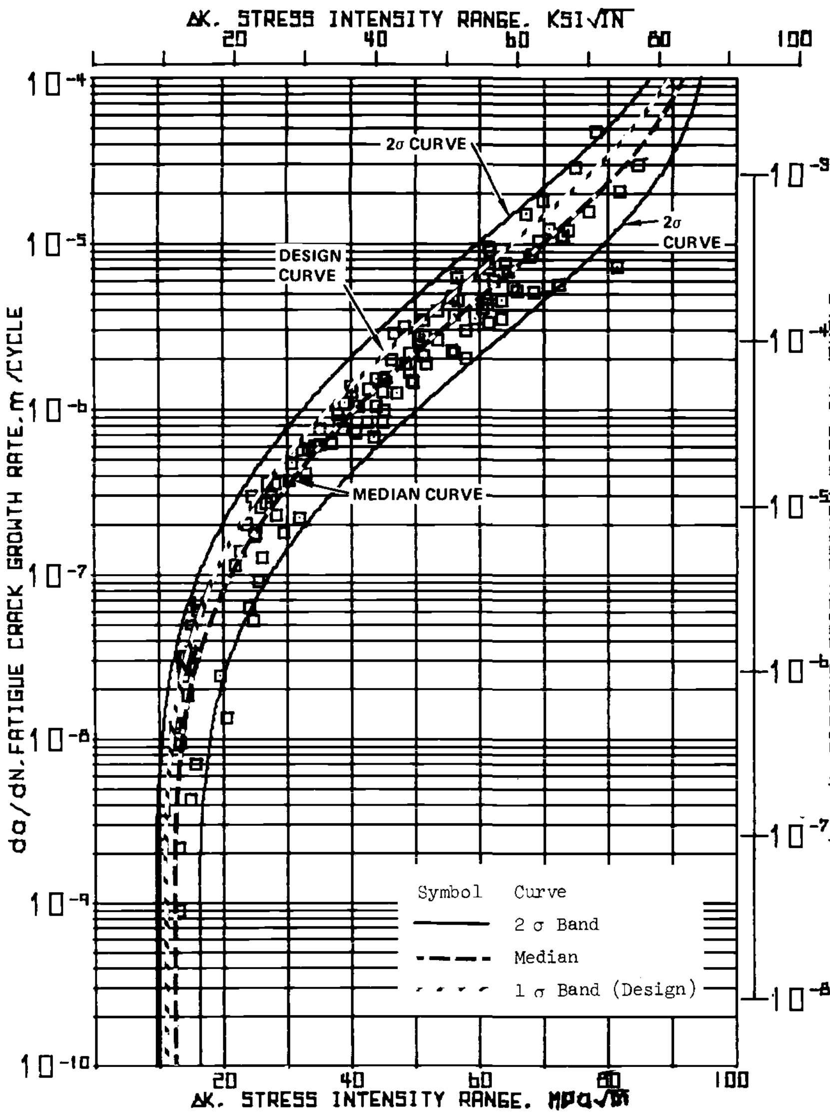

FIG. 1—*Fatigue crack propagation data for Ti-5Al-2.5Sn(ELI) at room temperature,* R = *0.5,* F = *10 Hz, showing 2σ band curves, median curve, and 1σ band (design) curve.*

TABLE 2—*Average tensile properties of Ti-5Al-2.5Sn(ELI) pancake forgings.*

Temperature	No. of Coupons	Data Source	Ultimate Tensile Strength MPa (ksi)	Yield Strength, 0.2% Offset, MPa (ksi)	% Elongation in 25.4 mm (1 in.)	% Reduction in Area	Apparent Tensile Modulus, GPa ($\times 10^6$ psi)
Room temperature	38	this program	827.4 (120.0)	783.2 (113.6)	16.8	42.9	119.3 (17.3)
		AMS492B specification	689.5 (100.0)	620.5 (90.0)	10.0	...	103.4 (15.0)
		RB0170-152 specification	689.5 (100.0)	620.5 (90.0)	10.0	...	137.9 (20.0)
		Nachtigall [*12*]	861.8 (125.0)	827.4 (120.0)	...	...	...
		Sullivan [*13*]	779.1 (113.0)	723.9 (105.0)	18.0	43.0	...
		Van Stone et al [*1*]	744.6 (108.0)	681.9 (98.9)	...	...	...
20 K (−423°F)	36	this program	1455 (211.1)	1379 (200.0)	16.2	27.9	130.3 (18.9)
		RB0170-152 specification	1310 (190.0)	1241 (180.0)	8.0	...	...
		Nachtigall [*12*]	1475 (214)	1413 (205)	...	...	...
		Sullivan [*13*]	1565 (227)	1462 (212)	7.0	...	...
		Van Stone et al [*1*]	1411 (204.7)	1306 (189.4)	...	...	...

1969) and the more stringent Rocketdyne standard, RB170–152 (dated 8 October 1973). In addition, results of three other studies are given for comparison. The work by Nachtigall [*12*] was conducted by using 16.13-mm (0.635-in.)-diameter coupons, that by Sullivan [*13*] was for coupons from 2.54-mm (0.1-in.) sheet, while that by Van Stone et al [*1*] was for 25.4-mm (1-in.)-thick plate. Van Stone et al [*1*] compared air-cooled and furnace-cooled tensile properties and found no significant difference.

Most tensile properties varied little from pancake to pancake when tested at room temperature. However, at 20 K (−423°F), modulus varied from 96.5 GPa (14.0×10^6 psi) to 160.9 GPa (24.5×10^6 psi); at room temperature, on the other hand, modulus varied from 103.4 to 125.5 GPa (15.0 to 18.5×10^6 psi). This variation indicated large measurement uncertainties at 20 K (−423°F), a definite problem. Percent elongation had a similar temperature

TABLE 3—*Fracture toughness test results.*

Coupon No.	Fracture Toughness (K_Q), MPa $\sqrt{m}$ (ksi $\sqrt{in.}$)[a]	Residual Strength Coefficient (R_{SC})[b]
	Room Temperature	
1CR-1	91.6 (83.4)	0.950
6CR-1	89.8 (81.7)	0.932
29CR-2	92.7 (84.4)	1.35
1RC-1	91.4 (83.2)	0.955
6RC-1	91.1 (82.9)	0.940
1LR-1	84.7 (77.1)	0.866
6LR-1	79.8 (72.6)	0.818
1LC-1	93.4 (85.0)	0.884
6LC-1	87.5 (79.6)	0.911
12RL-1	80.3 (73.1)	0.886
13RL-1	78.3 (71.3)	0.843
14CL-1	85.6 (77.9)	1.03
15CL-1	96.9 (88.2)	1.07
	20 K (423°F)	
1CR-2	61.8 (56.2)	0.312
6CR-2	63.5 (57.8)	0.342
1RC-2	63.7 (58.0)	0.339
6RC-2	65.5 (59.6)	0.327
1LR-2	58.2 (53.0)	0.310
6LR-2	57.7 (52.5)	0.307
1LC-2	60.0 (54.6)	0.312
6LC-2	54.4 (49.5)	0.276
12RL-6	70.5 (64.2)	0.341
13RL-6	67.0 (61.0)	0.335
14CL-6	71.6 (65.2)	0.365
15CL-6	75.3 (68.5)	0.376

[a] None of the coupons tested at room temperature met the requirements of ASTM E 399. All tests at 20 K did meet the requirements.

[b] Calculated per ASTM E 399 requirements.

dependence. All minimum specifications except for the apparent tensile modulus at room temperature were exceeded, and results compared quite favorably to results of other investigations. At both room temperature and 20 K (−423°F), tensile strength results of surface coupons slightly exceeded those of subsurface specimens. Percent elongation essentially did not change with decreased temperature, while percent reduction of area was still quite good at 20 K (−423°F).

Table 3 lists the results of the 25 fracture toughness tests conducted by using coupons from Pancakes 1 to 18 and 29. All coupons tested at 20 K (−423°F) met all the plane-strain criteria of ASTM E 399, while all coupons tested at room temperature failed to meet the criteria that $P_{max}/P_Q <$ 1.10 and that the thickness be greater than $(2.5\ K_Q/\sigma_{ys})^2$. A review of the 20 K (−423°F) results showed a dependence of K_{Ic} on direction. Samples in which the crack was aligned in the thickness direction (RL, CL) had the highest toughness. The apparent dependence of K_{Ic} on orientation existed in spite of the fact that no crystallographic texture was observed, as previously discussed.

The fracture toughness properties of Ti-5Al-2.5Sn(ELI) alloy are known to vary with temperature, which is consistent with these results. Values of 49.5 MPa $\sqrt{m}$ (45 ksi $\sqrt{in.}$) at −253°C (−423°F) have been reported [*14*] for ELI grade and 49.5 to 66 MPa $\sqrt{m}$ (45 to 60 ksi $\sqrt{in.}$) [*13*] for thin sheet material. Other data have indicated a wide range of fracture toughness values, depending on microstructure and specimen orientation [*15*]. Van Stone et al [*1*] found that although fracture toughness properties (K_{Ic}) at room temperature were similar for air- and furnace-cooled plate, the toughness of the air-cooled material at 20 K (−423°F) greatly exceeded that of the furnace-cooled material, namely 89 compared to 73 MPa $\sqrt{m}$ (81 to 66.1 ksi $\sqrt{in.}$). This result suggests that in the future Ti-5Al-2.5Sn(ELI) should possibly be air-cooled, not furnace-cooled as is the typical practice.

Fatigue Crack Propagation Results

Orientation Effects

The effect of specimen orientation on the fatigue crack propagation behavior of Ti-5Al-2.5Sn(ELI) at room temperature is shown in Figs. 2 to 5. The curves shown in these figures are the aforementioned 2σ scatter bands; extrapolations are indicated by dashed lines. Variation in growth rates within a coupon were often as large as the variation from one orientation to another. When the location of the data for each individual specimen was compared to the 2σ band for all data, the CL and RL orientation data were found to be more in the lower half of the data band for data at $R = 0.05$, $F = 10$ Hz. However, for Figs. 3 to 5 the same trend for CL and RL data was not discernable. Differences in propagation rates for cracks growing in the R or C direction were not observed. Data scatter within any specimen was gen-

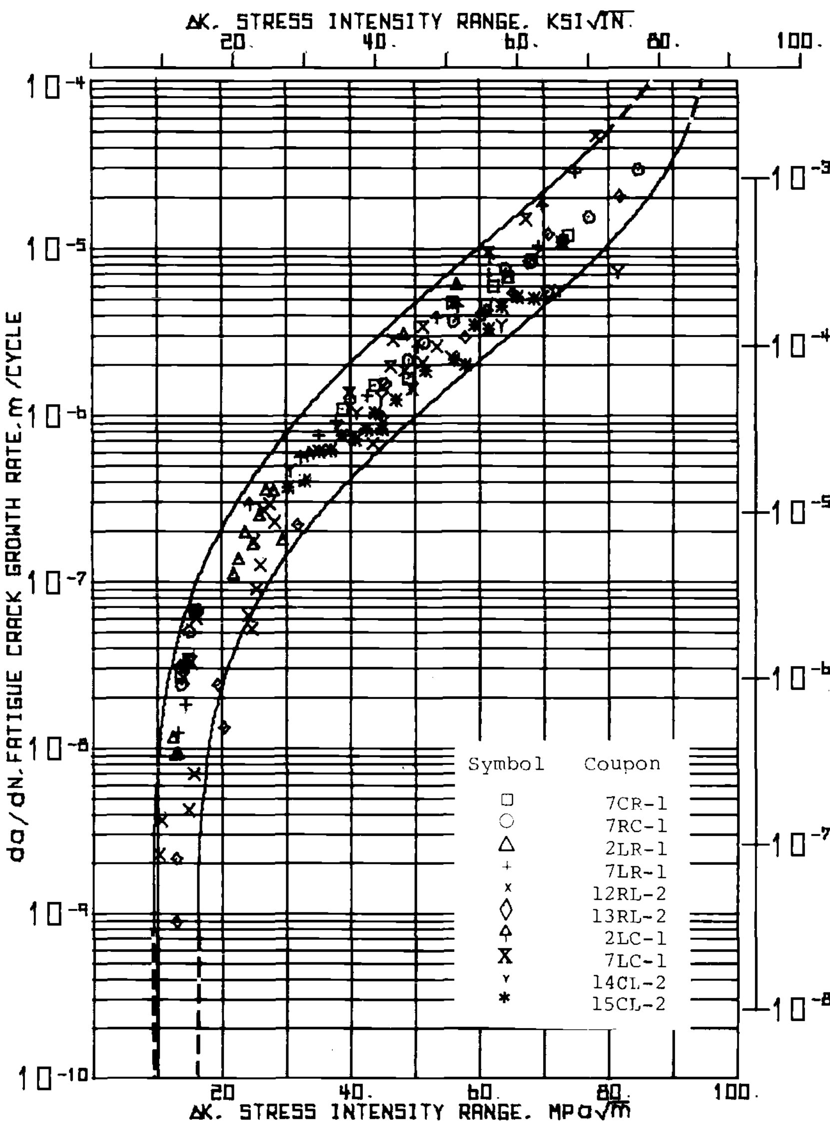

FIG. 2—*Effect of orientation on fatigue crack propagation behavior of Ti-5Al-2.5Sn(ELI) at room temperature,* R = *0.05,* F = *10 Hz.*

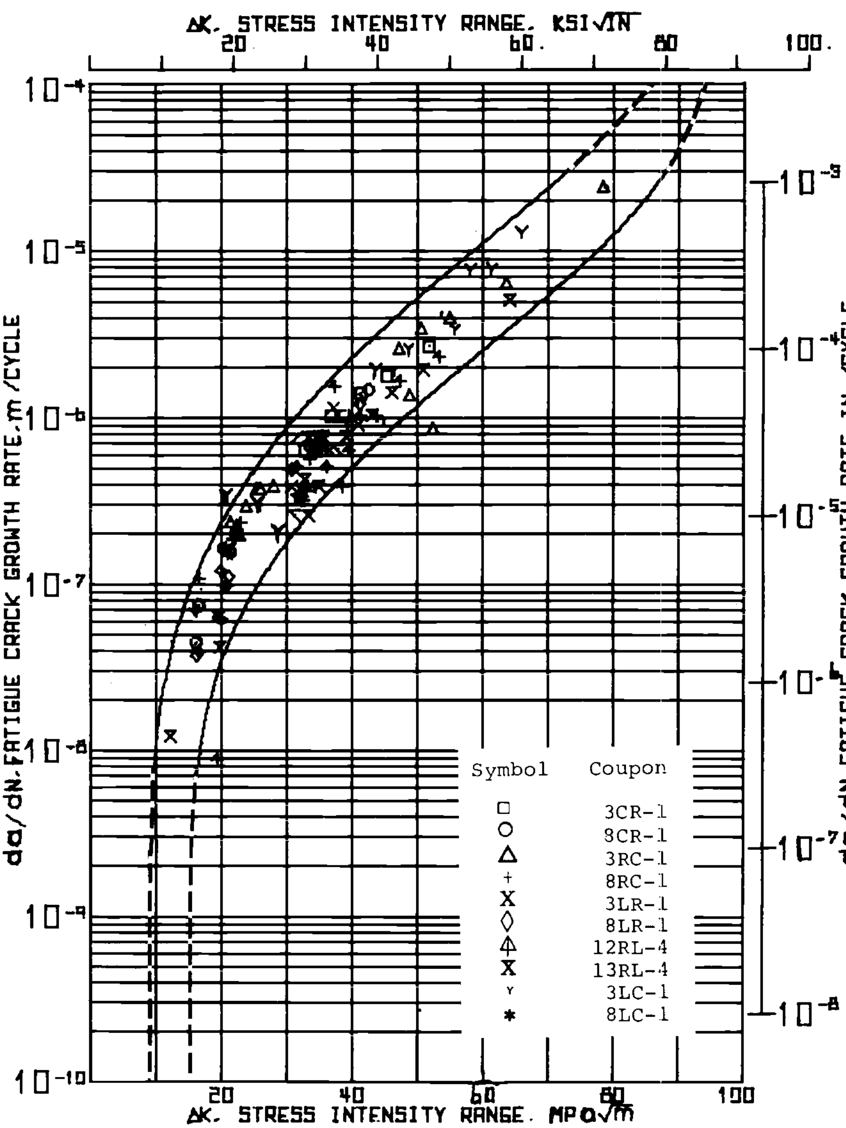

FIG. 3—*Effect of orientation on fatigue crack propagation behavior of Ti-5Al-2.5Sn(ELI) at room temperature,* R = *0.05,* F = *0.1 Hz.*

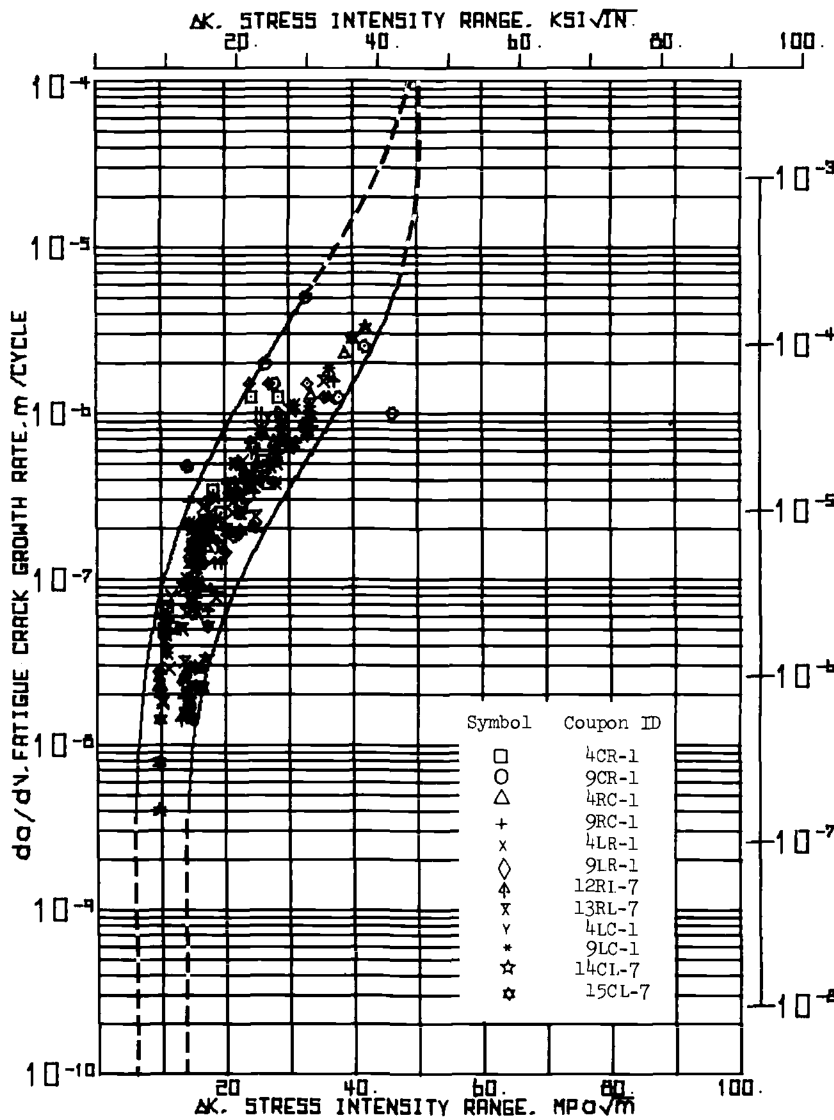

FIG. 4—*Effect of orientation on fatigue crack propagation behavior of Ti-5Al-2.5Sn(ELI) at room temperature,* R = *0.5,* F = *10 Hz.*

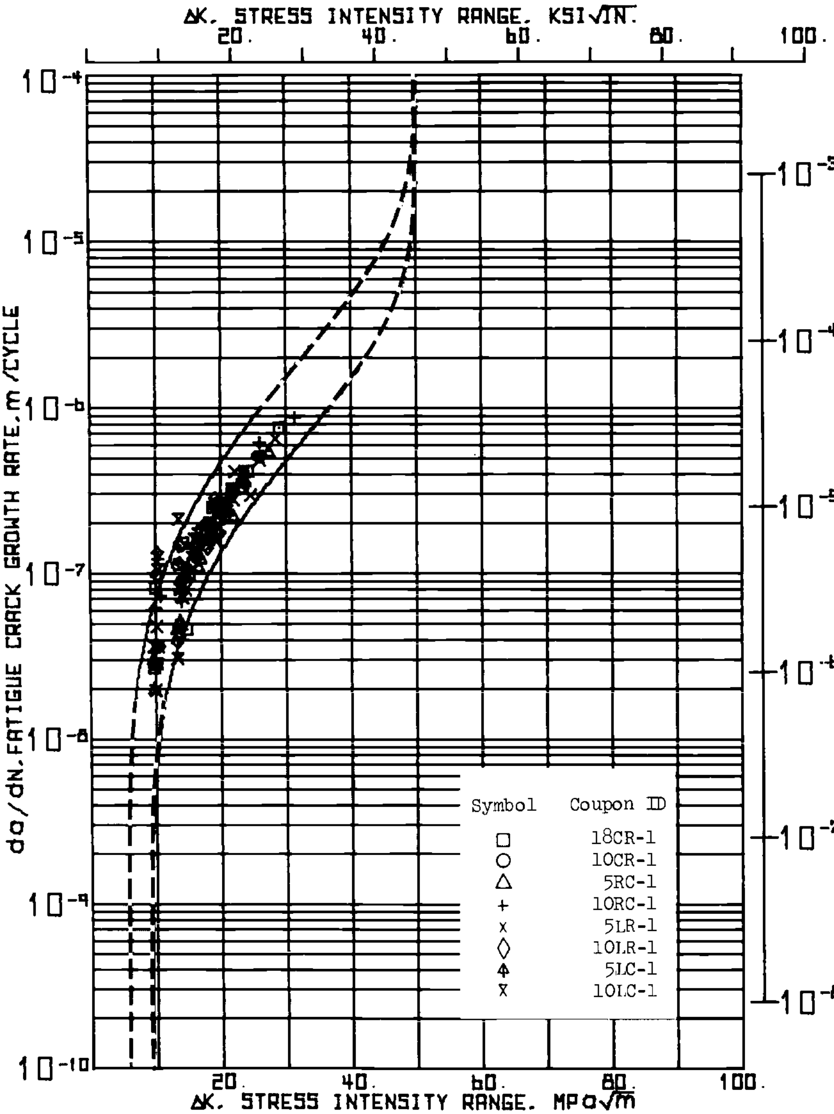

FIG. 5—*Effect of orientation on fatigue crack propagation behavior of Ti-5Al-2.5Sn(ELI) at room temperature,* R = *0.5,* F = *0.1 Hz.*

erally small except for specimens from Disk 9 (Fig. 4). For this disk, data scatter was greater than that for specimens from other disks.

Figures 6 to 8 show the effects of orientation on fatigue crack growth behavior at 20 K (−423°F). Study of these data again showed no unusually large orientation effect. Figure 9 is included for reference, since only one specimen was tested at $R = 0.5$ and $F = 0.1$ Hz at 20 K (−423°F).

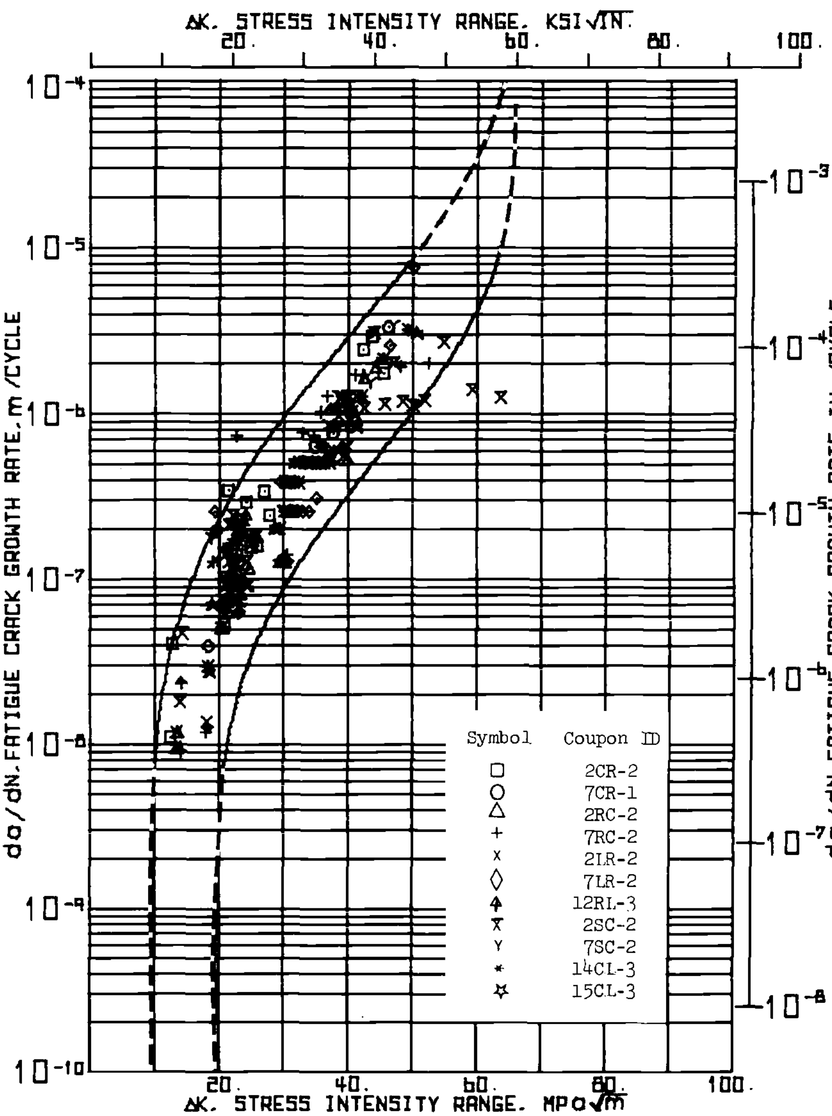

FIG. 6—*Effect of orientation on fatigue crack propagation behavior of Ti-5Al-2.5Sn(ELI) at 20 K (−423°F),* R = *0.05,* F = *10 Hz.*

Frequency Effects

The typical effect of frequency on fatigue crack growth rate is shown in Figs. 10 and 11. The data clearly show that no effect of frequency was observed at room temperature or at 20 K (−423°F). Curve shapes and thresholds were essentially identical.

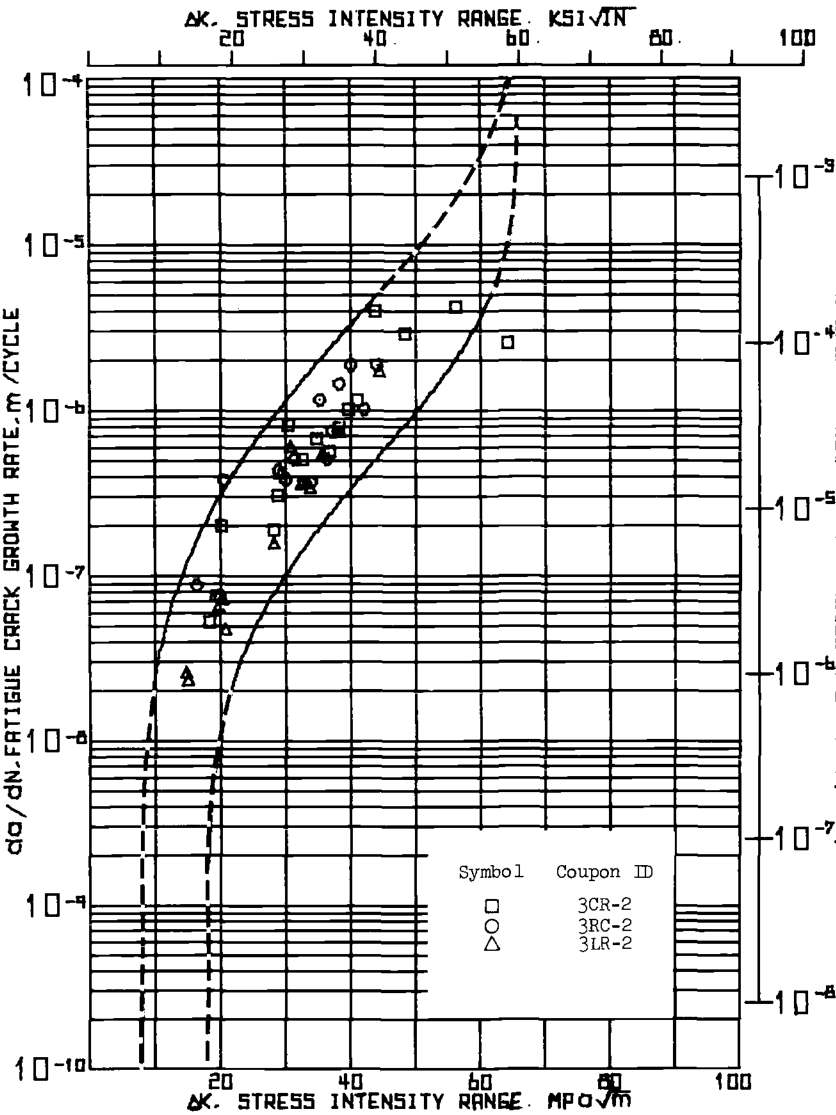

FIG. 7—*Effect of orientation on fatigue crack propagation behavior of Ti-5Al-2.5Sn(ELI) at 20 K (−423°F),* R = *0.05,* F = *0.1 Hz.*

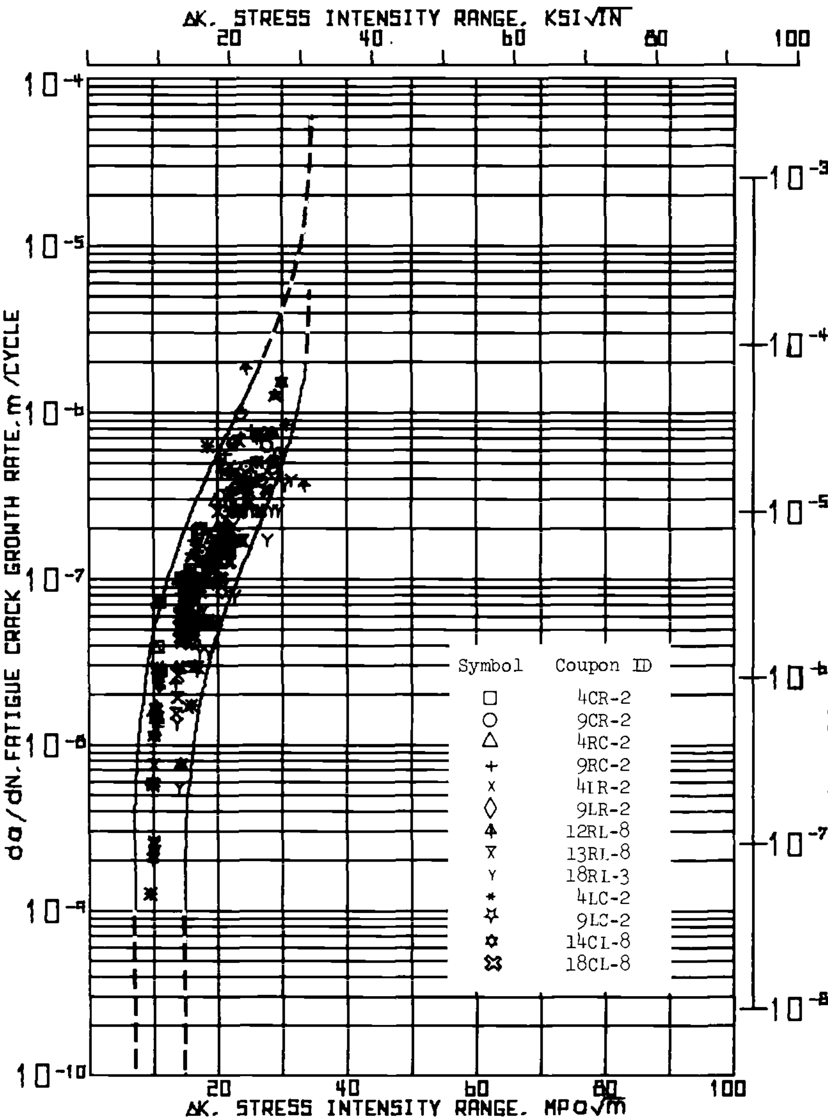

FIG. 8—*Effect of orientation on fatigue crack propagation behavior of Ti-5Al-2.5Sn(ELI) at 20 K (−423°F),* R = *0.5,* F = *10 Hz.*

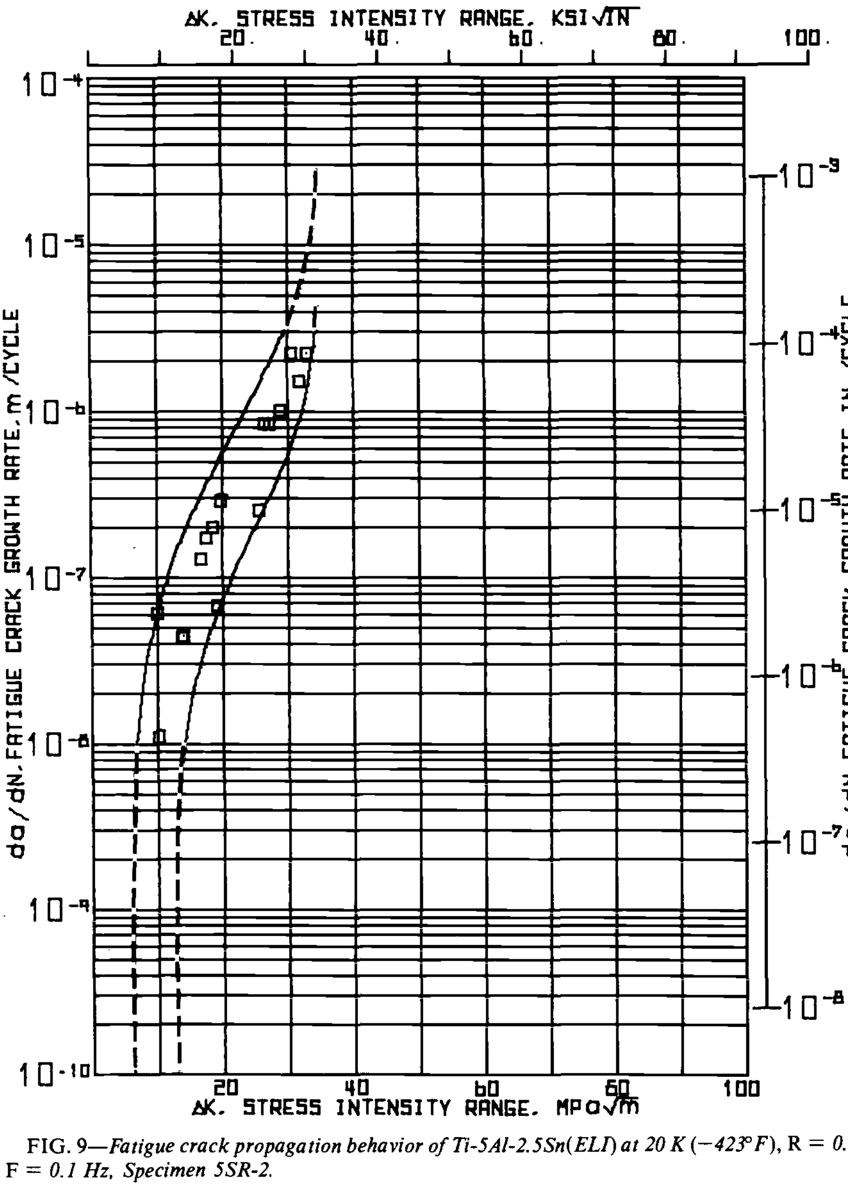

FIG. 9—*Fatigue crack propagation behavior of Ti-5Al-2.5Sn(ELI) at 20 K (−423°F)*, R = *0.5*, F = *0.1 Hz, Specimen 5SR-2.*

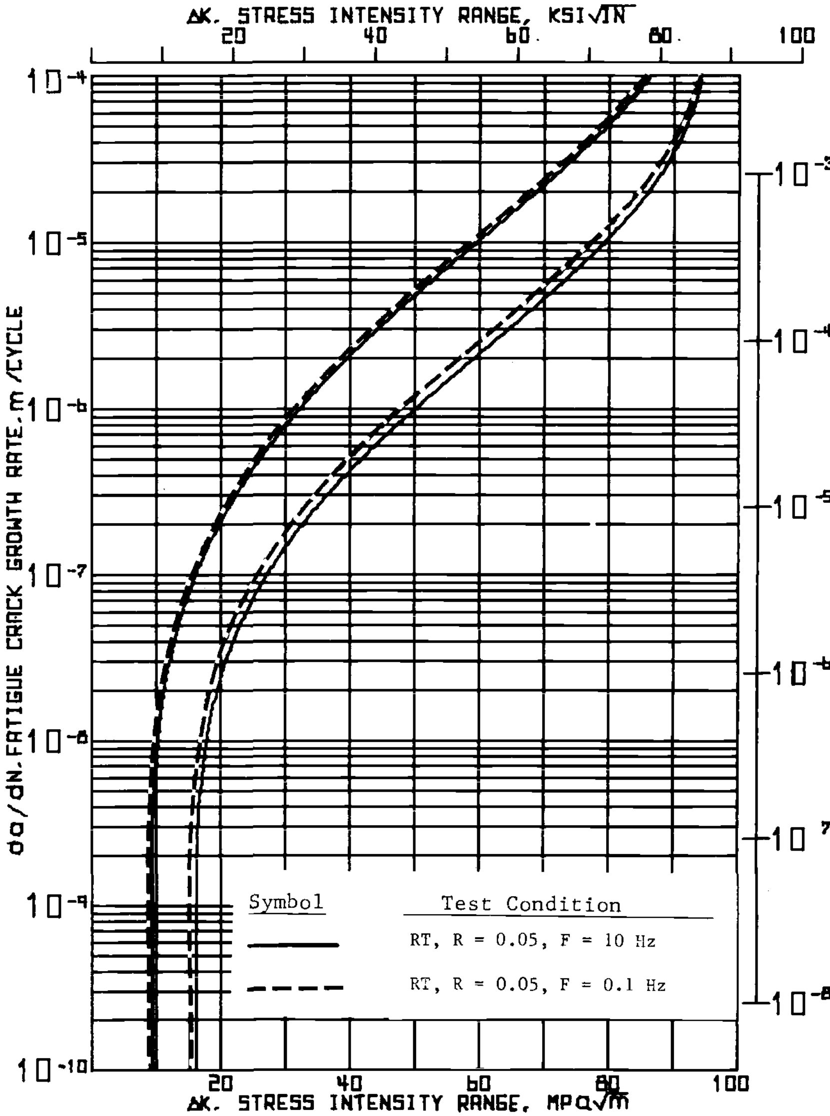

FIG. 10—*Comparison of fatigue crack propagation behavior of Ti-5Al-2.5Sn(ELI) at* F = *10 and 0.1 Hz,* R = *0.05, room temperature.*

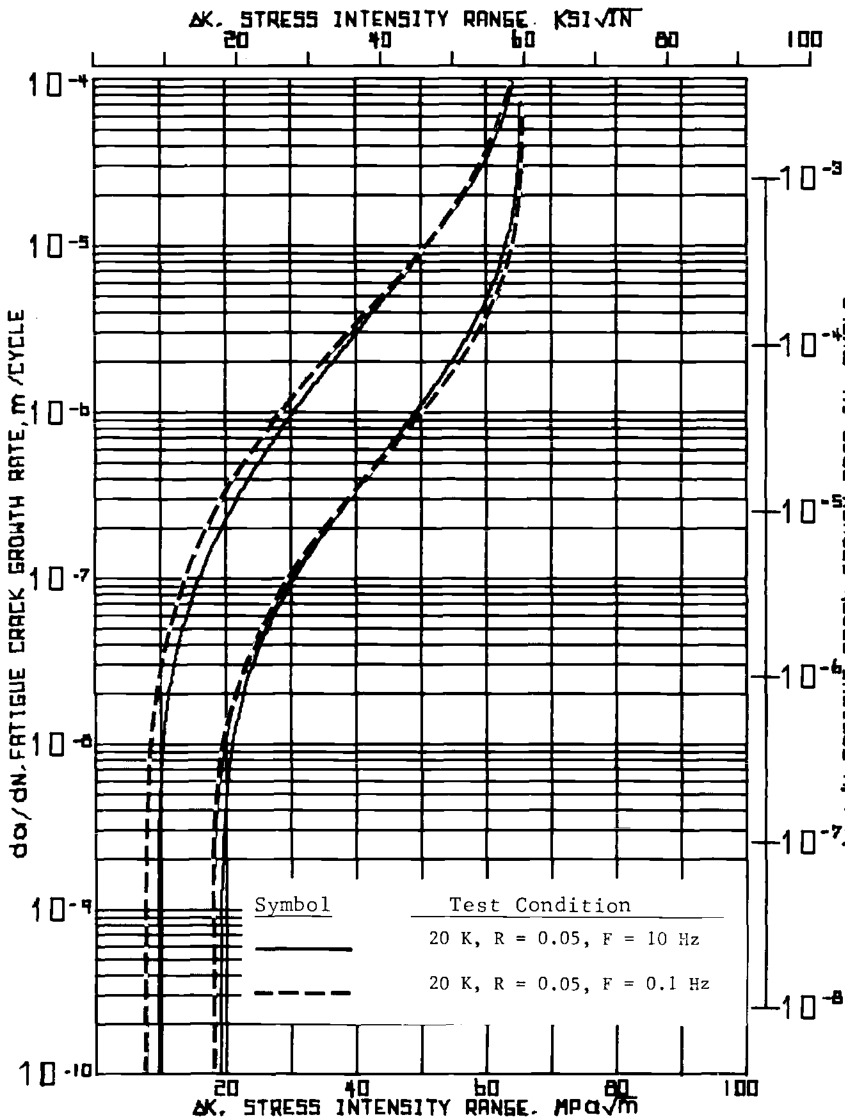

FIG. 11—*Comparison of fatigue crack propagation behavior of Ti-5Al-2.5Sn(ELI) at* F = *10 and 0.1 Hz,* R = *0.05, 20 K (−423°F).*

Effect of Range Ratio

Figures 12 and 13 show the typically observed effect of load ratio (R) on the fatigue crack growth behavior of this alloy. At both temperatures and both frequencies, the data at $R = 0.5$ were shifted to left or higher growth rates, which can be easily seen in the figures. The amount of the data shift was about the same for each temperature. The result was consistent with

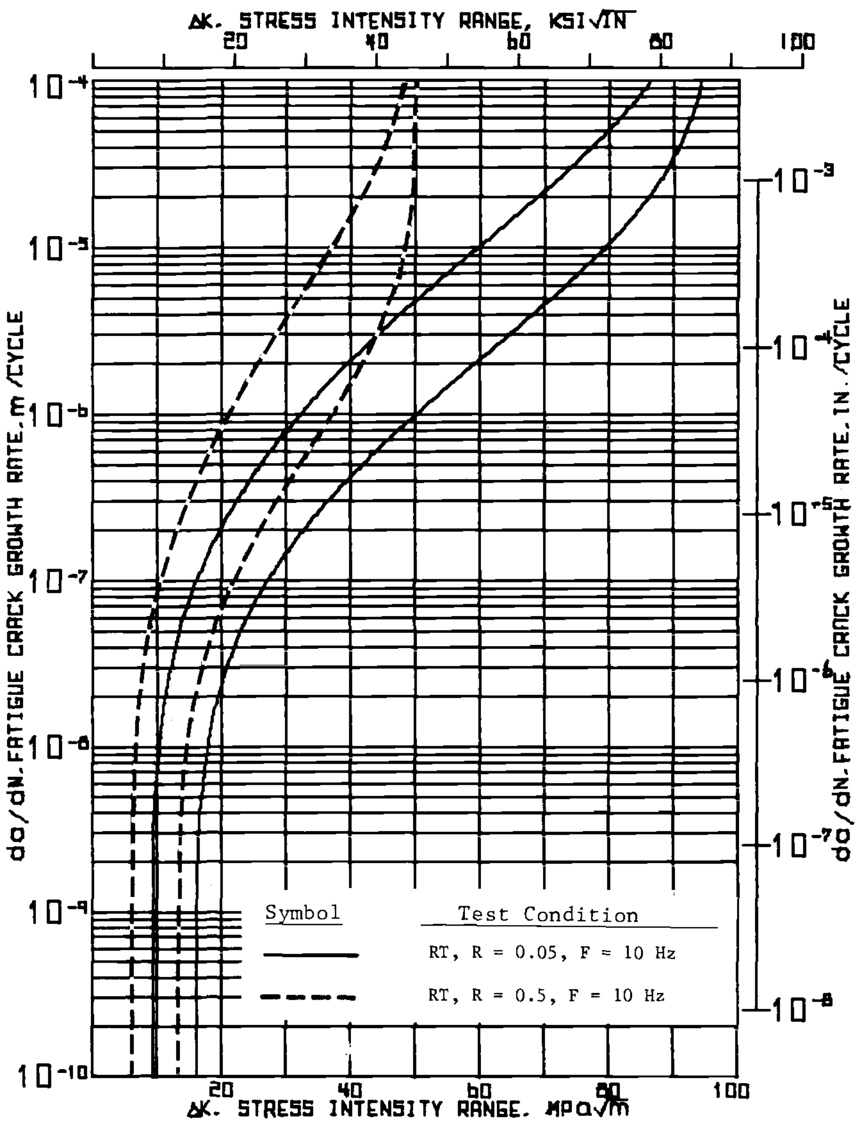

FIG. 12—*Comparison of fatigue crack propagation behavior of Ti-5Al-2.5Sn(ELI) at* R = *0.05 and 0.5,* F = *10 Hz, room temperature.*

other fatigue crack growth studies (see, for example, Ref *16*) and was expected. The only other observation was that except under 10-Hz conditions at room temperature, data at $R = 0.5$ appeared to have somewhat less scatter and hence tighter 2σ data scatter bands than the $R = 0.05$ data, perhaps because of less crack closure.

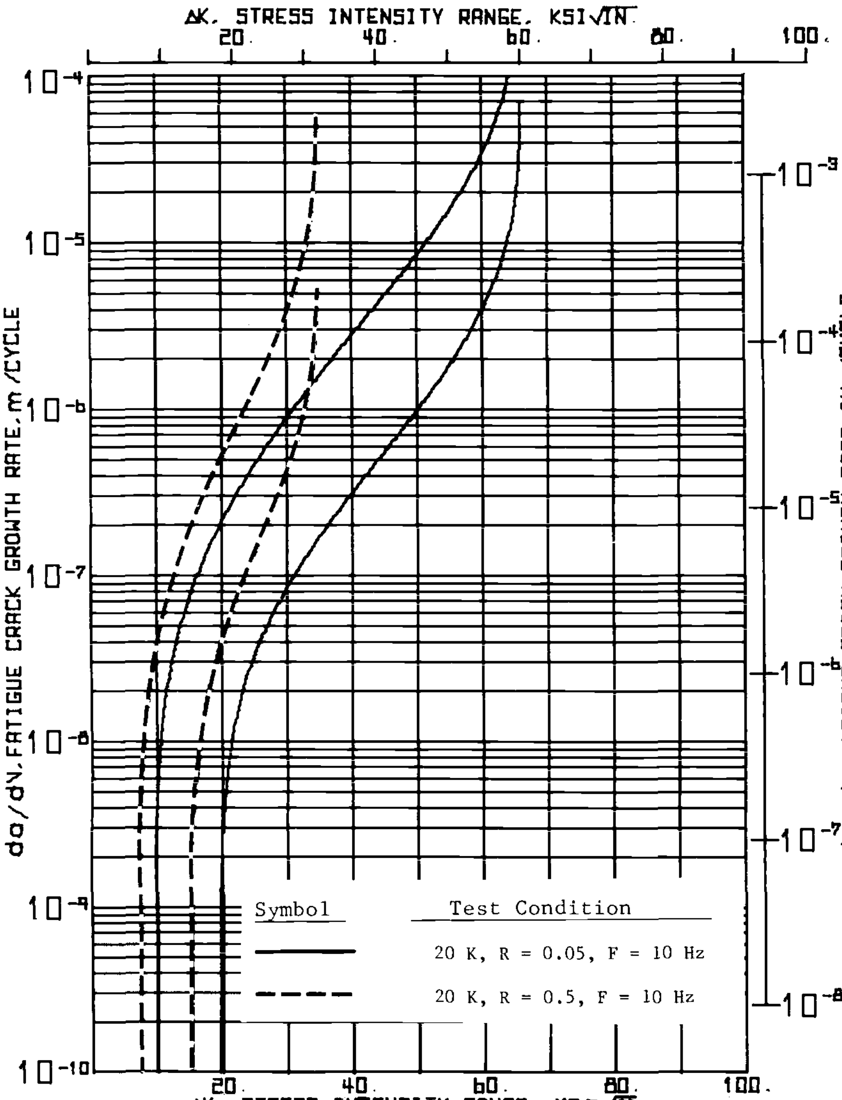

FIG. 13—*Comparison of fatigue crack propagation behavior of Ti-5Al-2.5Sn(ELI) at* R = *0.05 and 0.5,* F = *10 Hz, 20 K (−423°F).*

Effect of Temperature

The typical effect of temperature is shown in Figs. 14 and 15. At both R ratios, the extent of scatter was essentially the same at each temperature and frequency combination. In addition, there was no temperature effect at K levels below 44 MPa $\sqrt{m}$ (40 ksi $\sqrt{in.}$) at $R = 0.05$ and below 33 MPa $\sqrt{m}$ (30 ksi $\sqrt{in.}$) at $R = 0.5$. At higher ΔK levels, 20 K (−423°F) crack growth rates were faster than room temperature rates because of the lower fracture toughness at 20 K (−423°F).

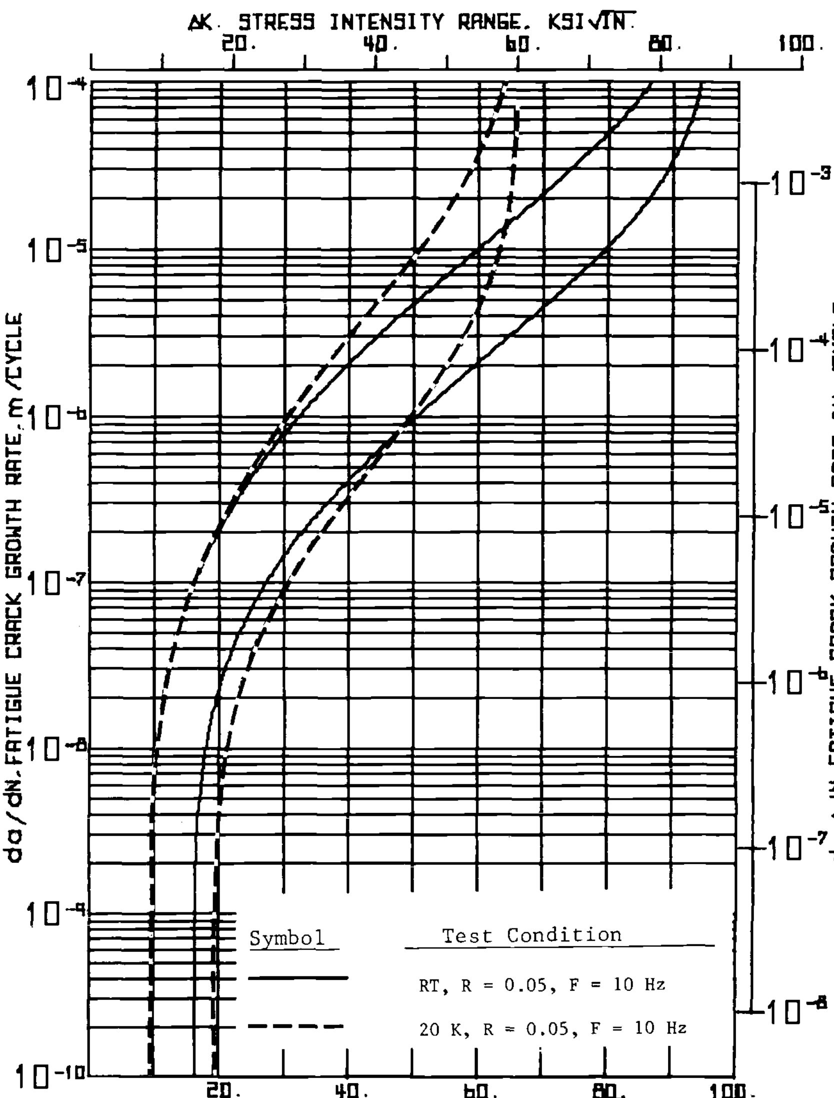

FIG. 14—*Comparison of fatigue crack propagation behavior of Ti-5Al-2.5Sn(ELI) at room temperature and 20 K (−423°F),* R = *0.05,* F = *10 Hz.*

Conclusions

Based on the results of this experimental program, the following conclusions are drawn:

1. Consistent homogeneous forgings were made from the Ti-5Al-2.5Sn (ELI) alloy.

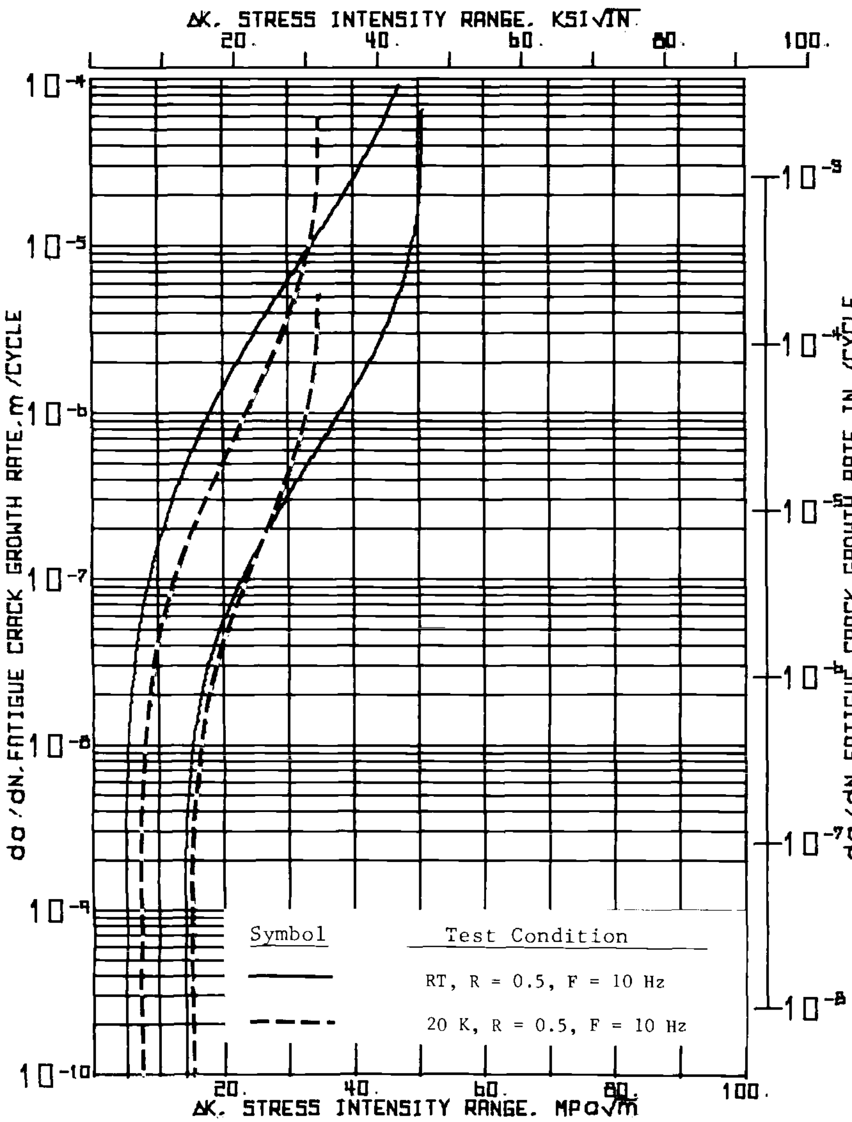

FIG. 15—*Comparison of fatigue crack propagation behavior of Ti-5Al-2.5Sn(ELI) at room temperature and 20 K (−423°F),* R = *0.5,* F = *10 Hz.*

2. Tensile and fracture toughness properties were excellent, met all specifications, and were consistent with data available in the literature.
3. The experimental compliance calibration was unaffected by temperature, except for a correction of modulus.
4. No significant effect of frequency or coupon orientation on fatigue crack propagation behavior was observed.
5. An increase in load ratio (R) increased fatigue crack growth rates.
6. Fatigue crack growth rates at 20 K (−423°F) were similar to room temperature growth rates at low ΔK levels, but faster at high ΔK levels because of the decrease in fracture toughness.

The last conclusion was extremely important for the spin pit fatigue crack growth study [2] conducted after this material evaluation program. Based on the results of this program, fatigue crack growth studies of disks spun in a spin pit were conducted at room temperature, because up to relatively high ΔK levels (44 MPa $\sqrt{\text{m}}$ [40 ksi $\sqrt{\text{in.}}$] at $R = 0.05$) growth rates at room temperature were identical to those obtained at the low temperature. The lack of any significant frequency or orientation effect in the range of interest for the spinning disks was also experimentally helpful.

Acknowledgments

This work was funded by the NASA-Lewis Research Center, Cleveland, Ohio, under Contract NAS3-18896. Kind appreciation is extended to W. E. Krupp, D. E. Pettit, and G. E. Bowie for their contributions to this work and to D. M. Riley for preparation of the manuscript.

References

[1] Van Stone, R. H., Low, J. R., and Shannon, J. L., "The Effect of Microstructure on the *Fracture Toughness of Titanium Alloys,*" Technical Report No. 2-Ti, NASA-Lewis Research Center, Cleveland, OH, Dec. 1974.

[2] Ryder, J. T., "Fracture Control of H-O Engine Components," NASA CR-135137, National Aeronautics and Space Administration, Cleveland, OH, Feb. 1977.

[3] *Titanium Alloy Handbook,* MCIC-HB-02, Metals and Ceramics Information Center (Battelle) and Air Force Materials Laboratory, Columbus, OH, Dec. 1972.

[4] Crossley, F. A., "Titanium-Rich End of the Titanium-Aluminum Equilibrium Diagram," *Transactions of the Metallurgical Society of AIME,* Vol. 236, No. 8, Aug. 1966, pp. 1174–1185.

[5] *Handbook of Chemistry and Physics,* 44th ed., Chemical Rubber Co., Cleveland, OH, 1968.

[6] Buczcek, M. J., Hall, G. S., Seagle, S. R., and Bomberger, H. B., "Grain Refinement in Titanium Alloys," AFML-TR-74-255, Air Force Materials Laboratory, Dayton, OH, Nov. 1974.

[7] "The Mechanical Properties of Ti-6Al-4V, 2-Inch Thick Plate With and Without a Small Addition of Yttrium," Reactive Metals Inc., Niles, OH, Feb. 1975.

[8] "Titanium Alloys Modified with a Trace of Yttrium," Reactive Metals Inc., Niles, OH, May 8, 1975.

[9] Ryder, J. T., Bowie, G. E., and Pettit, D. E., "Recent Considerations in Experimental Compliance Calibration of the WOL Specimen," *Engineering Fracture Mechanics,* Vol. 9, No. 4, Jan. 1977, pp. 901–923.

[10] Sandifer, J. P., and Bowie, G. E., "Double Exponential Functions that Describe Crack Growth Rate Behavior," *A Collection of Technical Papers on Structures and Materials,* AIAA-ASME-SAE 18th Structural Dynamics and Materials Conference, San Diego, 1977, pp. 39–42.
[11] Gumbel, E. J., *Statistics of Extremes,* Columbia University Press, New York, 1958.
[12] Nachtigall, A. J., "Strain Cycling Fatigue Behavior of Ten Structural Metals Tested in Liquid Helium (4 K), in Liquid Nitrogen (78 K), and in Ambient Air (300 K)," NASA TN D-7532, National Aeronautics and Space Administration, Cleveland, OH, Feb. 1974.
[13] Sullivan, T. L., "Behavior of Ti-5Al-2Sn (ELI) Titanium Alloy Sheet Parent and Weld Metal in the Presence of Cracks at 20 K," NASA TN D-6544, National Aeronautics and Space Administration, Cleveland, OH, Nov. 1971.
[14] Tiffany, C. F., Masters, J. N., and Hall, F. A., "Some Fracture Considerations in the Design and Analysis of Spacecraft Pressure Vessels," presented at the 1966 National Metal Congress, McCormick Place, Chicago, IL.
[15] Reuter, W. G., "Fracture Toughness of Ti-5Al-2.5Sn (ELI) Forging at −423°F," Aerojet Memoranda and Material R & D Reports for 30 Oct. 1969–26 Jan. 1971, San Diego, CA.
[16] Pettit, D. E., Ryder, J. T., Krupp, W. E., and Hoeppner, D. W., "Investigation of the Effects of Stress and Chemical Environments on the Prediction of Fracture in Aircraft Structural Materials," AFML TR-74-183, Air Force Materials Laboratory, Dayton, OH, Dec. 1974.

Spectrum Loading, Structures, and Applications

Noncryogenic Temperatures

James M. Cox, Donald E. Pettit, and Sharon L. Langenbeck

Effect of Temperature on the Fatigue and Fracture Properties of 7475-T761 Aluminum

REFERENCE: Cox, J. M., Pettit, D. E., and Langenbeck, S. L., "**Effect of Temperature on the Fatigue and Fracture Properties of 7475-T761 Aluminum,**" *Fatigue at Low Temperatures, ASTM STP 857,* R. I. Stephens, Ed., American Society for Testing and Materials, Philadelphia, 1985, pp. 241–256.

ABSTRACT: The effect of low-temperature toughness degradation on damage tolerance and life analysis methodology is discussed. Spectrum fatigue and fatigue crack growth tests were conducted and life predictions made on 7475-T761 aluminum. The retardation behavior was determined by conducting constant K single overload fatigue crack growth tests. The low-temperature environment (−54°C [−65°F]) improved the life of fatigue and fatigue crack growth tests subjected to several loading spectra. This may be partially attributable to stronger retardation effects at low temperatures. It is concluded that low temperature may be a factor in damage tolerance and life analysis only under certain conditions.

KEY WORDS: aluminum alloys, temperature, R-curve, fatigue, fatigue crack growth, spectrum (loading), life prediction, damage tolerance, retardation

For quite some time the problem of subcritical flaw growth and subsequent fracture of aircraft structural components has been recognized as a significant factor in the safety, maintainability, and life-cycle costs of modern aircraft. For traditional metallic structure, requirements such as MIL-A-83444 on Airplane Damage Tolerance Requirements have been developed that specify the general framework for damage tolerance analysis. One requirement common to these specifications is that the analysis be representative of structural behavior in typical operating environments. Aluminum aircraft structural design has been based, for the most part, on room or elevated temperature data. This practice seems to result from the belief that the face-centered cubic crystal structure of aluminum precludes the type of transition temperature effects that are prevalent in body-centered cubic steels [*1*].

Mr. Cox is a senior scientist and Mr. Pettit a group engineer in the Fatigue and Fracture Mechanics Laboratory of the Kelly Johnson R&D Center at Lockheed-California Co. in Burbank, CA 91520. Dr. Langenbeck is a research scientist in the Materials and Processes Department of Lockheed-California.

This belief in the low-temperature insensitivity of aluminum alloys was shattered in the mid-1970s. During that time, Wang [*2*] and Pettit and Van Orden [*3*], among others, reported a significant reduction in the toughness of several 7000 series aluminum sheet materials at low temperature. Since that time, Lockheed-California Company has been assessing if and how the low-temperature effects should be integrated into damage tolerance procedures. The work reported herein is part of that effort.

Background

Tension and R-curve toughness tests at room and lower temperatures on three different aluminum alloys were conducted in 1977 [*3*]. Summaries of the tension and *R*-curve data are reproduced here in Table 1 and Fig. 1, respectively. The tension tests showed that all three alloys exhibit a slight increase in tensile strength with decreasing temperatures while no significant variation was noted in the elongation or reduction-of-area values. The *R*-curve tests were conducted on the same three alloys according to ASTM Practice for *R*-Curve Determination (E 561). The apparent fracture toughness based on the maximum load and the initial crack length for the three materials is presented in Fig. 1 as a function of test temperature. The results show a major decrease in the apparent fracture toughness of the two 7000 series alloys but no degradation in the toughness of the 2024-T3 material.

Fractographic features of failed tension and *R*-curve specimens were observed by scanning electron microscopy (SEM). The 7000 series specimens (both tension and *R*-curve) exhibited a change in fracture mode, going from primarily ductile dimpled rupture at room temperature to flat quasi-cleavage as the test temperature was decreased. No change with temperature was observed in the fracture features for any of the 2024-T3 specimens, the fracture mode remaining that of microvoid coalescence and growth for all conditions.

Constant-amplitude fatigue crack growth (FCG) data ($R = +0.1$) were also generated for the 2024 and 7475 materials and are also presented in Ref *3*. Results for 2024-T3 showed no effect of temperature over the entire range of data (approximately 7.6×10^{-4} to 7.6×10^{-2} mm/cycle [3×10^{-5} to 3×10^{-3} in./cycle]). For the 7475-T761, however, an increasingly significant acceleration of the FCG rate was observed at −54°C (−65°F) relative to 22°C (72°F) data above a ΔK value of approximately 22 MPa $\sqrt{m}$ (20 ksi $\sqrt{in.}$), as shown in Fig. 2. Other researchers (see Abelkis et al [*4*]) have reported similar results at higher ΔK levels but slower crack growth rates for a −54°C (−65°F) environment at low ΔK levels for both 2024-T351 and 7475-T7651 alloys (i.e., a higher FCG threshold at −54°C [−65°F] than at room temperature). This is called a crossover effect since the crack growth curves actually cross over each other. While the data presented here do not go to as low a *da/dN* rate as the Abelkis data, they do go below the level at which crossover should have been evident. The crossover/no-crossover question will be discussed later in this paper.

TABLE 1—*Effect of test temperatures on tensile properties.*

Alloy	Temperature, °C	Yield Strength, MPa	Ultimate Strength, MPa	Elongation, %	Reduction of Area, %
2024-T3 (clad)	+22	297	455	20	25
	−54	304	469	24	28
7075-T76 (bare)	+22	497	552	11	15
	−54	518	573	11	19
7475-T761 (clad)	+22	428	490	12	19
	−7	462	524	13	21
	−29	462	531	11	19
	−54	469	538	12	19

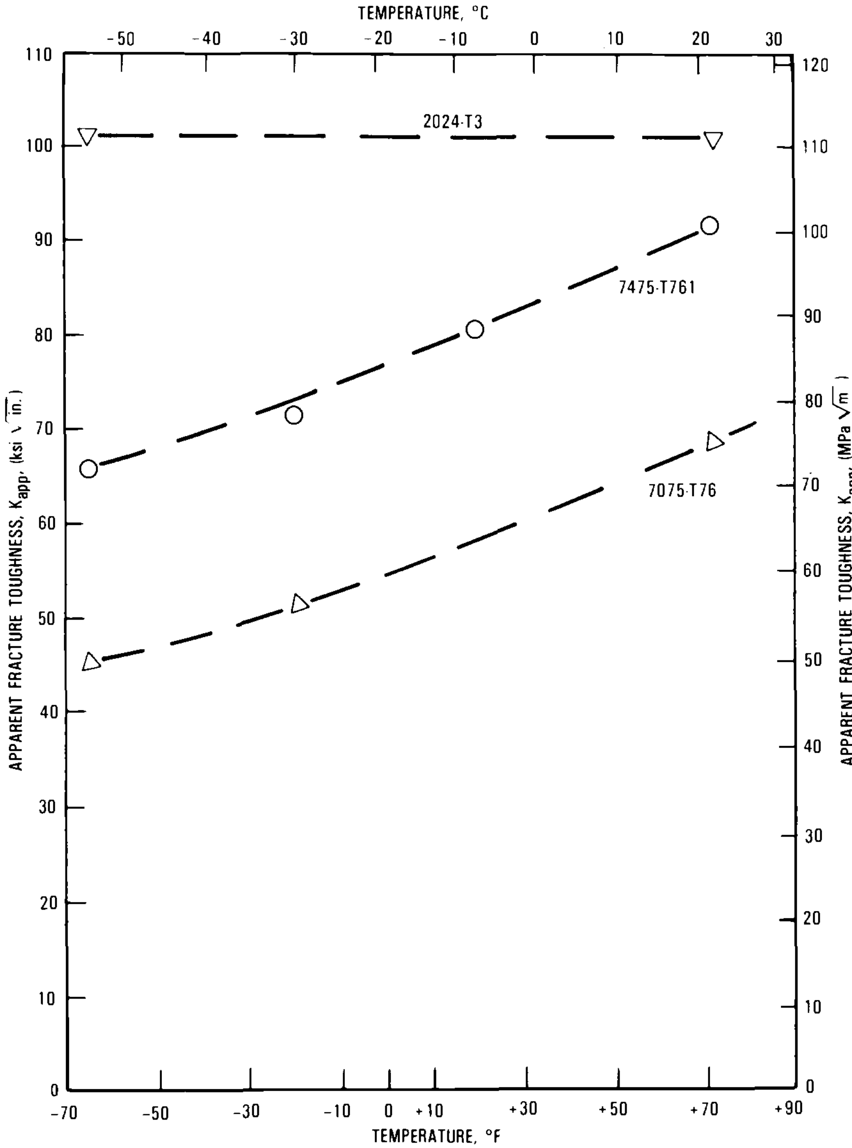

FIG. 1—*Effect of test temperature on the apparent fracture toughness of three aluminum alloys.*

Damage Tolerance Considerations

Testing up until the time of the publication of Ref *3* (1979) was aimed at determining what properties and alloys were affected by the low-temperature environment. The next step, which has been undertaken since then, was to determine how these property changes would affect damage tolerance life analyses. Obviously, The *R*-curve data directly affect these analyses in that the critical

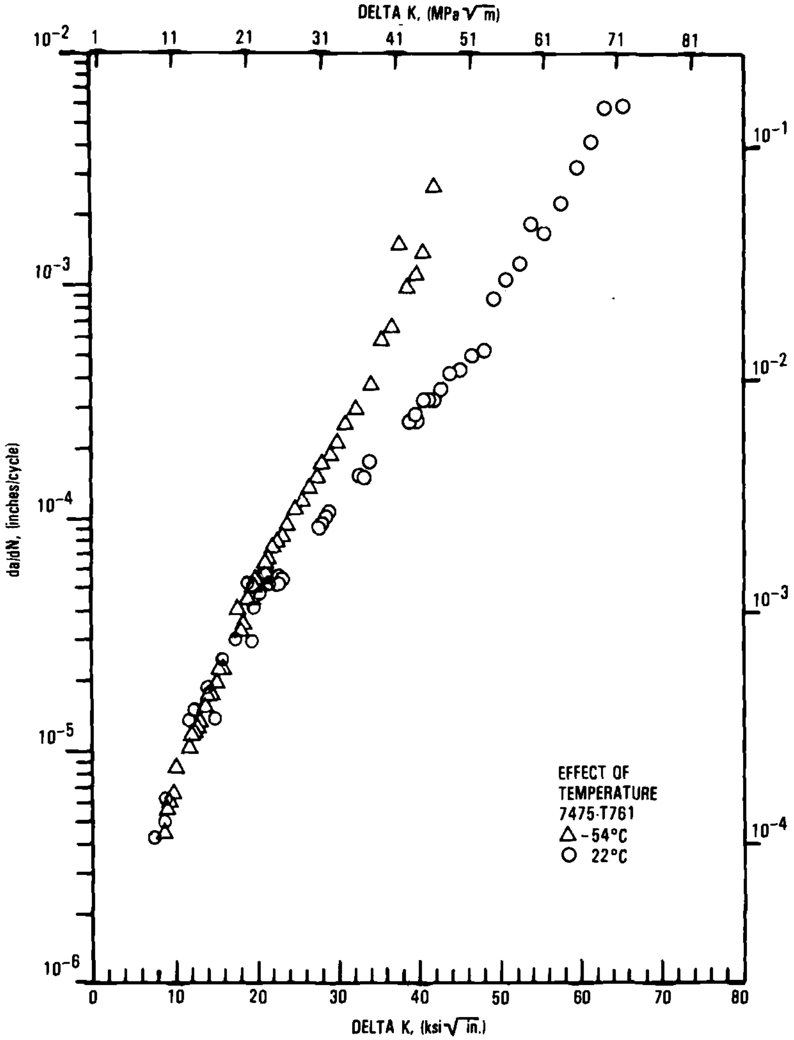

FIG. 2—*Effect of temperature on the fatigue crack growth behavior of 7475-T761.*

crack length is shorter at lower temperatures. The constant-amplitude FCG data are less significant, however, because few aircraft structures experience constant-amplitude loads. Since the 2024-T3 alloy had been insensitive to low temperatures on all tests conducted so far, the 7475-T761 material was the only alloy to be investigated in the remainder of the program. It should be noted that all tests were conducted at a constant temperature of either +22°C (+72°F) or −54°C (−65°F) (as opposed to a temperature spectrum). While this does not simulate the actual operating environment it does allow for three things: (1) ease and speed of testing, (2) simplification of analysis, and, probably most important, (3) the provision of what was believed to be a worst-case situation (i.e., −54°C [−65°F] 100% of the time). In this paper, "low temperature" refers to a −54°C (−65°F) environment.

Two aspects of making accurate life analyses that were investigated were spectrum fatigue and spectrum FCG. Spectrum FCG is more important analytically because most current damage-tolerance standards require the assumption of a pre-existent flaw. An important aspect of analyzing the impact of low temperature effects on life analysis is to determine the accuracy of current life prediction techniques. If the inaccuracies in current predictive capabilities are greater than the error introduced by not accounting for low temperature effects, then these effects may not need to be taken into account. Therefore life predictions based on constant-amplitude FCG data were made for the spectrum FCG tests.

For both the fatigue and the FCG tests the loading spectrum used was the 80-Flight Fighter Spectrum [*5,6*]. This spectrum sequence consists of 40 typical and 40 severe usage flights, simulating the mix of flights in an F-4 pilot training course conducted by the U.S. Air Force [*7*]. These flights are applied in a random order. For simplicity, the ground loadings are truncated at zero load, resulting in a tension-only load sequence. Figure 3 compares the 80-flight test spectra to mission mix spectra for the F-16, F-15, and A-7D from Refs *8*, *9*, and *10*, respectively. Load interaction effects for this spectrum are expected to be very high and were shown to be responsible for changes in experimental crack growth rates of a factor of four at room temperature [*5,6*].

Spectrum Fatigue Crack Growth

Four center crack tension (CCT) panels (specimen width $W = 102$ mm [4 in.] and thickness $B = 1.8$ mm (0.072 in.]) were fabricated from 7475-T761 aluminum sheet. Before these specimens were tested, life predictions were made based on the constant-amplitude FCG data previously presented in Fig. 2. Two predictions were made for each environment. In the first analysis the crack retardation caused by high tensile loadings in the spectrum was neglected (that is, no retardation). In the second analysis a slight variation of the retardation model of Willenborg et al was used [*11*]. The exact procedures used were identical to those outlined in Refs *5* and *6*.

The resulting life predictions (shown as open data points) as well as actual test data from the four specimens mentioned above are presented in Fig. 4. The analysis assuming retardation predicts significantly longer lives than that assuming no retardation and is more accurate when compared to the actual test data. The predictions premised on retardation, however, are slightly nonconservative when compared with the actual data. As expected, the analyses resulted in predictions of "shorter" lives for the −54°C (−65°F) tests than for the room temperature tests. However, the actual tests resulted in

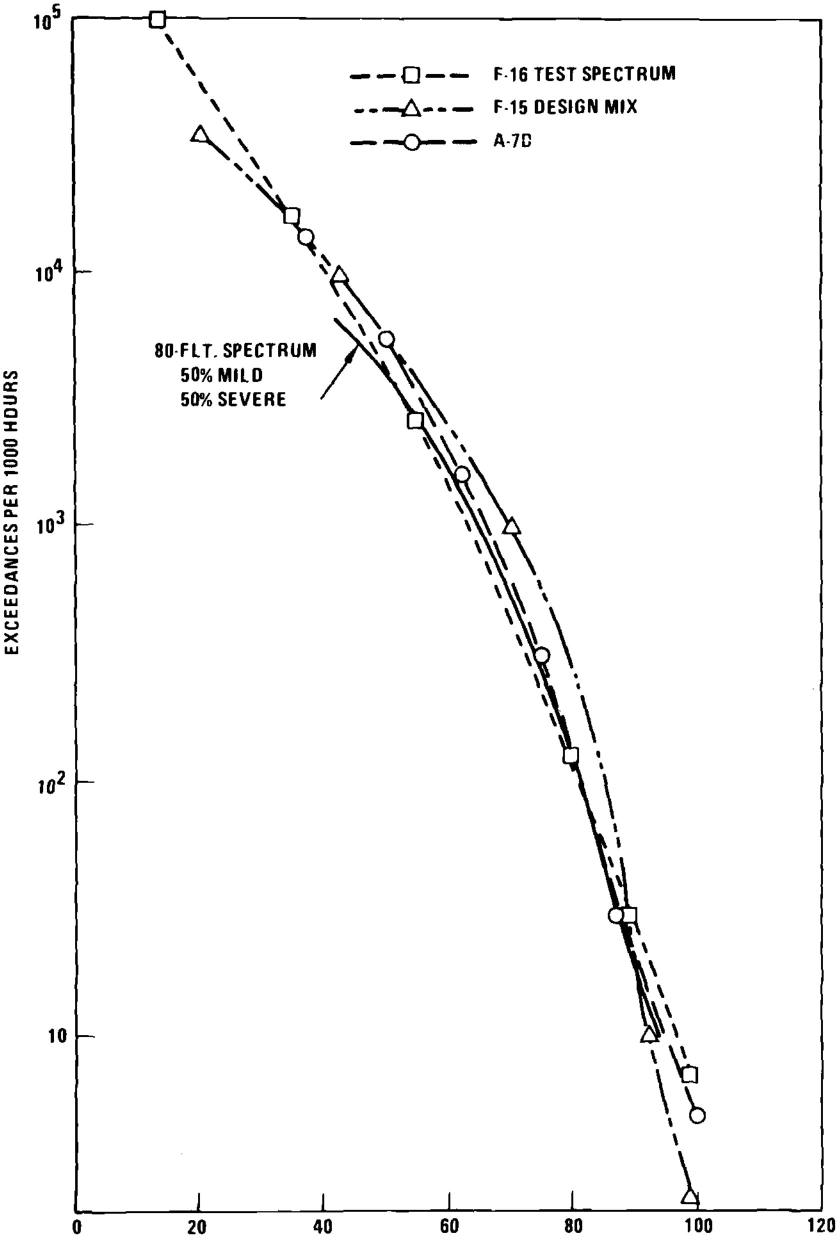

FIG. 3—*Comparison of 80-Flight Fighter Spectrum to other fighter spectra.*

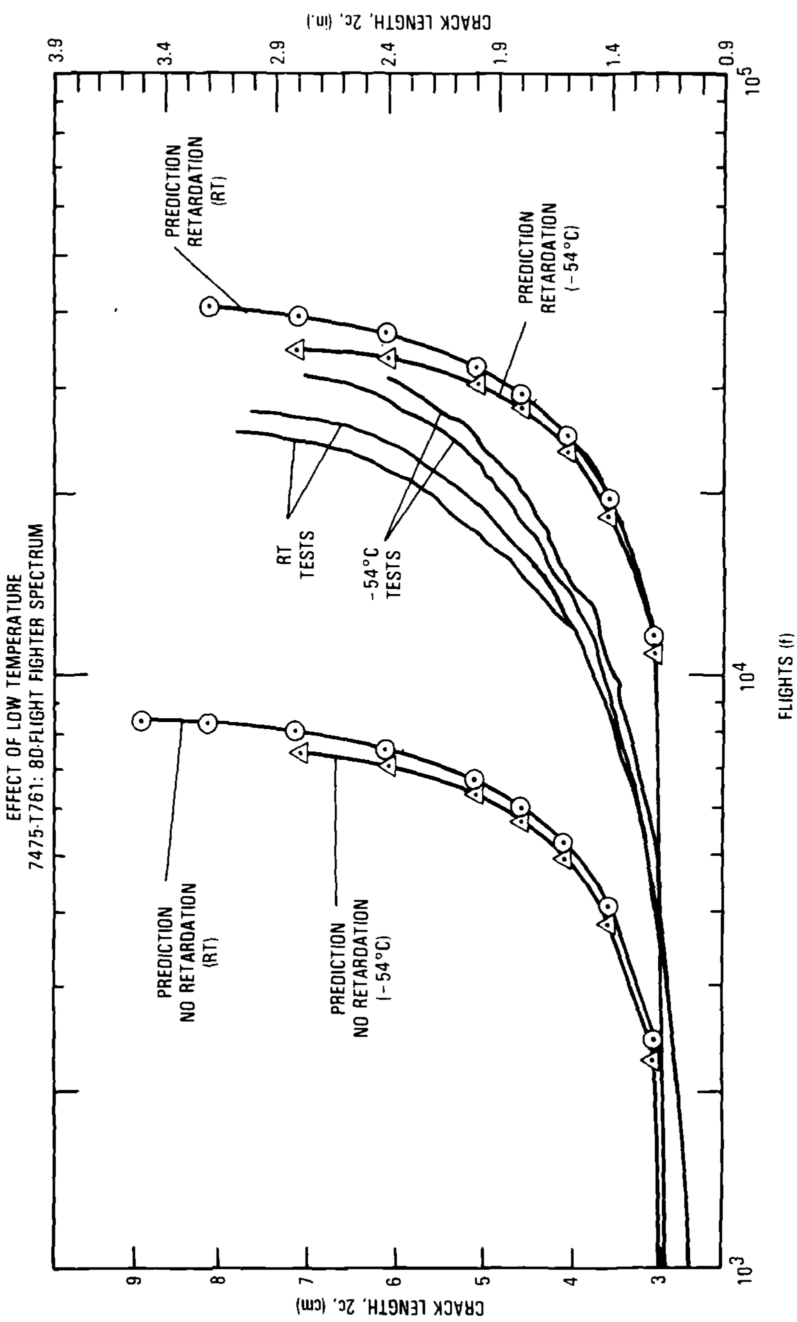

FIG. 4—*Life predictions based on constant-amplitude data from Fig. 2 and actual test data showing the effect of temperature.*

approximately 20% longer lives for the −54°C (−65°F) tests. This was true even though the low-temperature specimens failed at shorter crack lengths because of decreased toughness at that temperature. One possible explanation of this seemingly anomalous behavior is that the constant-amplitude FCG threshold is indeed lower at room temperature than at −54°C (−65°F), as determined by Abelkis et al [*4*]. If these constant-amplitude FCG data are used as input to the life prediction program described earlier, the results presented in Fig. 5 are generated. The relative positions calculated for the two temperatures now agree with the actual data (i.e., room temperature life is shorter than low-temperature life). These predictions do not, however, agree well with the actual data in absolute terms. One could argue that the model inherently overpredicts the lives in this instance. If this were true, however, it should overpredict them by a consistent amount. In this case the actual life is 61% of the predicted life at room temperature and only 37% at −54°C (−65°F). This difference seems to indicate that even if the constant-amplitude FCG behavior described by Abelkis et al [*4*] is the proper one, it may not by itself completely explain the spectrum FCG behavior.

All the predictions made so far (based on either of the constant-amplitude FCG data sets) assume that the material reacts to overloads (retardation) in the same manner independently of temperature. If temperature and retardation behavior are not independent of each other, the actual relationship between room temperature and −54°C (−65°F) data would be shifted from

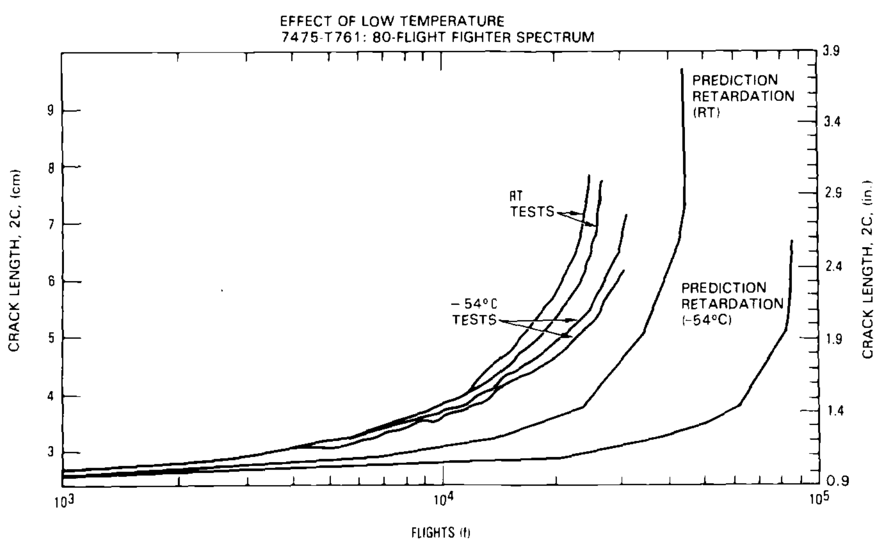

FIG. 5—*Life predictions based on constant-amplitude data from Abelkis et al [4] and actual test data showing the effect of temperature.*

that predicted. This factor could then account for the discrepancies between predicted and actual lives mentioned previously. To understand the temperature/retardation relationship it is necessary to isolate the phenomena.

Constant-*K* Single Overload Tests

To isolate retardation effects two things must be accomplished. First, only one overload should be dealt with at a time. Second, the overload effect should not be masked by increasing stress intensity factor due to crack growth. These requirements lead to the constant-*K* single overload tests described in this section.

Two center cracked tension (CCT) specimens ($W = 610$ mm [24.0 in.] and $B = 1.83$ mm [0.072 in.]) were fabricated from the same 7475-T761 sheet material used in the previous tests. One specimen was tested at room temperature, while the other was tested at −54°C (−65°F). All other testing parameters were identical. The specimens were subjected to the loading sequence shown in Fig. 6. The tests were conducted at three different constant-*K* levels per panel. The stress intensity factor was maintained at a constant by shedding load as the crack grew. In this way *K* was kept within approximately 10% of the average stress intensity factor for each level. At each *K* level ($K = 11, 22, 33$ MPa $\sqrt{m}$ [10, 20, 30 ksi $\sqrt{in.}$]) three different overload ratios ($U_{OL} = 1.2, 1.6, 2.0$) were applied. The overload ratio is described as the ratio of the overload stress intensity to the maximum stress intensity before the single overload cycle ($U_{OL} = K_{OL}/K_{max}$).

To analyze the data, the steady-state crack growth rate data (da/dN) before each overload were determined. Then after each overload the number of cycles required to reattain the previously determined steady-state da/dN rate were counted. This cyclic count was then defined as the "recovery cycles" for each U_{OL}, nominal ΔK, and temperature combination. The recovery cycle data are presented in Table 2. Figure 7 presents the data trends graphically. The data points have been left off for clarity. Each line in this figure represents a temperature (room or −54°C) and an overload ratio (1.2, 1.6, or 2.0). The arrows pointing down indicate that the steady-state rate was reattained on the first reading after the overload; therefore the locations of those lines with downward pointing arrows are a reflection of the intervals between crack readings rather than retardation effects. The arrows pointing up indicate that the steady-state rate was never reattained by the end of the test.

Obviously the temperature/retardation behavior is rather complicated. Analysis of that behavior is not helped by the fact that there are relatively few data points. The only obvious trend is that at low overload ratios ($U_{OL} = 1.2$) FCG was retarded at room temperature but not significantly at −54°C (−65°F). This indicates that a very mild spectrum may result in markedly different behavior than the more severe spectrums.

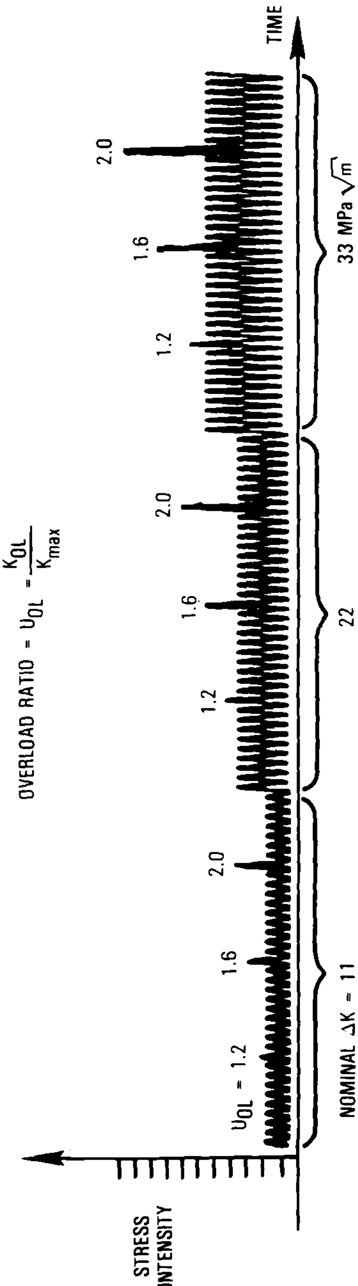

FIG. 6—*Constant-K single overload loading sequence.*

TABLE 2—*Effect of temperature on fatigue crack growth retardation.*

Nominal ΔK MPa $\sqrt{m}$	Overload Factor (U_{OL})	Cycles to Recovery (×1000) Room Temperature Right Crack	Room Temperature Left Crack	−54°C Right Crack	−54°C Left Crack
11	1.2	4	2	<1	<1
	1.6	6	3	4	4
	2.0	10	10	25	30
22	1.2	1.25	1.25	<0.75	<0.75
	1.6	3.74	3.74	4.5	5.25
	2.0	>22.05	12.75	10.75	10.25
33	1.2	0.65	0.35	<0.05	<0.05
	1.6	3.8	2.6	>7.1	5
	2.0	>43.7	>43.7	[a]	[a]

[a] Specimen failed upon application of this overload.

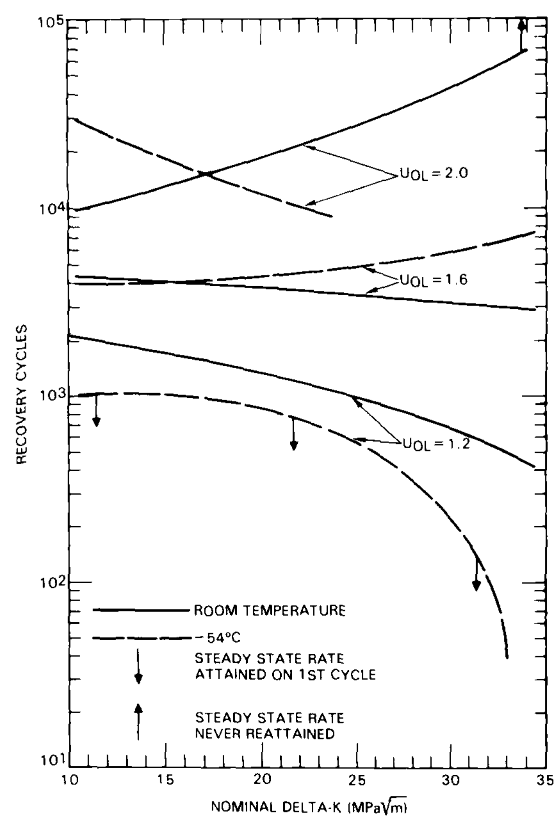

FIG. 7—*Effect of temperature on fatigue crack growth retardation.*

Spectrum Fatigue

The discussion so far has been concerned only with crack growth. Another area of concern is crack initiation at the different temperatures and is addressed by fatigue testing.

Fatigue specimens (190 by 38 by 1.8 mm [7.50 by 1.50 by 0.072 in.]) center-notched with a stress concentration factor (K_t) of seven were fabricated from 7475-T761 aluminum sheet. Six specimens were tested at room temperature and six at −54°C (−65°F). All specimens were subjected to the spectrum loading previously described. The results are presented in Fig. 8. The ordinate refers to the gross stress equivalent of the maximum load in the spectrum.

The room temperature specimens had consistently shorter lives than did the −54°C (−65°F) specimens. The tests were not monitored in a way that would allow the life attributable to crack initiation to be separated from that attributable to crack growth; however, based on the spectrum "actual" fatigue crack growth data previously discussed it seems that most of the difference in fatigue life can be attributed to crack growth, not crack initiation. This hypothesis is especially plausible when one considers the high K_t of the fatigue specimens. At lower K_t values temperature may indeed play a larger role in crack initiation.

Other Considerations

While all discussions so far have centered on low versus room temperature retardation behavior, there is another factor that could have affected the results. This other factor is the difference in humidity between a room temperature and a −54°C (−65°F) environment. Since some of the behavior observed could be attributed to humidity effects, repeating the tests in a dry room temperature environment could prove interesting.

Ongoing work on the spectrum fatigue crack growth behavior of 7000 series aluminum alloys at room temperature and −54°C (−65°F) is proceeding. Recent results indicate that both 7475-T7651 tested under a tension only-lower wing transport spectrum and 7075-T6 tested under the tension-compression Minitwist [*12*] transport spectrum also result in longer lives at −54°C (−65°F) when compared to room temperature. Both of these spectra are milder than the 80-Flight Fighter Spectrum.

Conclusions

The way in which the data affect life analysis, and thus design, is still unclear. Certain observations can, however, be made:

1. For all the alloys tested, use of room temperature static data is adequate.
2. Since 7075-T76 and 7475-T761 specimens both experience reduced toughness at low temperature, this should be taken into account in residual strength calculations. (The 2024-T3 specimens were not affected.)

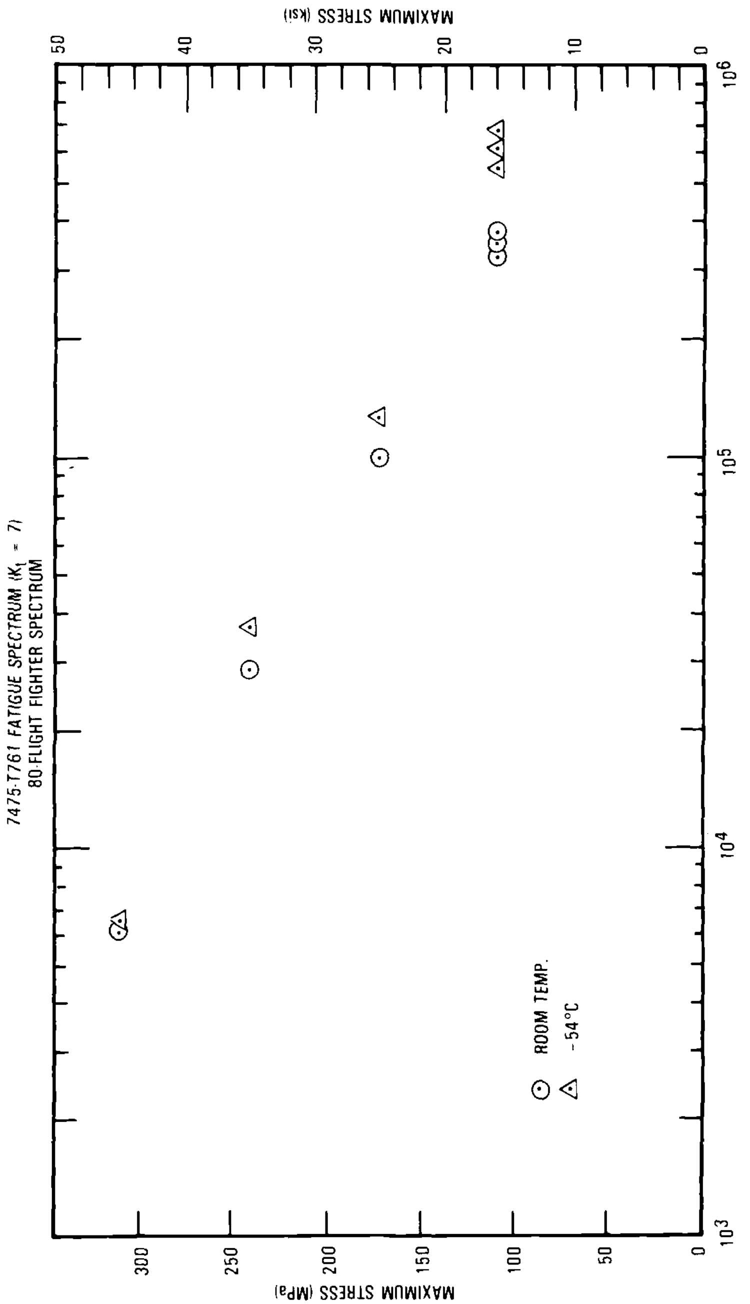

FIG. 8—*Effect of test temperature on spectrum fatigue behavior of 7475-T761 for center-notched sheet* (K_t = 7).

3. It is encouraging that, for all the alloy/spectrum combinations tested so far, the low-temperature spectrum FCG lives have been longer than the room temperature lives. If this trend continues for all other alloy/spectrum combinations, low temperature need not be considered in spectrum fatigue crack growth life analysis because room temperature predictions would be conservative.

Questions that still need to be answered are:

1. Does a crossover in constant-amplitude *da/dN* behavior (lower *da/dN* at −54°C) occur at lower ΔK? If it does, is it the sole reason for longer lives under spectrum loading at −54°C? Fractography may provide further insight.
2. How does low temperature affect fatigue crack initiation?
3. Does 7475-T761 react differently when subjected to a very mild spectrum, as is suggested by the constant-K single overload tests?
4. Is humidity a factor in the behavior so far observed?
5. Would a temperature spectrum combined with the loading spectrum have an effect?

Acknowledgments

This work was performed from 1979 to 1982 as part of the Lockheed-California Company Independent Research Program. Special thanks are given to T. R. Brussat, for his assistance in making the life predictions, and to W. Renslen, P. Mohr, D. Diggs, L. Silvas, L. Reed, and C. Spratt, for their competent performance in the laboratory.

References

[1] Flinn, R. A. and Trojan, P. K., *Engineering Materials and Their Application,* Houghton Mifflin, Boston, 1981, pp. 85–88.

[2] Wang, D. Y., "Plane Stress Fracture Toughness and Fatigue Crack Propagation of Aluminum Alloy Wide Panels," in *Progress in Flaw Growth and Fracture Toughness Testing, ASTM STP 536,* J. G. Kaufman, Ed., American Society for Testing and Materials, Philadelphia, 1972, pp. 334–349.

[3] Pettit, D. E. and Van Orden, J. M., "Evaluation of Temperature Effects on Crack Growth in Aluminum Sheet Material," in *Fracture Mechanics, ASTM STP 677,* C. W. Smith, Ed., American Society for Testing and Materials, Philadelphia, 1979, pp. 106–124.

[4] Abelkis, P. R., Harmon, M. B., Hayman, E. L., MacKay, T. L., and Orlando, J., "Low-Temperature and Loading Frequency Effects on Crack Growth and Fracture Toughness of 2024 and 7475 Aluminum," *Fatigue at Low Temperatures, ASTM STP 857,* R. I. Stephens, Ed., American Society for Testing and Materials, Philadelphia, 1985, pp. 257–273.

[5] Young, L. and Brussat, T. R., "Summary of 1975 Independent Research in Fatigue and Fracture Mechanics Methods," Report LR 27298, Lockheed California Company, Burbank, CA, Dec. 1975.

[6] Brussat, T. R., Chiu, S., and Creager, M., "Flaw Growth in Complex Structure, Vol. 1-Technical Discussion," AFFDL-TR-77-79, Air Force Flight Dynamics Laboratory, Air Force Systems Command, Wright-Patterson AFB, OH, Dec. 1977.

[7] "Syllabus of Instruction USAF Operational Training Course, F-4," TAC-Syllabus Course 111507B, Dept. of the Air Force, Tactical Air Command, Nov. 1972.

[8] Dill, H. D. and Potter, J. M., "Effects of Fighter Attack Spectrum on Crack Growth," AFFDL-TR-76-112, Air Force Flight Dynamics Laboratory, Air Force Systems Command, Wright-Patterson AFB, OH, 1976.
[9] Johnson, G. S., "F-16 Durability and Damage Tolerance Load Spectra," *Proceedings AF/Industry Workshop on Fatigue Spectra Development for Aircraft*, AFWAL-TM-81-61-FIBE, Air Force Wright Aeronautical Laboratories, Air Force Systems Command, Wright-Patterson AFB, OH, Dec. 1980, pp. 187–218.
[10] White, D. J., "Summary of Flight Spectra Development for Fighter Aircraft," *Proceedings AF/Industry Workshop on Fatigue Spectra Development for Aircraft*, AFWAL-TM-81-61-FIBE, Air Force Wright Aeronautical Laboratories, Air Force Systems Command, Wright-Patterson AFB, OH, Dec. 1980, pp. 323–348.
[11] Willenborg, J., Engle, R. M., and Wood, H. A., "A Crack Growth Retardation Model Using an Effective Stress Concept," AFFDL Technical Memorandum 71-1-FBR, Air Force Flight Dynamics Laboratory, Air Force Systems Command, Wright-Patterson AFB, OH, Jan. 1971.
[12] Lowak, H., de Jonge, J. B., Franz, J., and Schutz, D., "MINITWIST, A Shortened Version of TWIST," NRL-MR 79018 U, National Aerospace Laboratory, NRL, Amsterdam, The Netherlands, 1979.

Paul R. Abelkis, Marilyn B. Harmon, Elmer L. Hayman, Theron L. Mackay, and John Orlando

Low Temperature and Loading Frequency Effects on Crack Growth and Fracture Toughness of 2024 and 7475 Aluminum

REFERENCE: Abelkis, P. R., Harmon, M. B., Hayman, E. L., Mackay, T. L., and Orlando, J., **"Low Temperature and Loading Frequency Effects on Crack Growth and Fracture Toughness of 2024 and 7475 Aluminum,"** *Fatigue at Low Temperatures, ASTM STP 857,* R. I. Stephens, Ed., American Society for Testing and Materials, Philadelphia, 1985, pp. 257–273.

ABSTRACT: An experimental program was conducted to investigate the effect of low temperature (219 K [−65°F]) on the crack growth and fracture toughness of two aluminum alloys, 2024-T351 and 7475-T7651. Crack growth tests were performed with center-cracked panels and constant-amplitude and spectrum loadings. The spectrum represented a transport wing lower surface. The results show the 2024 alloy properties at low temperature to be equal to or better than the properties of that alloy at room temperature (RT), whereas some of the 7475 alloy properties decreased. In addition, tests were performed at RT and low temperature on 2024-T3 to evaluate the effect of loading frequency on crack growth. The results indicated a faster crack growth rate at lower frequencies.

KEY WORDS: crack growth, fracture toughness, low temperature, aluminum, fatigue tests

A subsonic commercial transport airframe structure is subjected to temperature variations from 219 K (−65°F) to more than 333 K (140°F). The airframe outer surface reaches the low temperature at cruise altitudes between 9100 and 12 200 m (30 000 and 40 000 ft). Therefore material data at such temperature extremes are needed for material selection and design, particularly with respect to damage tolerance requirements.

This paper presents the results of an experimental program on the effects

The authors are with McDonnell Douglas Corporation, Douglas Aircraft Company, Long Beach, CA 90846, where Mr. Abelkis is unit chief of structural mechanics, Mrs. Harmon a staff engineer in structural mechanics, Mr. Hayman unit chief of materials and process engineering, and Dr. Mackay a senior technical specialist in materials and process engineering. Mr. Orlando is retired.

of low temperature on crack growth and fracture toughness of two aluminum alloys (2024-T351 and 7475-T7651) and the effect of loading frequency on the crack growth of 2024-T3 at room and low temperature. The 2024 aluminum is used for wing lower surface and fuselage skin, while 7475 is considered for the wing lower skin. The experimental program investigated the following variables:

- Temperature: room temperature (RT) or low temperature (LT) of 219 K (−65°F).
- Loading: constant amplitude (CA) and spectrum.
- Loading frequency: 5 Hz, or 2 or 4 cycles/h.

Crack growth data were obtained at RT and 219 K (−65°F) under constant-amplitude or spectrum loading representing a transport wing lower surface. Residual strength tests were performed on most specimens at the end of crack growth testing.

The effect of loading frequency was investigated to reflect the slow change in fuselage skin hoop tension stress resulting from fuselage pressurization. Full pressure differential is typically reached at approximately 8500 m (28 000 ft) of altitude. It takes anywhere from 15 to 25 min for a jet transport to reach this altitude. This loading was represented in the tests by cycling at 2 or 4 cycles/h as opposed to the normal testing frequency of 5 Hz.

Experimental Program

The experimental program, summarized in Table 1, consisted of crack growth tests of 49 center-cracked panels. Tests were performed in a laboratory environment at either RT or at 219 K (−65°F). The program consisted of three distinct parts: (1) crack growth under constant-amplitude loading, (2) crack growth under spectrum loading, and (3) effect of frequency, for constant-amplitude loading, on crack growth. In Parts 1 and 2, at the end of the crack growth testing, the panels were loaded to failure to obtain residual strength/fracture toughness data.

Test Specimens

Four different sizes of center-cracked panels were used in the experimental program (Fig. 1). The panel width ranged from 50.8 mm (2.0 in.) to 610 mm (24 in.). The center crack was initiated as an electrical discharge machining slot (EDM) through the thickness. The slot was then precracked to a desired initial length. Most of the testing was done with the 305-mm (12-in.)-wide specimen. The 102-mm (4-in.) specimens were used to obtain the short crack, low-cycle-rate constant-amplitude loading crack growth data. The small, 50.8-mm (2-in.)-wide specimens were used in the frequency effect study be-

TABLE 1—*Experimental program summary.*

Test Type	Material	Thickness, mm (in.)	Specimen Width, mm (in.)	Loading[a]	Loading Frequency	Temperature, K (°F)	No. of Specimens
CA loading crack growth and K_c	2024-T351	4.76 (0.18)	101.6 (4)	CA, $R = 0$	1 to 30 Hz	RT	2
	2024-T351	6.35 (0.25)	304.8 (12)	CA, $R = 0.8$	1 to 30 Hz	RT	2
	2024-T351	4.76 (0.18)	101.6 (4)	CA, $R = 0$	1 to 30 Hz	219 (−65)	2
	2024-T351	6.35 (0.25)	304.8 (12)	CA, $R = 0.8$	1 to 30 Hz	219 (−65)	2
	7475-T7651	4.76 (0.18)	101.6 (4)	CA, $R = 0$	1 to 30 Hz	RT	2
	7475-T7651	6.35 (0.25)	304.8 (12)	CA, $R = 0.8$	1 to 30 Hz	RT	2
	7475-T7651	4.76 (0.18)	101.6 (4)	CA, $R = 0$	1 to 30 Hz	219 (−65)	2
	7475-T7651	6.35 (0.25)	304.8 (12)	CA, $R = 0.8$	1 to 30 Hz	219 (−65)	2
Spectrum loading crack growth and K_c	2024-T351	6.35 (0.25)	304.8 (12)	Baseline Spectrum (BS)	10 Hz	RT	3
	2024-T351	6.35 (0.25)	304.8 (12)	BS + 15%	10 Hz	RT	2
	2024-T351	6.35 (0.25)	304.8 (12)	BS − 15%	10 Hz	RT	2
	2024-T351	6.35 (0.25)	304.8 (12)	BS	10 Hz	219 (−65)	2
	2024-T351	6.35 (0.25)	304.8 (12)	BS + 15%	10 Hz	219 (−65)	2
	2024-T351	6.35 (0.25)	304.8 (12)	BS − 15%	10 Hz	219 (−65)	2
	7475-T7651	6.35 (0.25)	304.8 (12)	BS	10 Hz	RT	2
	7475-T7651	6.35 (0.25)	304.8 (12)	BS	10 Hz	219 (−65)	2
CA loading frequency effect on crack growth	2024-T3	1.0 (0.04)	50.8 (2)	CA, $R = 0$	5 Hz	RT	5
	2024-T3	1.0 (0.04)	50.8 (2)	CA, $R = 0$	2 cycles/h	RT	5
	2024-T3	1.3 (0.05)	609.6 (24)	CA, $R = 0.05$	5 Hz	219 (−65)	2
	2024-T3	1.0 (0.04)	50.8 (2)	CA, $R = 0$	4 cycles/h	219 (−65)	4

[a] Loading—crack growth direction was L–T in all tests except T–L in the frequency effect tests.

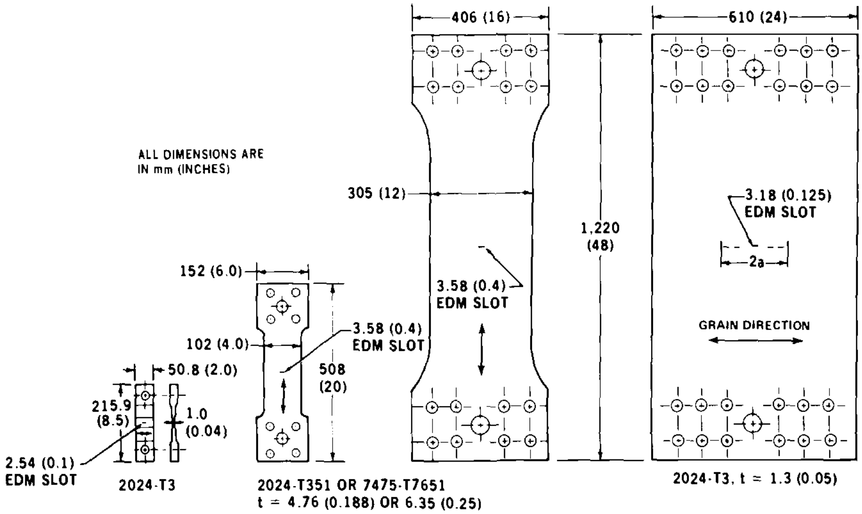

FIG. 1—*Test specimens.*

cause of the their initial use in the primary adhesively bonded structure (PABST) program [*1*], where they were used in low-frequency tests.

Testing Procedures

Except for the low-frequency loading tests, all tests were run in standard servohydraulic MTS or Schenck fatigue test machines at frequencies ranging between 1 and 30 Hz. The 2 cycles/h tests were run in a PABST program special test setup [*1*], where a large number of specimens were tested in series. The 4 cycles/h tests were run later in a Shore Western environmental fatigue testing facility.

The initial EDM slots were precracked under constant-amplitude loading; the maximum load did not exceed the maximum load of subsequent loadings. A 40X optical scope was used to visually monitor the crack growth on the surface of the specimen. In most cases, crack growth testing was terminated when the total crack length reached approximately one third of the specimen width. The specimen was then loaded to failure in order to obtain data to calculate the fracture toughness (K_c).

In the low-temperature tests in the MTS machine, the specimen was enclosed in a special chamber. Gaseous liquid nitrogen was pumped into it to maintain the low temperature. A specimen temperature-controlling thermocouple was used to operate a demand valve that determined the flow of the nitrogen. Crack lengths were optically measured through a window in the chamber. The frost from the specimen surface was cleared by venting dry nitrogen over the surface. However, in the low-frequency (4 cycles/h) and low-temperature test run in the special environmental test machine, the specimen was periodically removed and exposed to RT for crack length measurements.

Laboratory temperature and relative humidity were recorded during testing. Temperature typically ranged between 294 and 300 K (70 and 80°F) and relative humidity between 35 and 55%.

Loading

Three types of cyclic loadings were used: (1) constant amplitude between 1 and 30 Hz and $R = 0$ or 0.8, (2) spectrum loading representing a transport wing lower surface, and (3) low-frequency (2 or 4 cycles/h) at $R = 0$. The constant-amplitude loading varied as a function of specimen size and the desired crack growth rate. The spectrum loading consisted of a baseline spectrum representing a transport wing lower surface and two variations of this spectrum: a spectrum with all loads increased by 15% and a spectrum with all loads decreased by 15%. The main features of the baseline spectrum are:

- Flight-by-flight spectrum.
- Repeatable sequence = 1000 flights.
- Average of 64 cycles per flight.
- Highest stress = 184.8 MPa (26.8 ksi), lowest stress = −109.6 MPa (−15.9 ksi), lowest stress range = 18.6 MPa (2.7 ksi).
- Two typical flights are shown in Fig. 2*a*. There were 25 different flights in the spectrum, with respect to the number of cycles and their magnitude per flight.

The low-frequency loading rates are illustrated in Fig. 2*b*. For the 2 cycles/h loading, it took 5 min to reach the peak; the peak load was held for 15 min, then decreased to zero over 5 min, at which time the zero load was held for 5 min before load application started again. For the 4 cycles/h loading, the waveform was almost a square.

Results and Discussion

Crack Growth under Constant-Amplitude Loading

The *da/dN* curves for $R = 0$ and 0.8, at RT and at 219 K (−65°F), are presented in Fig. 3. The *a* versus *N* test data were approximated by a curve using constrained regression analysis techniques [2] and *da/dN* data were obtained by differentiating this curve. The stress intensity factor (K) was calculated as

$$K = \sigma\sqrt{\pi a \cdot \sec \pi a/w}$$

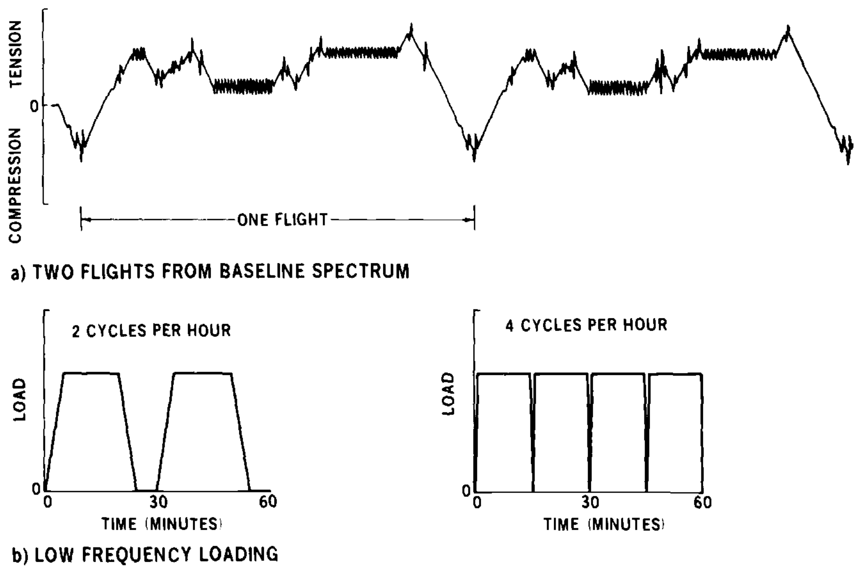

FIG. 2—*Spectrum and low-frequency loadings.*

where

σ = applied gross area stress,
a = half crack length, and
w = panel width.

Crack growth was slower at the low temperature at the lower ΔK values for 2024-T351 and 7475-T7651 material. This means that a higher threshold value ΔK_{th} existed for both materials at the low temperature. At the higher ΔK values, however, the crack growth rates at low temperature were about the same for 2024-T351 and higher for 7475-T651 than at RT. The higher rate for 7475-T7651 was due to the lower fracture toughness for this alloy at low temperature.

Crack Growth under Spectrum Loading

The results of crack growth tests under the transport wing lower surface spectrum at RT and at 219 K (−65°F) are shown in Fig. 4. Tests were run with the baseline spectrum on both 2024-T351 and 7475-T7651 material. Two variations of the baseline spectrum, with all loads increased or decreased 15%, were also tested with the 2024 material. In Fig. 4, a single curve shown for a given testing condition represents two tests whose results exhibited very little scatter. Where scatter was more pronounced, multiple curves are shown.

In all cases, crack growth at the low temperature was slower than at RT.

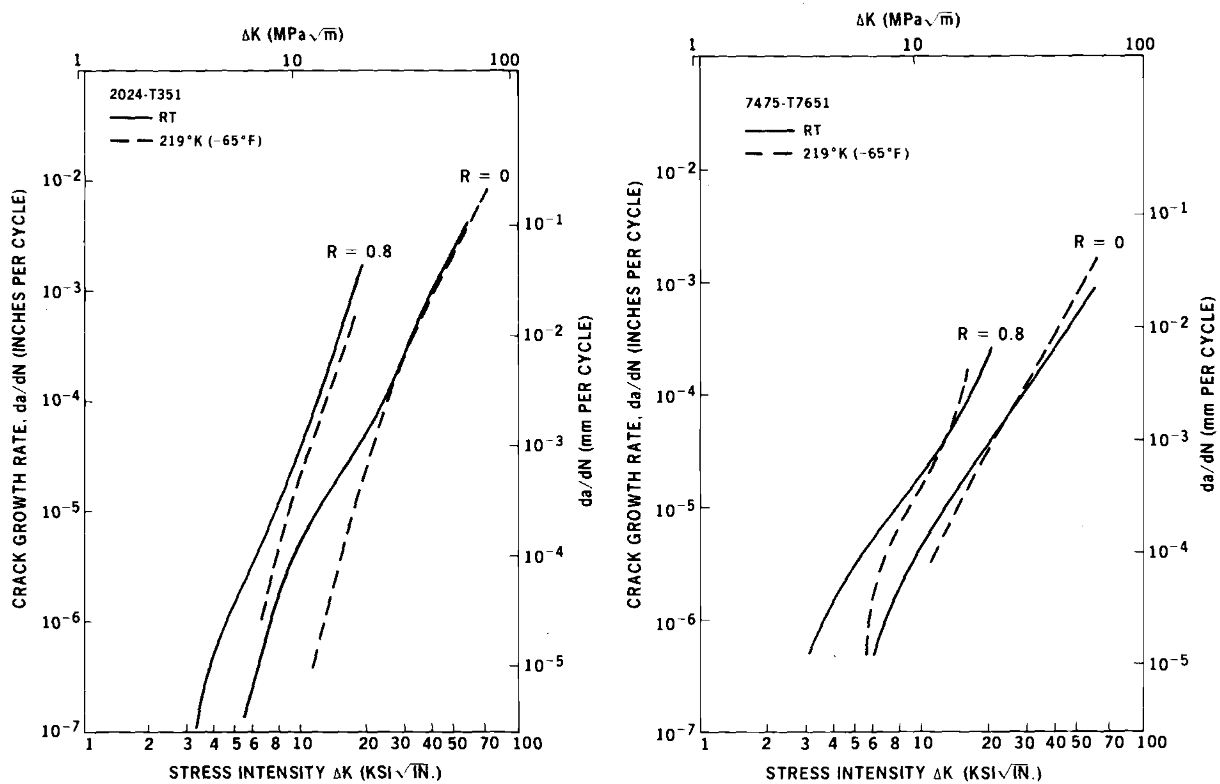

FIG. 3—*Comparison of room and low (219 K [−65°F]) temperature crack growth rates resulting from constant-amplitude loading for* (left) *2024-T351 and* (right) *7475-T7651;* t = *4.76 and 6.35 mm (0.18 and 0.25 in.).*

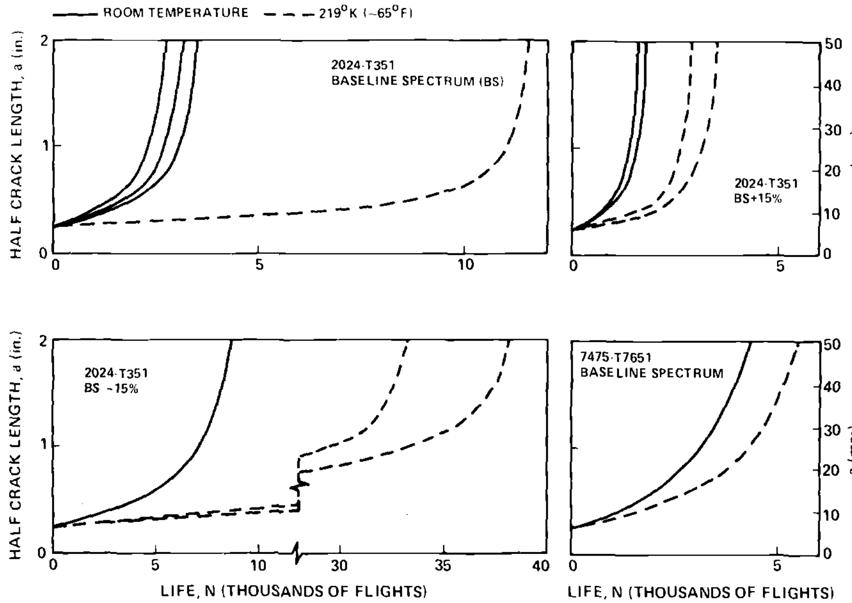

FIG. 4—*Crack growth resulting from transport wing lower surface spectrum loading at room and low (219 K [−65°F]) temperature for 2024-T351 and 7475-T7651;* t = *6.35 mm (0.25 in.).*

The crack growth life, from initial to final half crack length of 50.8 mm (2 in.) at the low temperature was anywhere from 1.25 to 4.13 times longer than at RT (Table 2). Note that crack growth behavior with spectrum variation for the 2024-T351 material was as expected: shorter lives when all loads in the spectrum were increased by 15% (BS + 15%) and longer lives for the spectrum with stresses decreased 15% (BS − 15%) for both temperatures.

Loading Frequency Effect on Crack Growth

The effect of loading frequency under constant-amplitude loading was investigated at RT and at 219 K (−65°F) using 2024-T3 1.0 and 1.3 mm (0.04 and 0.05 in.) thin sheet. Tests were run at 5 Hz to represent a frequency often used in laboratory tests and at 2 and 4 cycles/h to approach transport aircraft fuselage pressurization cyclic rates. The results, in terms of *da/dN* curves, are shown in Fig. 5. Crack growth was faster at the lower frequencies at both temperatures. In order to determine whether this is significant enough to be considered in planning full-scale structure tests, additional experimental testing, which would include spectrum loading and temperature cycling, would be required.

Note that these data, including tests with low loading frequencies, show a similar effect of low temperature on crack growth as the previous data for 2024-T351 in Fig. 3 (i.e., slower crack growth than at RT).

TABLE 2—*Comparison of crack growth lives for transport wing lower surface spectrum at room and low temperature.*

		RT[b]		LT[c]		
Material[a]	Spectrum	n^d	$\bar{N}^e$	n	$\bar{N}$	$\bar{N}_{LT}/\bar{N}_{RT}$
2024-T351	BS − 15%	2	8748	2	36 146	4.13
2024-T351	Baseline (BS)	3	3161	1	11 586	3.66
2024-T351	BS + 15%	2	1708	2	3 180	1.86
7475-T7651	BS	2	4389	2	5 474	1.25

[a] Specimen thickness (t) = 6.35 mm (0.25 in.).
[b] RT = room temperature.
[c] LT = low temperature = 219 K (−65°F).
[d] n = number of specimens tested.
[e] $\bar{N}$ = average life (flights) to grow half crack from 6.35 mm (0.25 in.) to 50.8 mm (2 in.).

Fracture Toughness

In most tests, at the end of the crack growth testing, the specimen was statically loaded to failure. The load was increased in incremental steps and held for 2 to 3 min, and the crack length was measured optically on the surface of the specimen at each step. The results are summarized in Table 3 for 2024-T351 and 7475-T7651 alloys. The plane stress fracture toughness (K_c) was calculated as

$$K_c = \sigma_c\sqrt{\pi a_c \cdot \sec \pi a/w}$$

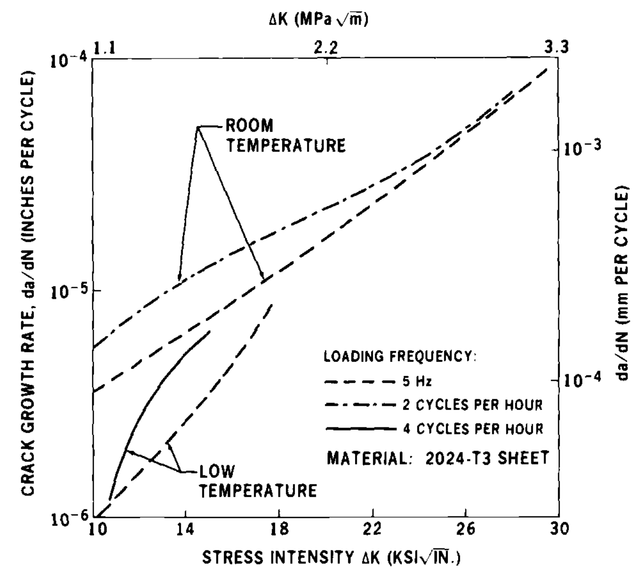

FIG. 5—*Effect of loading frequency on crack growth rates caused by constant-amplitude loading* (R = 0) *of 2024-T3* (t = *1.0 and 1.3 mm* [*0.04 and 0.05 in.*]) *at room and low* (*219 K* [*−65°F*]) *temperatures.*

TABLE 3—*Fracture toughness test results.*

	Specimen								
	Thickness		Width					$\bar{K}_c$[d]	
Material	mm	in.	mm	in.	Temperature[a]	Loading[b]	n[c]	MPa$\sqrt{m}$	ksi$\sqrt{in.}$
2024-T351	4.76	0.188	101.6	4	RT	CA	4	63.6	57.9
	6.35	0.25	101.6	4	RT	CA	4	64.4	58.6
	4.76	0.188	304.8	12	RT	CA	4	111.1	101.1
	6.35	0.25	304.8	12	RT	CA	4	106.7	97.1
	4.76	0.188	304.8	12	LT	CA	2	107.8	98.1
	6.35	0.25	304.8	12	LT	CA	2	110.0	100.1
	6.35	0.25	304.8	12	RT	spectrum	7	99.4	90.5
	6.35	0.25	304.8	12	LT	spectrum	5	110.9	100.9
7475-T7651	4.76	0.188	101.6	4	RT	CA	4	81.3	74.0
	6.35	0.25	101.6	4	RT	CA	4	77.6	70.6
	4.76	0.188	304.8	12	RT	CA	4	125.7	114.4
	6.35	0.25	304.8	12	RT	CA	4	125.2	113.9
	4.76	0.188	304.8	12	LT	CA	2	97.0	88.3
	6.35	0.25	304.8	12	LT	CA	1	90.3	82.2
	6.35	0.25	304.8	12	RT	spectrum	2	125.2	113.9
	6.35	0.25	304.8	12	LT	spectrum	2	98.7	89.8

[a] RT = room temperature; LT = low temperature = 219 K (−65°F).
[b] Loading used in the crack growth testing.
[c] n = number of specimens.
[d] $\bar{K}_c$ = average fracture toughness.

where

σ_c = applied gross area stress at instability,
a_c = half crack length at instability, and
w = panel width.

The crack length at instability was the last recorded value, plus an extrapolated increment, obtained by regression analysis, relative to the recorded stress (σ_c) at instability. Net section stress at instability was less than the yield stress for the materials tested.

The effect of low temperature (219 K [−65°F]) on K_c of the two materials tested is summarized in Table 4. It can be seen that the effect of low temperature on 2024-T351 was not significant, but a reduction of between 20 and 30% occurred in the fracture toughness value of the 7475-T7651 material. Also to be noted (Table 5) is the effect of specimen thickness, width, and previous loading on K_c at room and low temperatures. It can be seen that neither the small variation in material thickness nor the type of loading used in the crack growth testing had any significant effect on K_c at either temperature. However, both materials at RT showed a very significant increase (up to 75%) in K_c, with specimen width increasing from 101.6 mm (4 in.) to 304.8 mm (12 in.). In both cases, the ratio of total crack length at instability to specimen width was the same, about 0.38.

Comparison of 2024-T351 and 7475-T7651

The 2024 aluminum alloy has been in use in the aircraft industry for a long time, whereas the 7475 alloy is relatively new. Questions often arise about the superiority of one alloy over the other. It is not the intention of this paper to present a complete evaluation of the two alloys. Rather, the following discussion is limited to an evaluation of the crack growth and fracture toughness properties generated in this investigation at RT and low temperature of 219 K (−65°F).

Crack Growth under Constant-Amplitude Loading—The two alloys are compared at RT and low temperature in Figs. 6 and 7. At both temperatures, 2024-T351 was better (i.e., exhibited slower crack growth) at the lower values of ΔK, while the opposite is true at the higher values of ΔK, where 7475-T7651 was better.

Crack Growth under Spectrum Loading—A comparison of the crack growth lives under the baseline spectrum from Fig. 4 shows that the 7475-T7651 alloy had a longer life (4389/3161 = 1.39) at RT, while the opposite is true at the low temperature, where the 2024-T351 alloy had a longer life (11 586/5474 = 2.13). This behavior seems to correlate with the K_c behavior for the two alloys (Table 3), with the 7475 exhibiting higher K_c at RT but a lower value than 2024 at the low temperature.

TABLE 4—*Effect of low temperature on fracture toughness of 2024 and 7475 aluminum alloys.*

Specimen Thickness[a]		Previous Cyclic Loading	$(\bar{K}_c)_{LT}/(\bar{K}_c)_{RT}$[b]	
mm	in.		2024-T351	7475-T7651
4.76	0.188	CA	0.97	0.77
6.35	0.25	CA	1.03	0.72
6.35	0.25	spectrum	1.12	0.79

[a] Specimen width (w) = 304.8 mm (12 in.).
[b] LT = low temperature = 219 K (−65°F); RT = room temperature.

Fracture Toughness—Table 6 compares 2024-T351 and 7475-T7651 at room and low temperatures. Fracture toughness was higher for 7475-T7651 at room temperature but dropped below the 2024-T351 alloy at the low temperature.

Conclusions

Fracture Toughness and Crack Growth

The effect of low temperature (219 K [−65°F]) on the fracture toughness and crack growth characteristics of 2024-T351 and 7475-T7651 aluminum alloy sheet in the 4.76 to 6.35 mm (0.18 to 0.25 in.) thickness range, as compared to the room temperature properties, was found to be as follows:

Fracture Toughness—There was no significant effect on the 2024-T351 alloy, but the 7475-T7651 alloy fracture toughness was reduced up to 28%. This is similar to the effects observed by others in 2000 and 7000 series alloys in general and 2024 and 7475 alloys in particular [*3–5*]. This means that appropriate fracture toughness values at low temperature should be used in damage tolerance analysis critical crack length and residual strength calculations of 7000 series aluminum alloys for low-temperature environments.

Crack Growth Caused by Constant-Amplitude Loading—For the 2024-T351 alloy, the crack growth rate was lower at the lower ΔK values and about the same at the higher ones. For the 7475-T7651 alloy, the crack growth rate was lower at the lower ΔK values but higher at the larger ΔK values. Similar behavior has been observed by other investigators [*3–5*]. Reduction in the crack growth rates at the low ΔK values is not reported in Ref *5* because no tests were run in this range of ΔK values, below 11 MPa$\sqrt{\text{m}}$.

Crack Growth Caused by Spectrum Loading—The crack growth life for the transport wing lower surface spectrum for both materials was longer at the low temperature (Table 2). The life was significantly longer (by a factor of 1.86 to 4.13) for the three spectra tested with the 2024-T351 alloy, but only marginally longer (by a factor of 1.25) for the one spectrum tested with the

TABLE 5—*Effect of specimen thickness, width, and previous cyclic loading on the fracture toughness of 2024-T351 and 7475-T7651 at room and low temperature.*

Variable	Temperature[a]	Specimen Thickness mm	Specimen Thickness in.	Specimen Width mm	Specimen Width in.	Loading	$(\bar{K}_c)_a/(\bar{K}_c)_b$ 2024	$(\bar{K}_c)_a/(\bar{K}_c)_b$ 7475
Material thickness	RT	variable		101.6	4	CA	1.01	0.95
(a = 6.35 mm [0.25 in.];	RT	variable		304.8	12	CA	0.96	1.00
b = 4.76 mm [0.188 in.])	LT	variable		304.8	12	CA	1.02	0.93
Specimen width	RT	4.76	0.188	variable		CA	1.75	1.55
(a = 304.8 mm [12 in.];	RT	6.35	0.25	variable		CA	1.66	1.61
b = 101.6 mm [4 in.])								
Loading	RT	6.35	0.25	304.8	12	variable	0.93	1.00
(a = spectrum;	LT	6.35	0.25	304.8	12	variable	1.01	1.09
b = CA).								

[a] RT = room temperature; LT = low temperature = 219 K (−65°F).

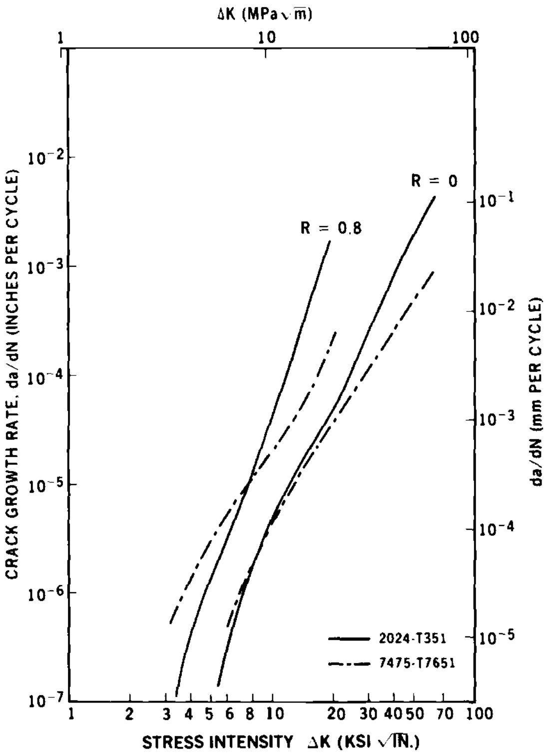

FIG. 6—*Comparison of 2024-T351 and 7475-T7651* (t = *4.76 and 6.35 mm* [*0.18 and 0.25 in.*]) *crack growth rates caused by constant-amplitude loading at room temperature.*

7475-T7651 alloy. Several observations and explanations can be given for this behavior:

1. The slower crack growth at the low temperature resulting from spectrum loading paralleled the slower crack growth rate caused by the constant-amplitude loading observed at the lower ΔK values (Fig. 3). Most of the spectrum crack growth was dominated by cycles with ΔK between 2.2 and 18.8 MPa$\sqrt{\text{m}}$ and R between 0.35 and 0.82.
2. The smaller difference in the 2024-T351 spectrum crack growth lives between low and room temperature as the spectrum loads were increased (BS − 15% spectrum, to BS, to BS + 15%), see Table 2, paralleled the decrease in the difference between room and low temperature *da/dN* of Fig. 3.
3. The smaller difference in the 7475-T7651 baseline spectrum crack growth lives between low and room temperature when compared with 2024-T351, 1.25 to 3.66 (Table 2), respectively, also followed the constant-amplitude *da/dN* data behavior (Fig. 3). In the range of $\Delta K = 2.6$

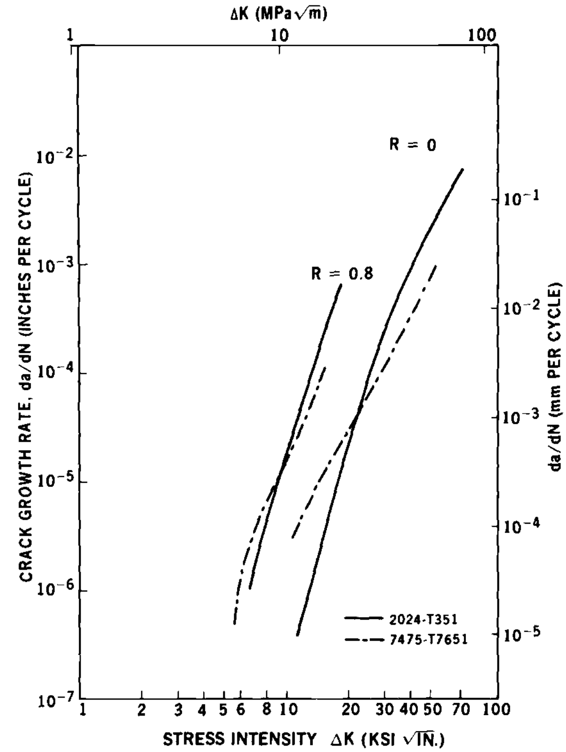

FIG. 7—*Comparison of 2024-T351 and 7475-T7651* (t = *4.76 and 6.35 mm* [*0.18 and 0.25 in.*]) *crack growth rates resulting from constant-amplitude loading at low* (*219 K* [*−65°F*]) *temperature.*

16.4 MPa$\sqrt{m}$ cycles, which dominated the baseline spectrum, not only was the difference between low and room temperature *da/dN* data smaller for the 7475 alloy, but the low temperature rates became higher for the higher ΔK and R cycles.

4. The 7475-T7651 spectrum loading results of this study are similar to those reported in Ref *6* for 7475-T7651 clad sheet subjected to a fighter and a transport wing spectrum, namely marginally longer crack growth lives at low temperature. The authors of Ref *6* also report experimental evidence, based on simple overload crack growth tests on the 7475-T7651 alloy, that retardation effects are different at low temperature when compared to room temperature, depending on the overload ratio. The validity of their suggested characterization of the spectrum load interaction effects on crack growth in terms of a single overload is perhaps too simplistic and requires further investigation. It does indicate, however, that the effect of low temperature on crack growth resulting from spectrum loading is more complicated than indicated by constant-amplitude loading *da/dN* data.

TABLE 6—*Comparison of 2024-T351 and 7475-T7651 fracture toughness at room and low temperature.*

Specimen						
Thickness		Width			Previous Cyclic	
mm	in.	mm	in.	Temperature[a]	Loading	$(\bar{K}_c)_{7475}/(\bar{K}_c)_{2024}$
4.76	0.188	101.6	4	RT	CA	1.28
6.35	0.25	101.6	4	RT	CA	1.20
4.76	0.188	304.8	12	RT	CA	1.13
6.35	0.25	304.8	12	RT	CA	1.17
6.35	0.25	304.8	12	RT	spectrum	1.21
4.76	0.188	304.8	12	LT	CA	0.90
6.35	0.25	304.8	12	LT	CA	0.82
6.35	0.25	304.8	12	LT	spectrum	0.88

[a] RT = room temperature; LT = low temperature = 219 K (−65°F).

In general, the effect of low temperature (219 K [−65°F]) on crack growth caused by transport and fighter wing lower surface spectra for 2024-T351 and 7475-T7651 alloys was a longer crack growth life than at room temperature. However, whether this is true for all types and severity of spectra, in particular for the 7475 alloy, is not entirely clear and the subject requires further study.

Comparison of 2024 and 7475 Alloys

Let us compare 2024-T351 and 7475-T7651 alloys, in the 4.76 to 6.35 mm (0.18 to 0.25 in.) thickness range, with respect to their crack growth and fracture toughness properties at room and the low temperature of 219 K (−65°F).

Constant-amplitude Loading Crack Growth—At room and low temperatures, 2024 was better (i.e., exhibited slower crack growth) at low ΔK values, whereas 7475 was better at the higher ΔK values (Fig. 7).

Spectrum Loading Crack Growth—For a wing lower surface spectrum, 7475 was slightly better at room temperature, but 2024 was significantly better at the low temperature; see the baseline spectrum tests (Table 2).

Fracture Toughness—7475 had the higher fracture toughness at room temperature by about 20%, but lost that advantage to 2024 by about 13% at low temperature (Table 6).

In an actual application of the two materials to a damage-tolerant structural design, the choice of the material will depend on the importance of the material behavior at the low temperature as well as other considerations.

Effect of Loading Frequency on Crack Growth

The crack growth caused constant-amplitude loading in 2024-T3 sheet at room and low (219 K [−65°F]) temperatures was found to be faster at low loading frequencies (2 and 4 cycles/h) that approach typical pressurization cycles of aircraft fuselage than at the typical laboratory testing frequency of 5 Hz. Whether this is significant enough to be considered in full-scale fuselage tests requires further consideration.

Acknowledgments

This paper is based on work performed at Douglas Aircraft Company in the Structural Mechanics Engineering Subdivision under the sponsorship of the Independent Research and Development (IRAD) program of the McDonnell Douglas Corporation.

References

[*1*] Potter, D. L., "Durability and Damage Tolerance Behavior of Adhesively Bonded Primary Structure," *Design of Fatigue and Fracture Resistant Structures, ASTM STP 761,* American Society for Testing and Materials, Philadelphia, 1982, pp. 373–407.

[*2*] Parks, J. and Wilson, B., "Derivation and Development of the Constrained Regression Technique," Memo 256.1668, McDonnell Aircraft Co., St. Louis, MO, 15 May 1975.

[*3*] Broek, D., "Fatigue Crack Growth and Residual Strength of Aluminum Alloy Sheet at Temperatures Down to −75°C," NLR TR 72096, National Aerospace Laboratory, the Netherlands, June 1972.

[*4*] Wang, D. Y., "Plane-Stress Fracture Toughness and Fatigue Crack Propagation of Aluminum Alloy Wide Panels," *Progress in Flaw Growth and Fracture Toughness Testing, ASTM STP 536,* American Society for Testing and Materials, Philadelphia, 1973, pp. 334–349.

[*5*] Pettit, D. E. and Van Orden, J. M., "Evaluation of Temperature Effects on Crack Growth in Aluminum Sheet Material," *Fracture Mechanics, ASTM STP 677,* American Society for Testing and Materials, Philadelphia, 1979, pp. 106–124.

[*6*] Cox, J. M., Pettit, D. E., and Langenbeck, S. L., "The Effect of Temperature on the Fatigue and Fracture Properties of 7475-T761 Aluminum," *Fatigue at Low Temperatures, ASTM STP 857,* American Society for Testing and Materials, Philadelphia, 1985, pp. 241–256.

Y. Kitsunai

Fatigue Crack Growth Behavior in Mild Steel Weldments at Low Temperatures

REFERENCE: Kitsunai, Y., "**Fatigue Crack Growth Behavior in Mild Steel Weldments at Low Temperatures,**" *Fatigue at Low Temperatures, ASTM STP 857,* R. I. Stephens, Ed., American Society for Testing and Materials, Philadelphia, 1985, pp. 274–292.

ABSTRACT: Fatigue crack growth rates for the base metal and welds of SM50A steel weldments were determined at temperatures ranging from room temperature down to 123 K. For the base metal, crack growth rates between room temperature and 188 K decreased slightly with decreasing temperature. At 123 K, the growth rate of the base metal increased markedly because of cyclic cleavage during striation growth. For the welds, no systematic correlation can be made between temperature and growth rate. The growth rates of the welds were lower than those of the base metal regardless of temperature because the crack tips in the weld specimens always existed in the field of compressive residual stresses. Therefore the growth rates of the welds were dominated by residual welding stress rather than temperature. The crack growth rates of the base metal and the welds with residual stresses under low temperatures were closely correlated with the effective stress intensity factor range (ΔK_{eff}), estimated based on crack closure measurements, when the crack growth mechanism was dominated by striation formation.

KEY WORDS: crack propagation, fatigue (materials), low temperatures, weldments, residual stress, crack closure, fractography, cleavage, striation

Various kinds of defects, such as inclusions or incomplete fusion, are often introduced into welded structures during the welding operation. Under repeated loading, these defects in the welds can serve as sites for the initiation of fatigue cracks that propagate to such an extent that unstable fracture occurs. In particular, fatigue cracks are quickly propagated at low temperatures, becoming unstable because of reduced fracture toughness of the welds. In cold areas, such welded structures as bridges, towers, and the like may be subjected to temperatures that fall to about 220 K. In general, however, these structures are fabricated of low-carbon structural steels rather than steels designed for low temperature service. For safe use of such structures at low temperature it is necessary to prevent unstable fracture induced by fatigue

Dr. Kitsunai is a senior researcher at the Mechanical Engineering Research Division, National Research Institute of Industrial Safety, Kiyose, Japan.

cracks growing from welding defects. Therefore reliable data on the fatigue crack growth rates of weldments at low temperatures are required for safely designing or determining the inspection period of such structures. Considerable work has been carried out on the fatigue crack growth of nonwelded materials at low temperatures [*1–6*]. However, studies of low-temperature effects on the fatigue crack growth rates of weldments have not been extensively performed [*7–10*].

The present study focused on the following issues in order to obtain fundamental data on the fracture properties of low-carbon structual steel weldments at low temperatures: (1) determining the effect of low temperatures on the fatigue crack growth behavior of the welds and the base metal, (2) evaluating the effect of residual welding stresses on the fatigue crack propagation of the welds, and (3) examining the mechanisms of crack growth at low temperatures.

Material and Specimens

The material used in this study was a structual steel plate (Japanese Industrial Standard SM50A) 3050 mm long, 1520 mm wide, and 16 mm thick. This plate has good weldability and has widely been used in the fabrication of welded structures. However, this plate is not a steel developed for use at low temperatures. The mechanical properties of the plate are given in Table 1; the chemical composition of the plate and weld metal is shown in Table 2. The plate was divided into eight strips, each 380 by 1520 by 16 mm, by fusion cutting across the rolling direction. A pair of the strips were machined with a double-V groove and butt-welded with a manual arc welding technique. The welding parameters are summarized in Table 3. Compact tension (CT) specimens were fabricated from the welded strips. The notch in the each specimen was oriented so that the crack passed through the weld parallel to the welding direction. The configuration of the weld specimens is shown in Fig. 1. After machining, some of the specimens were stress-relieved at 923 K for 3 h. The specimen geometry for the base metal was exactly the same as in Fig. 1, and the notch in each specimen was oriented perpendicular to the rolling direction.

TABLE 1—*Mechanical properties of the base metal.*

Test Temperature, K	Yield Strength, MPa	Tensile Strength MPa	Elongation, %
Room temperature	382	520	26
268	390	573	25
223	451	598	24
188	469	657	23
123	659	761	21

TABLE 2—*Chemical composition (weight percent) of base and weld metal.*

Metal	C	Si	Mn	P	S	Cu	Ni	Cr
Base metal	0.16	0.23	1.10	0.023	0.006	0.290	0.020	0.450
Weld metal	0.09	0.37	0.87	0.038	0.018	0.055	0.018	0.080

Experimental Procedures

Fatigue crack growth tests were carried out at room temperature (about 293 K) and 268, 223, 188, and 123 K using a 196 kN closed-loop servo-hydraulic fatigue machine at a frequency of 20 Hz. The load was varied sinusoidally, and the ratio of minimum to maximum load (R) was maintained at 0.05. The specimens were precracked at stress intensity factor ranges of 10 to 27 MPa $m^{1/2}$.

The temperature was controlled by an electromagnetic valve triggered to eject liquid nitrogen into the refrigeration chamber when the temperature rose above the set value and to shut off the flow when the temperature fell. The specimen temperature was monitored by a copper-constantan thermocouple that was spot-welded to the end of the specimen. The temperature was maintained within ±2 K of the set value during the tests. A diagram of the refrigeration system used is shown in Fig. 2.

Changes in a crack length during the fatigue tests at room temperature were measured by using a traveling microscope at 50 times with a vernier scale and stroboscopic illumination. For low temperatures, direct measurement of the crack length was not possible; therefore the crack length was measured by a crack gage much like a conventional strain gage. Moreover, fatigue marker bands (beach marks) were periodically placed on the fatigue fracture surface to provide a check on the results obtained by the crack gage. The crack growth rates were determined graphically by taking the slopes of the crack growth curve at various crack lengths. The results were expressed in terms of stress intensity factor range (ΔK), which is expressed as [*11*]

$$\Delta K = \frac{\Delta P}{B\sqrt{W}} \frac{(2+\alpha)}{(1-\alpha)^{3/2}} \times (0.886 + 4.64\alpha - 13.32\alpha^2 + 14.72\alpha^3 - 5.60\alpha^4) \quad (1)$$

where $\alpha = a/w$, ΔP is the applied load range, a is the crack length from the loading axis, W is the specimen width, and B is the specimen thickness.

Crack closure at the crack tip during fatigue crack growth was measured by using a strain gage mounted on the back surface of the specimen to evaluate the influence of low temperature and residual welding stress on the crack growth rate. The residual stress distributions in the weld specimens were measured with a sectioning method by using strain gages. Fatigue frac-

TABLE 3—*Welding parameters.*

Parameter	Value
Groove	double V
Electrode	JIS-D5016
Diameter of electrode	4, 5, and 6 mm
Current	180 to 290 A
Arc voltage	35 V
Welding speed	250 mm/min
Heat input	15.1 to 24.4 kJ/cm
Number of runs	6

ture morphologies were examined by using transmission and scanning electron microscopes to explore the mechanisms of crack growth at low temperatures.

Results and Discussion

Fatigue Crack Growth Behavior

Figure 3 shows the fatigue crack growth rates in the base metal at temperatures ranging from room temperature down to 123 K. As may be seen in the figure, the crack growth data at each temperature describe approximately linear relations on logarithmic coordinates over the entire range of ΔK. Hence the Paris power law [12], which is expressed in Eq 2, can be used as a basis for the aforementioned empirical data:

$$da/dN = C(\Delta K)^m \tag{2}$$

where da/dN is the crack growth rate and C and m are experimental constants that depend on material and environment (temperature). Table 4 gives the values of C and m determined by the method of least squares for the base

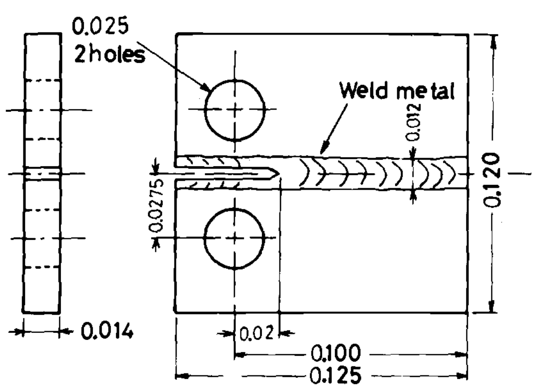

FIG. 1—*Configuration of weld specimen (dimensions in metres).*

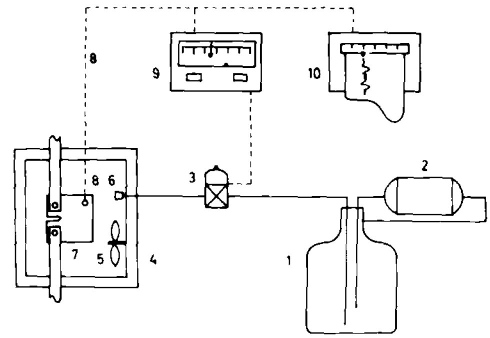

1. Liquid nitrogen vessel, 2. Compressor,
3. Electromagnetic valve, 4. Chamber, 5. Fan,
6. Nozzle, 7. Specimen, 8. Thermocouple,
9. Temperature controller, 10. Thermograph.

FIG. 2—*Diagram of refrigeration system.*

metal and the welds. For a given ΔK, the crack growth rates of the base metal decreased slightly with decreasing temperatures, except at 123 K. The reduction in the crack growth rates at low temperatures may be expected because of increased work-hardening rates and yield strength. The Young's modulus of the base metal remained approximately constant, since the influence of Young's modulus on the growth rate was negligible. The growth rates at 123 K were markedly increased as compared with those of the other temperatures; discontinuous crack growth was often observed where the value of ΔK exceeded about 25 MPa $m^{1/2}$. The acceleration of the growth rates at 123 K was associated with the occurrence of cyclic cleavage. For temperatures below 223 K, the transition from fatigue to unstable fracture during fatigue crack growth occurred in the high ΔK regions. The maximum stress intensity factor (K_{max}) at final failure—that is, fatigue fracture toughness (K_{fc})—had a tendency to decrease with decreasing temperatures. In the high ΔK region near final failure, the size of the plastic zone at the crack tip often became larger than the uncracked ligament of the specimen. Under such conditions, valid data for the growth rates can not be obtained, since the growth rates are no longer correlated with ΔK. Therefore the data that did not satisfy the criterion in Eq 3 were neglected in the calculation of C and m in Eq 2; these data are marked with a slash in the figures. A criterion has been proposed in ASTM Test for Constant-Load-Amplitude Fatigue Crack Growth Rates Above 10^{-8} m/Cycle (E 647) to indicate the valid range for the crack growth rates in a CT specimen with respect to ΔK:

$$W - a \geq (4/\pi)\,(K_{max}/\sigma_y)^2 \tag{3}$$

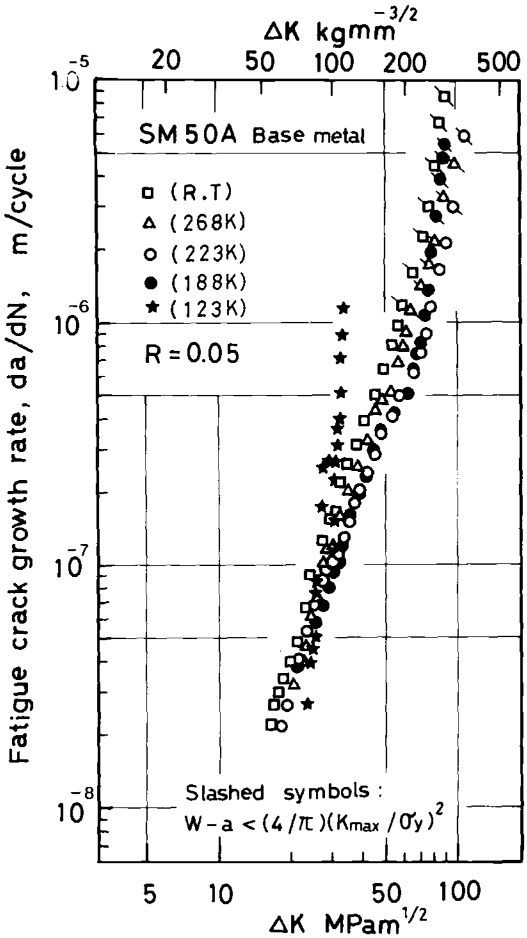

FIG. 3—*Fatigue crack growth rates of base metal as a function of* ΔK.

where σ_y is yield strength. From Fig. 3 it can be seen that most of the final failure in the base metal specimens occurred by general yielding of the uncracked ligament of the specimen, even at low temperatures. Figure 4 shows the relationship between the fatigue crack growth exponent (m) and the reciprocal of the test temperature ($1/T$) for the base metal. The exponent m has a tendency to decrease, approaching a value of 2 at a reciprocal temperature of about 5×10^{-3} K^{-1}. This result may be related to the small-scale yielding at the crack tip that is achieved with decreasing temperatures. When the temperature was further decreased, the value of m increased markedly because of the reduced fracture toughness of the specimens.

Fatigue crack growth rates for the non-stress-relieved welds are shown in

TABLE 4—*Regression constants*[a] *for the fatigue crack growth law* $da/dN = C(\Delta K)^m$.

Temperature, K	C	m	K_{fc}, MPa m$^{1/2}$
	Base Metal		
Room temperature	2.16×10^{-12}	3.26	...
268	2.11×10^{-12}	2.89	...
223	2.11×10^{-11}	2.36	127.9
188	7.16×10^{-12}	2.57	100.7
123	5.27×10^{-20}	8.58	35.7
	Non-Stress-Relieved Welds		
Room temperature	6.11×10^{-19}	5.54	...
268	1.26×10^{-14}	4.32	...
223	5.00×10^{-15}	4.26	142.8
188	1.04×10^{-16}	5.08	110.9
123	1.09×10^{-28}	13.50	40.5
	Stress-Relieved Welds		
Room temperature	7.92×10^{-13}	3.44	...
223	9.65×10^{-13}	3.25	114.3
188	1.02×10^{-13}	3.97	66.4
123	3.51×10^{-13}	3.53	30.7

[a] Units for da/dN were m/cycle; for ΔK, MPa m$^{1/2}$.

Fig. 5. In addition, the crack growth rate for the base metal at room temperature is given by a straight line in the same figure for the sake of comparison. The crack growth rates for the non-stress-relieved welds were considerably lower than for the base metal. In this case, no systematic correlation can be seen between temperature and growth rate. The value of K_{fc} decreased with decreasing temperature because of the reduced fracture toughness of the weld. Hence the crack growth rates of the non-stress-relieved welds may not be related to temperature, but the temperature had a remarkable effect on

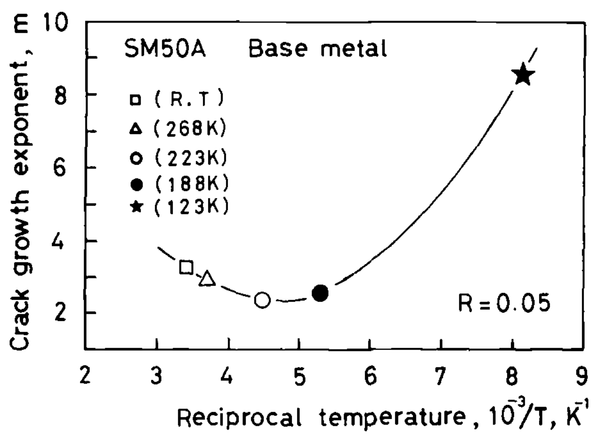

FIG. 4—*Relationship between fatigue crack growth exponent* (m) *and reciprocal temperature* (1/T) *for base metal.*

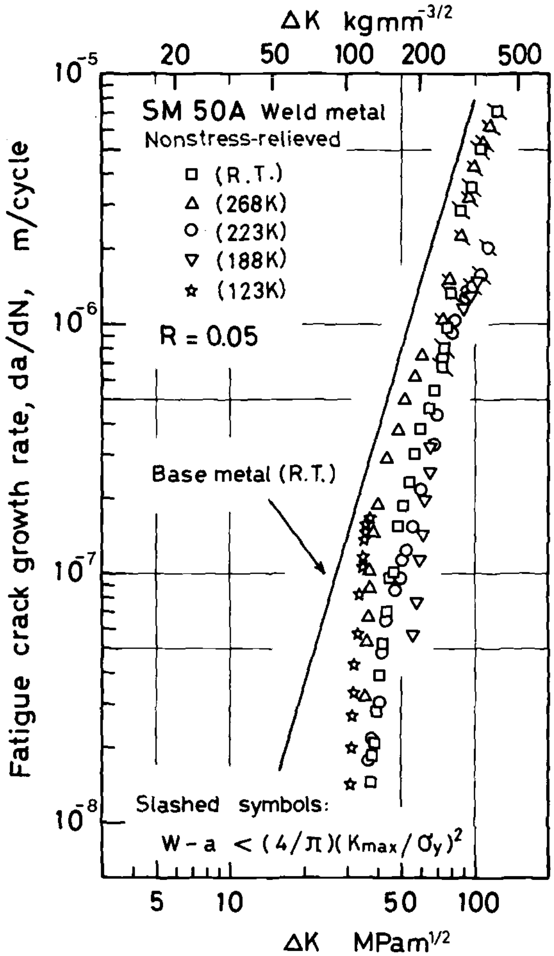

FIG. 5—*Fatigue crack growth rates of non-stress-relieved weld specimens as a function of* ΔK.

the condition of final failure for all the metals. Figure 6 shows how the crack growth rates of the stress-relieved welds increased as compared with those of the non-stress-relieved welds; they were approximately the same or slightly lower than those of the base metal because of the relief of residual stresses in the specimens. The observed retardation of crack growth in the non-stress-relieved welds is attributed to the presence of compressive residual stresses introduced by welding. Consequently, the crack growth rates of the welds are dominated by residual stress rather than temperature.

Distribution of Residual Stresses

Figure 7 shows an example of the distribution of residual stress in the crack growth plane of the non-stress-relieved weld specimen. As shown in

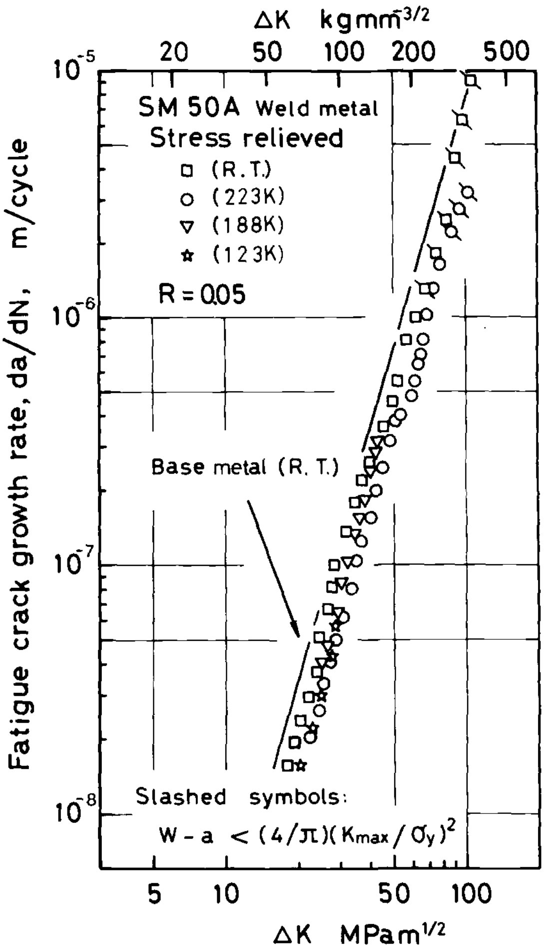

FIG. 6—*Fatigue crack growth rates of stress-relieved weld specimens as a function of* ΔK.

the figure, the longitudinal residual stress (σ_{RY}), which lies in the direction of the external applied stress, is compressive near the tip of notch and near the end of the specimen, while tensile residual stress exists near the center of the specimen. The transverse residual stress (σ_{RX}), which is parallel to the direction of crack growth, is tensile regardless of location. The most significant component of residual stress is the longitudinal residual stress, and the combination of applied stress and longitudinal residual stress may play an important role in fatigue crack growth. On the other hand, the transverse residual stress may have little influence on the crack growth rate. Judging from the result for σ_{RY} in Fig. 7, the vicinity of the crack tip in welds in CT specimens may always be in the field of compressive residual stress, even if the crack should extend. In the case of center-cracked tension (CCT) weld specimens, it is re-

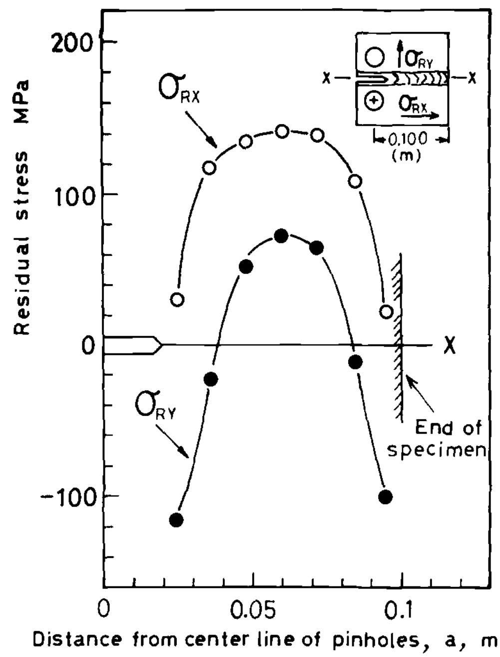

FIG. 7—*Residual stress distributions in the plane of crack growth of a non-stress-relieved weld specimen.*

ported that the distribution of residual stresses tends to remain the same, even after the extension of the crack [*13*]. For these reasons, the growth rates of the non-stress-relieved welds in CT specimens were found to be lower than those of the base metal specimens. The measurements of the residual welding stresses suggest that the crack growth rates of CCT specimens would be greater for welds than for base metal, because σ_{RY} would be tensile at the crack tip, as suggested by Bucci [*14*].

Crack Closure

Crack closure [*15*] is useful for explaining the effect of environment [*16,17*] or loading history [*18,19*] on fatigue crack growth behavior. In particular, the influence of stress ratio [*20*] on fatigue crack growth rate is correlated with the effective stress intensity factor range (ΔK_{eff}), which is based on the assumption that propagation occurs only when the crack tip completely opens. The influence of residual stresses on growth rate may be related to crack closure. For example, compressive residual stress perpendicular to the plane of the crack counteracts the applied crack opening load, thereby decreasing the ΔK value calculated from the external applied stress. Crack closure may also be influenced by temperature as well as stress. The influence of the temperature and residual welding stress on fatigue crack growth rate were therefore analyzed by using the crack closure concept [15]. Crack opening load (P_{op}) during crack growth was measured by the unloading elastic compliance method using a subtractive circuit [20]; effective load ratio (U) was determined from the value of (P_{op}). The parameter U is defined as [15]

$$U = (P_{max} - P_{op})/(P_{max} - P_{min}) = \Delta K_{eff}/\Delta K \tag{4}$$

The curves in Fig. 8 show some examples of the relationship between load P and subtraction signal β. The signal β on the abscissa is expressed as $\beta = \delta - \alpha P$, where δ is the crack opening displacement and α is the adjustable coefficient of the subtractive circuit for the unloading elastic compliance method [20]. The vertical lines of the P–β curves in Fig. 8 indicate that the cracks are completely open, while the portions that deviate from the vertical indicate that the cracks are closed. Crack opening load is defined as the load at which the β value begins to increase in the P–β curve.

Figure 9 shows the relationship between U and ΔK for the base metal specimens. The value of U in the low ΔK region decreased with decreasing temperature, except at 123 K. The U value in the high ΔK region increased because the uncracked ligaments of the specimens were gradually coming close to yielding. At 123 K, it was often difficult to measure P_{op} because of the contribution of cyclic cleavage. Figure 10 shows the relationship between U and the crack length ratio a/W for the weld specimens. The value of U in the weld specimens increased with increasing a/W. This result occurred because the residual welding stress in the specimens was relieved with increasing crack length. In addition, this result suggests that the distribution of re-

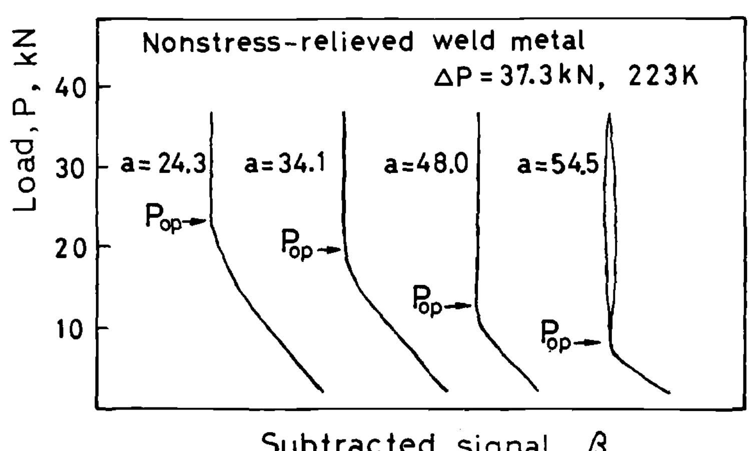

FIG. 8—*Typical traces of applied load* (P) *versus subtracted signal* (β), *corresponding to crack opening displacement.*

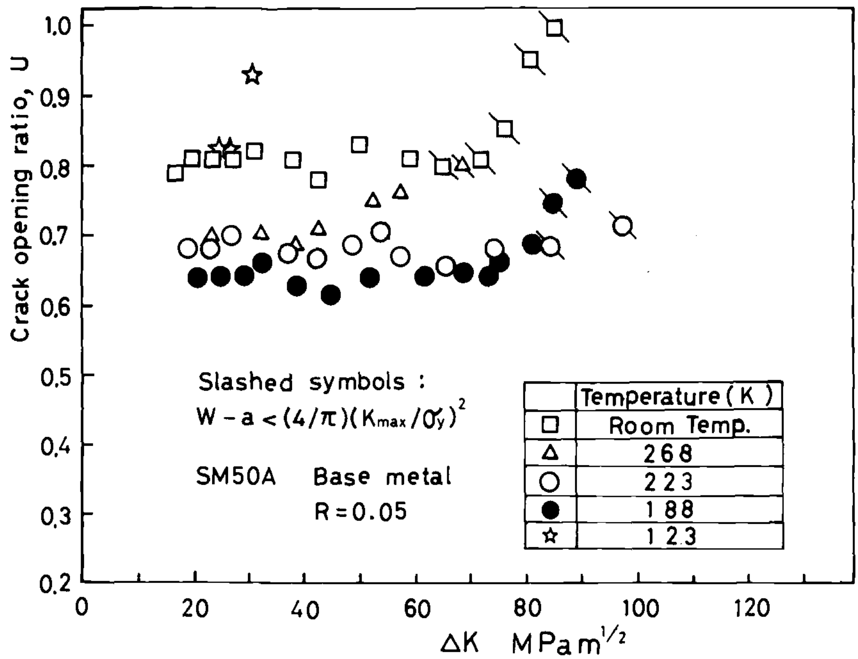

FIG. 9—*Relationship between effective load ratio* (U) *and* ΔK *for base metal.*

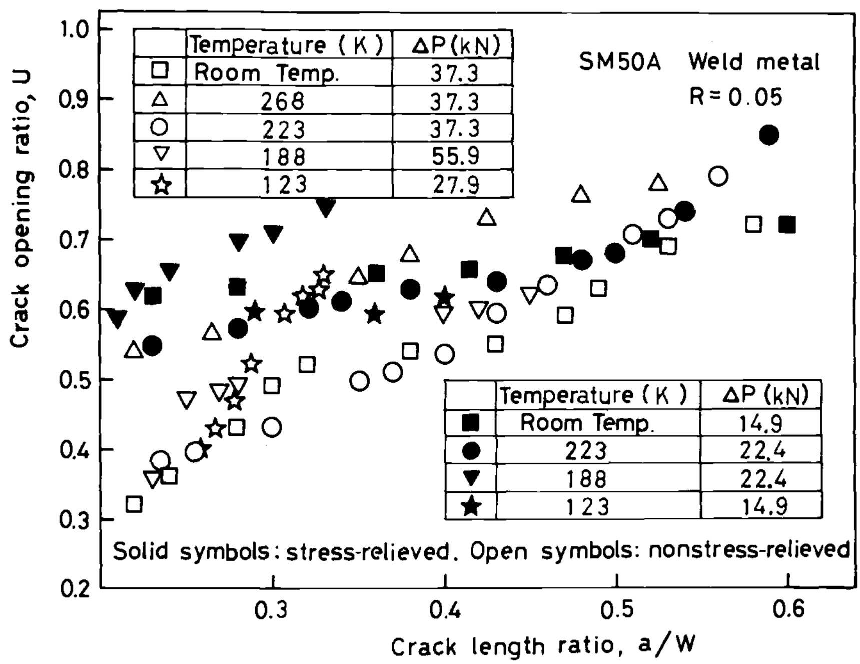

FIG. 10—*Relationship between effective load ratio* (U) *and crack length ratio* (a/W) *for non-stress-relieved and stress-relieved weld specimens.*

sidual stress in the weld specimens will not be changed in spite of changes in crack length.

The crack growth rates of the base metal and weld specimens shown in Figs. 3, 5, and 6 were replotted against ΔK_{eff} instead of ΔK. The result for the base metal (except for the data at 123 K) is shown in Fig. 11. The data for the base metal fall on a straight line with a gradient of 2.9, regardless of temperature. The crack growth rates of the base metal at 123 K were difficult to plot against ΔK_{eff}, since the values of P_{op} could not be determined with high accuracy because of the occurrence of cleavage during the crack growth. Figure 12 shows the fatigue crack growth rates in the non-stress-relieved and stress-relieved welds as a function of ΔK_{eff}. The crack growth

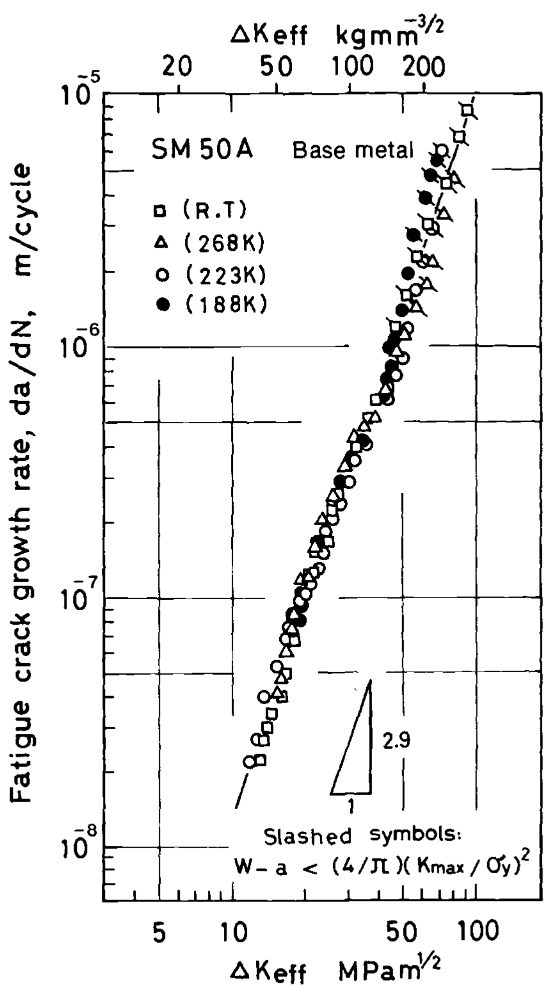

FIG. 11—*Fatigue crack growth rates of base metal as a function of* ΔK_{eff}.

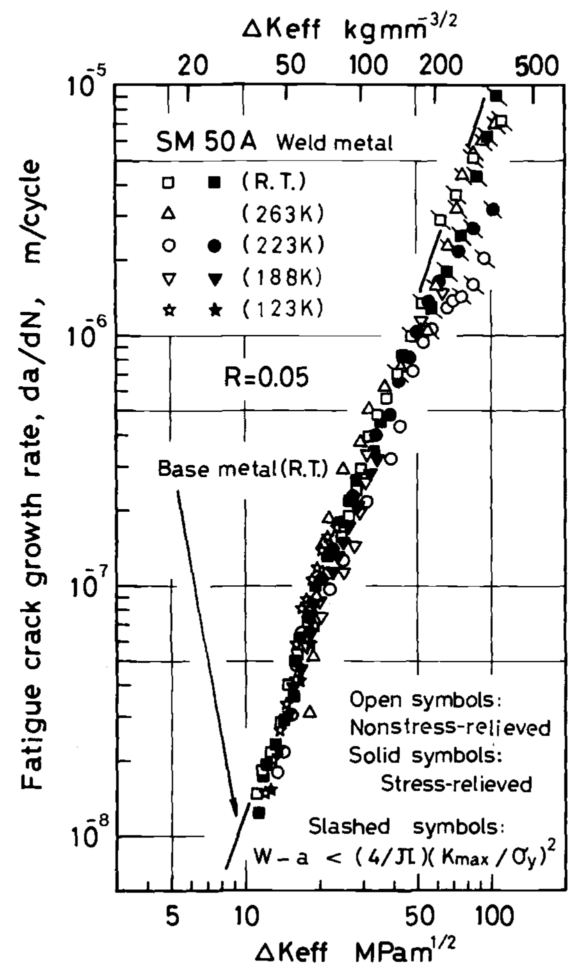

FIG. 12—*Fatigue crack growth rates of non-stress-relieved and stress-relieved weld specimens as a function of* ΔK_{eff}.

rates of the base metal at room temperature as a function of ΔK_{eff} are superimposed on the same figure for comparison. As may be seen in the figure, the crack growth rates of the welds and the base metals are closely correlated with ΔK_{eff} regardless of residual stress and temperature, except in the high ΔK_{eff} region.

Crack Growth Mechanisms

Fractographic analysis indicated that fatigue crack growth in the base metal was dominated by the mechanism of striation formation at temperatures ranging from room temperature down to 188 K. A similar tendency was also recognized in the weld specimens. Some examples of striations in the base metal and the non-stress-relieved welds at 223 K are shown in Fig. 13. Striation spacings obtained from each location on the fracture surfaces of the base metal and the non-stress-relieved weld specimens tested at 223 K are plotted against ΔK in Fig. 14. It was found that the striation spacings in the base metal were larger than in the weld specimens in the low ΔK region. The discrepancy in the striation spacing may be caused by the residual stresses in the weld specimens. Hence the striation spacing was also replotted against ΔK_{eff}. It was found that the striation spacings in the base metal and weld specimens were closely correlated with ΔK_{eff} as well as crack growth rates, in spite of the residual stresses (Fig. 15).

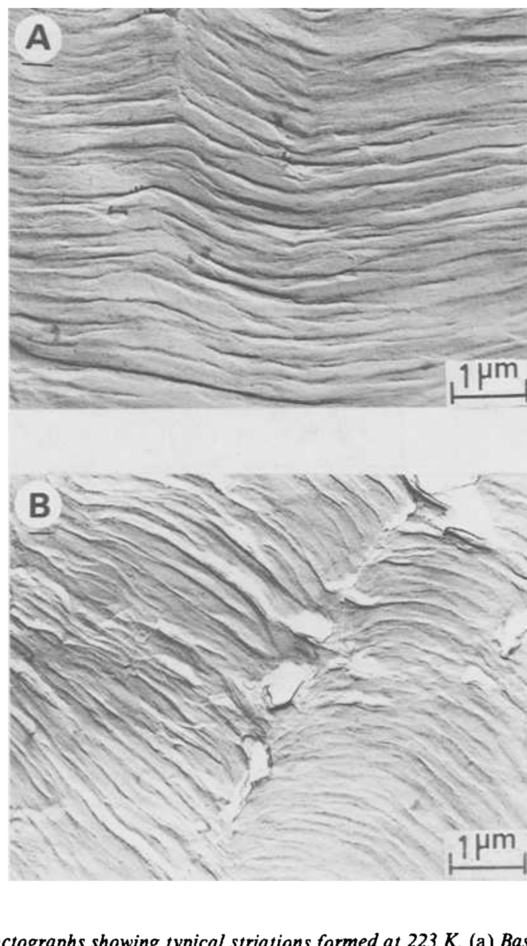

FIG. 13—*Fractographs showing typical striations formed at 223 K.* (a) *Base metal,* $\Delta K = 49.3$ *MPa* $m^{1/2}$, $da/dN = 4.34 \times 10^{-7}$ *m/cycle.* (b) *Welds,* $\Delta K = 61.3$ *MPa* $m^{1/2}$, $da/dN = 2.16 \times 10^{-7}$ *m/cycle.*

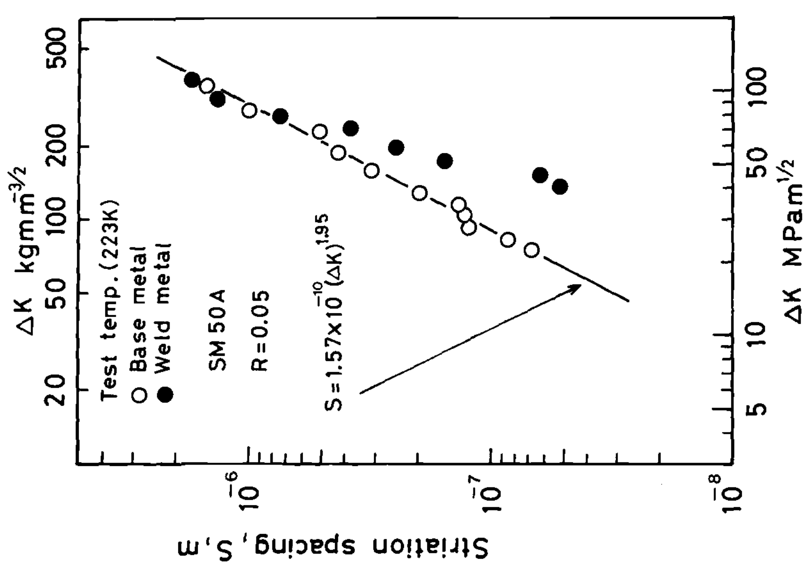

FIG. 14—*Striation spacings in base metal and non-stress-relieved welds as a function of* ΔK.

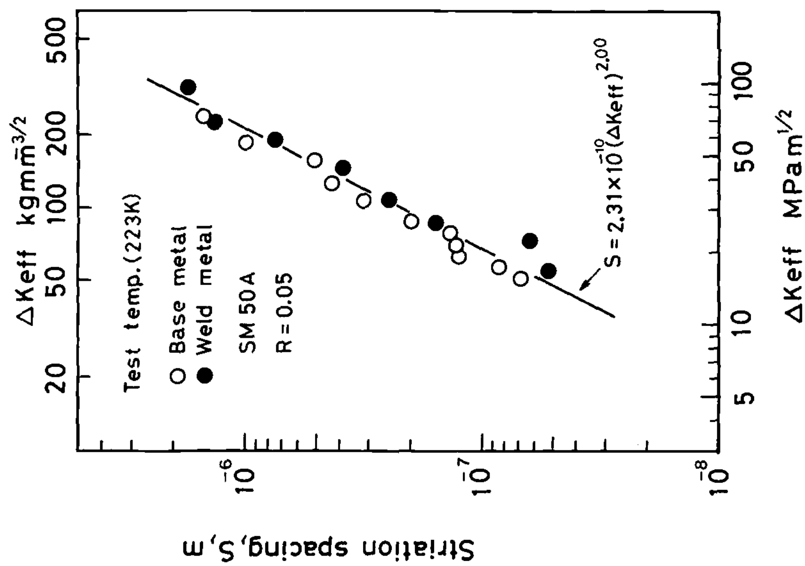

FIG. 15—*Striation spacings in base metal and non-stress-relieved welds as a function of* ΔK_{eff}.

In the base metal tested at 123 K, the traces of cleavage that show the evidence of cyclic cleavage were formed like bands on the fracture surface at ΔK values above 25 MPa $m^{1/2}$ (Fig. 16). The cleavage width (Δa) tended to increase with increasing ΔK. Figure 17 shows the relationship between Δa and maximum plastic zone size (R_y) at the crack tip. As may be seen in the figure,

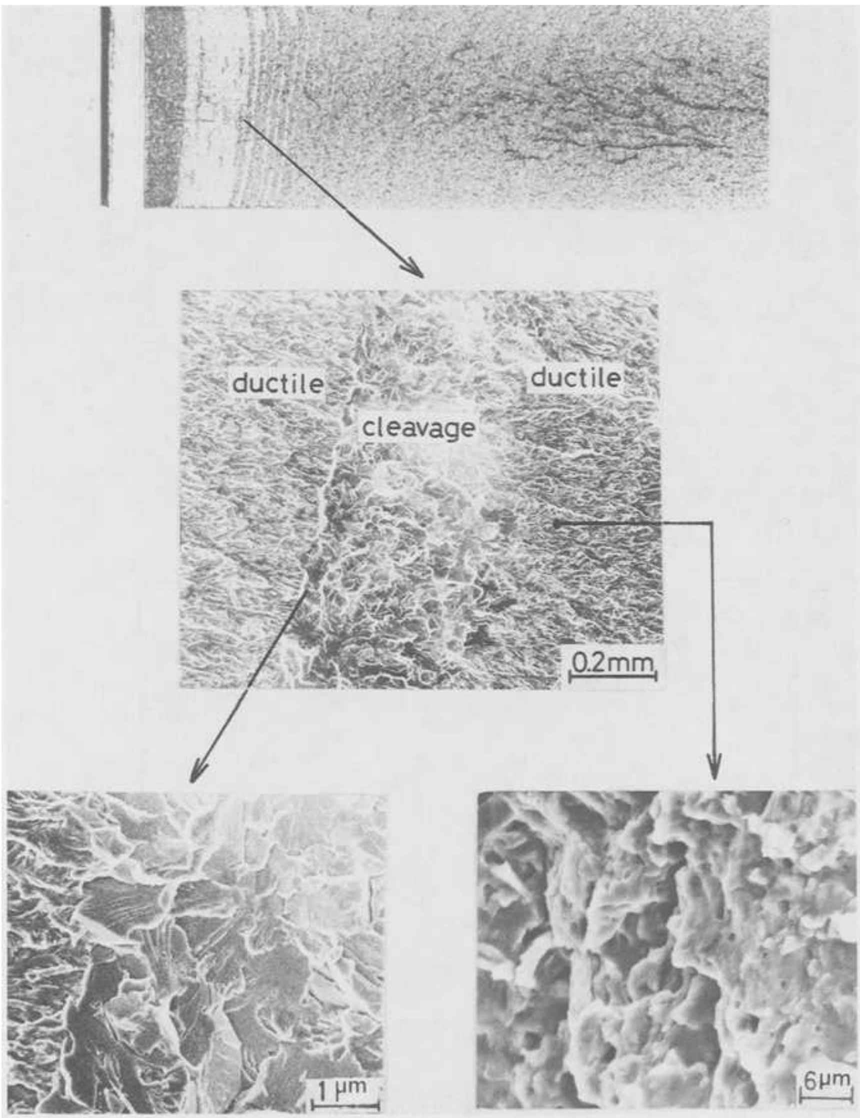

FIG. 16—*Fractographs showing cyclic cleavage of base metal at 123 K.*

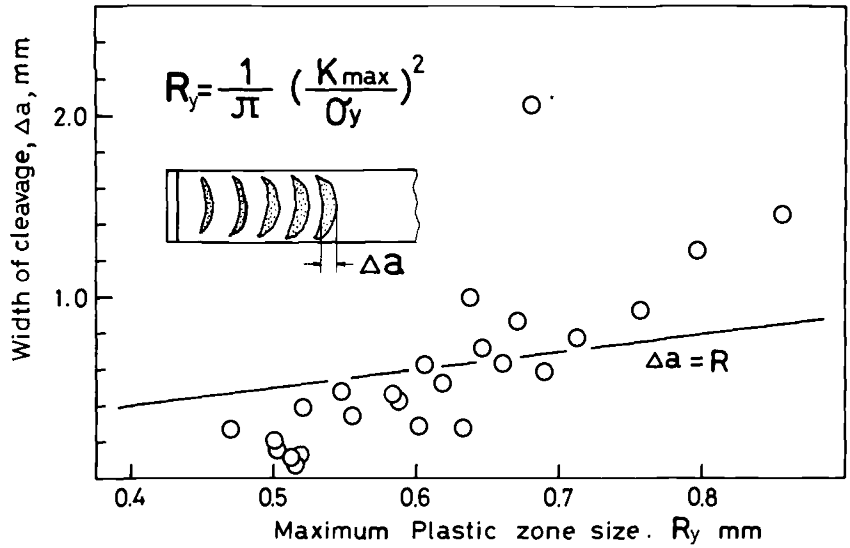

FIG. 17—*Relationship between width of cleavage* (Δa) *and plastic zone size* (R_y).

the size of Δa is approximately the same as R_y. Hence the presence of cyclic cleavage may be related to local embrittlement caused by work hardening in the plastic zone ahead of the fatigue crack. Fractographic examination indicated that the acceleration of crack growth in the base metal at 123 K was associated with the occurrence of cleavage during striation formation.

Conclusions

Several conclusions were drawn from this study:

1. Fatigue crack growth rates in the base metal of structural steel weldments at temperatures ranging from room temperature down to 188 K decreased slightly with decreasing temperatures. In this case, the mechanism of crack growth was dominated by striation formation.

2. At 123 K, the fatigue crack growth rate of the base metal was considerably increased in the high ΔK region by the occurrence of cleavage during striation formation.

3. Fatigue crack growth rates of the welds were found to be lower than in the base metal, regardless of temperature, because the crack tip in the CT weld specimens was always in the field of compressive residual stresses introduced by welding.

4. When crack growth mechanisms were dominated by striation formation, the fatigue crack growth rates of the base metal and the welds were closely correlated with ΔK_{eff} (as estimated from the crack closure experiments), regardless of temperature and residual stress.

References

[1] Person, N. L. and Wolfer, G. C. in *Properties of Materials for Liquefied Natural Gas Tankage, ASTM STP 579,* American Society for Testing and Materials, Philadelphia, 1975, pp. 80–95.
[2] Tobler, R. L. and Reed, R. P., *Advances in Cryogenic Engineering,* Vol. 22, 1977, pp. 35–46.
[3] Moody, N. R. and Gerberich, W. W., *Materials Science and Engineering,* Vol. 41, 1979, pp. 271–280.
[4] Tschegg, E. and Stanzl, S., *Acta Metallurgica,* Vol. 29, 1981, pp. 33–40.
[5] Lucas, J. P. and Gerberich, W. W., *Materials Science and Engineering,* Vol. 51, 1981, pp. 203–212.
[6] Liaw, P. K. and Fine, M. E., *Metallurgical Transactions A,* Vol. 12, 1981, pp. 1927–1937.
[7] Bucci, R. J., Greene, B. M., and Paris, P. C. in *Progress in Flaw Growth and Fracture Toughness Testing, ASTM STP 536,* American Society for Testing and Materials, Philadelphia, 1973, pp. 206–228.
[8] Kelsey, R. A., Nordmark, G. E., and Clark, J. W. in *Fatigue and Fracture Toughness Cryogenic Behavior, ASTM STP 556,* American Society for Testing and Materials, Philadelphia, 1974, pp. 159–185.
[9] Sarno, D. A., Bruner, J. P., and Kampschaefer, G. E., *Welding Research Supplement,* Vol. 53, Nov. 1974, pp. 486–494s.
[10] McHenry, H. I. and Reed, R. P., *Welding Research Supplement,* Vol. 56, Apr. 1977, pp. 104–112s.
[11] Srawley, J. E., *International Journal of Fracture,* Vol. 12, 1976, pp. 475–476.
[12] Paris, P. C. and Erdogan, F., *Journal of Basic Engineering, Transactions of ASME,* Series D, Vol. 85, 1963, pp. 528–534.
[13] Ohta, A., Sasaki, E., Kamakura, M., Kosuge, M., et al, *Transactions of the Japan Welding Society,* Vol. 12, Apr. 1981, pp. 31–38.
[14] Bucci, R. J. in *Fracture Mechanics: Thirteenth Conference, ASTM STP 743,* American Society for Testing and Materials, Philadelphia, 1981, pp. 28–47.
[15] Elber, W. in *Damage Tolerance in Aircraft Structures, ASTM STP 486,* American Society for Testing and Materials, Philadelphia, 1971, pp. 230–242.
[16] Buck, O., Frandsen, J. D., and Marcus, H. L., *Engineering Fracture Mechanics,* Vol. 7, 1975, pp. 167–171.
[17] Irving, P. E., Robinson, J. L., and Beevers, C. J., *Engineering Fracture Mechanics,* Vol. 7, 1975, pp. 619–630.
[18] Elber, W. in *Fatigue Crack Growth under Spectrum Loads, ASTM STP 595,* American Society for Testing and Materials, Philadelphia, 1976, pp. 236–250.
[19] Pelloux, R. M., Faral, M., and McGee, W. M., in *Fracture Mechanics: Twelfth Conference, ASTM STP 700,* American Society for Testing and Materials, Philadelphia, 1980, pp. 35–48.
[20] Ohta, A., Kosuge, M., and Sasaki, E., *International Journal of Fracture,* Vol. 14, 1978, pp. 251–264.

R. I. Stephens, A. Fatemi, H. W. Lee, S. G. Lee, C. Vacas-Oleas, and C. M. Wang

Variable-Amplitude Fatigue Crack Initiation and Growth of Five Carbon or Low-Alloy Cast Steels at Room and Low Climatic Temperatures

REFERENCE: Stephens, R. I., Fatemi, A., Lee, H. W., Lee, S. G., Vacas-Oleas, C., and Wang, C. M., "**Variable-Amplitude Fatigue Crack Initiation and Growth of Five Carbon or Low-Alloy Cast Steels at Room and Low Climatic Temperatures,**" *Fatigue at Low Temperatures, ASTM STP 857,* R. I. Stephens, Ed., American Society for Testing and Materials, Philadelphia, 1985, pp. 293–312.

ABSTRACT: Five common cast steels were subjected to SAE transmission history at room temperature and three low climatic temperatures using an as-drilled keyhole notched compact specimen. The three low temperatures were −34, −45, and −60°C. These temperatures were both above and below nil ductility transition temperatures. Three fatigue criteria were specifically monitored: crack initiation defined by the first visible surface crack Δa equal to 0.25 mm, Δa equal to 2.5 mm, and final fracture. All low-temperature total fatigue lives were equal to or better than at room temperature for four of the five cast steels. All steels exhibited crack initiation lives at low temperatures equal to or better than at room temperature. Fatigue crack growth life tended to increase as the temperature was lowered, and then this trend reversed. Scanning electron fractographic analysis showed all ductile type fatigue crack growth mechanisms above or below the nil ductility transition temperature.

KEY WORDS: fatigue (materials), cast steel, low temperature, crack initiation, notches, crack growth, spectrum loading, fractography, mechanisms, striations, nil ductility transition

Nomenclature

Δa	Fatigue crack extension from the keyhole notch, mm
Δa_f	Final fatigue crack extension at fracture, mm
A	Keyhole specimen net section area, m^2
c	Distance from the neutral axis to the keyhole notch, m
CVN	Charpy V-notch

Dr. Stephens is a professor in the Mechanical Engineering Department of The University of Iowa in Iowa City, IA 52242. The other authors are all research assistants or former research assistants in the Materials Engineering Division, The University of Iowa.

$2H$	Keyhole specimen height, mm
I	Keyhole specimen net section moment of inertia, m^4
K_t	Theoretical elastic stress concentration factor
LEFM	Linear elastic fracture mechanics
M	Bending moment, N·m
N_1	Number of applied blocks to crack initiation, defined as $\Delta a = 0.25$ mm
N_2	Number of applied blocks to grow a crack to $\Delta a = 2.5$ mm
N_f	Number of applied blocks to final fracture
N_f-N_1	Number of applied blocks of fatigue crack growth
NDT	Nil ductility transition
P	Applied load, kN
P_{max}	Positive peak load in the load spectrum, kN
T/H	SAE transmission history
SEM	Scanning electron microscope
w	Specimen width, mm
σ_{nom}	Nominal elastic normal stress at the keyhole notch, MPa

Low temperature fatigue behavior, principally at −45°C, has been reported for five low-carbon or low-alloy cast steels [1–3]. The behavior has included monotonic and cyclic stress-strain, low- and high-cycle unnotched axial fatigue, fatigue crack growth rates, and fatigue crack initiation and growth from a notch under two variable-amplitude spectra. Additional research has been carried out using three different low climatic temperatures involving fatigue crack initiation and growth and fracture tests using a keyhole compact type specimen and SAE transmission history. The keyhole specimen, variable-amplitude spectrum, and low temperatures represent a complete fatigue situation under realistic simulated service conditions for the five commonly used low-carbon or low-alloy cast steels.

Very little low-temperature fatigue behavior under variable-amplitude spectra has been reported, and constant-amplitude tests, on the other hand, too often do not properly represent real component or structural behavior. Thus the objective of this research is to simulate real fatigue crack initiation and growth conditions to better our understanding of fatigue at low climatic temperatures. Three temperatures were chosen to represent low climatic temperatures found in much of the populated world: −34, −45, and −60°C. The three temperatures were both above and below the NDT temperature and the CVN transition regions for the five cast steels.

Materials and Test Procedures

The five carbon or low-alloy steels investigated were:

- SAE 0030 (normalized and tempered)
- SAE 0050A (normalized and tempered)

- C-Mn (normalized, quenched, and tempered)
- Mn-Mo (normalized, quenched, and tempered)
- 8630 (normalized, quenched, and tempered)

The pouring, heat treatment, chemistry, microstructure, average monotonic and cyclic properties, and constant-amplitude fatigue behavior at both room temperature and −45°C are given in another paper in this volume [1]. Room temperature ultimate strengths for the five cast steels ranged from 496 to 1144 MPa. At −45°C both monotonic and cyclic strength properties S_y, S_u and S_y' increased by an average of about 10%. Both 0030 and 0050A have fine-grained (ASTM E 112, No. 8 or 9) ferritic-pearlitic microstructures, while the other steels are tempered martensite. All five cast steels contained normal inclusions and porosity and represent typical castings found in industry. Test specimens were machined from the castings.

Standard 10 by 10 mm Charpy V-notch specimens were tested with a standard pendulum impact test machine from −73 to 121°C. Two specimens were tested at each of about ten different temperatures within this range for each of the five cast steels. The CVN energy versus temperature results are shown in Fig. 1. Standard drop weight tests were also run in order to obtain NDT temperatures, which are superimposed as X's in Fig. 1. Also superimposed on the five CVN curves are four vertical lines that represent the four test temperatures involved in this research. The three low test temperatures are in the lower transition region for C-Mn, Mn-Mo, and 8630 steels and essentially in the lower shelf region for 0030 and 0050A steels. The lower shelf

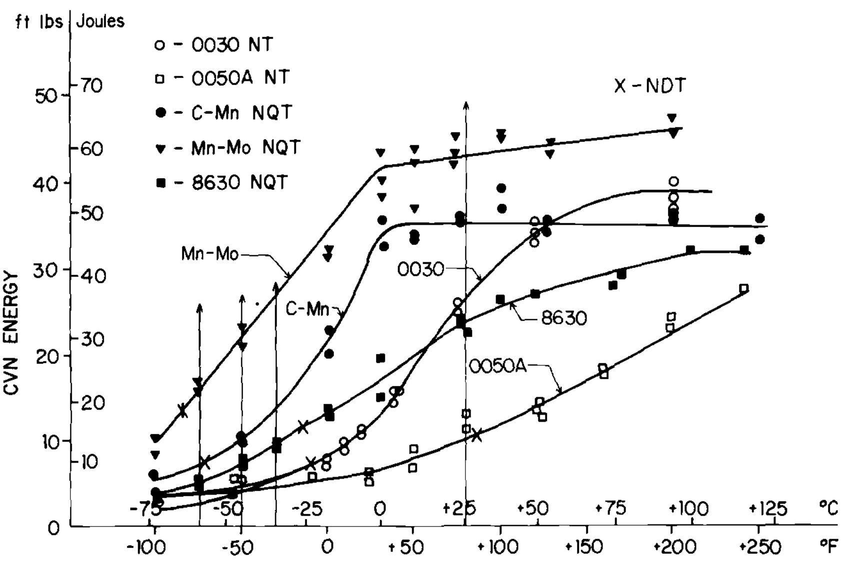

FIG. 1—*Charpy V-notch behavior and NDT temperature.*

region for 0050A, however, exists up to about −4°C, which is well above the three low-temperature test conditions. The lateral contraction and the percent crystalline fracture were consistent with respect to the energy values given in Fig. 1. All tests were below the NDT temperature for 0050A steel, including the one at room temperature, while all low-temperature tests were below the NDT temperature for 0030 and 8630 steels. For C-Mn and Mn-Mo steels, all test temperatures were essentially equal to or above the NDT temperature. Thus a variety of NDT/test temperature ranges were involved in this research.

The SAE transmission history (abbreviated T/H) was used in this research (Fig. 2). It has predominantly tensile loadings along with significant compressive loads. A total of 1710 reversals make up one T/H history block; most of the load ranges are of relatively small magnitude. A keyhole compact type specimen (Fig. 3), 8.2 mm thick, was used in conjunction with the T/H history. The 4.76-mm-diameter notch was left in the as-drilled condition without additional reaming or polishing to better simulate actual component field conditions. A theoretical elastic stress concentration factor $K_t = 4$ was determined by using several different finite element models and programs with $H/w = 0.6$. The test specimens were polished on one surface in order to better monitor fatigue crack initiation and growth. Polishing scratches were perpendicular to the direction of crack growth.

Variable-amplitude fatigue tests using the transmission history were run under load control at 12 Hz using an automated profiler in conjunction with an 89-kN closed-loop electrohydraulic test system. The block history was repeated until specimen fracture. Low-temperature tests were conducted in an automated CO_2 chamber from −34 to −60°C. Fatigue crack initiation and crack growth were monitored with a ×33 traveling telescope. Crack growth increments between about 0.25 and 2.5 mm were monitored on one side of the specimen until fracture. About 15% of the room temperature tests also had an electropotential monitoring system to better aid in detecting crack initiation at the notch. Fatigue crack initiation was quantitatively defined as the first visible surface crack length of $\Delta a = 0.25$ mm that could be observed with the optical telescope to be emanating from the keyhole notch. The electropotential system, however, always indicated cracks had initiated at the notch interior shortly before they were observed on the surface. The number of blocks involved in this difference was small and therefore the chosen criterion for crack initiation appears quite reasonable from an engineering point of view. A crack length (Δa) measured from the notch equal to 2.5 mm was also specifically monitored, since this value was previously selected by the SAE Fatigue Design and Evaluation Committee as a limiting value of crack initiation used with notch strain analysis prediction methods [*4*]. This value is also a reasonable crack length, where linear elastic fracture mechanics (LEFM) analysis becomes quite applicable. Most of the multiple initiated interior cracks and surface cracks had also coalesced into one major crack at this point.

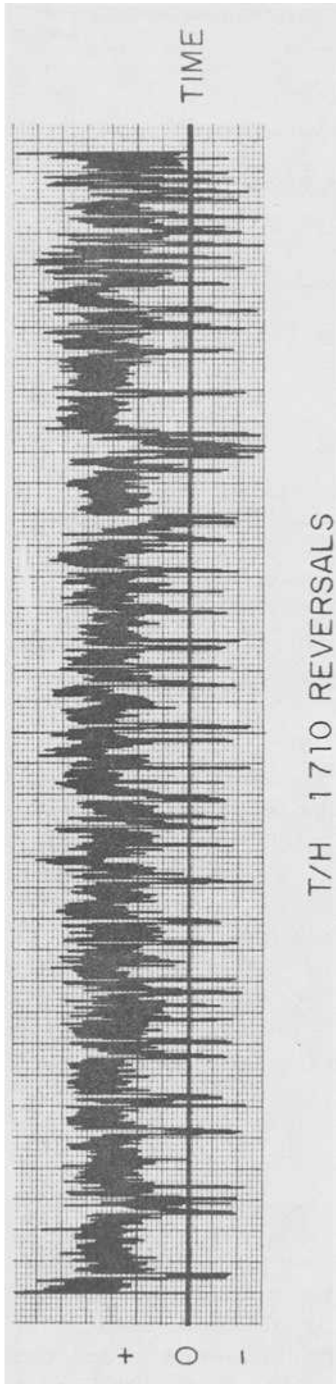

FIG. 2—*SAE transmission history* (T/H).

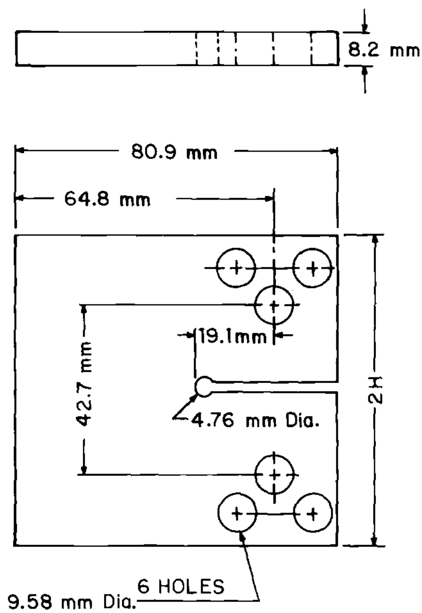

2H = 77.7 mm H/w = 0.60

FIG. 3—*Keyhole notch specimen.*

The T/H block history begins and ends with zero load. The first and last load in each block has the same peak value (P_{max}). A single value of P_{max} was chosen for comparative tests with the five cast steels at the four test temperatures. Previously, three load levels had been used at room temperature and −45°C [*2*]. The single load choice provided reasonable test time per specimen and produced fatigue lives from 130 to 1050 blocks, which is equivalent to approximately 2×10^5 to 2×10^6 reversals. Tests lasted from about 2 to 20 h and were run at least twice for all test conditions.

The compact specimen was predominantly a bend specimen with a small axial contribution. Nominal elastic stresses (σ_{nom}) at the keyhole notch can be calculated from

$$\sigma_{nom} = \frac{P}{A} + \frac{Mc}{I} \tag{1}$$

where P is the applied load, A is the net section area, M is the bending moment, c is the distance from the neutral axis to the keyhole notch, and I is the net section moment of inertia. Values of peak σ_{nom} for the peak load level was 314 MPa. Since K_t at the notch was 4, all specimens were subjected to localized plasticity at the keyhole notch on the first loading.

Test Results

The variable-amplitude test results using the keyhole compact specimen with the T/H load spectrum are shown in Table 1; the first column gives the material and the next four major columns separate the four test temperatures. For a given temperature, four subcolumns are shown, giving applied blocks to three different life criteria and then the crack extension Δa_f at fracture. The variable N_1 represents the number of applied blocks to crack initiation, defined as $\Delta a = 0.25$ mm; N_2 represents the number of applied blocks to $\Delta a = 2.5$ mm; and N_f represents the number of applied blocks to final fracture as measured on a test specimen. The macroscopic fatigue cracks grew essentially perpendicular to the applied load in almost all cases. A general deviation from this plane was usually within ± 5 deg. For a given test specimen, only one predominant surface crack grew past $\Delta a \approx 2.5$ mm; however, several surface cracks sometimes initiated from the keyhole notch. These multiple small cracks either became nonpropagating cracks or coalesced with the predominant crack.

As may be seen in Table 1, very little scatter occurred for the three life criteria for all five cast steels. The scatter for life to fracture for primarily duplicate tests was less than a factor of 1.4. Somewhat greater scatter, but less than a factor of 2.3, occurred for crack initiation life (N_1) to $\Delta a \approx 0.25$ mm. This can be attributed to the as-drilled keyhole notch surface roughness variation, multiple interior cracks, and the exact decision as to when a surface crack was visible.

The number of blocks ranged from 15 to 75% of total life for crack initiation, 5 to 50% to then grow the crack from $\Delta a = 0.25$ mm to $\Delta a = 2.5$ mm, followed by 0 to 70% to grow the crack from 2.5 mm to fracture. Thus all three regions, in general, significantly contributed to the total life of the five cast steels except where substantial brittleness occurred in the 0050A steel at the two lowest temperatures. This indicates the importance of including crack initiation, growth of short cracks from notches, and growth of longer cracks in a total fatigue life prediction procedure.

In order to obtain a better visualization of the influence of lower temperatures on variable-amplitude fatigue crack initiation, growth, and total life, the data of Table 1 are plotted in Fig. 4. Here blocks to crack initiation (open data points) and blocks to fracture (solid data points) are plotted versus test temperature for all five cast steels. Straight line segments have been drawn from one test temperature to another through the average of the data for better visualization. The NDT temperatures have been marked with an X on each abscissa. This figure clearly shows the small scatter for a given test condition and the influence of the four test temperatures on each of the five cast steels. It is seen that as the temperature was lowered from room temperature to $-60°$C, the average fatigue crack initiation life for all five cast steels was essentially equal to or better than that at room temperature by a factor of less than 2.5. The greater increases occurred in Mn-Mo and 8630 steel at the

TABLE 1—*T/H history blocks to three crack length criteria.*[a]

	Room Temperature				−34°C				−45°C				−60°C			
Material	N_1	N_2	N_f	Δa_f, mm	N_1	N_2	N_f	Δa_f, mm	N_1	N_2	N_f	Δa_f, mm	N_1	N_2	N_f	Δa_f, mm
0030	79	102	169	...	...	...	...	...	...	...	...	...	...	...	...	...
	67	77	141	20	89	163	254	18	80	144	219	13	88	117	186	10
	35	78	130	16	130	186	304	16	68	145	248	13	78	120	158	6
0050A	103	155	297	21	101	190	289	14	55	130	212	6	142	...	153	2
	100	236	399	19	155	188	281	11	100	168	271	9	156	172	172	3
C-Mn	105	141	285	21	72	222	489	22	139	287	606	23	175	210	412	21
	92	147	288	20	152	251	530	24	91	190	640	20	166	229	468	22
Mn-Mo	100	197	635	23	133	531	799	21	306	368	629	24	256	323	506	17
	209	295	551	24	150	316	621	22	252	350	...	...	373	442	684	20
8630	250	338	532	29	479	559	959	24	696	741	946	19	758	830	1050	19
	258	340	597	28	393	447	744	20	390	438	705	20	585	635	870	15

[a] N_1 = number of applied blocks to crack initiation, defined as $\Delta a = 0.25$ mm.
N_2 = number of applied blocks to grow a crack to $\Delta a = 2.5$ mm.
N_f = number of applied blocks to final fracture.
Δa_f = final fatigue crack extension at fracture.

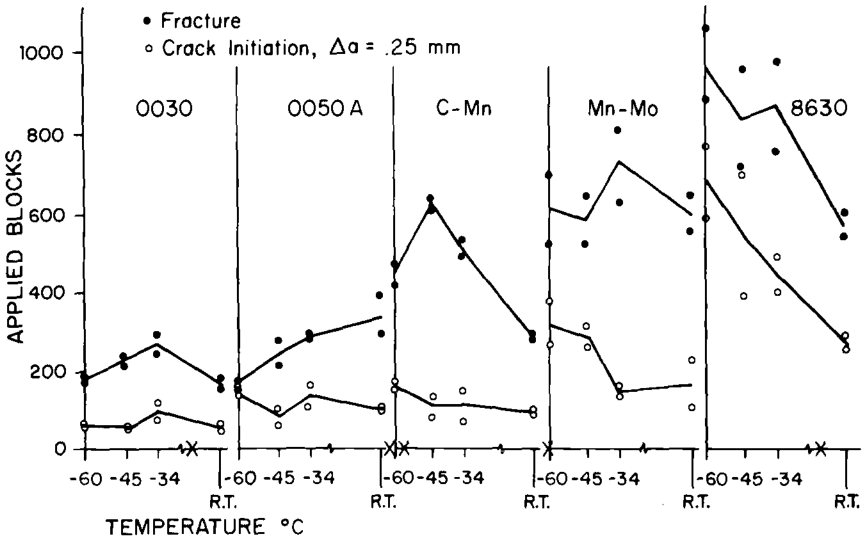

FIG. 4—*Average fatigue life to crack initiation* (N_I) *and fracture* (N_f) *with T/H loading; peak* σ_{nom} = *314 MPa.*

lower temperatures. Total life to fracture at low temperature was also essentially equal to or better than that at room temperature by less than a factor of 2.5, except for 0050A steel. This steel showed a continuous drop in total fatigue life as the temperature was lowered from room temperature to −60°C. Thus even though the lower temperatures were not detrimental to fatigue crack initiation life, in 0050A steel the lower temperatures were quite detrimental to total fatigue life.

Average fatigue crack growth life can be determined from Fig. 4 for each of the test conditions by subtracting the average applied blocks to crack initiation from the average applied blocks to fracture. These values are plotted in Fig. 5, where it is evident that, except for 0050A steel, the crack growth life

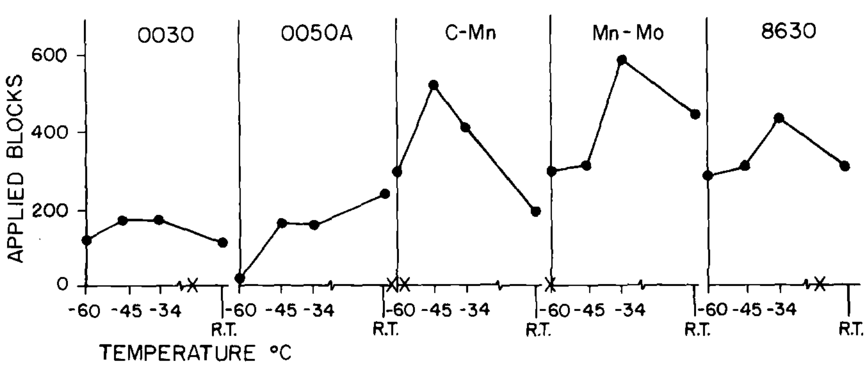

FIG. 5—*Average fatigue crack growth life* ($N_f - N_I$) *with T/H loading; peak* σ_{nom} = *314 MPa.*

tends to first increase as the temperature is lowered, reach a maximum, and then decrease. Again, the NDT temperatures have been marked with an X on each abscissa. For 0050A steel the crack growth life decreased at all lower test temperatures. The maximum fatigue crack growth life at the lower temperatures for the four steels was between 1.3 and 2.5 times greater than at room temperature. However, at −60°C only C-Mn had better fatigue crack growth life than at room temperature.

Fatigue crack extension from the keyhole notch (Δa) is plotted versus applied blocks (initiation blocks omitted) in Fig. 6 at the four different test temperatures for the five cast steels. The figure is for T/H loading with peak σ_{nom} equal to 314 MPa. Only crack extension up to about 10 mm is shown, since the rates become quite high and are substantially similar beyond this length. More than half of the curves in Fig. 6 are somewhat sigmoidal in shape in that the crack growth rate starts out high for short cracks, then decreases as the crack grows 1 or 2 mm from the keyhole notch, and then increases until fracture. The change in curvature at the short crack lengths can be due to the interaction of the local notch plasticity with the crack tip and to multiple crack interaction effects. It is seen that the fatigue crack growth rates at the different temperatures confirm the trends found in Fig. 5. As the temperature is decreased for a given steel, fatigue crack growth rates are lower, but as the temperature is decreased even further, the rates revert to higher values that approach or surpass those at room temperature. Thus the increases in fatigue crack growth rates as the temperature was lowered contributed to the poor lower temperature fatigue crack growth life. In addition, the crack lengths at final fracture for 0050A at the two lowest temperatures are shown to be very short.

Final crack lengths at fracture (Δa_f) for all five steels at the four test temperatures are plotted in Fig. 7. Here it is evident for 0030, 0050A, and 8630 steel that crack lengths at fracture decreased as the temperature was lowered. For 0030 and 0050A the decrease was very large. Thus shorter crack lengths at fracture and hence lower fracture toughness at the lower temperatures also contributed to the eventual lower fatigue crack growth life at the lower temperatures.

Macrofractography and Microfractography

Macrofractography

Macroscopic fractographs are shown in Fig. 8 for each of the five cast steels for the T/H spectrum with peak σ_{nom} equal to 314 MPa at the four test temperatures. The fatigue crack initiation, crack growth, and final fracture regions are shown. In all cases the fatigue crack initiated from the keyhole notch (bottom of photos) and grew toward the top of the photos. Despite the variable-amplitude loading, no beach marks are evident in any of the specimens. In all tests, Mode I fatigue crack growth existed. Initiation and coalescence of multiple interior cracks at the keyhole notch is evident in most specimens. The roughness in the fatigue crack growth region varies from material to material and also at the four different test temperatures. In some cases it was difficult to distinguish the end of the fatigue crack growth region because of the increased roughness at longer crack lengths. Additional specific macroscopic characteristics evident in Fig. 8 for each steel are given below.

0030—The greatest roughness occurred in 0030 steel. This tendency increased at the lower temperatures. The final macroscopic fracture region showed substantial ductility and necking at room temperature and essentially brittle fracture at the three lower temperatures.

0050A—The fatigue crack growth regions in 0050A steel were quite smooth at all four temperatures. The decrease in crack length at fracture as the temperature decreased is quite evident. A substantial jump in the fatigue crack region just before fracture is evident at −45°C. The final fracture region at room temperature contained only a slight amount of necking and shear lips. At the lower temperatures, however, no necking or shear lips existed and the fracture regions were completely flat, with bright and shiny brittle fractures. Thus at all temperatures, final macroscopic brittle fracture existed.

C-Mn—The size and roughness of the fatigue crack growth region were essentially independent of test temperature in C-Mn steel. Necking with slight shear lips existed in the final fracture region at all four temperatures. These are less at −60°C, with some brittleness mixed in with the primarily ductile fracture. The final macroscopic fractures were completely ductile at the other three temperatures.

Mn-Mo—The size and roughness of the fatigue crack growth region were similar at all temperatures except −60°C in Mn-Mo steel. The shorter fatigue crack length at fracture for −60°C is evident. Appreciable necking existed at all temperatures except −60°C. Shear lip size decreased as the temperature was lowered. However, final macroscopic fracture areas were still ductile at all temperatures.

8630—Less roughness occurred in the fatigue crack growth region at the lower temperatures in 8630 steel. The decrease in final crack length at fracture for the lower temperatures is evident. At −60°C a substantial jump in the fatigue crack region just before fracture is seen. The final fracture region has appreciable shear lips at room temperature and −34°C, with only small shear lips at −45°C and none at −60°C. No bright shiny brittle fracture regions existed at any of the four test temperatures. The final fractures, however, went from appreciable macroscopic slant or mixed-mode fracture at room temperature to Mode I at the two lower temperatures.

Scanning Electron Microscopy

Fracture surfaces from the different test temperatures were examined with scanning electron microscopy (SEM) from ×50 to ×3500 magnification. The

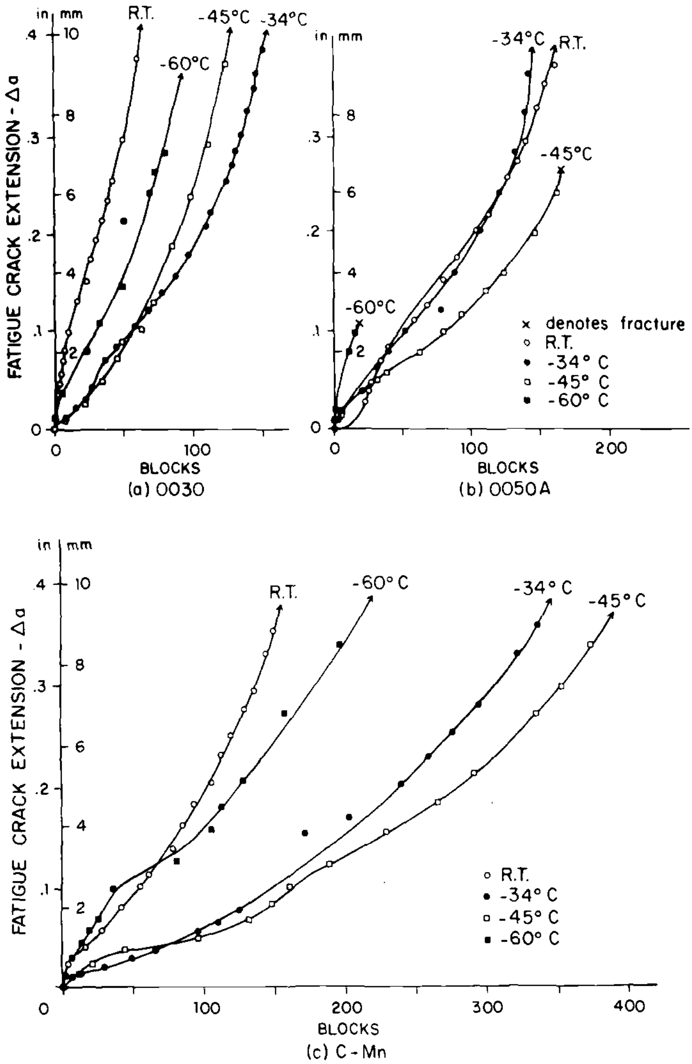

FIG. 6—*Fatigue crack extension from the keyhole notch versus applied T/H blocks; peak* σ_{nom} *= 314 MPa.*

fracture surfaces were mounted normal to the SEM electron beam. Two to four independent fatigue crack initiation sites were found for the different test specimens. These sites were usually from the as-drilled keyhole notch scratches; however, some were formed at inclusions or porosity directly adjacent to the notch edge. The fatigue crack growth regions were much more irregular than for constant-amplitude loading [*1,2*], and striations were fewer, more poorly defined, and more difficult to locate. They were often flat because of crack closure and rubbing between the two crack surfaces. Substantial numbers of inclusions, porosity, and secondary cracks existed on the

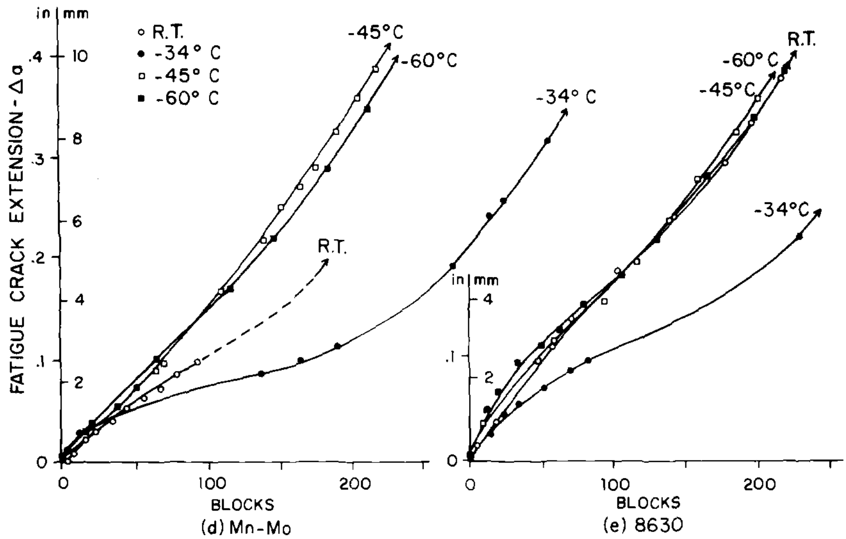

FIG. 6—*Continued.*

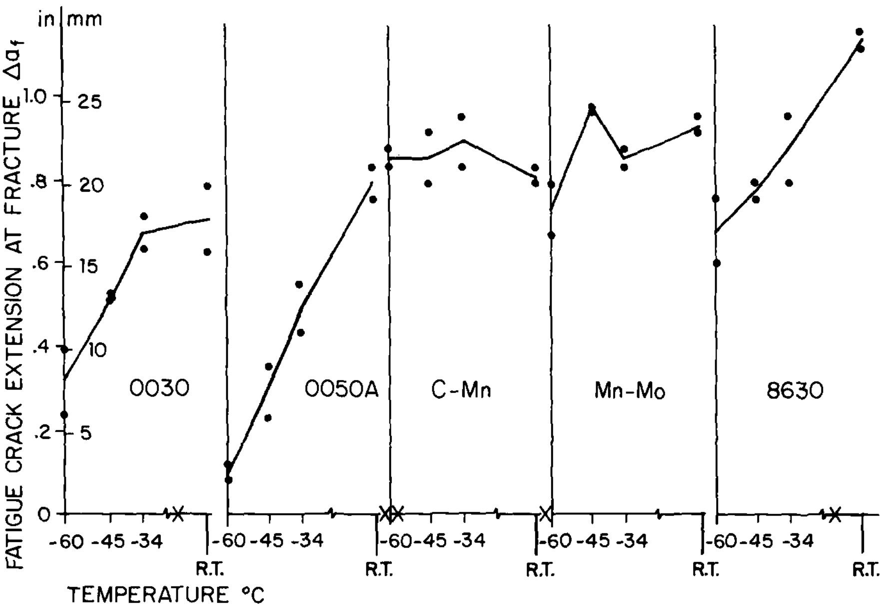

FIG. 7—*Average fatigue crack extension at fracture with T/H loading; peak σ_{nom} = 314 MPa.*

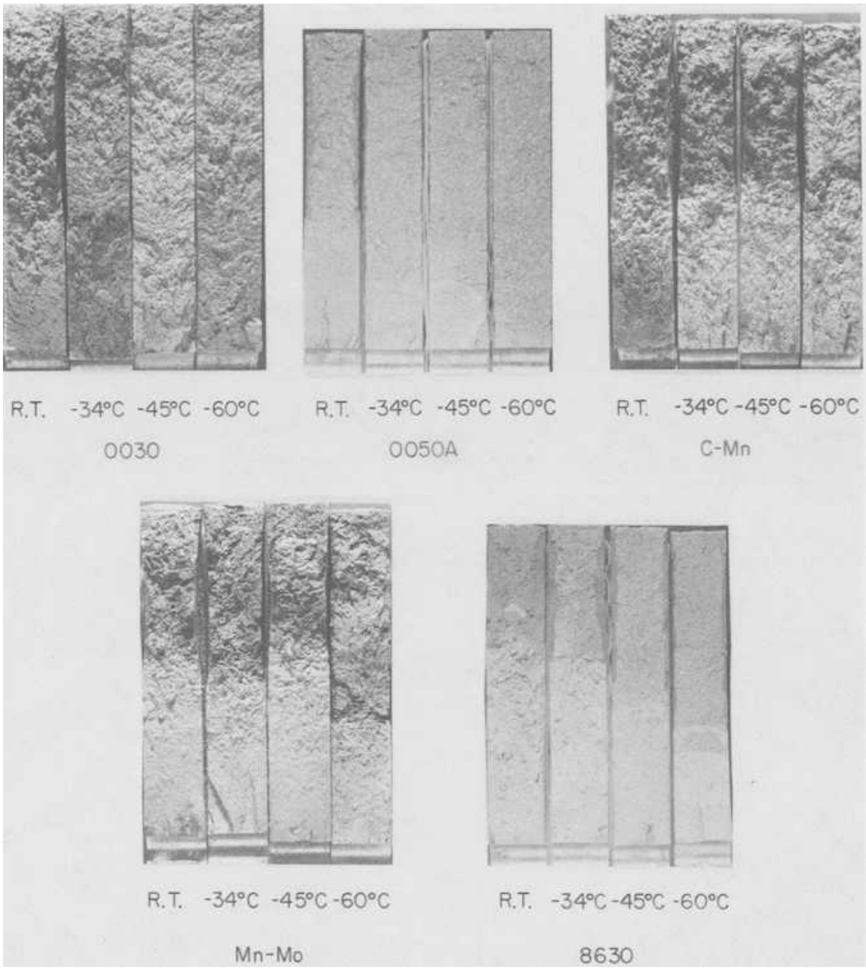

FIG. 8—*Macroscopic fracture surfaces for T/H loading; peak* σ_{nom} = *314 MPa.*

fracture surfaces at all temperatures. These increased in number at the longer crack lengths.

Typical SEM fractographs taken with magnification between ×1000 and ×3000 are shown in Fig. 9 for each of the five steels at room and low temperatures. Fatigue cracks grew from bottom to top in the photographs. The fatigue crack growth morphology did not change significantly at any of the test temperatures, except near impending final fracture for a few of the very low temperature tests. In general, the fatigue crack growth behavior from room temperature to −60°C was transcrystalline and ductile, with and without striations. Just before impending fracture, a few mixed cleavage facets were found dispersed within the ductile fatigue matrix at lower temperatures.

These regions, however, contributed very little to the overall fatigue crack growth life or total life of an individual test.

The final fracture region was usually quite distinct from the fatigue region. Final fractures ranged from 100% ductile dimples to 100% cleavage. Mixed modes also existed. Specific microscopic characteristics for each steel are given below.

0030—The greatest number of striations with the variable amplitude histories occurred in 0030 steel at room temperature (Fig. 9*a*). The more flattened regions are shown at lower temperatures. Some mixed cleavage facets and ductile fatigue occurred at all three low temperatures just before fracture. The final fracture region exhibited ductile dimples at room temperature, mostly cleavage at −34°C, and all cleavage at the two lowest temperatures.

0050A—Striations were very scarce under all temperature conditions in 0050A steel; however, fatigue crack growth was still ductile (Fig. 9*b*). Some mixed cleavage facets and ductile fatigue occurred at the two lowest temperatures just before fracture. The final fracture region exhibited cleavage at all temperatures.

C-Mn and Mn-Mo—Fatigue crack growth was ductile at all temperatures in C-Mn and Mn-Mo steel. There were very few striations, and they were usually flattened (Figs. 9*c* and 9*d*). Some mixed cleavage facets and ductile fatigue occurred at −60°C just before fracture. Final fracture regions had ductile dimples at all test temperatures; however, some cleavage also became evident at −45°C and somewhat more evident at −60°C.

8630—For 8630 steel, fatigue crack growth was ductile at all temperatures, with only a few striations present (Fig. 9*e*). At room temperature the final fracture region was all ductile dimples, while at −34°C mixed dimples and cleavage existed. At the lowest temperatures, final fractures were completely by cleavage.

Discussion

For 0030, 0050A, and 8630 cast steels, all the low-temperature fatigue tests were performed below the NDT temperature and in or near the lower shelf CVN region (Fig. 1). The low temperatures, however, were equal to or above the NDT temperature and in the transition CVN region for C-Mn and Mn-Mo cast steels. Even under the above mixed conditions for the five cast steels, the average variable-amplitude fatigue crack initiation life for all three low climatic temperatures was approximately equal to or better than that at room temperature, but by less than a factor of 2.5. Thus the NDT temperature and the lower shelf CVN region did not provide sufficient information for possible transitions in fatigue crack initiation and propagation mechanisms. Since these low temperatures were determined to be reasonable low climatic temperatures for most of the populated world, it appears that these

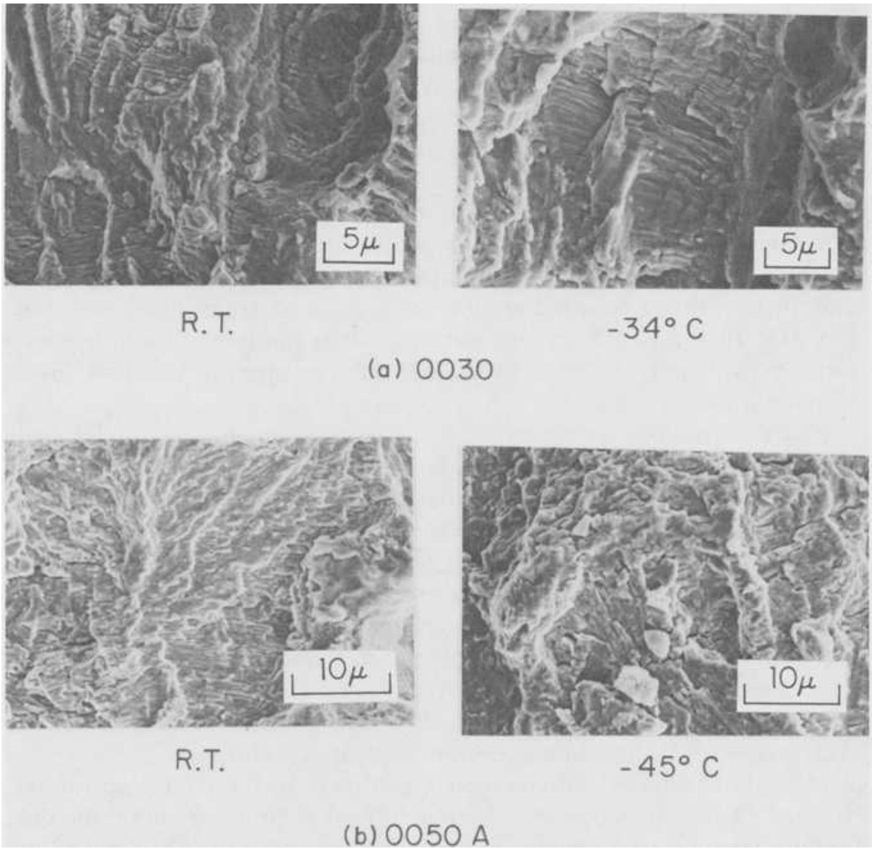

FIG. 9—*SEM fractographs for T/H tests; peak* σ_{nom} = *314 MPa.*

five cast steels should perform adequately in components, judging only from fatigue crack initiation. However, 0050A in particular had extremely poor fatigue crack growth life at low temperatures because of higher crack growth rates and lower fracture toughness. This cast steel would not be desirable for use at low climatic temperatures. It should be noted, however, that the NDT temperature for 0050A was essentially room temperature, which is well above these low climatic temperatures.

Fatigue crack growth life and rates for the other four cast steels under variable-amplitude loading were better at −34°C than at room temperature (Figs. 5 and 6), but this behavior tended to reverse as the temperature was lowered to −45 or −60°C. Decreases in fracture toughness at the lower temperatures partially contributed to the lower fatigue crack growth life in several of the steels. The reversal in fatigue crack growth rates has previously been shown for constant-amplitude loading [*5–8*]. This reversal in crack

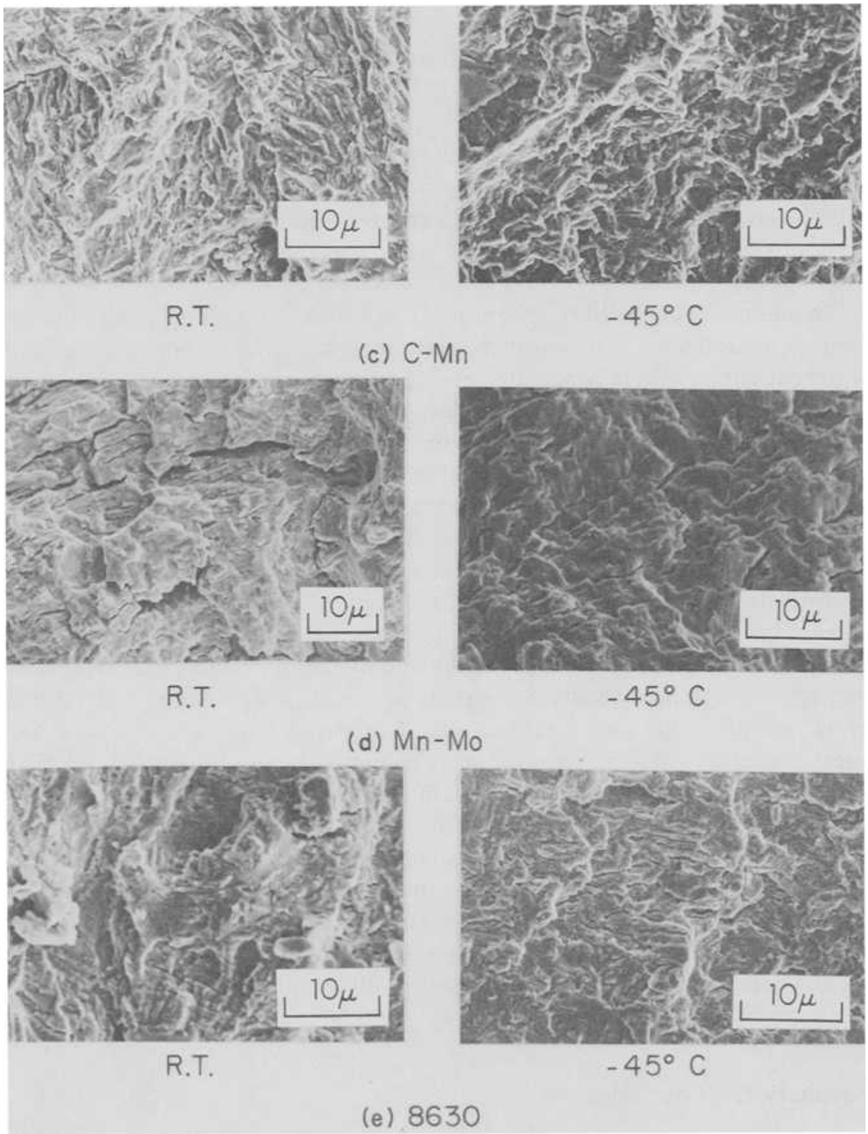

FIG. 9—*Continued.*

growth rates primarily occurred below the NDT temperature and in the lower shelf CVN region for the constant amplitude tests [5–8]. In this variable-amplitude research, four of the five cast steels behaved in this same manner; however, Mn-Mo exhibited accelerated fatigue crack growth at temperatures above the NDT temperature and in the lower CVN transition region. This is just one isolated case of detrimental fatigue crack growth behavior above the NDT temperature. Thus it appears reasonable that many steels with operating temperatures below NDT temperatures and lower shelf CVN regions should have fatigue crack initiation and growth resistance equal to or better than at room temperature. Additional research is needed to confirm this finding, particularly under variable-amplitude loadings including impact.

The microscopic SEM fractographic analysis did not really clarify the increases or decreases in macroscopic fatigue crack growth rates at the four different temperatures, since the general microscopic fracture surfaces were all quite similar and ductile at all test temperatures. Some exceptions occurred before impending fracture, with the formation of dispersed cleavage facets. However, negligible fatigue life exists at that point.

The selection or comparison of cast steels based on fatigue resistance is an important engineering decision. The five cast steels subjected to the T/H spectrum can be compared on the basis of fatigue crack initiation life (N_1), crack growth life ($N_f - N_1$), or total fatigue life (N_f) at the different temperatures. This complete comparison can be made from Table 1 and Figs. 4 and 5. From Fig. 4 it is seen for both room and low temperatures that 8630 steel has the best fatigue resistance, based on both variable-amplitude fatigue crack initiation life and total life. The Mn-Mo steel is ranked second for these conditions. It also, however, has the highest monotonic and cyclic yield strength of the five cast steels. Crack initiation life for the other three steels were essentially equivalent. The ferritic-pearlitic steels, 0030 and 0050A, in general have the lower total fatigue life resistance. Crack growth life is shown in Fig. 5, where it is seen that the martensitic steels C-Mn, Mn-Mo, and 8630 in general have the greater fatigue crack growth resistance at the various temperatures. These rankings are consistent with variable-amplitude results reported previously [2]; however, different loading spectra could produce different rankings.

Summary and Conclusions

1. Fatigue life for crack initiation, short crack growth from the notch, and long crack growth were significant at all test temperatures except for 0050A steel at the two lowest temperatures. Thus total fatigue life predictions of notched components should consider crack initiation, growth of short cracks under the influence of the notch plastic zone, and growth of longer crack lengths away from the notch influence.

2. Except for 0050A cast steel, the average total low-temperature fatigue lives were equal to or better than at room temperature. The increase in crack initiation life was within a factor of 2.5, as was the increase in total fatigue life to fracture. Crack growth life, however, tended to increase as the temperature was lowered and then this trend reversed as the temperature was further lowered. This reversal was due to increased crack growth rates and decreased fracture toughness. The 0050A steel had a continuous decrease in fatigue crack growth life for all lower temperatures; however, its NDT temperature was at room temperature, which is well above the three low test temperatures.

3. The SEM analysis indicated that fatigue crack growth was transcrystalline and ductile with and without observable striations at all temperatures. Final fracture region morphology depended upon both material and temperature. Final fracture surfaces ranged from 100% ductile dimples to 100% cleavage. Thus fatigue crack growth mechanisms were independent of final fracture mechanisms.

4. Ductile fatigue mechanisms can exist at temperatures below the NDT temperature and within the lower shelf CVN energy regions. It appears that if operating temperatures are above the NDT temperature and lower shelf CVN regions, then fatigue crack initiation life and fatigue crack growth life can be equivalent to or better than at room temperature.

5. In general, the three martensitic cast steels (8630, Mn-Mo, and C-Mn) had better fatigue resistance with the variable-amplitude loading spectrum at the four test temperatures than the ferritic-pearlitic 0030 and 0050A cast steels.

6. The 0030, C-Mn, Mn-Mo, and 8630 cast steels appear suitable for low climatic temperature conditions (0050A steel is excluded). This can only be stated for the nonwelded condition, since weldments were not considered.

Acknowledgments

The authors would like to thank the Steel Founders' Society of America, The University of Iowa, and contributing companies who financially sponsored this research.

References

[1] Stephens, R. I., Chung, J. H., Lee, S. G., Lee, H. W., Fatemi, A., and Vacas-Oleas, C., "Constant-Amplitude Fatigue Behavior of Five Carbon or Low Alloy Cast Steels at Room Temperature and −45°C," in *Fatigue at Low Temperatures, ASTM STP 857*, R. I. Stephens, Ed., American Society for Testing and Materials, Philadelphia, 1985, p. 140.

[2] Stephens, R. I., Chung, J. H., Fatemi, A., Lee, H. W., Lee, S. G., Vacas-Oleas, C., and Wang, C. M., "Constant- and Variable-Amplitude Fatigue Behavior of Five Cast Steels at Room Temperature and −45°C," *ASME Journal of Materials and Technology*, Vol. 106, No. 1, Jan. 1984, p. 25.

[3] Stephens, R. I., Njus, G. O., and Fatemi, A., "Fatigue Crack Growth Under Constant- and Variable-Amplitude Loading of Cast Steel at Room and Low Temperature," in *Advances in Fracture Research*, ICF-5, Vol. 4, 1981, Pergamon Press, U.K., p. 1807.

[4] Wetzel, R. M., Ed., *Fatigue under Complex Loading,* Society of Automotive Engineers, Warrendale, PA, 1977.
[5] Gerberich, W. W., and Moody, N. R., "A Review of Fatigue Fracture Topology Effects on Threshold and Growth Mechanisms," in *Fatigue Mechanisms, ASTM STP 675,* J. T. Fong, Ed., American Society for Testing and Materials, Philadelphia, 1979, p. 292.
[6] Kawasaki, T., Yokobori, T., Sawaki, Y., Nakanishi, S., and Izumi, H., "Fatigue and Fracture Toughness and Fatigue Crack Propagation in 5.5% Ni Steel at Low Temperature," in *Fracture 1977,* ICF-4, Vol. 3, University of Waterloo Press, Waterloo, Ont., Canada, June 1977, p. 857.
[7] Tobler, R. L., and Reed, R. P. "Fatigue Crack Growth Resistance of Structural Alloys at Cryogenic Temperature," in *Advances in Cryogenic Engineering,* Vol. 24, K. D. Timmerhaus, R. P. Reed, and A. F. Clark, Eds., Plenum Press, New York, 1978, p. 82.
[8] Stephens, R. I., Chung, J. H., and Glinka, G., "Low Temperature Fatigue Behavior of Steels—A Review," Paper 790517, *SAE Transactions,* Vol. 88, 1980, p. 1892.

Summary

Summary

The sixteen papers included in this volume describe tests conducted from room temperature to 4 K (−269°C). Twenty specific temperatures investigated are shown in Table 1 in both Kelvin (K) and Celsius (°C). Seven papers dealt with cryogenic temperatures involving liquid nitrogen (77 K), liquid hydrogen (20 K), or liquid helium (4 K); the other nine dealt with noncryogenic low temperatures. A wide range of metal alloys was investigated along with one cryogenic fiberglass epoxy laminate. The specific metal alloys investigated under fatigue conditions are given in Table 2. In addition, Tobler and Cheng investigated cryogenic fatigue crack growth summary behavior for Region II of the sigmoidal da/dN–ΔK curve (where a is crack length, N is applied cycles, and K is stress intensity factor) for the following metal alloy families: ferritic nickel steels, austenitic stainless steels, and aluminum, nickel, and titanium base alloys. Welds were also considered in several papers.

Thirteen papers had as their subject fatigue crack growth (FCG) under constant-amplitude loading, four papers discussed spectrum fatigue crack growth behavior, two papers investigated low-cycle strain-controlled fatigue behavior using smooth axial specimens, one paper examined axial stress-controlled S–N (where S is applied stress and N is cycles to failure) behavior, and one paper studied fatigue crack initiation from a notched keyhole specimen. (Some papers discussed several topics.) Thus the predominant subject matter of this volume is fatigue crack growth under constant-amplitude loading conditions. The other areas of study, however, also add substantially to the overall understanding of fatigue at low temperatures.

Constant-amplitude fatigue crack growth tests were carried out with compact type, (CT), center cracked panel (CCP), and bend specimens; the CT specimen was the predominant configuration. All cracks were considered as long cracks. Specimen thickness varied from about 1 to 25 mm. The load ratio ($R = P_{min}/P_{max}$) was primarily 0 or 0.1 except for a few tests at $R = 0.35$, 0.5, 0.7, and 0.8. Test frequencies ranged from 2 cycles/h to 100 Hz. Compliance methods, using a crack opening displacement (COD) gage, and optical microscopes were the two most common methods of obtaining low-temperature crack length measurements. One investigation used the electropotential method; another used a strain gage for monitoring crack growth. Low-temperature environments included liquid nitrogen, liquid hydrogen, and liquid helium at cryogenic temperatures. Noncryogenic tem-

TABLE 1—*Test temperatures.*

K	R.T.	273	268	239	233	228	223	219	213	190	188	173	153	140	123	113	99	77	20	4
°C	R.T.	0	−5	−34	−40	−45	−50	−54	−60	−83	−85	−100	−120	−133	−150	−160	−174	−196	−253	−269

TABLE 2—*Metal alloys investigated.*

Alloy	Cryogenic Temperatures	Noncryogenic Temperatures
Aluminum	...	2024-T351, 7475-T761, 7475-T7651
Magnesium	Mg-Nd-Zr, Mg-Y-Cd, Mg-Y-Cd-Zb	...
Titanium	Ti-5Al-2.5Sn	Ti-30Mo
Austenitic stainless steel	304,310,316, Mod A-286	304
Manganese stainless steel	18Mn, 32Mn, 35Mn	25Mn
Other steels and iron	4340	Iron, HSLA, Fe-Si, mild steel Cast steels: 0030, 0050A, C-Mn, Mn-Mo, 8630

peratures were controlled by evaporating liquid nitrogen along with a heater control system. In one study an automated CO_2 system was used for temperatures between 239 and 213 K (−34 and −60°C).

The constant-amplitude fatigue crack growth behavior was analyzed in terms of *da/dN* versus applied ΔK or versus effective ΔK. In the one paper that dealt with $R = -1$, ΔK was taken as the positive range (i.e., $K_{max} - 0$). The effective ΔK value was principally equal to $K_{max} - K_{op}$, where K_{op} is the crack opening value usually obtained from compliance readings. Four papers included the entire sigmoidal *da/dN*–ΔK behavior, three papers included only threshold or near-threshold behavior, and six papers were concerned with *da/dN* values of about 10^{-8} m/cycle or greater.

Constant-amplitude FCG resistance at low temperatures was found to be better, worse, about the same, or mixed compared with room temperature FCG. The FCG behavior was dependent upon the test temperature and the material. When several low temperatures were reported, the FCG resistance usually increased as the temperature was lowered; however, continued lowering of the test temperature caused either a continuation or a reversal of the FCG resistance. It was concluded that prediction of beneficial or detrimental low-temperature FCG behavior for a given alloy depends upon what low temperature value is being considered. Quite often, mixed FCG behavior existed at a given temperature (i.e., at low ΔK values the FCG rate was lowered and at higher ΔK values the FCG rate increased at low temperatures). Thus at higher ΔK a crossover (or at least convergence) of the low temperature and room temperature *da/dN*–ΔK curves often occurred. Crossover has occurred in many alloy systems; in these investigations, crossovers occurred in 4340 steels and Ti-5Al-2.5Sn at cryogenic temperatures and in 7475 aluminum, mild steel, and in several cast steels and magnesium alloys at noncryogenic temperatures. Crossover at higher *da/dN* or ΔK values is attributed here to decreases in static and cyclic fracture toughness (K_c and K_{fc} respectively) at low temperatures and to a transition from ductile-type fatigue crack growth mechanisms, to a mixed ductile/cleavage mode, and finally to a cleavage mode as da/dN or ΔK increases. This crossover or convergence resulted in the Paris exponent (n) increasing at low temperatures. Values of n as high as 8 were reported at low temperatures.

In some tests, the entire sigmoidal curve was shifted to the left at low temperatures, which indicated beneficial behavior at all ΔK values at low temperature. In other tests, where only threshold and near threshold results were obtained, low-temperature ΔK_{th} values were equal to or greater than those at room temperature. Thus, under all low-temperature conditions reported here, the applied ΔK_{th} at low temperature was never less than the applied ΔK_{th} at room temperature. This improved, or at least equivalent, low-temperature ΔK_{th} occurred in aluminum, magnesium, and titanium alloys, ferritic and martensitic steels (wrought and cast), and in austenitic stainless steels. In many cases the low-temperature fatigue crack growth mechanisms in the ΔK_{th} or near-ΔK_{th} region were ductile transgranular; in several cases, however, they were found to be cleavage modes that yet had ΔK_{th} values equal to or greater than at room temperature.

Analysis of FCG data was based heavily upon electron fractography findings and crack closure measurements. Crack closure at room temperature appears to be much more important at low ΔK values than at high values. The findings also indicate the importance of crack closure at low-temperature near-threshold conditions. Crack closure has been attributed to oxides, geometry, and reversed crack tip plasticity. Under the low-temperature test conditions, humidity or moisture is very low; hence low-temperature crack closure can be attributed more to reversed crack tip plasticity, geometry, and Mode II displacements. In some cases the authors indicated that crack closure was the important consideration in the low-temperature near-threshold results, including R ratio effects, and in other cases the fracture process was suggested as being of greater importance. The applied ΔK_{th} values at low temperatures were found to be both R ratio dependent and somewhat independent.

One of the more influential factors on FCG of body-centered-cubic (bcc) metal alloys is the ductile/brittle transition phenomenon. Several authors included monotonic transition conditions, namely Charpy V-notch, notched slow bend, or drop weight test data. These values, however, did not quantitatively correlate well with ductile/brittle transitions under fatigue conditions. However, under cyclic conditions, when cleavage was present, the cleavage percentage increased as the temperature was lowered, which is consistent with monotonic transition results. These investigations indicate that FCG ductile/brittle transitions occur at temperatures below monotonic transitions.

Constant-amplitude FCG of welds was investigated in three papers. In each case the FCG behavior of the weld metal was reasonably similar to that of the base metal. All the previous statements made for base metals appear applicable to weld metals. No major differences appeared, except that residual stresses caused much greater complications. One author suggested that residual stresses rather than low temperature was the dominant factor in his weld results.

Spectrum FCG results were reported for 2024 and 7475 aluminum alloys at 219 K (−54°C) and with five cast steels at three low climatic temperatures between 239 K (−34°C) and 213 K (−60°C). The chosen spectra represented typical load histories that could be found in the specific application. The effect of room temperature tensile overloads on FCG at 20 K was also investigated with 4340 steel and 304 stainless steel. These overloads were found to be beneficial. The FCG resistence for both aluminum alloys under spectrum loading was better at 219 K (−54°C) than at room temperature (including that for single tensile overloads with 7475). Under constant-amplitude conditions, the 219 K (−54°C) temperature FCG resistance compared to that at room temperature was better for 2024 but a crossover existed for 7475. Thus 2024 spectrum FCG results at low temperature were in agreement with constant-amplitude FCG results. For 7475, however, the spectrum and constant-amplitude low-temperature results were partially in conflict. The authors explained this conflict by noting that most loadings in the spectrum caused low values of K_{max} or ΔK, which would then be consistent with the constant-amplitude results. Spectrum FCG life with four of the five cast steels tended to increase as the temperature was lowered and then a reversal occurred. Even so, at all test temperatures investigated, four of the five cast steels had better FCG resistance at the low climatic temperatures than at room temperature. The fifth cast steel, 0050A, where nil ductility transition (NDT) temperature was room temperature, had a continuous decrease in spectrum FCG resistance as the temperature was lowered. These reversals and the poor FCG resistance were attributed to changes in crack growth rates and decreases in cyclic fracture toughness. Under constant-amplitude conditions, crossovers occurred in several of these cast steels including 0050A. Thus correlations between constant- and variable-amplitude FCG at low temperatures still remain conjectural. However, the crack initiation life in these five cast steels, defined as a visible surface crack of 0.25 mm emanating from a keyhole notch ($K_t = 4$), was always greater at the three low climatic temperatures than at room temperature.

Two papers included cyclic changes under strain-controlled low-cycle fatigue conditions at cryogenic and noncryogenic temperatures. The results indicated that both cyclic strain softening and hardening can be present at these low temperatures. Greater cyclic softening was evident in 300 series and high manganese stainless steels at cryogenic temperatures than at room temperature. The authors suggested this softening was influential in increasing the low cycle fatigue life at the cryogenic temperatures. Under the cyclic conditions the upper and lower yield points found under monotonic conditions in low or medium strength cast steels were removed at both room and low climatic temperatures. Cyclic yield strengths generally increased about 10% for the five cast steels investigated. At 228 K (−45°C) the smooth specimen fatigue resistance of the five cast steels was greater than at room temperature at long lives but was similar or decreased at short lives. This behavior seems to parallel much of the FCG behavior.

A fiberglass epoxy laminate uniaxial specimen was designed and tested at room temperature and 20 K. The specimen design was satisfactory, and the test results indicated that *S–N* tests at 20 K had greater life than at room temperature. The laminate was considered satisfactory for the intended cryogenic purpose.

The results of these 16 papers taken together indicate that low-temperature fatigue resistance is much more sensitive to chemical composition and microstructure than fatigue resistance at room temperature. In many situations, metal alloy systems designed for a specific temperature range may be very successful under fatigue conditions. However, ductile/brittle transitions, lower cyclic fracture toughness, and increased composition and microstructure sensitivity at low temperature still tend to create a strong concern involving fatigue at low temperature. Cumulative experience and proper simulated and field testing will be keys to the success of a product under cyclic loading at low temperature. The needed principal research is to determine a relationship between low-temperature fatigue resistance and one or several of these factors: composition, microstructure, and a simple parameter such as one from a monotonic test of notched or smooth configurations at the prescribed test temperature.

R. I. Stephens
Mechanical Engineering Department, The University of Iowa, Iowa City, IA; symposium chairman and editor

Index

ISBN 0-8031-0411-1